3D KINEMATIC AND STRENGTH BEHAVIOR OF GRANULAR MATERIALS AT THE PARTICLE-LEVEL

A Dissertation Presented for the

Doctor of Philosophy

Degree

The University of Tennessee, Knoxville

Mehmet Burak Cil

May 2015

To my wife Saliha and my son Ahmet Asım

&

To my family

ACKNOWLEDGEMENT

Firstly, I would like to express my sincere appreciation to my academic advisor Dr. Khalid Alshibli for his guidance, constant encouragement and support throughout my graduate study. He has provided an excellent academic environment to advance my skills and technical knowledge. His professional advice and assistance have been invaluable and have helped me to become an independent researcher. I would like to thank my committee members Dr. Dayakar Penumadu, Dr. Angel Palomino, and Dr. Eric Drumm for their valuable suggestions and constructive comments.

I am grateful to Dr. Mark Rivers, Dr. Peter Kenesei and Dr. Ulrich Lienert for their help during experiments and data analysis at Advanced Photon Source (APS). My special thanks go to Dr. Kenesei for sharing his expertise with me. He taught me how to use Fable and DIGIgrain, and patiently answered all my questions about 3DXRD technique.

I would like to thank my officemates and friends, Andrew Druckrey, Ala'a Qasem, Maha Jarrar and Dr. Isaac Jeldes, for all of the help and support they provided. Also, I would like to acknowledge the financial support provided by National Science Foundation.

Finally, I am thankful to my wife Saliha, my son Ahmet Asım, my father Ahmet, my mother Şengül, and my sisters Şeyma and Hatice for their endless love, understanding, and continuous support during my Ph.D. study.

ABSTRACT

The macro-scale behavior of uncemented granular materials is governed by the particle-to-particle interactions. Therefore, accurate assessment of the micro-scale mechanics is essential for better understanding of the fundamental behavior of granular materials. Particle fracture phenomenon and force transmission mechanisms in natural granular assemblies such as sands have not been fully understood due to the lack of micro-scale experimental measurements. The objective of this dissertation is to provide key quantitative measurements about these issues using powerful non-destructive experimental 3D x-ray diffraction (3DXRD) and synchrotron micro-tomography (SMT) techniques, as well as distinct element method (DEM). 3DXRD was employed to measure the volume-averaged lattice strain of individual silica sand particles within a sand assembly under 1D compression loading condition. The evolution and distribution of particle fracture, particle fracture mechanism and deformation characteristics of sand particles subjected to 1D compression across the scales were also investigated and quantified using SMT and DEM methods. Sand particles were modeled in DEM as crushable agglomerates composed of many spherical sub-particles that were linked by parallel bonds. DEM simulations were first calibrated and validated using laboratory experiments, and then were used to quantify micro-scale processes including the contact force network, and the fracture mechanics of crushable agglomerates. In addition, DEM was adopted to examine particle kinematic behavior and the influence of boundary conditions in triaxial testing.

In first set of lattice strain measurements performed on a column composed of three sand particles, the normal strain along the loading direction increased in a linear fashion as the compression proceeded until one of the sand particle fractured. However, significant variation and fluctuations were observed in the measured lattice strain tensor components of sand particles for relatively larger specimen due to complex deformation behavior and a non-homogenous contact force network. The SMT images and DEM model revealed that particle fracture concentrates at certain locations close to the loading platen, and the onset of particle fracture and specimen yielding occur at the same strain level in a 1D compression test. Finally, triaxial test DEM simulations showed that a flexible membrane better replicates the uniformly applied confining stress compared to a rigid boundary.

TABLE OF CONTENTS

LIST OF TABLES

LIST OF FIGURES

CHAPTER 1

INTRODUCTION

Background

Granular materials are composed of discrete solid particles with ranges of particle size and morphology. They are the second most manipulated material after water (de Gennes 1999) and are utilized in many engineering and industrial applications including the pharmaceutical industry, food processing, chemical industry, mining, civil engineering projects and energy production. A better understanding of the fundamental behavior of granular materials is necessary in order to improve the performance of applications and processes involving particulate systems and to minimize failures such as landslides, liquefaction during earthquakes, and slope failures. Although extensive research has been performed during the last six decades in the field of geomechanics, many questions remain unanswered.

The response of granular materials to applied stresses is highly complex and influenced by several internal and external factors, including material state (density), applied stress, material fabric and the physical properties of individual particles (size and morphology). When a particulate system is subjected to a macroscopic loading, the applied stress is transmitted through particle contacts, and the deformation occurs in the form of particle motion (translation and/or rotation) or particle deformation (fracture). The discrete nature of granular media at the micro-scale is inherently discontinuous and anisotropic, and plays a fundamental role on the macro-scale response.

Extensive research has been performed to investigate the constitutive behavior and deformation characteristics of granular materials in the geomechanics research community. The majority of the studies until 1990s focused on the macroscopic behavior of the material. Similarly, most of the constitutive models described the granular media with continuum theories to characterize and model its behavior. However, phenomenological approaches fail to represent the influence of micro-scale intrinsic properties. During this period, researchers could not investigate particle-to-particle interactions under shear/uniaxial loading due to the incapability of conventional approaches in attaining micro-scale data. However, this trend has changed in the last two decades thanks to advances in experimental and numerical approaches which provide new opportunities to investigate the micromechanical behavior.

Researchers extensively used distinct element method (DEM) and advanced imaging techniques such as x-ray computed tomography (CT) and synchrotron x-ray micro tomography (SMT) to gain insight into the deformation characteristics of granular materials. DEM which is the most commonly used numerical method in the field of geomechanics, permits acquiring micromechanical information such as particle motion and inter-particle contact forces. The main limitation of the DEM approach is its inability to reproduce the complex particle morphology. X-ray CT and SMT can yield high-resolution 3D images of geomaterials which allows in situ monitoring of deformation mechanism and particle kinematics under various loading conditions. However, inter-particle contact forces cannot be measured using 3D imaging techniques, which is the major shortcoming of these techniques.

Although previous studies made valuable contributions to advance our understanding of the fundamental behavior of granular materials, the force transmission mechanism on natural materials has not been fully understood due to the lack of contact force measurements. Moreover, particle fracture phenomenon which plays a significant role on macroscopic mechanical behavior has not been examined in situ non-destructively in the literature. This dissertation is intended to present key measurements about these issues since understanding the characteristics of heterogeneous contact network, kinematic properties of particles and particle fracture phenomenon in granular soils at particle and specimen scales in 3D is crucial to comprehend the role of particle-level interactions on macroscopic response. Furthermore, such micromechanical information is necessary to develop a micromechanics-based constitutive model that will help to prepare better design guidelines and to provide optimized engineering solutions for maximum design performance.

In order to characterize the underlying micromechanics of granular material response, this dissertation utilized from the powerful capabilities of three-dimensional x-ray diffraction (3DXRD), DEM and SMT techniques. An overview of the research plan is shown in Figure 1.1. 3DXRD is a revolutionary non-destructive experimental technique for structural characterization of crystalline materials. It allows robust determination of the crystallographic orientation, position and shape of individual grains embedded in a polycrystalline. Polycrystalline materials are composed of many crystalline grains, and each grain has a particular orientation. Therefore, grain does not refer to "particle" term which is commonly used in geomechanics studies. Since each silica sand particle is a single crystal, 3DXRD has the potential to measure the deformation of each individual sand particle within a sand assembly during macroscopic loading. 3DXRD provides a unique opportunity to directly acquire information about the interaction of individual particles.

DEM is a computationally efficient numerical approach to model the independent interactions of particles using an explicit time stepping algorithm. DEM was the preferred technique to simulate the complex mechanical behavior of granular media since most of the continuum-based numerical approaches do not take into account the discrete nature at micro-scale. Although the particles in DEM are assumed as rigid (unbreakable), the particle fracture can be

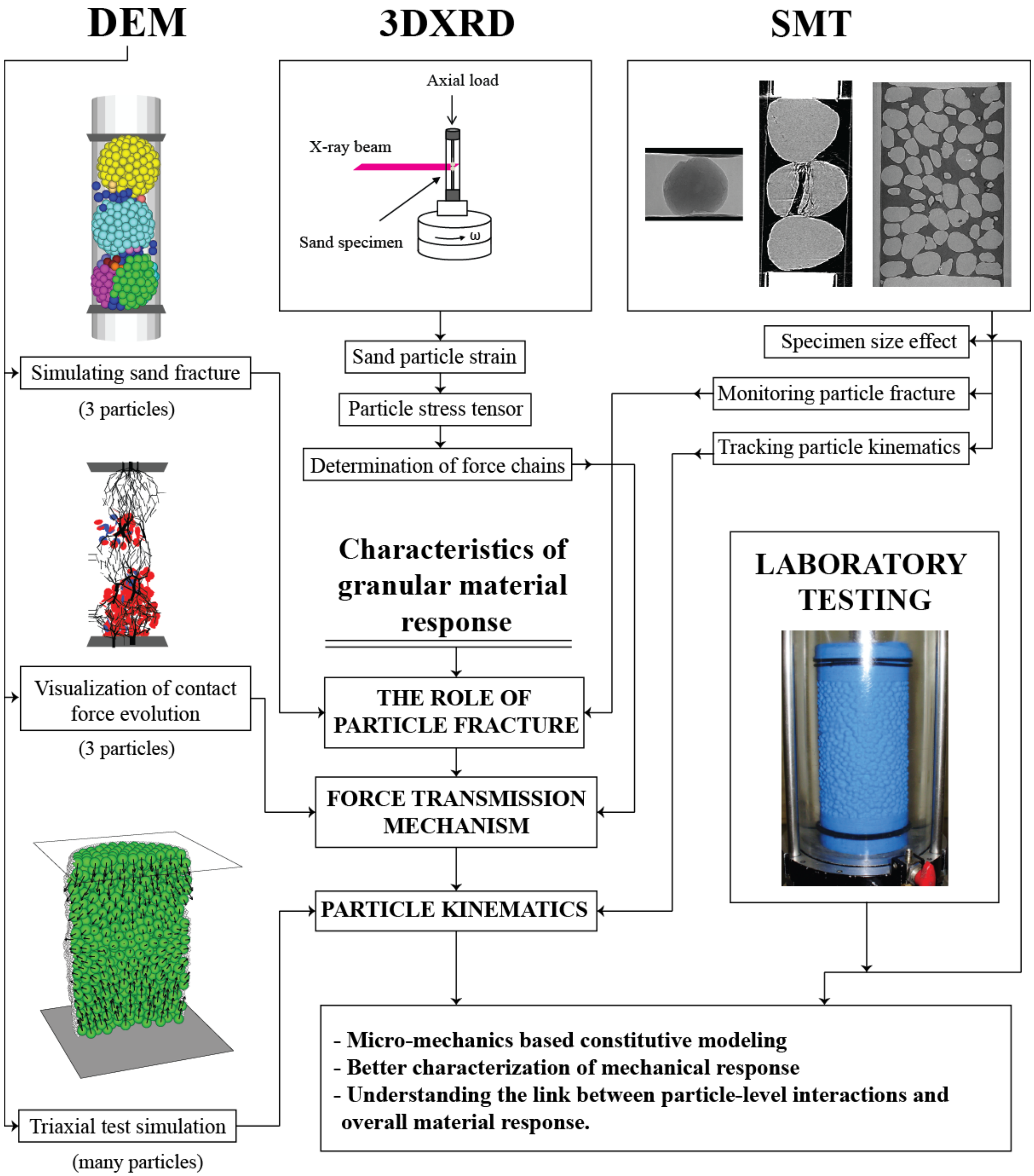

Figure 1.1. The roadmap and objectives of the dissertation.

modeled with agglomerate of spherical sub-particles that are bonded at the contact points. Physical element tests at different specimen scales can be simulated in a virtual environment using DEM. Moreover, DEM permits visualizing the contact force network, bond breakages in agglomerates and attaining full particle kinematics (translational and rotational) throughout the simulation.

SMT is a non-destructive 3D imaging technique that can produce 3D high-resolution images of material using x-ray transmission. SMT enables images to be acquired with enhanced spatial resolution (typically between 1 and 10 μm), which makes it favorable among the 3D imaging techniques and sufficient for quantitative analysis of images of granular media under various loading conditions. 3D SMT images provide an excellent opportunity to monitor the evolution and distribution of particle fracture and deformation behavior in a sand assembly at micro- and macro-levels. Although 3DXRD, DEM and SMT techniques have powerful capabilities, they have some limitations which are summarized in Table 1.1.

Objectives

The main objective of this dissertation is to characterize the micromechanical behavior of granular soils using advanced experimental and numerical techniques. Quantitative measurements acquired at the particle-level will help to advance our understanding of the relationship between particle-scale interactions and the macroscopic response. The specific objectives of the dissertation are described as follows:

- Measure the lattice strain tensor of individual sand particles within a granular assembly non-destructively during 1D compressional loading. These measurements will provide

Table 1.1. The limitations/disadvantages of 3DXRD, DEM and SMT techniques.

Technique	Limitations / Disadvantages
3DXRD	• A synchrotron x-ray facility is required to perform experiments. • The number of grains that can be indexed in a diffraction data is limited due to spot overlap problem. • Diffraction spots broaden and ultimately overlap as a result applied deformation. Therefore, the diffraction spots can be tracked and indexed up to a certain deformation limit (Lauridsen *et al.* 2001).
DEM	• The available computational power limits the maximum number of particles that can be used in a DEM model. • Simplified particle shapes (e.g., spheres, ellipsoids) are generally adopted in DEM simulations due to difficulty in reproducing the complex particle morphologies.
SMT	• A synchrotron x-ray facility is required to perform experiments. • The specimen size is relatively small compared to the specimen sizes used in conventional laboratory experiments. • The lengthy scanning time (typically 10-30 minutes) to acquire SMT images is a limitation for some applications (Werth *et al.* 2010).

key answers to understand the force transmission mechanism in a particulate system for the first time.

- Monitor the evolution and distribution of particle fracture and the deformation behavior of sand assemblies across the scales (single particle to laboratory-size specimen).
- Determine the role of particle fracture phenomenon in the constitutive behavior of granular assembly.
- Obtain and quantify micro-scale processes such as kinematic properties of particles, contact forces and fracture of individual particles in granular materials under compressive loading.

Dissertation Outline

The dissertation starts with the introduction and review of the literature (Chapters 1 and 2). Chapters 3 through 9 are specific studies that have been published or will be published in peer-reviewed technical journals or conference proceedings. A brief summary of each chapter is presented here:

Chapter 1 presents an introduction to the research problem, and describes the motivation and objectives of the dissertation.

Chapter 2 presents background information on DEM and 3DXRD methods. Initially, a brief review of DEM, some of the previous DEM studies and particle flow code in three dimensions (PFC3D) are described. Then, the basics of x-ray diffraction phenomenon and the geometric principles of 3DXRD are summarized.

Chapter 3 describes the use of 3DXRD technique to measure particle-averaged lattice strain of individual silica sand particles under 1D compressional loading. The details of the experimental work, diffraction data analysis and lattice strain calculation are explained. The evolution of the elastic lattice strain and volumetric strain of individual sand particles as a function of applied load are evaluated and discussed.

Chapter 4 presents the experimental assessment of the deformation characteristics of silica sand particles using combined 3DXRD and SMT methods. The advantages of combining these two powerful techniques and their basic principles are presented. The computation of the lattice stress tensor from the lattice strain measurements obtained in Chapter 3 are explained and the stress-strain relationships of individual sand particles are discussed.

Chapter 5 builds on the work of Chapter 3. The same technique is applied on a specimen composed of a larger number of natural silica sand particles. Moreover, SMT capabilities were incorporated in the same experiment setup, which allowed combining SMT and 3DXRD methods to gain insight into the deformation characteristics of sand particles.

Chapter 6 presents a DEM study that adopts a new approach to simulate the fracture of silica sand particles. The details of the proposed DEM model are explained. The fracture mechanics of particles under compression are examined using DEM simulations and 3D SMT images at different specimen scales.

In Chapter 7, the particle fracture model presented in Chapter 6 is applied to specimens composed of a larger number of particles. The evolution of particle fracture and deformation behavior of silica sand specimens subjected to 1D compression are investigated with the help of

SMT and DEM methods. The role of particle fracture on the macroscopic behavior of granular materials is discussed.

In Chapter 8, the particle fracture modeling approach introduced in Chapter 6 is improved such that the 3D physical shape of sand particles were closely captured in the DEM model by mapping the 3D volume data from SMT images. The influence of packing configuration of spherical sub-particles that constitute crushable agglomerate is also investigated.

In Chapter 9, the constitutive behavior and particle kinematic properties of granular materials in triaxial testing are characterized using DEM and CT. Particle kinematics obtained from CT measurements are compared with the DEM simulation results. The influence of boundary conditions in triaxial test simulation, and the capability of the DEM model in reproducing particle-level interactions are discussed.

Chapter 10 presents a summary of the major findings and outcomes of the dissertation, and some recommendations for future work.

References

de Gennes, P. G. (1999). "Granular matter: a tentative view." Reviews of Modern Physics, 71(2), S374-S382.

Lauridsen, E. M., Schmidt, S., Suter, R. M., and Poulsen, H. F. (2001). "Tracking: a method for structural characterization of grains in powders or polycrystals." Journal of Applied Crystallography, 34, 744-750.

Werth, C. J., Zhang, C. Y., Brusseau, M. L., Oostrom, M., and Baumann, T. (2010). "A review of non-invasive imaging methods and applications in contaminant hydrogeology research." J Contam Hydrol, 113(1-4), 1-24.

CHAPTER 2

LITERATURE REVIEW

Introduction

The following Chapters of the dissertation (Chapter 3 through Chapter 9) focus on specific studies and each of these chapters includes a relevant literature review in its introduction. Rather than repeating same material here, this Chapter explains some of the related research background which will serve as a foundation for the rest of the dissertation. Distinct element method (DEM), some of the previous DEM applications and particle flow code in three dimensions (PFC3D) are initially described. Then, some fundamental concepts about x-ray diffraction, the experimental setup and geometric principles of the three-dimensional x-ray diffraction (3DXRD) technique are presented.

Distinct Element Method (DEM)

DEM is a discontinuum-based numerical approach that models the movement and interactions of individual elements/bodies in a granular assembly using an explicit time stepping scheme. DEM was initially developed to study rock mechanics (Cundall 1971), and then used to model the behavior of granular media by Cundall and Strack (1979). It is the most widely used particle-based discrete element modeling code in geomechanics research studies. DEM provides a unique opportunity to obtain quantitative particle-scale measurements such as particle rotation, particle displacement, and contact forces, which are difficult to quantify using conventional experimental techniques. DEM technique enables simulating independent motion of each particle in a granular media, which is ignored in continuum-based tools such as the Finite Element Method (FEM).

DEM allows performing experiments in a virtual laboratory, in which internal measures such as void ratio, particle shape, and particle size distribution can be varied easily to examine the effect of a particular parameter on the behavior of granular materials. Furthermore, the same specimen can be generated and tested repeatedly at different loading conditions, which is difficult to achieve in the laboratory due to variation of fabric in the preparation of each specimen.

Previous studies

DEM is used in a variety of disciplines including chemical engineering, pharmaceutical industry, process engineering and geotechnical engineering. Despite the wide use of DEM in research studies, it has been rarely adopted in industrial applications, which may change in the near future with the help of advances in computational power and improvements in DEM codes (O'Sullivan 2011). After the development of the original DEM code BALL by Cundall and Strack (1979), many researchers adopted the modified version of this code in their investigations. PFC2D and PFC3D (Itasca 2008) which are the improved versions of BALL in 2D and 3D, respectively, are the most commonly employed commercial DEM codes by the geomechanics research community. Moreover, new commercial codes (DEM solutions 2014) and open source codes (e.g., Kozicki and Donzé 2008) have become available in recent years (O'Sullivan 2011). Although the majority of the DEM studies model the behavior of particulate systems, the response of fine-grained soil is also simulated using DEM by a few researchers (Lu *et al.* 2008, Peron *et al.* 2009). This Chapter mostly focuses on the applications of DEM to granular materials.

Several researchers adopted DEM to model laboratory tests including triaxial, plane strain, and direct shear tests. Powrie *et al.* (2005) carried out several plane strain test simulations with a flexible membrane using PFC3D software. Each particle was formed by bonding two spheres with a high parallel bond. They found that boundary constraints (the roughness of loading platens) have a significant influence on the formation of shear bands. Cui and O'Sullivan (2006) performed direct shear simulations using 3DDEM program and found similar responses between the macro-scale behavior of DEM simulations and experiments on idealized steel spheres. They examined the micromechanical behavior of the granular material during direct shear test and identified considerable stress and strain variations within the specimen. Belheine *et al.* (2009) simulated drained triaxial tests of Labenne sand in 3D using spherical particles. Rolling resistance was included in the DEM model to represent the actual sand particle roughness. They investigated the influence of micro-parameters on the overall material response and found that both local friction and rolling resistance value affect the peak stress. Lee *et al.* (2012) modeled a series of drained and undrained triaxial compression tests in 3D with BLOKS3D DEM code. They used polyhedral particles to obtain realistic particle shapes. The flexible membrane in triaxial test simulations was represented with 120 rigid rectangular cuboid discrete elements. They found a reasonable agreement between simulation and experimental results and concluded that using relatively larger particle sizes is the main reason for errors observed in DEM simulations.

DEM has been widely used to understand the development of strain localization phenomenon in granular materials. Iwashita and Oda (2000) investigated the underlying micromechanics of shear band formation by conducting 2D biaxial test simulations with a flexible membrane using modified DEM (MDEM), which considers the rolling resistance at the contacts. They observed that particles form column-like structures (force chains), which carry the majority of the load in axial direction, during the hardening process until the peak stress. These column-like structures buckle during the strain softening, which results in the formation of a high rotation gradient in a narrow shear zone. They explained the shear band phenomenon in granular materials with this micro-deformation mechanism using the biaxial simulation results. Moreover, several DEM studies were performed to investigate the characteristics of shear bands (thickness and inclination) and to identify the influence of material properties in strain localization (e.g., Iwashita and Oda 1998, Hu and Molinari 2004, Mohamed and Gutierrez 2010).

Pioneering DEM studies generally adopted idealized disc/spheres to represent particles in 2D/3D simulations. These idealized particle shapes are unable to represent the irregular particle morphologies observed in real granular materials. Progress in computational resources and DEM codes enabled researchers to employ complex particles shapes such as clusters of spheres (Katagiri *et al.* 2010), ellipsoids (Ng 2009), and polygons (Peña *et al.* 2007). Recently, some researchers proposed new approaches to better reproduce the actual particle morphologies. Andrade *et al.* (2012) used Non-Uniform Rational Basis-Splines (NURBS) in the granular element method (GEM) to closely capture the actual shape of the particles that can be acquired via x-ray CT technique. Mollon and Zhao (2013) utilized Fourier descriptors to generate realistic particle shapes for 3D DEM applications.

Although, DEM was generally used in small-scale geomechanics studies, some field scale applications were also modeled using DEM. Jiang *et al.* (2006) performed 2D cone penetration simulations to understand the effect of the friction coefficient between the soil and penetrometer. They simulated only half of the problem due to symmetry, and significant variations in displacement and velocity fields were found around the penetrometer. Arroyo *et al.* (2011) modeled cone penetration in a calibration chamber in 3D. They applied the cone/chamber size effect correction to cone penetration resistance, and obtained similar findings to the experimental data. Some researchers also investigated the material-machinery interaction with the help of DEM (Nezami *et al.* 2007, Huang and Detournay 2008).

Particle Flow Code in Three Dimensions (PFC3D)

PFC3D is a commercial software developed by Itasca (Itasca 2008) and used to simulate the independent interaction of a collection of particles by adopting the distinct element algorithm as described by Cundall and Strack (1979). Particles in PFC3D model are considered to be incompressible (rigid), and have a finite stiffness and inertia. They are allowed to overlap at contact points and the overlapping region is assumed as negligibly small (soft contact approach). Since circular/spherical particles can only interact at contact points, each particle contact consist of two particles. The particles at a contact may be linked together with a bond which can resist both force and moment. More complex particle shapes can be generated in PFC3D using the clump logic which is implemented by attaching two or more overlapping particles together. The clump is a rigid element and has the same contact behavior as spherical particles (Itasca 2008).

In a PFC3D model, the particulate system and boundary conditions are defined initially based on the test or application to be simulated. Then, the contact constitutive model and material properties (interparticle friction, stiffness and particle density) are specified. The standard Hertz and linear contact models and a variety of alternative contact models are available in PFC3D (Itasca 2008). Particles may need to be bonded together to reproduce the effect of adhesion or cementation, which depends on the structure of the simulated material. PFC3D provides two types of bonding models (Itasca 2008): (1) contact bond and (2) parallel bond. Both of these bond types hold two particles together like a glue until the bond breaks. The contact bond acts over a vanishingly small area and resists only normal and shear forces. On the other hand, the parallel bond acts over a circular cross-section on the contact plane of two bonded particles. It mimics the effect of cementatious material and can resist both force and moment. These bonds break if the normal or shear stress value at the contact exceeds the specified bond strength values (Itasca 2008).

In PFC3D, the movement and interaction of particles are considered as a dynamic behavior which is simulated by adopting an explicit forward time-stepping algorithm. This algorithm is represented by a calculation cycle (see Figure 2.1) and implemented by repetitive application of Newton's second law and force-displacement law (Itasca 2008). Initially, the contact information is updated at the beginning of each time step based on the known particle and wall positions in the system (Itasca 2008). Contacts that form and break during the simulation are identified automatically. Relative movement between two contacting elements and the specified contact constitute model are used to determine contact forces at each contact using force-displacement law (Itasca 2008). Newton's second law is employed to update the translational and rotational motion of each particle resulting from the applied forces (Itasca 2008). Velocities and accelerations are assumed as constant during each timestep. These sets of calculations are repeated at each time step during simulation, and the response of the particulate system is predicted. The primary requirement of the central difference time integration scheme adopted by PFC3D is that the timestep should be small to maintain the stability of the computed solution (Itasca 2008).

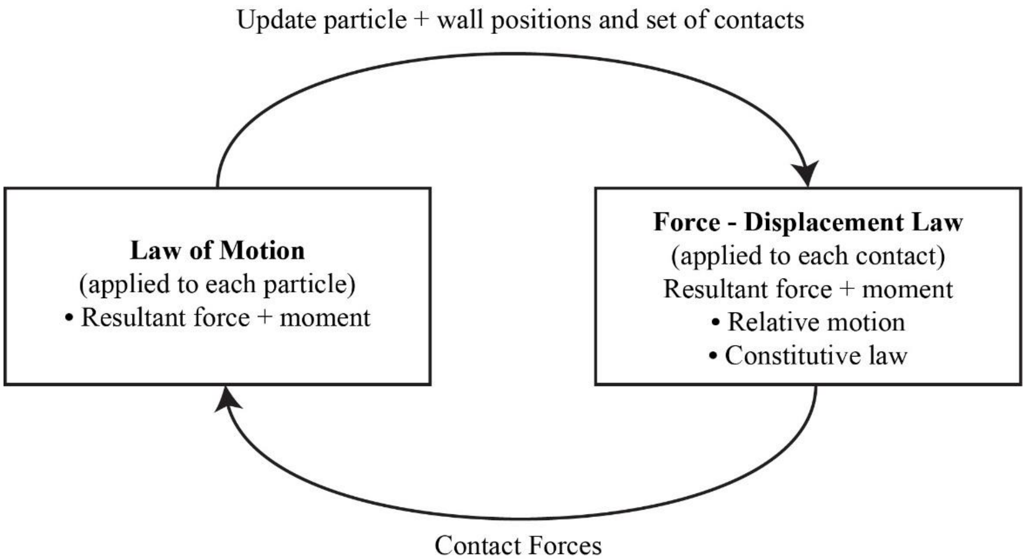

Figure 2.1. Calculation cycle in PFC3D (Itasca 2008).

Fundamentals of Three Dimensional X-ray Diffraction (3DXRD)

Introduction to x-ray diffraction

Crystalline materials consist of a uniquely oriented atomic structure which exhibits a periodic pattern in three dimensions (Cullity and Stock 2001). The translational symmetry of crystals can be represented with lattice theory, which is a network of points that are arranged as a set of identical points, lattice points, in 3D space (Cullity and Stock 2001). The crystal lattice is constructed according to the periodic atomic structure. The smallest repeated element in a crystal lattice is called unit cell, and its vertices are lattice points. Crystallographic unit vectors (axes) **a**, **b**, and **c** are used to define the geometry of the unit cell (He 2009). The lengths of the edges of a unit cell (a, b, c) and the angles between them (α, β, γ) are together defined as the lattice parameters (constants) of the unit cell (He 2009). Crystallographic unit vectors and lattice parameters are illustrated in Figure 2.2.

Many microstructural properties of crystals and x-ray diffraction phenomenon can be better understood and formalized by defining directions and planes that have a different density of atomic elements. The crystal (lattice) direction is a line between the origin of the lattice and a particular point. Crystal directions which are also called lattice vectors are expressed with three indices (u, v, w) (He 2009). Indices are the axis coordinates of the end point of the vector and can have positive or negative values. If the end point coordinates are non-integers, they are multiplied by suitable numbers to get to the closest integer value. Square brackets, [*uvw*], are used to refer to a specific vector direction, and a family of directions is represented by triangular brackets <*uvw*> (He 2009). Three crystal directions ([001], [111], [100]) are depicted in Figure 2.3.

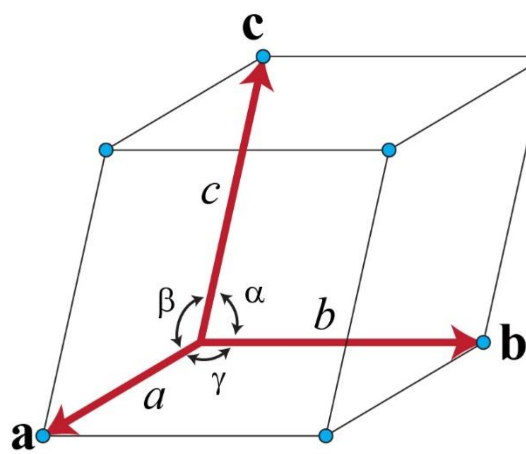

Figure 2.2. Illustration of a unit cell, crystallographic vectors and lattice parameters. Adapted from He (2009).

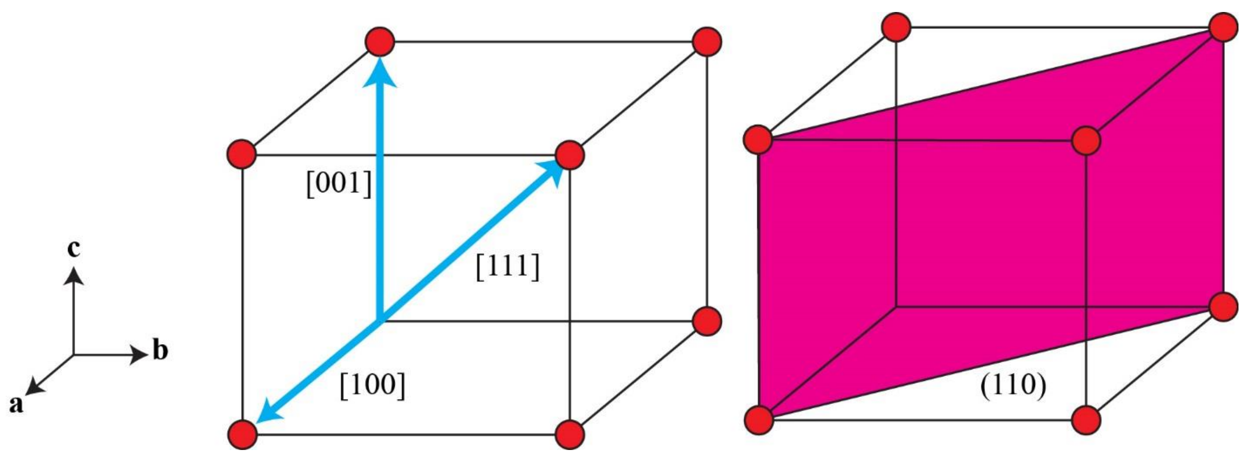

Figure 2.3. Indices of three lattice directions (left), and Miller indices of a lattice plane (right).

Crystallographic (lattice) planes are imaginary planes linking lattice points. In a crystal lattice, the orientation of planes is expressed with a special notation system known as Miller indices (He 2009). Planes are described with three integers (*h, k, l*) which are determined by taking the reciprocal value of the intercepts of the plane on the unit cell axes (He 2009). If a plane is parallel to an axis, the corresponding Miller index for that particular axis is 0. In crystallography, the Miller indices are written between round brackets (*hkl*) to refer to a specific crystallographic plane (see (110) plane in Figure 2.3). On the other hand, a family of crystallographic planes is expressed with curly brackets,{*hkl*} (He 2009).

Diffraction theory and Bragg's Law

When an x-ray beam impinges on a specimen, some of the photons are scattered away from the incident beam direction. If the wavelength of scattered x-rays does not change, this phenomenon is called elastic (coherent) scattering (He 2009). These scattered x-rays produce diffraction data, which is directly related to the electron distribution of the material. In crystalline materials, some of the diffracted beams constructively interfere and this process produces a unique diffraction pattern, which can be used to identify the properties of the periodic atomic structure (He 2009).

The diffraction phenomenon in crystals was initially discussed by the German physicist Max von Laue in 1912 (Cullity and Stock 2001). Then, Bragg's Law (Figure 2.4) was introduced by W. Lawrence Bragg to describe the necessary conditions for x-ray diffraction in crystals (Bragg 1913). The Bragg Law is expressed with the following equation:

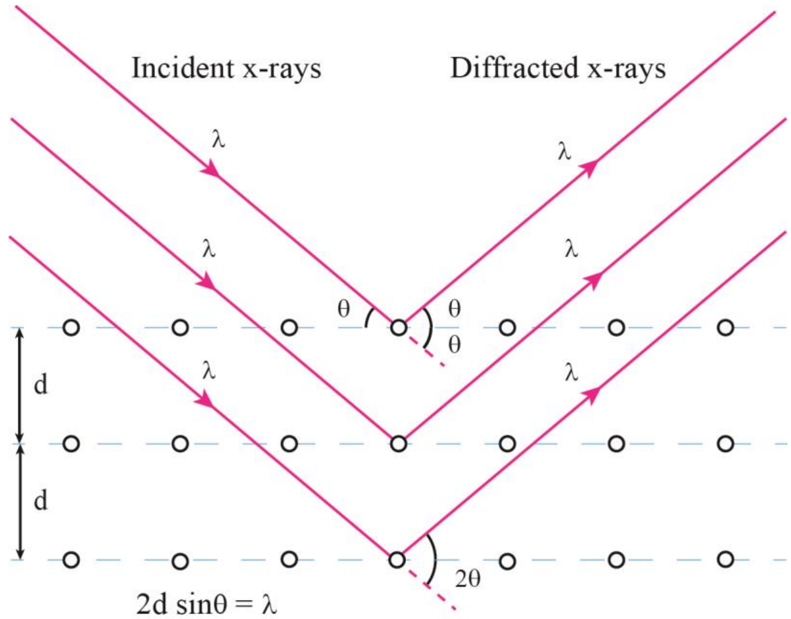

Figure 2.4. Bragg's Law reflection.

$$2d\sin\theta = n\lambda \tag{2.1}$$

where d is the distance between two adjacent crystallographic planes, λ is the wavelength of the incident x-ray beam, θ is the angle between the diffraction plane and the incident beam, and n is the order of diffraction. In experimental applications, the angle between the transmitted beam and diffracted beam (2θ) is generally used in x-ray diffraction data analysis rather than θ.

According to this mathematical description, x-rays that are scattered from two adjacent planes with an interplanar distance d interfere constructively and give rise to the diffracted beam only if they are in phase. To satisfy this Bragg condition, the path difference of these scattered x-rays should be equal to a whole number of the wavelength of the incoming x-ray ($n\lambda$) (Cullity and Stock 2001).

Reciprocal lattice

Reciprocal lattice is the Fourier transform of the direct (real) space lattice in reciprocal space. It provides a simple and useful geometrical basis to understand and formulize x-ray diffraction phenomenon in crystals. Three reciprocal lattice vectors (axes) **a***, **b***, **c*** that share a common origin are used to define the unit cell of the reciprocal lattice in reciprocal space (He 2009). Each reciprocal lattice vector is equal to the cross product of two real lattice vectors. The reciprocal lattice unit vectors are defined using real lattice vectors **a**, **b**, **c** as following (He 2009):

$$\mathbf{a}^* = \frac{(\mathbf{b} x \mathbf{c})}{\mathbf{a} \cdot \mathbf{b}\, x\, \mathbf{c}} \tag{2.2}$$

$$\mathbf{b}^* = \frac{(\mathbf{c}x\mathbf{a})}{\mathbf{a}\cdot\mathbf{b}\,x\,\mathbf{c}}$$

$$\mathbf{c}^* = \frac{(\mathbf{a}x\mathbf{b})}{\mathbf{a}\cdot\mathbf{b}\,x\,\mathbf{c}}$$

The unit cell of reciprocal lattice has six reciprocal lattice parameters **(*a**, *b**, *c**,** *α*, β*, γ*)* similar to the real space unit cell. The inter-axial angles of reciprocal space (*α*, β*, γ**) are related to the real space inter-axial angles (*α, β, γ*) as described in the following equations:

$$\cos\alpha^* = \frac{\cos\beta\,cos\,\gamma - \cos\alpha}{\sin\beta\sin\gamma}$$

$$\cos\beta^* = \frac{\cos\alpha\,cos\,\gamma - \cos\beta}{\sin\alpha\sin\gamma} \tag{2.3}$$

$$\cos\gamma^* = \frac{\cos\alpha\,cos\,\beta - \cos\gamma}{\sin\alpha\sin\beta}$$

The magnitude of unit vectors in reciprocal space is inversely proportional to the magnitude of corresponding unit vectors in real space. The relations between the lattice vectors of real space lattice and reciprocal space lattice can be expressed as (He 2009):

$$\mathbf{a}\cdot\mathbf{a}^* = \mathbf{b}\cdot\mathbf{b}^* = \mathbf{c}\cdot\mathbf{c}^* = 1 \tag{2.4}$$

$$\mathbf{b}\cdot\mathbf{a}^* = \mathbf{c}\cdot\mathbf{a}^* = \mathbf{a}\cdot\mathbf{b}^* = \mathbf{c}\cdot\mathbf{b}^* = \mathbf{b}\cdot\mathbf{c}^* = \mathbf{a}\cdot\mathbf{c}^* = 0 \tag{2.5}$$

3D reciprocal lattice is constructed by stacking the reciprocal lattice unit cell in all three dimensions. Figure 2.5 shows the unit cell and lattice vectors of the real lattice and reciprocal lattice in 3D. Each lattice point in reciprocal space lattice is expressed with three integers (*hkl*) which corresponds to crystallographic planes (*hkl*) in real space lattice (He 2009). A reciprocal

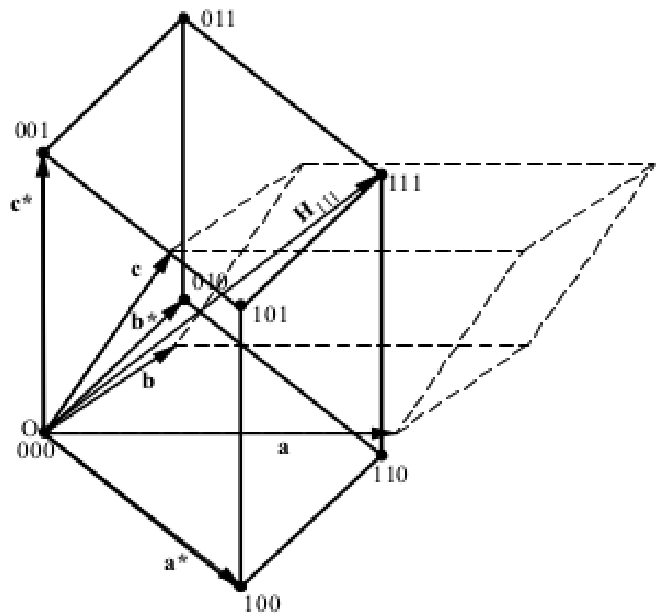

Figure 2.5. Illustration of the unit cell of real lattice (dash lines) and reciprocal lattice (solid lines) (He 2009).

lattice vector ($\mathbf{g}_{hkl}$) extends from origin to the specific reciprocal lattice point (*hkl*). $\mathbf{g}_{hkl}$ is perpendicular to the crystallographic lattice planes (*hkl*), and its magnitude is equal to the reciprocal of the interplanar spacing (d-spacing) of lattice planes (*hkl*) in direct space (He 2009). $\mathbf{g}_{hkl}$ and its magnitude can be expressed as follows (He 2009):

$$\mathbf{g}_{hkl} = h\mathbf{a}^* + k\mathbf{b}^* + l\mathbf{c}^* \tag{2.6}$$

$$|\mathbf{g}_{hkl}| = \frac{1}{d_{hkl}} \tag{2.7}$$

Synchrotron radiation at Advanced Photon Source (APS)

With the development of third generation synchrotron radiation facilities, high energy (hard) x-rays have become available to perform research in a variety of scientific fields. The characteristics of high energy x-rays (high penetration power and high flux) make them suitable for studying a wide range of materials. Currently, a limited number of third generation synchrotron x-ray sources are available in all over the world due to high construction and maintenance costs. Since the experiments for this dissertation were performed in beamline 1-ID at APS, Argonne National Laboratory (ANL), Lemont, IL, USA, the descriptions provided in this section will be specific to APS, but other facilities also adopt similar set ups. High energy x-rays are generated in multiple steps at the APS facility (see Figure 2.6). Initially, electrons emitted from an electron gun are accelerated to 450 MeV in a linear accelerator (linac) (Advanced Photon Source 2014). After that, electrons are sent to the booster synchrotron where they travel in an oval-shaped path directed by electromagnets and are accelerated to an energy state of 7 GeV via electric fields in four radio frequency (rf) cavities (Advanced Photon Source 2014). Then, the electrons are sent to the storage

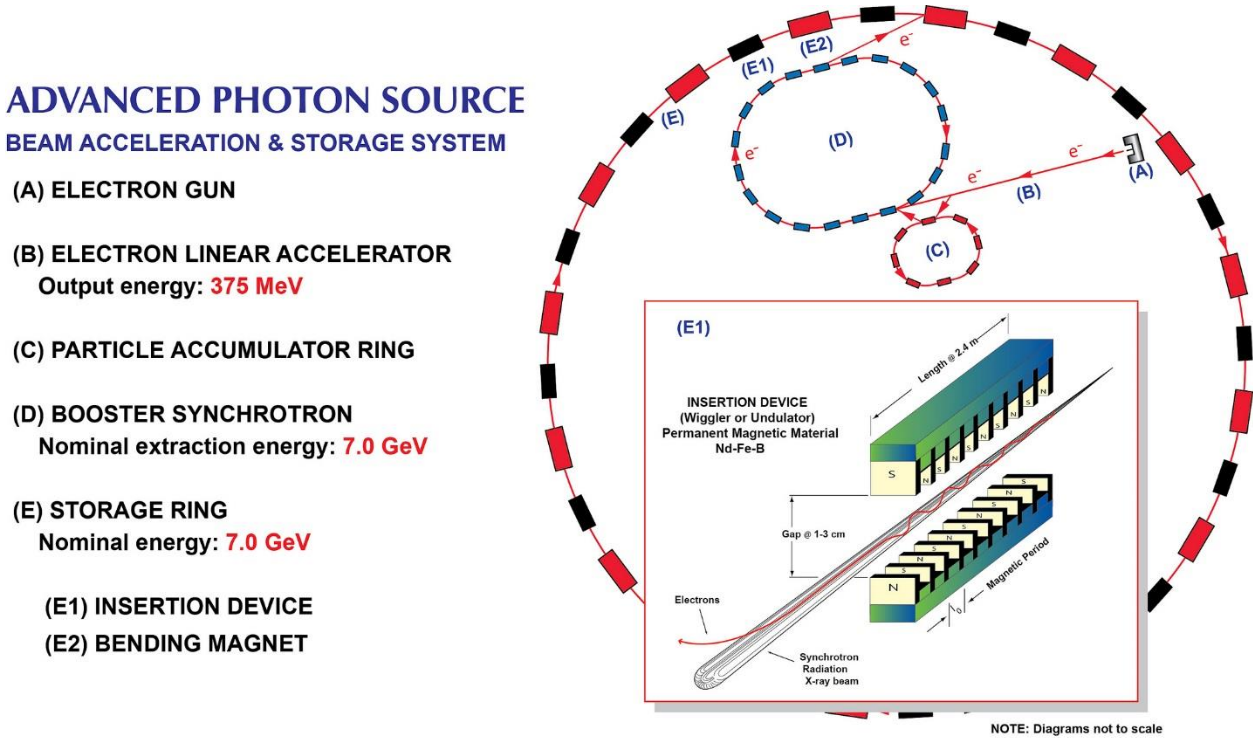

Figure 2.6. Configuration of the APS synchrotron facility (Fenner 2013).

ring where they rotate in a circular path under low pressure (Advanced Photon Source 2014). More than specially designed 1000 electromagnets generate an electromagnetic field which produces a narrow beam with low angular divergence by focusing the high-energy electrons (Advanced Photon Source 2014). The flux and brilliance of the x-rays, which are critical in x-ray studies, are maximized in third generation synchrotron storage rings. Insertion devices (undulators or wigglers) are employed to generate high energy x-rays from accelerated electrons (Advanced Photon Source 2014).

Beamline 1-ID at APS

The x-ray radiation source of 1-ID beamline at APS is Undulator A, which is composed of a series of dipole magnets (Shastri *et al.* 1998). When an electron passes through the strong magnetic field generated by dipole magnets, it oscillates, and synchrotron radiation is produced to use in the beamline. The high-energy x-rays pass through a series of specially designed optics before using them in the final experimental hutch. A monochromator is used to select the desired energy level in the range of 50 keV to 100 keV for each particular application. The arrangement of optics used for a typical far-field diffraction experiment in 1-ID beamline is showed in Figure 2.7. The first element is a premonochromater which includes two cryogenically cooled bent Si (111) Laue crystals (Shastri 2004). The high energy x-ray beam is collimated by compound reflective lenses (CRL) which are followed by the four-Si (111)-reflection high resolution monochromator. Finally, Si saw-tooth refractive lenses are placed after the monochromator to produce a line-focused x-ray beam in the end-station (Shastri *et al.* 2007).

Strain measurements are performed with a far-field detector configuration which provides the volume, volume-averaged strain, orientation and center of mass position of the grains. The geometry of the far-field high-energy diffraction in the C hutch of the 1-ID beamline is shown in Figure 2.8 where 2θ is the angle between the transmitted beam and diffracted beam, ω is the angular position of the rotation stage, η is the azimuthal angle on the 2D panel detector and is measured relative to the vertical axis, and D is the distance between the detector and specimen.

The specimen is mounted on a stage which can translate (in x, y, z directions) and rotate (about y axis) perpendicular to the incoming beam direction. The specimen is illuminated with the x-ray beam while rotating it in ω with $\Delta\omega$ angular increments. During the rotation, some parts of the illuminated volume that satisfy the Bragg condition produce diffracted beams (Poulsen 2004). These diffracted beams pass through the specimen and are acquired by a 2D detector as diffraction spots. The diffraction data of far-field experiments in 1-ID beamline is generally recorded by a 2D flat-panel amorphous silicon detector (model GE Revolution 41RT) whose dimensions are 410 mm x 410 mm (2048 x 2048 pixels) (Lee *et al.* 2008).

Coordinate systems

In order to explain and formulize the geometric principles of x-ray diffraction in 3D space, four Cartesian coordinate systems are defined: the global (laboratory) system ($\mathbf{x}_l$, $\mathbf{y}_l$, $\mathbf{z}_l$), the rotated (ω) system ($\mathbf{x}_\omega$, $\mathbf{y}_\omega$, $\mathbf{z}_\omega$), the sample system ($\mathbf{x}_s$, $\mathbf{y}_s$, $\mathbf{z}_s$) and the Cartesian grain system ($\mathbf{x}_c$, $\mathbf{y}_c$, $\mathbf{z}_c$) (Lauridsen *et al.* 2001). These coordinate systems are denoted with l, ω, s and c subscripts, respectively. The majority of the studies, including this dissertation, use the described convention in the data analysis, but a slightly different convention system was adopted in 1-ID beamline at

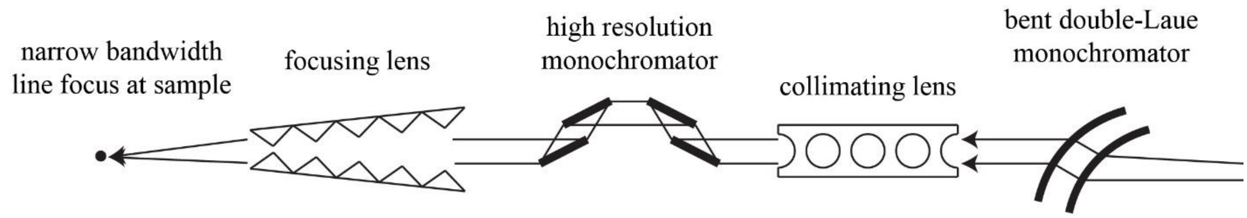

Figure 2.7. The arrangement of x-ray optics for a typical far-field diffraction experiment in 1-ID beamline of APS (Shastri *et al.* 2007, Lienert *et al.* 2010).

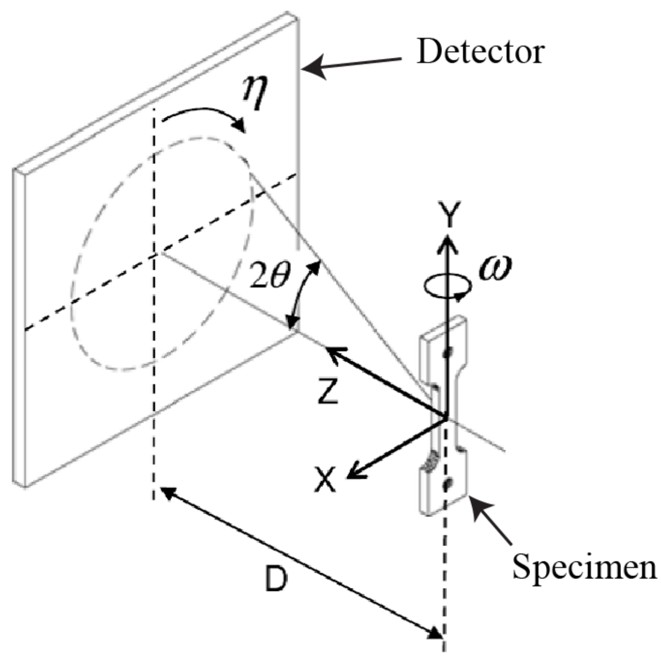

Figure 2.8. Convention system in the 1-ID-C hutch at APS (Efstathiou *et al.* 2010, Obstalecki 2011).

APS (see Figure 2.8). The global (laboratory) coordinate system used in this study is a fixed right-handed Cartesian coordinate system defined in Figure 2.9.

The direction of $\mathbf{x}_l$ axis points along the incident x-ray beam, the direction of $\mathbf{y}_l$ axis is perpendicular to $\mathbf{x}_l$ axis. The $\mathbf{z}_l$ axis is normal to the horizontal **x-y** plane and represents the ω rotation axis. The rotated (ω) system is fixed to the ω rotation stage and it coincides with the global coordinate system at ω=0° (Lauridsen *et al.* 2001). The following transformations are described for an arbitrary diffraction vector (**g**), which is normal to the diffracting crystallographic planes. The scattering vector transformations between the coordinate systems are performed according to following equations (Lauridsen *et al.* 2001):

$$\mathbf{g}_l = \mathbf{\Omega}\mathbf{g}_\omega$$

$$\mathbf{g}_\omega = \mathbf{S}\mathbf{g}_s \qquad (2.8)$$

$$\mathbf{g}_s = \mathbf{U}\mathbf{g}_c$$

Where $\mathbf{\Omega}$ is the rotation matrix and expressed as follows:

$$\mathbf{\Omega} = \begin{bmatrix} \cos\omega & -\sin\omega & 0 \\ \sin\omega & \cos\omega & 0 \\ 0 & 0 & 1 \end{bmatrix} \qquad (2.9)$$

The sample system is rigidly attached to the sample, and **S** represents the orientation of the sample on the rotation stage (Lauridsen *et al.* 2001). If the tilt of the sample system relative to the rotated system is ignored, **S** is generally taken as identity matrix (**I**). **U** (orientation matrix) is used to describe the orientation of a single grain relative to the sample system and expressed with Euler angles $(\phi, \varphi_1, \varphi_2)$ (Bunge 1982) as follows (Lauridsen *et al.* 2001):

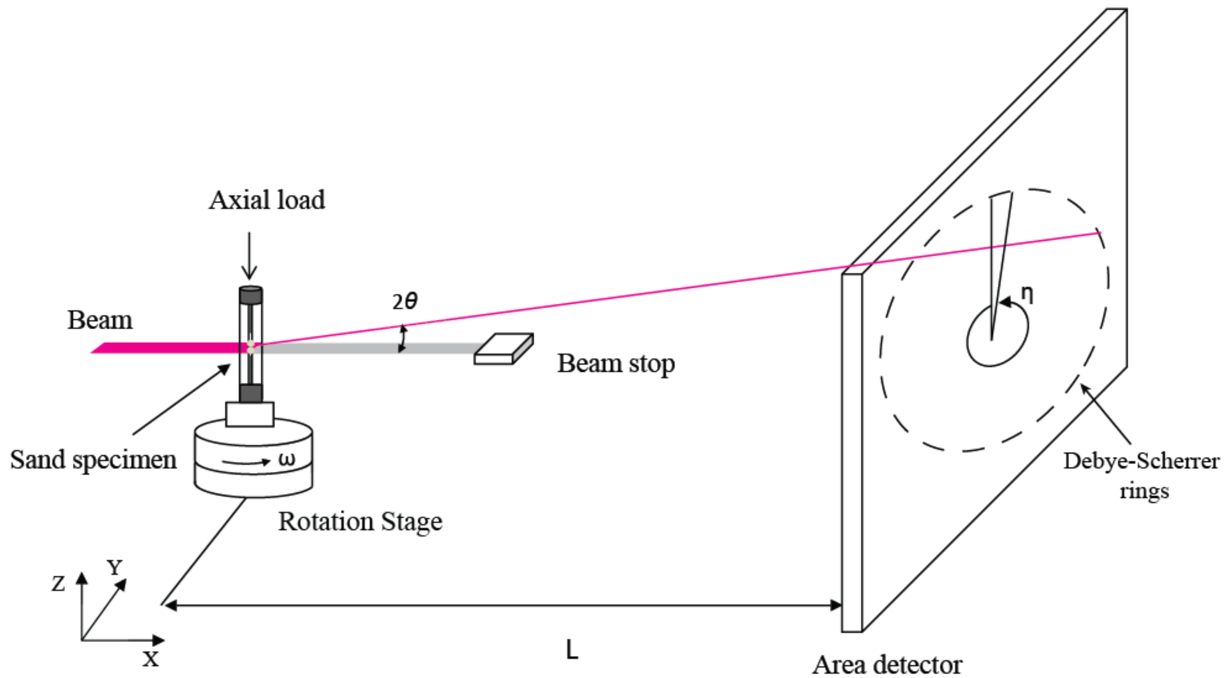

Figure 2.9. Schematic of far-field diffraction experiment setup.

$$\mathbf{U} = \begin{bmatrix} \boldsymbol{c\varphi_1 c\varphi_2 - s\varphi_1 s\varphi_2 c\phi} & \boldsymbol{-c\varphi_1 s\varphi_2 - s\varphi_1 c\varphi_2 c\phi} & \boldsymbol{s\varphi_1 s\phi} \\ \boldsymbol{s\varphi_1 c\varphi_2 + c\varphi_1 s\varphi_2 c\phi} & \boldsymbol{-s\varphi_1 s\varphi_2 + c\varphi_1 c\varphi_2 c\phi} & \boldsymbol{-c\varphi_1 s\phi} \\ \boldsymbol{s\varphi_2 s\phi} & \boldsymbol{c\varphi_2 s\phi} & \boldsymbol{c\phi} \end{bmatrix} \tag{2.10}$$

Where $\boldsymbol{c}$ and $\boldsymbol{s}$ represent cosine and sine functions, respectively. The Cartesian grain coordinate system is fixed with respect to the reciprocal space. The following relationship is used to transform the diffraction vector in reciprocal space ($\mathbf{g}_{hkl}$) into the Cartesian grain coordinate system (Lauridsen *et al.* 2001):

$$\mathbf{g_c} = \mathbf{B}\mathbf{g}_{hkl} \tag{2.11}$$

B is the conversion matrix described as follows (Lauridsen *et al.* 2001):

$$\mathbf{B} = \begin{bmatrix} a^* & b^*\cos\gamma^* & c^*\cos\beta^* \\ 0 & b^*\sin\gamma^* & -c^*\sin\beta^*\cos\alpha \\ 0 & 0 & c^*\sin\beta^*\sin\alpha \end{bmatrix} \tag{2.12}$$

Where (***a**, *b**, *c****, *α*, β*, γ**) represent the lattice parameters in reciprocal space, and *α* is one of the inter-axial angles of unit cell in real space lattice:

$$\cos\alpha = \frac{\cos\beta^* \, cos\,\gamma^* - \cos\alpha^*}{\sin\alpha^* \sin\beta^*} \tag{2.13}$$

By combining all the transformations described above, the following relationship is obtained between the scattering vector in global coordinate system, and the scattering vector in reciprocal space (Lauridsen *et al.* 2001):

$$\mathbf{g}_{\boldsymbol{l}} = \mathbf{\Omega SUB}\mathbf{g}_{hkl} \tag{2.14}$$

The diffraction vector in global coordinate system is computed based on Bragg's law and given as (Lauridsen *et al*. 2001):

$$\mathbf{g}_{l} = \frac{2\pi}{\lambda}\begin{bmatrix} \cos 2\theta - 1 \\ -\sin 2\theta \sin \eta \\ \sin 2\theta \cos \eta \end{bmatrix} \tag{2.15}$$

These coordinate transformations and geometric descriptions provide a basis for the lattice strain computations which will be presented in Chapters 3 through 5.

References

Advanced Photon Source (2014). <www.aps.anl.gov/>. (accessed November 12, 2014).

Andrade, J. E., Lim, K. W., Avila, C. F., and Vlahinic, I. (2012). "Granular element method for computational particle mechanics." *Computer Methods in Applied Mechanics and Engineering*, 241, 262-274.

Arroyo, M., Butlanska, J., Gens, A., Calvetti, F., and Jamiolkowski, M. (2011). "Cone penetration tests in a virtual calibration chamber." *Geotechnique*, 61(6), 525-531.

Belheine, N., Plasslard, J. P., Donze, F. V., Darve, F., and Seridi, A. (2009). "Numerical simulation of drained triaxial test using 3D discrete element modeling." *Computers and Geotechnics*, 36(1-2), 320-331.

Bragg, W. L. (1913)."The diffraction of short electromagnetic waves by a crystal." *Proceedings of the Cambridge Philosophical Society*, 4.

Bunge, H. J. (1982). *Texture analysis in materials science : mathematical methods*, Butterworths, London; Boston.

Cui, L., and O'Sullivan, C. (2006). "Exploring the macro- and micro-scale response of an idealised granular material in the direct shear apparatus." *Geotechnique*, 56(7), 455-468.

Cullity, B. D., and Stock, S. R. (2001). *Elements of X-ray Diffraction*, Pearson-Prentice Hall, New Jersey.

Cundall, P., and Strack, O. (1979). "A Discrete Numerical model for Granular Assemblies." *Geotechnique*, 29(1), 47-65.

Cundall, P. A. (1971)."A computer model for simulating progressive, large-scale movements in blocky rock systems." *Proc. Symp. Int. Rock Mech.*, Nancy, France, Paper No II-8.

DEM solutions (2014). "EDEM." <www.dem-solutions.com/>. (accessed October 10, 2014).

Efstathiou, C., Boyce, D. E., Park, J. S., Lienert, U., Dawson, P. R., and Miller, M. P. (2010). "A method for measuring single-crystal elastic moduli using high-energy X-ray diffraction and a crystal-based finite element model." *Acta Mater*, 58(17), 5806-5819.

Fenner, R. (2013). "Advance Photon Source, Electron Accelerator Diagram." *Argonne National Laboratory*, <https://www.flickr.com/photos/97432701@N03/9152651692/in/photostream/>. (accessed December 4, 2014).

He, B. B. (2009). *Two-dimensional X-ray Diffraction*, John Wiley & Sons, Hoboken, New Jersey.

Hu, N., and Molinari, J. F. (2004). "Shear bands in dense metallic granular materials." *J Mech Phys Solids*, 52(3), 499-531.

Huang, H., and Detournay, E. (2008). "Intrinsic Length Scales in Tool-Rock Interaction." *International Journal of Geomechanics*, 8(1), 39-44.

Itasca (2008). *Particle Flow Code in Three Dimension (PFC3D) Version 4.0*, Itasca, Consulting Group Inc., Minneapolis, MN.

Iwashita, K., and Oda, M. (1998). "Rolling Resistance at Contacts in Simulation of Shear Band Development by DEM." *Journal of Engineering Mechanics*, 124(3), 285-292.

Iwashita, K., and Oda, M. (2000). "Micro-deformation mechanism of shear banding process based on modified distinct element method." *Powder Technol*, 109(1–3), 192-205.

Jiang, M. J., Yu, H. S., and Harris, D. (2006). "Discrete element modelling of deep penetration in granular soils." *International Journal for Numerical and Analytical Methods in Geomechanics*, 30(4), 335-361.

Katagiri, J., Matsushima, T., and Yamada, Y. (2010). "Simple shear simulation of 3D irregularly-shaped particles by image-based DEM." *Granular Matter*, 12(5), 491-497.

Kozicki, J., and Donzé, F. V. (2008). "A new open-source software developed for numerical simulations using discrete modeling methods." *Computer Methods in Applied Mechanics and Engineering*, 197(49–50), 4429-4443.

Lauridsen, E. M., Schmidt, S., Suter, R. M., and Poulsen, H. F. (2001). "Tracking: a method for structural characterization of grains in powders or polycrystals." *Journal of Applied Crystallography*, 34(6), 744-750.

Lee, J. H., Aydiner, C. C., Almer, J., Bernier, J., Chapman, K. W., Chupas, P. J., Haeffner, D., Kump, K., Lee, P. L., Lienert, U., Miceli, A., and Vera, G. (2008). "Synchrotron applications of an amorphous silicon flat-panel detector." *J Synchrotron Radiat*, 15(5), 477-488.

Lee, S. J., Hashash, Y. M. A., and Nezami, E. G. (2012). "Simulation of triaxial compression tests with polyhedral discrete elements." *Computers and Geotechnics*, 43(0), 92-100.

Lienert, U., Brandes, M., Bernier, J., Mills, M., Miller, M., Li, S., Hefferan, C., Lind, J., and Suter, R. (2010)."3DXRD at the Advanced Photon Source: Orientation Mapping and Deformation Studies." *31st Riso Int. Symp. On Materials Science*, *Technical University of Denmark.*

Lu, N., Anderson, M. T., Likos, W. J., and Mustoe, G. W. (2008). "A discrete element model for kaolinite aggregate formation during sedimentation." *International Journal for Numerical and Analytical Methods in Geomechanics*, 32(8), 965-980.

Mohamed, A., and Gutierrez, M. (2010). "Comprehensive study of the effects of rolling resistance on the stress–strain and strain localization behavior of granular materials." *Granular Matter*, 12(5), 527-541.

Mollon, G., and Zhao, J. D. (2013). "Generating realistic 3D sand particles using Fourier descriptors." *Granular Matter*, 15(1), 95-108.

Nezami, E. G., Hashash, Y. M. A., Zhao, D., and Ghaboussi, J. (2007). "Simulation of front end loader bucket–soil interaction using discrete element method." *International Journal for Numerical and Analytical Methods in Geomechanics*, 31(9), 1147-1162.

Ng, T.-T. (2009). "Particle shape effect on macro- and micro-behaviors of monodisperse ellipsoids." *International Journal for Numerical and Analytical Methods in Geomechanics*, 33(4), 511-527.

O'Sullivan, C. (2011). "Particle-Based Discrete Element Modeling: Geomechanics Perspective." *International Journal of Geomechanics*, 11(6), 449-464.

Obstalecki, M. (2011). "In situ measurement of lattice strain using synchrotron radiation and a conical slit system." MS Thesis, University of Illinois at Urbana-Champaign.

Peña, A. A., García-Rojo, R., and Herrmann, H. J. (2007). "Influence of particle shape on sheared dense granular media." *Granular Matter*, 9(3-4), 279-291.

Peron, H., Delenne, J. Y., Laloui, L., and El Youssoufi, M. S. (2009). "Discrete element modelling of drying shrinkage and cracking of soils." *Computers and Geotechnics*, 36(1-2), 61-69.

Poulsen, H. F. (2004). *Three-dimensional X-ray diffraction microscopy: mapping polycrystals and their dynamics*, Springer.

Powrie, W., Ni, Q., Harkness, R. M., and Zhang, X. (2005). "Numerical modelling of plane strain tests on sands using a particulate approach." *Geotechnique*, 55(4), 297-306.

Shastri, S. (2004). "Combining flat crystals, bent crystals and compound refractive lenses for high-energy X-ray optics." *J Synchrotron Radiat*, 11(2), 150-156.

Shastri, S. D., Almer, J., Ribbing, C., and Cederstrom, B. (2007). "High-energy X-ray optics with silicon saw-tooth refractive lenses." *J Synchrotron Radiat*, 14(2), 204-211.

Shastri, S. D., Dejus, R. J., and Haeffner, D. R. (1998). "Experimental Characterization of APS Undulator A at High Photon Energies (50-200 keV)." *J Synchrotron Radiat*, 5(2), 67-71.

CHAPTER 3

STRAIN TENSOR DETERMINATION OF COMPRESSED INDIVIDUAL SILICA SAND PARTICLES USING HIGH-ENERGY SYNCHROTRON DIFFRACTION

This Chapter is a modified version of the paper published in: Alshibli, K., Cil, M. B., Kenesei, P., and Lienert, U. (2013). "Strain tensor determination of compressed individual silica sand particles using high-energy synchrotron diffraction." *Granular Matter*, 15(5), 517-530.

Abstract

The three-dimensional x-ray diffraction (3DXRD) nondestructive technique was used to measure lattice strains within individual sand particles subjected to compressive loading. Three experiments were conducted on similar single columns of silica sand particles with particle sizes between 0.595 mm and 0.841 mm. In each experiment, three sand particles were placed inside an acrylic mold with an inner diameter of 1 mm. Multiple in situ 3DXRD scans were acquired for each sand column as compressive load was increased. The volume-averaged lattice strain tensor was calculated for each sand particle. In addition, particle orientation and volumetric strain were calculated for individual sand particles. The axial normal strain ε_{zz} exhibited a linear response in the range of 0 to 10^{-3} when the applied compressive axial load (F) increased from 0 to ~30 N when one particle in the sand column fractured. Stress tensor of individual particles was calculated from the acquired lattice strain measurements and elastic constants of silica sand that were reported in the literature. To the best of our knowledge, there have been no reported experimental measurements of the lattice strain tensor measurements within individual silica sand particles. The quantitative measurements reported in this paper at the particle level are very valuable for developing, validating or calibrating micromechanics-based finite element and discrete element models to predict the constitutive behavior of granular materials. 3DXRD represents an exciting

new non-destructive technique to directly measure constitutive behavior at the scale of individual particles.

Introduction

The constitutive behavior and deformation characteristics of uncemented granular materials are to a large extent derived from the fabric or geometry of the particle structure and inter-particle friction resulting from normal forces acting on particles or particle groups. Granular materials consist of discrete particles with fabric (microstructure) that changes under loading. Microstructure (or fabric) is defined as the arrangement of particles, particle groups, and the associated pore space. Extensive research has been conducted to describe the constitutive behavior and deformation characteristics of granular materials using the theory of plasticity (Dafalias 1983, Manzari and Dafalias 1997), micro-polar theory (De Borst 1991, Gudehus 1996, Alsaleh *et al.* 2006), distinct element method (DEM) (Cundall 1989, Bardet and Proubet 1991, Oda and Kazama 1998), and coupled continuum-DEM models (Regueiro and Yan 2011). Some of these models provide excellent predictions of the strength behavior and deformation mode of granular materials; however, despite recent technological advances, calibration of such models using representative material parameters has always been a challenge.

In the last few decades, several experimental techniques were utilized to capture the particle-to-particle interaction under shear/uniaxial loading. Most of these efforts were limited to shearing relatively large cylindrical rods or circular/oval discs under simple shear or plane stress/strain loading configurations and used optical methods to track deformations (Rowe 1962, Oda *et al.* 1982, Calvetti *et al.* 1997). Some investigations involved stabilizing the specimen with epoxy, cutting thin sections, and using two-dimensional (2D) microscopy to study the internal fabric of granular materials. Photoelastic materials were also used to visualize stress distribution and force chains in granular materials (Allersma 1982, vanDoorn and Behringer 1997, Geng *et al.* 2003, Majmudar and Behringer 2005); however, it is very difficult to extract force values from these images. Furthermore, all research using photoelasticity was applied to 2D loading conditions.

X-ray computed tomography (CT) has emerged as a powerful non-destructive 3D scanning technique to study geomaterials. Alshibli and Reed (2010) compiled papers that report the latest advances in research on applying CT to characterize properties of geomaterials. Synchrotron micro-computed tomography (SMT) offers a significant enhancement to 3D imaging when compared to industrial CT systems by producing images with a higher resolution (in the order of 5 micron/voxel). For example, Hasan and Alshibli (2012) acquired excellent measurements of particle translation and rotation and the change of fabric during shearing of silica sand. Although CT and SMT can produce a 3D density map of the scanned specimen that can be used to identify particle position, morphology, and void space, they cannot provide measurements of contact stresses and strain measurement at particle contacts.

Neutron diffraction tomography, which can also yield 3D images of scanned objects, is more sensitive to hydrogen content and has better penetration power through metal containers surrounding the specimen. It is ideal for applications that involve detection of water within the scanned specimen. Neutrons are seldom absorbed by the sample as assumed in the radon transformation, but are more often scattered by elastic and inelastic collisions with nuclei and phonons (Butler 2010). Still, the transformation yields very useful 3D images. Most of the neutron diffraction images in the literature are blurred with a resolution an order of magnitude lower than

CT images. For example, Penumadu *et al.* (2009) used neutron diffraction to measure lattice strains in the bulk of silica sand and found a significant difference between the global and lattice strain-stress relationship. Frischbutter *et al.* (2000) used the same technique to measure lattice strain in geological samples and found a significant difference between lattice strain and strain measured by strain gauges. Darling *et al.* (2004) reported similar measurements and reached similar conclusions.

Three-dimensional x-ray diffraction (3DXRD) microscopy is a promising technique that has the potential to measure lattice strains and crystallographic orientation of crystalline materials. It is based on transmission geometry that can be applied in both layered and bulk materials (Lienert *et al.* 1998, Poulsen *et al.* 2001, Poulsen *et al.* 2003, Poulsen 2004, Oddershede *et al.* 2010). It allows nondestructive 3D mapping of polycrystalline materials and monitors in situ dynamic processes of the bulk specimens. It also permits structural characterization of individual grains embedded in polycrystals. The volume, strain, phase, and orientation of hundreds of grains/particles can be monitored simultaneously (Jensen *et al.* 2008). 3DXRD represents a new opportunity to directly acquire information about the interaction of individual particles. Current applications of 3DXRD focus primarily on polycrystalline metals. Poulsen (2004) introduced 3DXRD technique and its potential applications in materials science. Martins *et al.* (2004) measured the elastic strains of individual aluminum grains as a function of tensile load. Jensen *et al.* (2008) demonstrated that 3DXRD could be used to monitor recrystallization in metallurgical processes, grain migration during recrystallization, solid-state nucleation, and grain growth during phase transformations. Hall *et al.* (2011) presented preliminary results of 3DXRD scanning on

Ottawa sand specimens that were subjected to 1D loading. However, their analysis did not include extracting lattice strain tensor measurements from the data.

The main objective of this paper is to determine volume-averaged lattice strain tensor components of individual silica sand particles under axial loading condition using the 3DXRD microscopy. Beamline 1-ID of the Advanced Photon Source (APS), Argonne National Laboratory, USA, was used to acquire the scans for three sand specimens. Analyzing 3DXRD data is typically a challenging task. The authors have developed evaluation codes in MATLAB augmented by open source scientific programs called Fable (Fable 2011) and DIGIgrain developed by Kenesei (2012) to analyze the data to extract lattice strain tensor values. To the best of our knowledge, there have been no reported experimental measurements of the lattice strain tensor measurements within individual silica sand particles.

Principle of 3DXRD Microscopy

The incident monochromatic synchrotron x-ray beam is scattered on the orderly arranged atoms of a crystalline material. The diffracted x-ray beams obey Bragg's law:

$$2d_{hkl} \sin \theta_{hkl} = \lambda \quad (3.1)$$

where λ is the wavelength of the incident beam, θ_{hkl} is the angle of the incident beam to the lattice planes with distance of d_{hkl}. The subscript *hkl* denotes the lattice planes *(hkl)* with Miller indices of *h*, *k*, and *l*. Accordingly, the diffracted beams can be observed only in the directions that fulfill the Bragg condition (Eq. (3.1)) and constructive interference can be obtained as defined by selection rules on Miller indices according to the crystal symmetries and atomic form factors. A simple visual interpretation of the diffraction geometry is shown in Figure 3.1, where the incident x-ray beams are reflected on the set of lattice planes *(hkl)* like on a mirror, and the angle of the diffracted beam to the incident beam is $2\theta_{hkl}$. Thus, the diffracted peak positions from a powder-like sample are located on the Debye-Scherrer rings. The knowledge of wavelength λ, and the measurement of the diffraction angle $2\theta_{hkl}$ provide information about the lattice spacing d_{hkl}, which is in direct correspondence with the lattice strain projected to the normal of the given lattice planes. A family of parallel lattice planes with spacing d_{hkl} is described by a reciprocal lattice vector, later referred to as g-vector. As the applied compressive stress increases, the crystal gets distorted, and the lattice spacings (g-vectors) change according to the constitutive response of the material. More detailed information about the 3DXRD geometry can be found in the literature (Poulsen 2004).

In the high-energy 3DXRD measurements (typically 50–100 keV x-ray), since the diffraction angles are usually less than 15^{o}, several diffraction rings can be measured simultaneously using a large area detector. An additional benefit of applying high-energy x-rays is the high penetration through the sample, which enables investigation of millimeter-sized samples. Rotating the polycrystalline sample around the loading axis permits the detection of diffraction peaks from several sets of lattice planes of each crystallite, which fulfills the Bragg condition and provides information about several projections of the lattice strain to determine the volume-averaged strain tensor of individual particles.

Experiments

The sand used in the experiments is natural uniform silica sand known as ASTM 20-30 Ottawa sand with particle size between 0.595 mm (Sieve No. 30) and 0.841 mm (Sieve No. 20). It

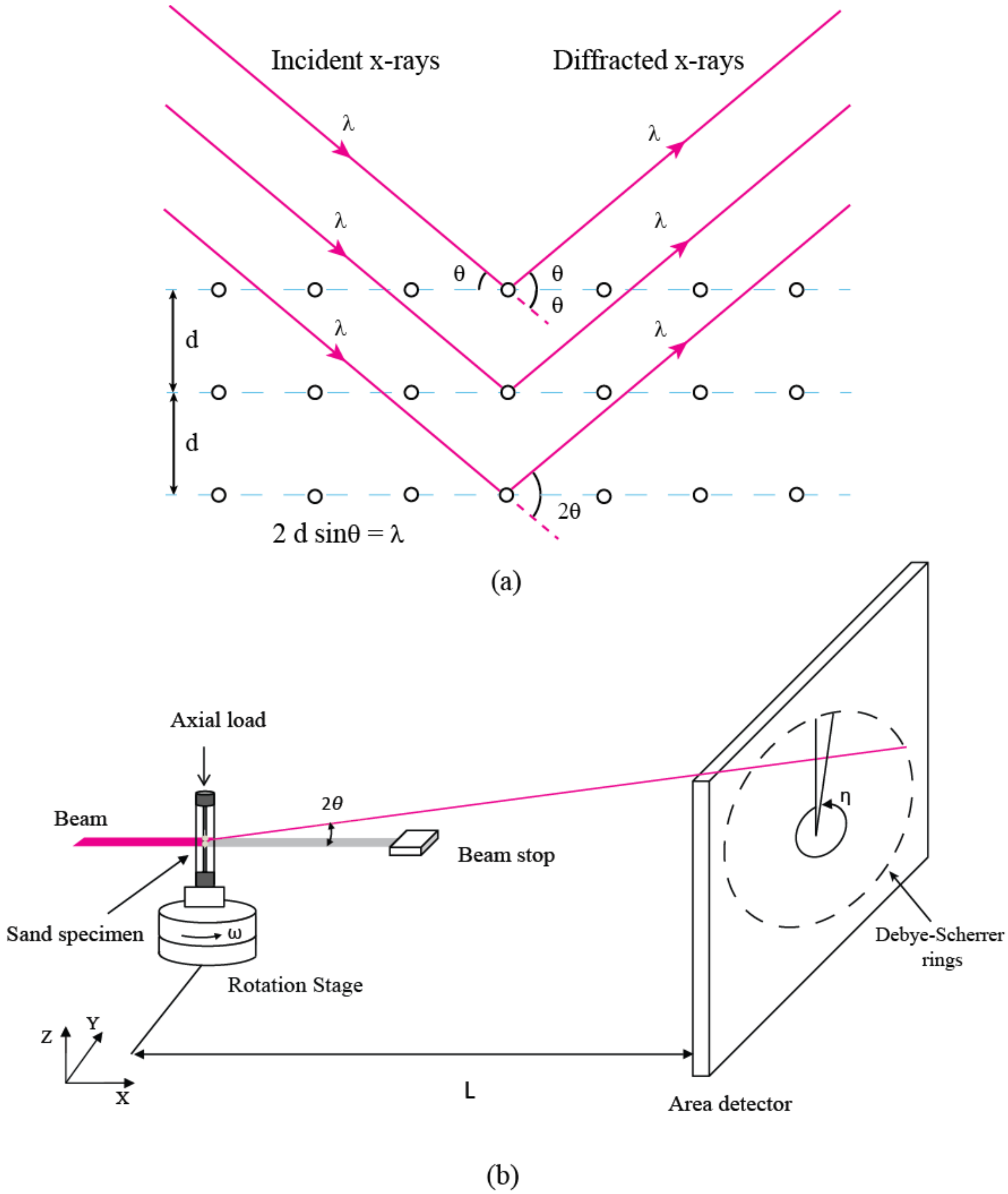

Figure 3.1. Schematic illustration of (a) Bragg diffraction; and (b) far field 3DXRD measurement geometry.

was mined from Ottawa, Illinois, USA. To investigate the crystallographic structure of the sand particles, laboratory-based powder diffraction x-ray analysis was performed on a sample of the sand. Diffraction patterns of the sample showed that α-quartz (SiO_2, Space group P3221) is the only detectable mineral in the sample, confirming the chemical composition as 99.8% SiO_2 as provided by the manufacturer, U.S. Silica Company. Lattice parameters of crystalline materials are usually determined using conventional XRD. Lattices are typically expressed using three lattice constants known as *a*, *b*, and *c*, and three angles (α, β, γ) between the lattice vectors in the 3D lattice space. We used XRD to measure the lattice constants of the sand powder as follows: a = 4.916 Å, b = 4.916 Å, c = 5.4054 Å and the angles are $\alpha = 90^o$, $\beta = 90^o$, $\gamma = 120^o$. These values are very close to lattice constants of α-quartz that were reported by Levien *et al.* (1980).

Crystallographic orientation spread within individual sand particles was also investigated using polarized light microscopy. A sample of the sand was illuminated with the polarized light and rotated, and the change in the transmitted light was observed to determine the crystallographic perfection of the sand particles. During the rotation, the intensity of transmitted light seems to be uniform throughout the surface in most of the sand particles and only a few exhibited anisotropic optical behavior. These observations demonstrated that most of the particles had a nearly single crystal particle structure, which is in agreement with the findings of Hall *et al.* (2011).

A special test cell was fabricated to conduct the experiments. Three sand particles were placed inside a 1 mm cylindrical hole at the center of a 15 mm acrylic cylindrical mold (Figure 3.2). The load was measured at the top and the bottom end plates using two load cells. The bottom load cell was attached to the aluminum base plate of the cell. An acrylic spacer was used to hold the cylindrical mold that contained the sand particles. The load of particles on the bottom load

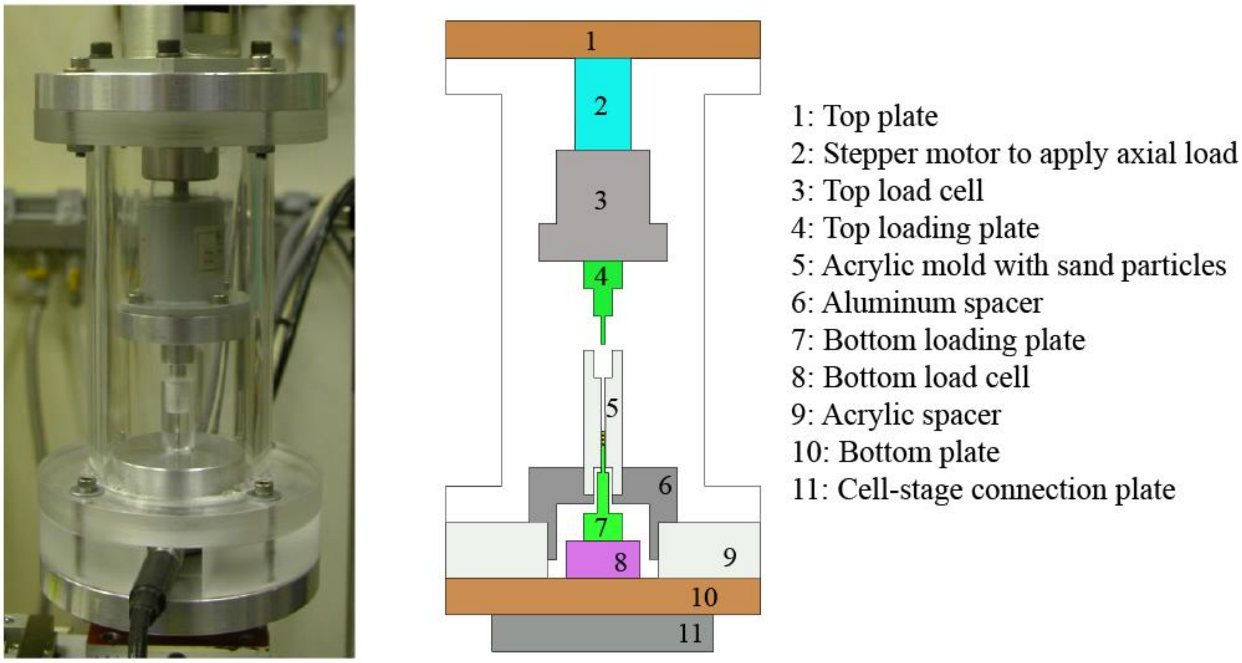

Figure 3.2. Photo and schematic of 1D compression test cell.

plate was transmitted through tungsten carbide rod with a diameter of 0.8 mm and a height of 12.7 mm. The acrylic mold was placed on the top of the bottom loading plate extension without any friction between them. Then, three particles were placed inside the mold using a special aluminum funnel with 1 mm diameter. To prevent possible plugging or jamming of particles inside the 1 mm hole, only three particles were used in the experiments. The height of the sand column ranged from 1.7 mm to 2.4 mm. Finally, the top loading plate was set in place and the test cell was assembled. This experimental setup permits the loads to be measured at the top and bottom of the sand column to quantify the influence of friction between sand particles and mold walls.

The test cell was mounted on the sample stage of beamline 1-ID at APS. The specimen was subjected to axial loading at a constant displacement rate using a computerized stepper motor. The sand particles were illuminated by a high-energy x-ray beam with a size of 0.8 mm × 1.0 mm and an energy of 80.725 keV that corresponds to wavelength of 0.15358 Å. Diffraction data were detected by an area detector that was positioned at a horizontal distance of 1593 mm (L in Figure 3.1b) from the specimen. The beam was centered on each particle in the sand column, and a rotation scan was acquired for a beam height of 0.8 mm. In the case of the middle particle, for example, the beam height partially included the two adjacent sand particles. The sand column was scanned before the axial load was applied; it was then loaded until the desired compressive load was reached and the scan was performed while the stepper motor position was held. Multiple 3DXRD scans were acquired at the load levels shown in Figure 3.3a. Compression forces, displacement, stress, and strain are taken to be positive throughout this paper according to the sign convention in the field of geotechnical engineering. Figure 3.3b shows an example SMT image series of a similar specimen in a similar loading test. The SMT images were acquired using Sector

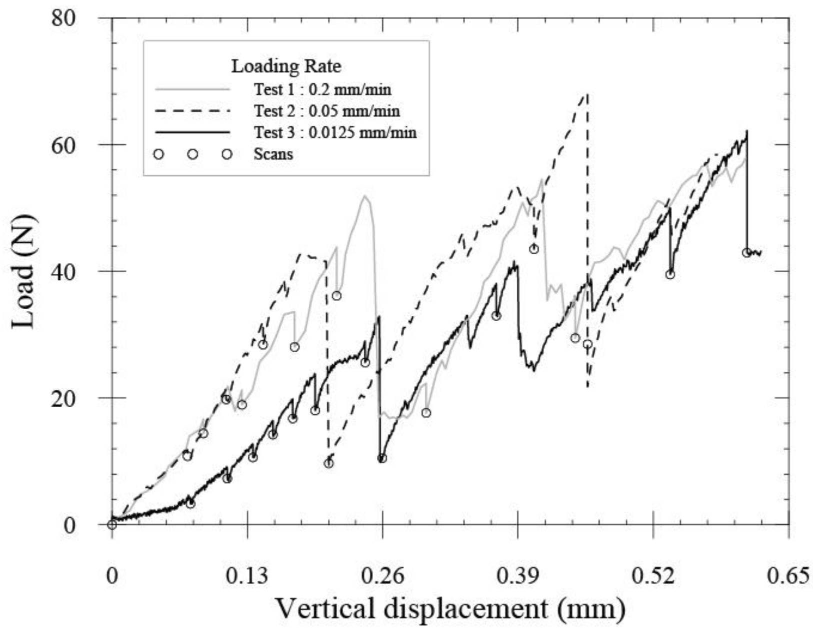

(a)

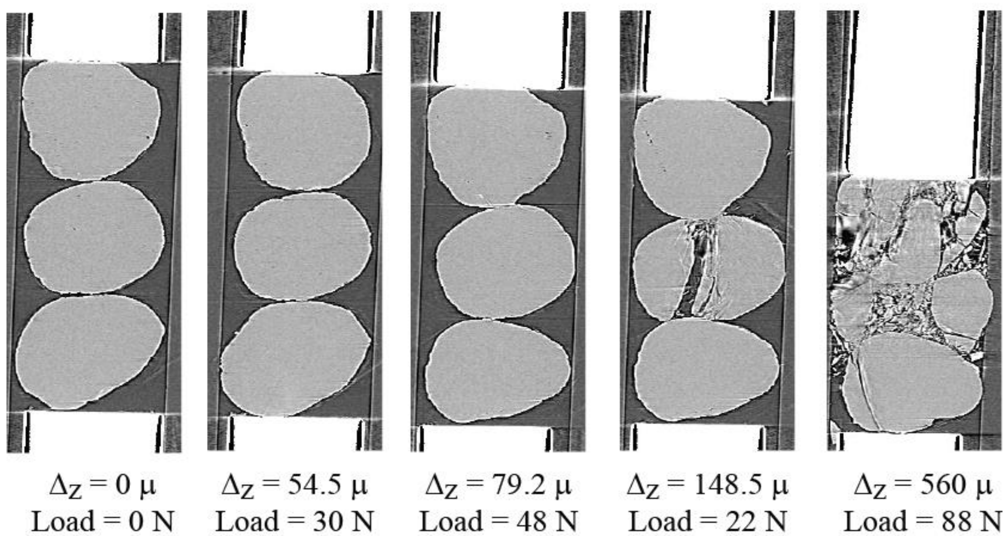

(b)

Figure 3.3. (a) Load versus displacement relationship of the three 1D compression experiments. Only top load cell measurements are plotted. (b) SMT images of a similar specimen. Compression is positive.

13 beamline at APS and have proved very helpful in the selection of the load steps for the diffraction measurements.

Three specimens were scanned using 3DXRD at multiple loads. Each specimen consisted of three sand particles, which were loaded at different displacement rates (0.0125 mm/min, 0.05 mm/min, and 0.20 mm/min). 3DXRD data were acquired while the specimen was rotated at a constant angular velocity about an axis perpendicular to the beam direction. An intensity distribution image of the diffracted spots (called the ω-slice) was recorded at each rotation interval of $\Delta\omega$. The raw diffraction data consist of 180 stacked images recorded while the specimen was rotated ω from -90° to 90° with $\Delta\omega = 1°$ integration interval at each loading stage for each particle.

Diffraction Data Analysis

The scanning dataset represents a map of the 3D reciprocal space distribution of the investigated particle. Figure 3.4 depicts an example image of the diffraction data. The discrete peaks appeared at the location predicted by the Bragg condition as expected, and no significant overlap of the measured spots was observed. Figure 3.4 clearly demonstrates the behavior of the spots under the effect of progressive loading. Reflections appear and disappear at specific η, ω, and 2θ positions as extended spots according to the imperfections and defects of the crystals. The deformation leads to displacement of spots on the detector according to the particle rotation and lattice distortion. Therefore, reflections may move through $\{\eta, \omega, 2\theta\}$ space during the deformation process. Moreover, small particle fragments formed as a result of particle fracture and resulted in an increase in the number of spots.

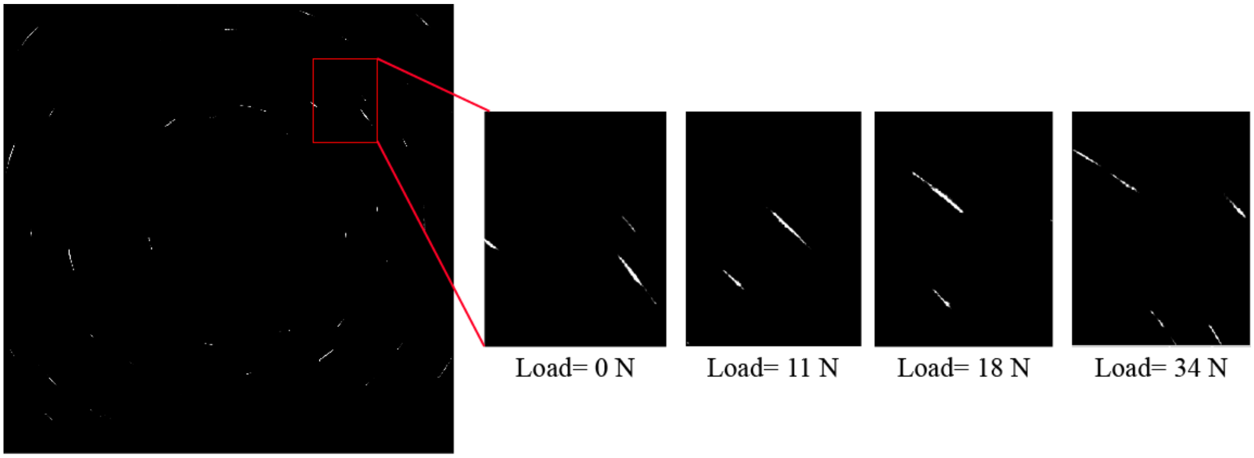

Figure 3.4. The translation of the diffraction spots as axial load increases. The spots begin to move along the azimuthal direction η with increasing load in different directions. Diffraction spots broaden in two directions and new reflections appear with increasing load due to new fragments generated after particle fracture. Also, diffraction spots move along the azimuthal direction η on the detector plane and broadened in two directions due to particle orientation change and deformation.

As an example, Figure 3.5 provides η-ω maps of the center layer of the sand column. The images represent the measured diffraction spots recorded in the first Debye-Scherrer ring with $2\theta_{\{100\}} = 2.07°$ at selected load steps. Before particle fracture, a significant orientation change or particle rotation occurs, then the particle disintegrates into several small fragments. These images show that the deformation causes certain changes in the structure of sand particles.

The analysis of the diffraction data consists of three primary stages: (i) preprocessing and peak search; (ii) g-vector calculation and indexing; and (iii) orientation; and strain computation and error analysis. The preprocessing and peak search steps were performed using the DIGIgrain program. In the preprocessing stage, DIGIgrain applies dark current and background correction on the raw data. After data correction, it uses a sophisticated 3D searching algorithm for segmenting the extended, sometimes slightly overlapping diffraction spots and evaluates the peak positions (center of the spot profile) with high precision taking into account the spatial distortion of the detector. The peak search algorithm offers many options for identifying the peaks properly and can be efficiently customized for various datasets. During the peak search, the peaks can be filtered by size, position, intensity, and shape, and the slightly overlapping peaks can be separated based on the 3D intensity profile of the spots. The DIGIgrain algorithm successfully eliminated the spot overlapping and spatial distortion effects and provided the reduced dataset for further analysis. The 2D raw diffraction data was reduced into a simple text file for each scan that includes a compact list of peaks and their properties such as center position, integrated intensity, statistical descriptors, etc.; these files were used as input for the Fable program.

Armed with the knowledge of the best possible peak positions, one can calculate the g-vectors using the ImageD11 application of Fable (Wright 2005), which considers the detector

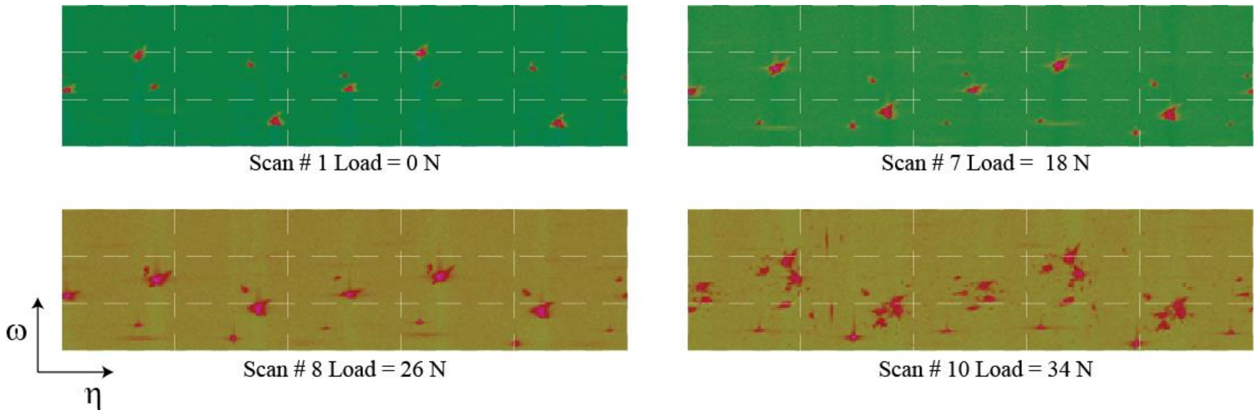

Figure 3.5. Example η-ω maps of the center layer of the sand column of Test 3 for selected load steps.

calibration parameters such as the detector tilt, distance, and pixel size determined from powder diffraction measurements on a calibrant (LaB_6). Then, the GrainSpotter application of Fable (Schmidt 2010) can be used to assign the measured g-vectors to individual particles. This process is called indexing. GrainSpotter identifies the particle orientations via searching in the orientation space based on the value of completeness, which is defined as the ratio of the number of the found and expected g-vectors belonging to a particle. In this paper, approximately 150 g-vectors were assigned to each particle per scan. The results were summarized in an output file that includes the center of mass position and orientation (in form of the U-matrix) of each detected particle, the angle between the theoretical and the measured diffraction vector (called internal angle), and the list of the diffraction spots assigned to the particle.

Silica sand particles rotate and translate significantly in real 3D space due to their discrete nature. Due to significant rotations of the investigated particles, assigning measured spots to a specific particle was challenging. Therefore, a visual validation process was implemented by comparing the spots identified by GrainSpotter and those measured during the diffraction scan. Figure 3.6 shows an example image of the spot matching for load step 2 and ring 2θ=2.07° with a Miller index of {010}. GrainSpotter successfully indexed all spots that appeared in the η-ω maps. This visualization was repeated for consecutive load steps at different Debye-Scherrer rings. This evaluation process confirmed accurate indexing of particles and determined the sequence of particle identifiers in each loading step, resulting from the independent indexing procedure, to follow the orientation and strain history of the individual particles over the load steps. This visual matching method increased the confidence in the accuracy of the particle identification procedure.

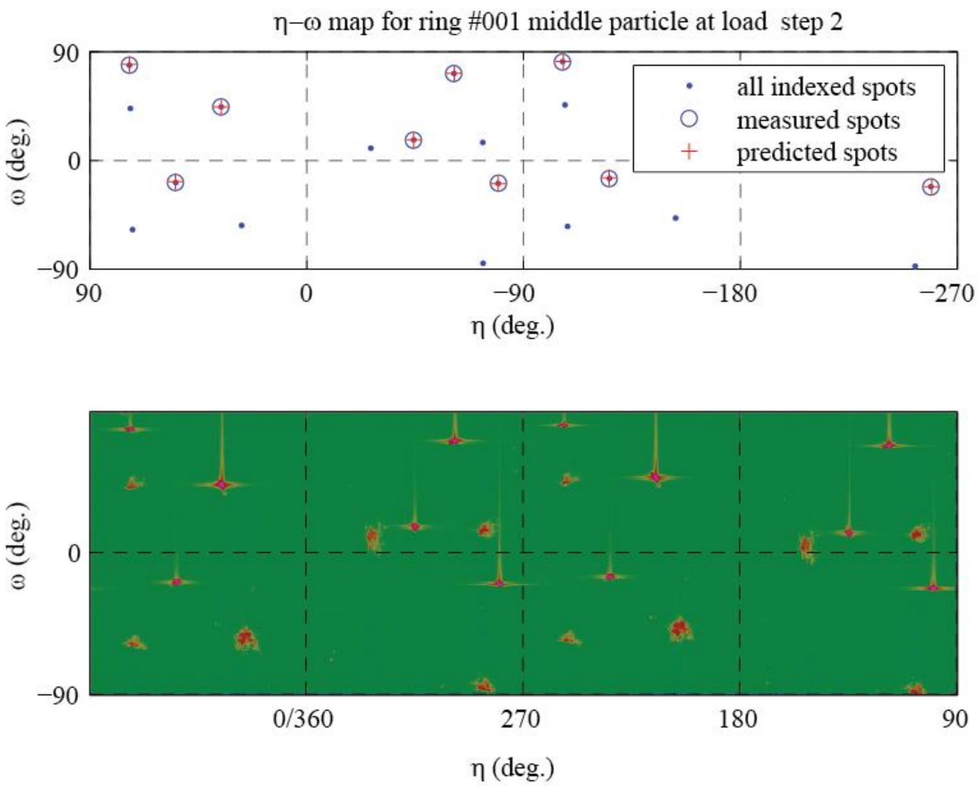

Figure 3.6. Visual comparison of the reflection spots that were measured and predicted by GrainSpotter for a reference particle for load steps 0 to 2.

Results

Track particle orientation

The rotations of particles were evaluated analytically. The misorientation angle of the particle with reference to an orientation before loading was calculated based on the indexing results for each load step. A particle could rotate such that only the rotation axis changes but not the misorientation angle with respect to the reference orientation. In order to detect this change, Δ orientation which compares the actual orientation relative to the previous one instead of a fixed reference was also determined. The particle with the minimum misorientation angle was identified as the candidate for the reference particle in continuous loading. The result was also confirmed by comparing the detected spots of selected particles in each load step. An example development of the misorientation angle of a particle relative to the initial condition as a reference orientation and the variation of Δ orientation are depicted in Figure 3.7a, which confirms the assumed significant rotation of the particle as a rigid body.

The rotation path of the middle particle of Test 3 is also illustrated in Figure 3.7b in Rodrigues space. Rodrigues vectors are an axis/angle representation of orientations, the direction of the vector is parallel to the rotation axis and the length is proportional to the rotation angle around the axis (e.g. Morawiec and Field (1996)). Rodrigues representation is chosen since the crystal symmetry is easily represented by the fundamental zone consisting of a hexagonal prism for the trigonal symmetry of quartz. Also, distortions of the distances between orientations are rather small in Rodrigues representation. In the present case, the particle orientation is fully contained in one octant of the fundamental zone which is shown in Figure 3.7b together with projections onto the xyz planes of the sample coordinate system. It is seen that the z-component is

Figure 3.7. (a) The variation of misorientation angle and Δ orientation for the middle particle of Test 3 at consecutive loads. (b) The orientation trajectory of the middle particle of Test 3 in Rodrigues space representation. 1/8 octant of the fundamental zone (red lines) is shown. The coordinates refer to the sample system as defined in Figure 3.1b. The blue circles indicate particle orientations at different loads (the initial orientation is marked by a solid green circle). The orientation trajectory is indicated by the solid lines connecting the load-dependent orientation vectors. The projections of the orientation trajectory onto the xy, yz, and xz sample planes are also shown.

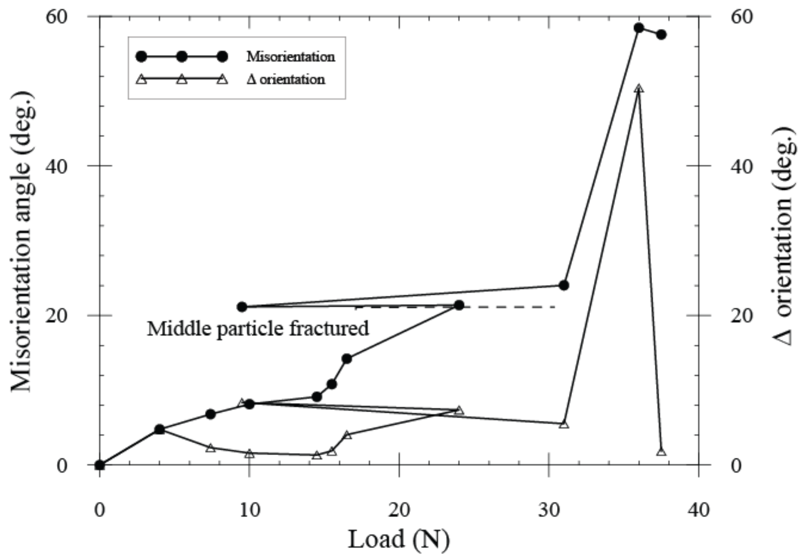

(a)

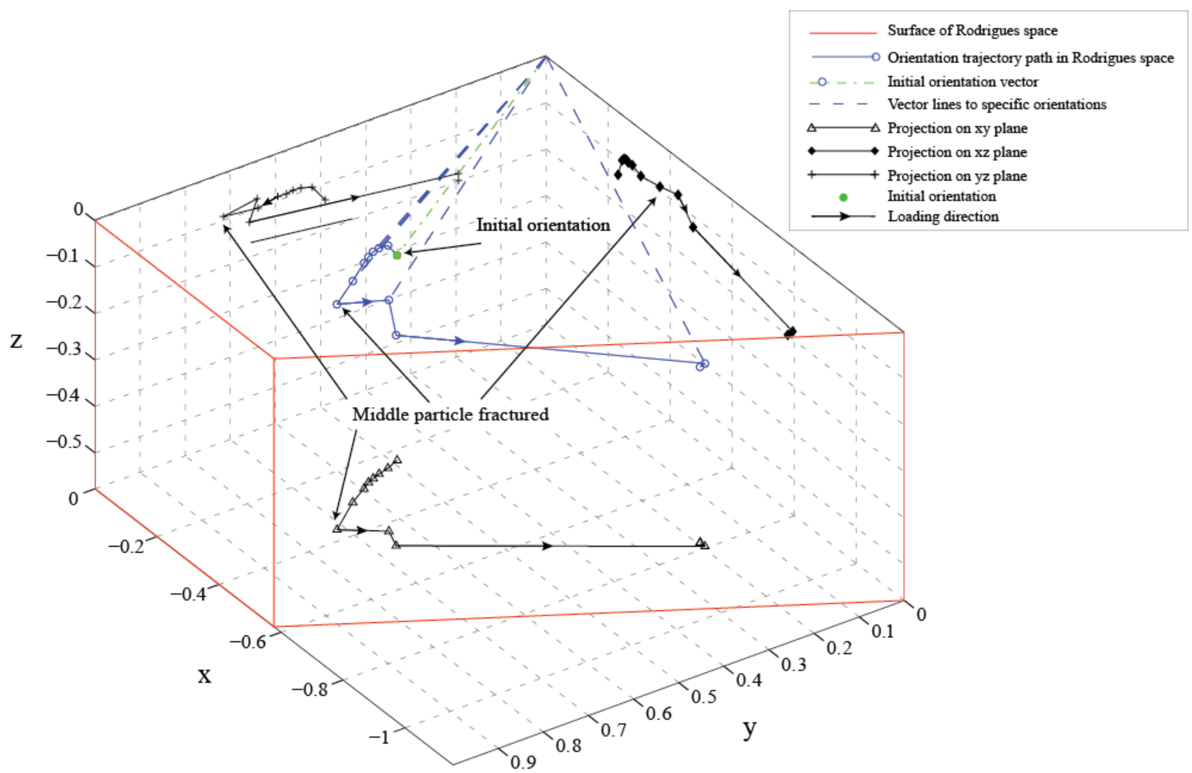

(b)

Figure 3.7. Continued.

small compared to the in-plane xy-components which means that the particle mainly rotated around axes that are perpendicular to the loading direction. Second, initially the rotation path was smooth around a fixed axis (mostly the length of the Rodrigues vector changes, not the direction). Note that the diffraction approach provides an orientation resolution of about 0.1° which is far better than SMT imaging of particles. However, diffraction data are subjected to the ambiguity set by point group symmetry (trigonal). Large orientation changes, which are expected when particles fracture, can only be determined to the uncertainty of crystal symmetry operations. For example, referring to Figure 3.7b, the discontinuity occurring at the fracture (between points #8 and #9) may indicate that the rotation path actually extends outside of the fundamental zone. However, the correct symmetry element could be identified from simultaneous SMT data since the external shape of the particle is observed rather than the orientation of the crystal lattice.

As mentioned earlier granular particles translate and rotate when they are sheared. Particle rotation and the associated interlocking and moment contribute significantly to the shearing resistance of a bulk of granular materials. The results of this paper demonstrated that 3DXRD offers an excellent tool to accurately measure particle rotation with a high accuracy (about 0.1°), which provides valuable measurements to calibrate constitutive models to better capture the behavior of granular materials.

Lattice strain tensor measurements

The lattice-strain calculation using 3DXRD data is based on the evaluation of the 2θ shifts of the peak positions, which is achieved by measuring the relative changes of reference-vector length to an unloaded lattice condition. The strain tensor components represent the average deformation of all unit cells within the particle as a function of the applied load. For each g-vector (indexed by i, where $i = 1 \dots N$) of a particle, the projected strain in a specific direction described by unit directional vectors (l_i, m_i, n_i) can be expressed as follows (Margulies *et al.* 2002):

$$\varepsilon_i = (l_i \quad m_i \quad n_i)\hat{\varepsilon}\begin{pmatrix} l_i \\ m_i \\ n_i \end{pmatrix} = (l_i \quad m_i \quad n_i)\begin{pmatrix} \varepsilon_{xx} & \varepsilon_{xy} & \varepsilon_{xz} \\ \varepsilon_{xy} & \varepsilon_{yy} & \varepsilon_{yz} \\ \varepsilon_{xz} & \varepsilon_{yz} & \varepsilon_{zz} \end{pmatrix}\begin{pmatrix} l_i \\ m_i \\ n_i \end{pmatrix} \qquad (3.2)$$

where ε_i is calculated using the length of the g-vectors in the unloaded (g_i^0) and loaded (g_i) cases as:

$$\varepsilon_i = \frac{g_i - g_i^0}{g_i^0} \qquad (3.3)$$

As mentioned earlier, the number of the experimentally evaluated projected strains N for one particle is on the order of 100, while the number of unknown strain tensor components is only 6. Therefore, we can build an over-determined equation system to determine the unknown strain tensors, which can be solved for $\hat{\varepsilon}$ using the least-squares approach. For simplicity, we change to a contracted 6-component vector notation for the symmetric tensors at this point, as:

$$\hat{\varepsilon} \rightarrow \tilde{\varepsilon} = (\varepsilon_{xx} \quad \varepsilon_{yy} \quad \varepsilon_{zz} \quad 2\varepsilon_{xy} \quad 2\varepsilon_{xz} \quad 2\varepsilon_{yz})^{T} \qquad (3.4)$$

The projected strains after simplifying the right side of Equation (3.2) are:

$$\varepsilon_i = \varepsilon_{xx} l_i^2 + \varepsilon_{yy} m_i^2 + \varepsilon_{zz} n_i^2 + 2\varepsilon_{xy} l_i m_i + 2\varepsilon_{xz} l_i n_i + 2\varepsilon_{yz} m_i n_i, \qquad (3.5)$$

by which the linear equation system to be solved can be written in short form as:

$$\{\varepsilon_i\} = [A]\tilde{\varepsilon} \qquad (3.6)$$

where $\{\varepsilon_i\}$ denotes the N-element vector constructed from the projected strains and [A] is an N x 6 component matrix constructed as:

$$[A] = \{l_i^2 \quad m_i^2 \quad n_i^2 \quad 2l_i m_i \quad 2l_i n_i \quad 2m_i n_i\} \tag{3.7}$$

where the components are calculated from lattice g-vectors as:

$$(l_i \quad m_i \quad n_i)^T = \frac{\mathbf{g}_i}{|\mathbf{g}_i|} \tag{3.8}$$

Since the scans were acquired by rotating the specimen from -90° to 90°, the set of planes that satisfy the Bragg condition gave rise to diffraction spot on the detector twice—belonging to both (h,k,l) and (-h,-k,-l) indices—during this rotation. These symmetrical spots are called Friedel pairs, an example of which can be identified clearly in the $\eta-\omega$ map shown in Figure 3.6. Symmetrical spots appear in the η ranges [-90°, 270°] and [270°, 90°]. The g-vectors of the Friedel pair spots are anti-parallel and originate from the same lattice planes (Ludwig *et al.* 2009). Averaging Friedel pairs reduces errors in experimental lengths of g-vectors. In this paper, including Friedel pairs in the analysis resulted in negligible differences in the strain tensor calculations due to the large number of measured g-vectors; therefore, we decided not to include them in the analysis.

Strain calculations were performed using a MATLAB script developed by the authors. The ideal *g*-vectors before loading were determined as the reference condition based on the lattice constants obtained from the powder diffraction. The change in the diffraction vectors in each load increment was determined by normalizing measurements with respect to the initial, supposedly strain-free, condition. The error that stems from the particle position relative to the rotation center was also considered in the analysis, and offsets of the particle position were also included. The number of *g*-vectors used in strain tensor computation ranged between 125 and 156 after filtering out the mistakenly indexed g-vectors.

3DXRD data were collected for three similar uniaxial compression experiments and were used to calculate the lattice strain tensors of individual sand particles. The experimental configuration and parameters were kept the same in the three tests with exception of the loading rate. The results of the three experiments are similar to each other. For brevity, only the results of Test 3 are presented in detail; the results of Tests 1 and 2 are only summarized in Table 3.1. Figure 3.8 presents the load-versus-lattice-strain relationships of the three sand particles of Test 3, which displays the lattice strain components that were determined based on the global coordinate system (i.e., experiment coordinate system shown in Figure 3.1b).

The top and bottom load cells were used to record the compressive loads at both ends of the sand column and therefore to determine the load transmitted by the sand column. The difference between the two load measurements represents the friction force between the particles and the walls of the acrylic tube. The difference in loads was less than 0.5 N in the three tests. Referring to Figure 3.8, ε_{zz} represents the normal strain along the loading direction. It increased in a nearly linear fashion as the compressive load increased until one of the sand particles fractured (middle particle in Test 3). Once a sand particle fractures, the small fragments of the particle will have a relatively large translation and rotation and will produce multiple diffraction spots causing unreliable strain measurements for the fractured particle. Furthermore, one particle fracture leads to instant load drop and rearrangement of other particles in the system. These two complex mechanisms caused the drastic shift of the strain measurements after middle particle fracture. ε_{xx}

Table 3.1. Elastic lattice strain values for Tests 1 and 2 and associated statistical fit function for ε_{zz}

Test	Particle	Load, F (N)	ε_{xx} (%)	ε_{yy} (%)	ε_{zz} (%)	ε_{xy} (%)	ε_{xz} (%)	ε_{yz} (%)	Fit function for ε_{zz}
1	Bottom*	0	0	0	0	0	0	0	$F = 820.3\ \varepsilon_{zz}$
		14.75	-0.0021	-0.0036	0.0383	-0.0038	0.0028	-0.0018	$R^2= 0.800$
		19.75	0.0074	0.0000	0.0160	0.0046	0.0035	0.0064	
		28.5	0.0155	-0.0004	0.0259	0.0093	0.0053	0.0102	
		35.25	0.0080	0.0026	0.0277	0.0070	0.0052	0.0086	
	Middle	0	0.0000	0.0000	0.0000	0.0000	0.0000	0.0000	$F = 333.9\ \varepsilon_{zz}$
		14.75	0.0059	0.0013	0.0383	0.0024	-0.0049	-0.0054	$R^2= 0.993$
		19.75	0.0119	-0.0004	0.0510	0.0040	-0.0094	-0.0066	
		28.5	0.0113	-0.0037	0.0837	0.0087	-0.0103	-0.0056	
		35.25	0.0109	-0.0131	0.1125	0.0120	-0.0163	-0.0095	
	Top	0	0.0000	0.0000	0.0000	0.0000	0.0000	0.0000	$F = 416.5\ \varepsilon_{zz}$
		14.75	0.0088	-0.0039	0.0370	-0.0090	-0.0167	-0.0033	$R^2= 0.999$
		19.75	0.0106	-0.0069	0.0475	-0.0112	-0.0193	-0.0059	
		28.5	0.0098	-0.0125	0.0697	-0.0115	-0.0238	-0.0085	
		35.25	0.0075	-0.0099	0.0828	-0.0111	-0.0276	-0.0053	
2	Bottom	0	0.0000	0.0000	0.0000	0.0000	0.0000	0.0000	$F = 340.4\ \varepsilon_{zz}$
		10.75	-0.0064	-0.0021	0.0308	-0.0057	-0.0023	0.0043	$R^2= 0.998$
		18.75	-0.0123	-0.0068	0.0590	-0.0091	0.0049	0.0027	
		27.85	-0.0147	-0.0110	0.0792	-0.0122	0.0023	0.0039	
	Middle	0	0.0000	0.0000	0.0000	0.0000	0.0000	0.0000	$F = 357.1\ \varepsilon_{zz}$
		10.75	-0.0044	0.0017	0.0263	-0.0017	0.0105	0.0032	$R^2= 0.995$
		18.75	-0.0056	-0.0052	0.0483	-0.0011	0.0099	0.0045	
		27.85	-0.0160	-0.0071	0.0817	0.0053	0.0169	0.0066	
	Top	0	0.0000	0.0000	0.0000	0.0000	0.0000	0.0000	$F = 366.4\ \varepsilon_{zz}$
		10.75	0.0021	-0.0012	0.0249	-0.0005	0.0006	-0.0052	$R^2= 0.997$
		18.75	-0.0122	-0.0003	0.0496	0.0007	-0.0019	-0.0078	
		27.85	-0.0175	-0.0051	0.0784	0.0004	0.0005	-0.0095	

* Particle fractured at small load (14.75 N).

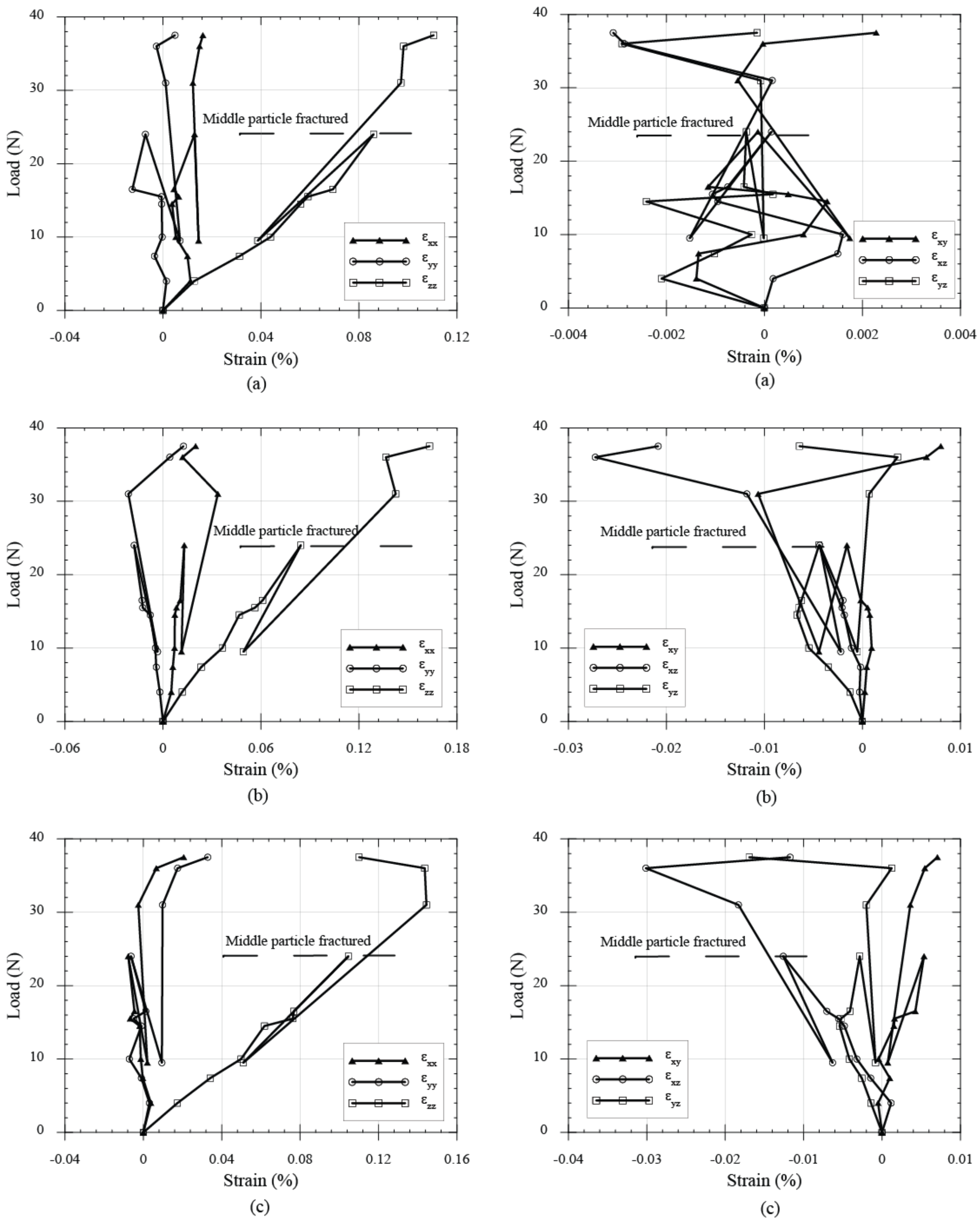

Figure 3.8. Evolution of lattice strain measurements as a function of axial load for Test 3 for (a) top particle, (b) middle particle, and (c) bottom particle.

and ε_{yy} represent normal strains in the lateral directions, which should exhibit similar trends if the sand particles exhibit isotropic behavior, centered in the mold and spherical (i.e., each sand particle will have continuous contact with the mold wall). However, as depicted in Figure 3.3b, the non-spherical shape of the particles and the small space between the mold walls and the particles, allowed the particles to establish contact with one side of the mold, and the increase in axial load resulted in compression strain (positive values) in one of the lateral directions (e.g., ε_{xx} in Figure 3.8) and expansion strain (negative values) in the other lateral direction (ε_{yy} in Figure 3.8). In some cases, ε_{xx} and ε_{yy} changed trend direction (i.e., switched from compression to tension or vice versa) as the test proceeded because some sand particles translated and rotated as the load increased, which changed the stress at the particle-mold wall contact. Also, silica sand exhibits anisotropic elastic behavior as will be discussed in the following sub-section which contributes to observing different ε_{xx} and ε_{yy} values. In all cases, ε_{xx} and ε_{yy} values were very small (less than 0.03% for Test 3 before particle fracture).

Figure 3.8 also shows the normal and shear strain components for the three sand particles of Test 3. The shear strain values sometimes exhibited inconsistent trend as the load increased or if there was a continuous increase or decrease in a particular direction up to the fracture point. All shear strain values for the top particle fluctuated throughout the test. On the other hand, a nonlinear continuous ε_{xz} and ε_{yz} were observed in the middle and bottom particles with the exception of a few data points. The ε_{xy} curve varied in compression close to the zero strain line. Moreover, the shear strain values were about 15 folds smaller than the normal strain tensor components in all cases. Since shear strain is primarily influenced by the contact point orientation, loading mode, particle shape, and fabric, we did not expect a well-defined trend in shear strains as particles translated and rotated as the loading progressed, which caused particles to establish or lose contact with the mold walls. Elastic anisotropy might have contributed to such behavior.

Volumetric lattice strain (ε_v) of individual sand particles under the influence of compressive loading is depicted in Figure 3.9. ε_v was calculated as the summation of the three normal strains (i.e., $\varepsilon_v = \varepsilon_{xx} + \varepsilon_{yy} + \varepsilon_{zz}$). Figure 3.9 shows that the volume of silica sand particles decreased (i.e., particle volume decreased) in a nearly linear fashion as the compressive load increased up to particle fracture. This was expected since it represented the elastic volumetric strain.

The lattice axial strains (ε_{zz}) of all tracked particles of the three tests are plotted in Figure 3.10, which shows the results up to fracture of one of the particles in the sand column. All particles exhibited linear load versus strain responses with a small increase of the curve slope as the loading rate increased from 0.0125 mm/min to 0.20 mm/min. The change of the slope with loading rate is in agreement with global load versus displacement measurements shown in Figure 3.3a, where higher loading rate caused an increase in the overall stiffness of the sand column.

Strain calculations for Tests 1 and 2 are summarized in Table 3.1. Compressive load (F) versus ε_{zz} measurements follow an almost perfect linear-elastic behavior up to fracture point with the exception of one particle (bottom particle of Test 1, see Table 3.1 and Figure 3.10) where we suspect that a partial fracture, which caused erratic behavior for loads higher than 14.75 N, took place before complete disintegration. A linear regression fit function of F versus ε_{zz} is also listed in the last column of Table 3.1. A high correlation coefficient ($R^2 \geq 0.993$) was found between F

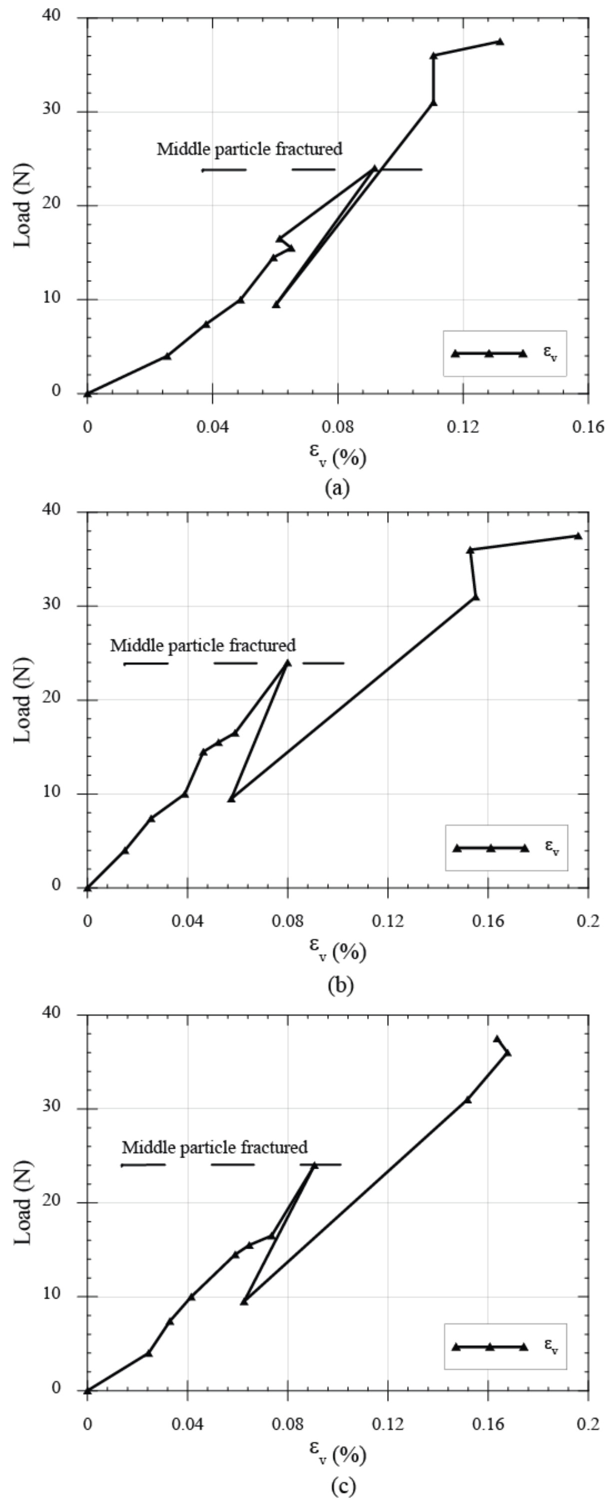

Figure 3.9. Volumetric strain versus load for (a) top particle, (b) middle particle, and (c) bottom particle of Test 3.

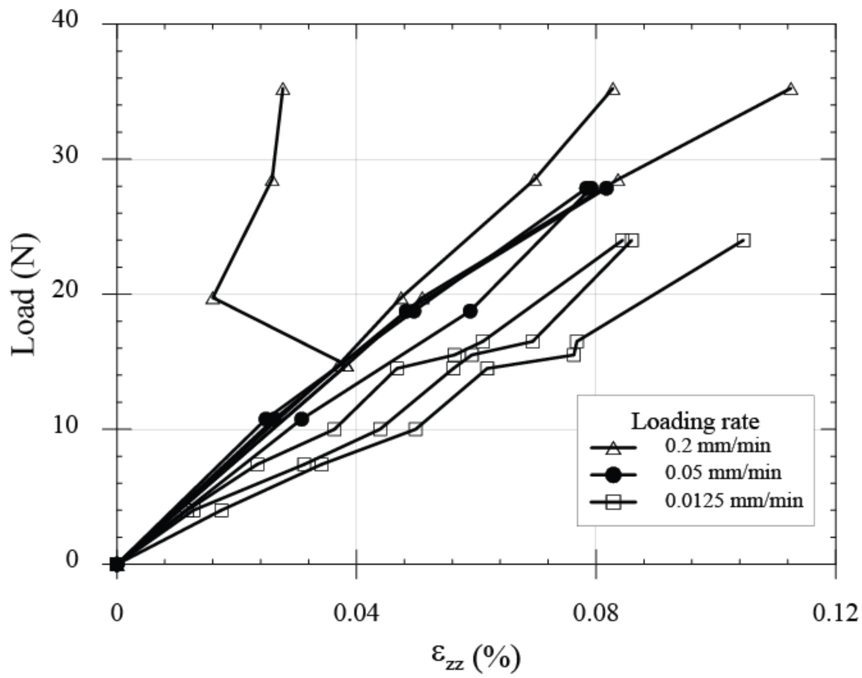

Figure 3.10. Axial strain values (ε_{zz}) for all particles up to first particle fracture point at different loading rates.

and ε_{zz} for all particles except the bottom particle of Test 1, which demonstrates the accuracy of the measurements.

Lattice strain-stress relationship

The lattice strain and stress tensors are linearly related through the elastic constants which form a fourth-rank tensor. Because strain and stress tensors are symmetric, the full equation can be contracted to (Heyliger *et al.* 2003):

$$\sigma_i = c_{ij}\varepsilon_j \qquad i, j = 1 \dots 6 \tag{3.9}$$

Here, the Voigt contraction was used. c_{ij} is the elastic stiffness tensor. The components c_{ij}^c are given in contracted notation and refer to a crystal frame orthonormal coordinate system$\{\hat{\boldsymbol{x}}, \hat{\boldsymbol{y}}, \hat{\boldsymbol{z}}\}$. The values of c_{ij} were obtained by expanding the c_{ij}^c to a fourth-rank tensor, transforming it to the sample frame (the change of basis matrix given by **U*****R** as described below), and back contracting.

For the trigonal crystal system, $\hat{\boldsymbol{x}}$ and $\hat{\boldsymbol{z}}$ are parallel to the **a**- and **c**-axis, respectively. It is important to note that the **U**-matrix in the Fable convention is defined as the change of basis matrix from an orthonormal coordinate system $\{\widehat{\boldsymbol{x}^*}, \widehat{\boldsymbol{y}^*}, \widehat{\boldsymbol{z}^*}\}$ attached to the reciprocal crystal frame ($\widehat{\boldsymbol{x}^*}, \widehat{\boldsymbol{z}^*}$ parallel to **a*** and **c***, respectively) to the sample frame. Therefore, the change of basis matrix from the $\{\hat{\boldsymbol{x}}, \hat{\boldsymbol{y}}, \hat{\boldsymbol{z}}\}$ system to the sample system is given by **U*****R** where **R** is the change of coordinate matrix from the real $\{\hat{\boldsymbol{x}}, \hat{\boldsymbol{y}}, \hat{\boldsymbol{z}}\}$ to the reciprocal $\{\widehat{\boldsymbol{x}^*}, \widehat{\boldsymbol{y}^*}, \widehat{\boldsymbol{z}^*}\}$ crystal coordinate systems (a 30° rotation around the c-axis). The stress tensors were then expanded from the contracted forms obtained using Equation (3.9) for which the experimental strain tensors were contracted to Voigt notation.

Figure 3.11a shows the evolution of the stress tensor components for the first seven applied load steps of the middle particle of Test 3. We note first that quartz has a significant elastic anisotropy, as indicated by Young's moduli of 79.4 GPa and 103 GPa in the a- and c-axis directions, respectively, and a much larger directional variation of the Poisson ratio (Heyliger *et al.* 2003). Thus anisotropic elasticity should be applied when converting lattice strains into stresses. The stress components showed a remarkably linear load dependence and uniaxial loading state over the first four applied loading steps. σ_{zz} component exhibits a linear variation in stress-strain plot under uniaxial loading as expected. On the other hand, σ_{xx} and σ_{yy} components show compressional and tensional behavior under the effect of several factors including rotation, translation, boundary effect, and contact points. We concluded that the interactions of particles with the wall of the mold were initially small and that the experimental uncertainty on the stress components was on the order of a few MPa. Significant changes of the loading state observed during loading step five were attributed to a rearrangement of the particles. One now can easily generate the stress-strain plot for any particle using lattice strain measurements as input to calculate stress tensor. Figure 3.11b shows an illustrative example for the stress-strain relationships for the normal strain components for the middle particle of Test 3. Shear stress-strain components were not plotted in Figure 3.11b since they are very small when compared to normal stress-strain components.

Summary and Conclusions

3DXRD technique was successfully used to collect diffraction data and use those data to calculate in situ elastic lattice strain measurements of individual silica sand particles and track

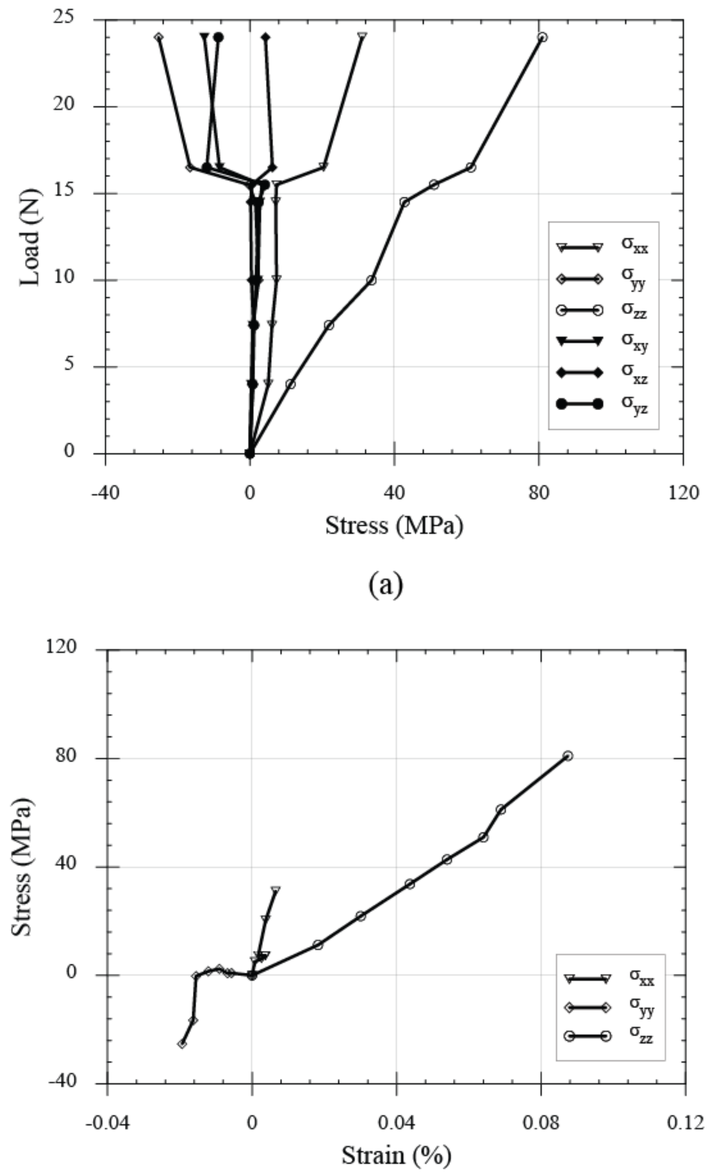

(a)

(b)

Figure 3.11. (a) Applied load versus sample frame stress tensor components of the middle particle of Test 3, and (b) stress versus strain variation for the middle particle of Test 3.

particle orientation under the effect of 1D compressive loading. The axial normal strain ε_{zz} exhibited a linear response in the range of 0 to 10^{-3} to the applied axial load between 0 and 30 N up to particle fracture. The relationship between F and ε_{zz} fits a linear regression model with a very high correlation coefficient ($R^2 \geq 0.993$), which represents the linear elastic deformation of the sand particles. The volumetric strain decreased linearly with applied load up to particle fracture. An increase in the loading rate caused an increase in the slope of the load versus ε_{zz} relationships. The stress tensor was calculated using the elastic constants of quartz from literature and the lattice strain tensor. Experimental quantification of the evolution of particle orientation, lattice strain and stress tensors of silica sand provided valuable key measurements for the constitutive behavior of individual silica sand particles and can be used to develop, validate, or calibrate micromechanics-based finite element and discrete element methods to predict the constitutive behavior of granular materials.

Acknowledgments

This material is based upon work supported by the National Science Foundation (NSF) under Grant No. (CMMI-1156436). The 3DXRD data were collected using the x-ray Operations and Research Beamline 1-ID and SMT scans were collected using the X-ray Operations and Research Beamline Station 13-BMD at the Advanced Photon Source (APS), Argonne National Laboratory (ANL). We thank Dr. Mark Rivers of (APS) for help in performing the SMT scans. We also acknowledge the support of GeoSoilEnviroCARS (Sector 13), which is supported by the National Science Foundation - Earth Sciences (EAR-1128799), and the Department of Energy, Geosciences (DE-FG02-94ER14466). Use of the Advanced Photon Source, an Office of Science

User Facility operated for the U.S. Department of Energy (DOE) Office of Science by Argonne National Laboratory, was supported by the U.S. DOE under Contract No. DE-AC02-06CH11357

References

Allersma, H. G. B. (1982)."Photo-elastic Stress Analysis and Rate of Strain on the Measured In Situ Shear Strength of Soils." *IUTAM Conference on Deformation and Failure of Granular Materials*, Balkema, 345-353.

Alsaleh, M. I., Voyiadjis, G. Z., and Alshibli, K. A. (2006). "Modelling strain localization in granular materials using micropolar theory: Mathematical formulations." *International Journal for Numerical and Analytical Methods in Geomechanics*, 30(15), 1501-1524.

Alshibli, K. A., and Reed, A. (2010). *Advances in Computed Tomography for Geomaterials: Geox2010*, John Wiley & Sons, Hoboken, NJ, USA.

Bardet, J. P., and Proubet, J. (1991). "A Numerical Investigation of the Structure of Persistent Shear Bands in Granular Media." *Geotechnique*, 41(4), 599-613.

Butler, L. G. (2010). "Progress Towards Neutron Tomography at the US Spallation Neutron Source." *Advances in Computed Tomography for Geomaterials*, John Wiley & Sons, Inc., 366-373.

Calvetti, F., Combe, G., and Lanier, J. (1997). "Experimental micromechanical analysis of a 2D granular material: relation between structure evolution and loading path." *Mechanics of Cohesive-frictional Materials*, 2(2), 121-163.

Cundall, P. A. (1989). "Numerical experiments on localization in frictional materials." *Archive of Applied Mechanics*, 59(2), 148-159.

Dafalias, Y. F. (1983). "Corotational rates for kinematic hardening at large plastic-deformations." *J Appl Mech-T Asme*, 50(3), 561-565.

Darling, T. W., TenCate, J. A., Brown, D. W., Clausen, B., and Vogel, S. C. (2004). "Neutron diffraction study of the contribution of grain contacts to nonlinear stress-strain behavior." *Geophys Res Lett*, 31(16), L16604.

De Borst, R. (1991). "Simulation of strain localization: a reappraisal of the Cosserat continuum." *Engineering computations*, 8(4), 317-332.

Fable (2011). <http://sourceforge.net/apps/trac/fable/wiki>. (accessed October 19, 2012).

Frischbutter, A., Neov, D., Scheffzuk, C., Vrana, M., and Walther, K. (2000). "Lattice strain measurements on sandstones under load using neutron diffraction." *J Struct Geol*, 22(11-12), 1587-1600.

Geng, J. F., Reydellet, G., Clement, E., and Behringer, R. P. (2003). "Green's function measurements of force transmission in 2D granular materials." *Physica D*, 182(3-4), 274-303.

Gudehus, G. (1996). "A comprehensive constitutive equation for granular materials." *Journal of the Japanese Geotechnical Society : soils and foundation*, 36(1), 1-12.

Hall, S., Wright, J., Pirling, T., Andò, E., Hughes, D., and Viggiani, G. (2011). "Can intergranular force transmission be identified in sand?" *Granular Matter*, 13(3), 251-254.

Hasan, A., and Alshibli, K. (2012). "Three dimensional fabric evolution of sheared sand." *Granular Matter*, 14(4), 469-482.

Heyliger, P., Ledbetter, H., and Kim, S. (2003). "Elastic constants of natural quartz." *J Acoust Soc Am*, 114(2), 644-650.

Jensen, D. J., Offerman, S. E., and Sietsma, J. (2008). "3DXRD characterization and modeling of solid-state transformation processes." *Mrs Bull*, 33(6), 621-629.

Kenesei, P. (2012). "DIGIgrain." < http://sourceforge.net/apps/trac/digigrain/wiki>. (accessed October 19, 2012).

Levien, L., Prewitt, C. T., and Weidner, D. J. (1980). "Structure and Elastic Properties of Quartz at Pressure." *Am Mineral*, 65(9-10), 920-930.

Lienert, U., Schulze, C., Honkimaki, V., Tschentscher, T., Garbe, S., Hignette, O., Horsewell, A., Lingham, M., Poulsen, H. F., Thomsen, N. B., and Ziegler, E. (1998). "Focusing optics for high-energy X-ray diffraction." *J Synchrotron Radiat*, 5, 226-231.

Ludwig, W., Reischig, P., King, A., Herbig, M., Lauridsen, E. M., Johnson, G., Marrow, T. J., and Buffiere, J. Y. (2009). "Three-dimensional grain mapping by x-ray diffraction contrast tomography and the use of Friedel pairs in diffraction data analysis." *Review of Scientific Instruments*, 80(3), 033905-033909.

Majmudar, T. S., and Behringer, R. P. (2005). "Contact force measurements and stress-induced anisotropy in granular materials." *Nature*, 435(1079), 1079-1082.

Manzari, M. T., and Dafalias, Y. F. (1997). "A critical state two-surface plasticity model for sands." *Geotechnique*, 47(2), 255-272.

Margulies, L., Lorentzen, T., Poulsen, H. F., and Leffers, T. (2002). "Strain tensor development in a single grain in the bulk of a polycrystal under loading." *Acta Mater*, 50(7), 1771-1779.

Martins, R. V., Margulies, L., Schmidt, S., Poulsen, H. F., and Leffers, T. (2004). "Simultaneous measurement of the strain tensor of 10 individual grains embedded in an Al tensile sample." *Mat Sci Eng a-Struct*, 387, 84-88.

Morawiec, A., and Field, D. P. (1996). "Rodrigues parameterization for orientation and misorientation distributions." *Philosophical Magazine A*, 73(4), 1113-1130.

Oda, M., and Kazama, H. (1998). "Microstructure of shear bands and its relation to the mechanisms of dilatancy and failure of dense granular soils." *Geotechnique*, 48(4), 465-481.

Oda, M., Konishi, J., and Nemat-Nasser, S. (1982). "Experimental Micromechanical Evaluation of Strength of Granular Materials: Effects of Particle Rolling." *Mech Mater*, 1, 269-283.

Oddershede, J., Schmidt, S., Poulsen, H. F., Sorensen, H. O., Wright, J., and Reimers, W. (2010). "Determining grain resolved stresses in polycrystalline materials using three-dimensional X-ray diffraction." *Journal of Applied Crystallography*, 43(3), 539-549.

Penumadu, D., Dutta, A., Luo, X., and Thomas, K. (2009). "Nano and neutron science applications for geomechanics." *KSCE J Civ Eng*, 13(4), 233-242.

Poulsen, H. F. (2004). *Three-dimensional X-ray diffraction microscopy: mapping polycrystals and their dynamics*, Springer.

Poulsen, H. F., Margulies, L., Schmidt, S., and Winther, G. (2003). "Lattice rotations of individual bulk grains: Part I: 3D X-ray characterization." *Acta Mater*, 51(13), 3821-3830.

Poulsen, H. F., Nielsen, S. F., Lauridsen, E. M., Schmidt, S., Suter, R. M., Lienert, U., Margulies, L., Lorentzen, T., and Juul Jensen, D. (2001). "Three-dimensional maps of grain boundaries and the stress state of individual grains in polycrystals and powders." *Journal of Applied Crystallography*, 34(6), 751-756.

Regueiro, R. A., and Yan, B. (2011). "Concurrent Multiscale Computational Modeling for Dense Dry Granular Materials Interfacing Deformable Solid Bodies." *Bifurcations, Instabilities and Degradations in Geomaterials*, R. Wan, M. Alsaleh, and J. Labuz, eds., Springer Berlin Heidelberg, 251-273.

Rowe, P. W. (1962). "The Stress-Dilatancy Relation for Static Equilibrium of an Assembly of Particles in Contact." *Proceedings of the Royal Society of London. Series A. Mathematical and Physical Sciences*, 269(1339), 500-527.

Schmidt, S. (2010). "GrainSpotter v. 0.82. ." <http://fable.svn.sourceforge.net/svnroot/fable/GrainSpotter>. (accessed October 19, 2012).

vanDoorn, E., and Behringer, R. P. (1997). "Dilation of a vibrated granular layer." *Europhys Lett*, 40(4), 387-392.

Wright, J. (2005). "*ImageD11*." <http://sourceforge.net/apps/trac/fable/wiki/imaged11>. (accessed October 19, 2012).

CHAPTER 4

COMBINED HIGH-ENERGY SYNCHROTRON X-RAY DIFFRACTION AND COMPUTED TOMOGRAPHY TO CHARACTERIZE CONSTITUTIVE BEHAVIOR OF SILICA SAND

This Chapter is a modified version of the paper published in: Cil, M. B., Alshibli, K., Kenesei, P., and Lienert, U. (2014). "Combined high-energy synchrotron X-ray diffraction and computed tomography to characterize constitutive behavior of silica sand." *Nuclear Instruments and Methods in Physics Research Section B: Beam Interactions with Materials and Atoms*, 324, 11-16.

Abstract

The deformation behavior of silica sand particles under one-dimensional (1D) loading compression was investigated using nondestructive 3D synchrotron micro-computed tomography (SMT) and three dimensional x-ray diffraction (3DXRD). High-resolution SMT images were used to monitor particle-to-particle interactions, and the onset and propagation of fracture mechanism in a column composed of three silica sand particles. Particle-averaged lattice strain tensors within individual sand particles were measured using the 3DXRD technique and were then used to calculate the stress tensor components via the general elastic stress-strain relationship. The normal stress component in the axial direction (σ_{zz}) exhibited a nearly linear increasing trend in all sand particles. Shear stress components were in general small relative to the normal stress components and displayed no systematic trend. Knowing lattice strains, stresses, and particle kinematic behavior, one can formulate and develop a micromechanics-based constitutive model to fully characterize strength properties and deformation characteristics of granular materials.

Introduction

The common use of granular materials in various engineering and science applications promotes the need to develop advanced constitutive models to better predict the macroscopic response of discrete systems under various loading conditions. Many constitutive models were developed based on the elasto-plastic theory and continuum mechanics in which the discrete nature of the particulate system on the microscale-level was not taken into account (e.g., Manzari and Dafalias 1997, Borja and Andrade 2006, Russell and Khalili 2006). The stress-strain behavior of granular materials is governed by complex micromechanical processes including particle translation, rotation, and fracture, which need to be considered while developing a comprehensive mathematical model. The first prerequisite of developing a micromechanics-based constitutive model is to measure micro-scale properties of the material. Distinct element method (DEM), introduced by Cundall and Strack (1979), provided a framework to investigate the independent interaction of individual particles and permitted acquiring particle-level measurements including contact forces, which are impossible to obtain using conventional experimental techniques (O'Sullivan and Cui 2009). DEM's applicability for modeling engineering applications is limited, however, by its inability to represent real particle morphology and the expensive computational time necessary for large specimens.

The limitations of numerical and theoretical approaches motivated many researchers to explore alternative options, and promising new powerful experimental techniques such as x-ray computed tomography (CT) have emerged as alternative solutions to gain insight into micromechanical processes that occur during the deformation of granular media (Matsushima *et al.* 2007). X-ray CT and its advanced version, synchrotron micro-computed tomography (SMT), are non-invasive 3D imaging techniques that have been used in a wide range of applications including geomaterial studies. SMT can yield a high-resolution 3D image of particulate system which allows in situ monitoring of the deformation mechanisms and particle kinematics (e.g., Andò *et al.* 2012, Hasan and Alshibli 2012). However, SMT does not provide measurements of inter-particle forces or strains within the particle itself.

Three dimensional x-ray diffraction (3DXRD) is a revolutionary non-destructive experimental technique for characterizing the structure of polycrystalline materials. It allows robust determination of the crystallographic orientation, position, and shape of individual grains embedded in the bulk of specimen with a high resolution. Moreover, 3DXRD provides a unique opportunity to investigate the deformation behavior of microstructural elements under macroscopic loading (Margulies *et al.* 2002, Lienert *et al.* 2004, Martins *et al.* 2004, Oddershede *et al.* 2010); the kinetics of grains during recrystallization (Lauridsen *et al.* 2003, Poulsen *et al.* 2011); the nucleation and growth processes in solid-state phase transformation (Offerman *et al.* 2002); and the rotation of grains under deformation (Poulsen *et al.* 2003). Moreover, many models associated with the evolution and interaction of microstructures can be validated and improved with the help of measurements acquired through the 3DXRD method (Jensen *et al.* 2008). Poulsen (2004) presented the basic principles, instrumentation, and groundbreaking applications of 3DXRD. The majority of 3DXRD applications were utilized in studies related to metals. On the granular materials side, Hall *et al.* (2011) presented preliminary results of 3DXRD scanning on Ottawa sand specimens that were subjected to one-dimensional (1D) loading. However, their analysis did not include extracting lattice strain tensor measurements from the data.

In this study, SMT and 3DXRD methods are combined to gain insight into the deformation characteristics of sand particles under 1D loading condition. The main objective of this paper is to describe the experimental methodologies of both techniques and to determine grain-averaged stress-strain tensors of individual silica sand particles.

Experimental Techniques

SMT scanning technique

SMT is a non-destructive 3D imaging technique that has been extensively used in various fields such as biological and geological specimen studies in the last few decades. It can produce 3D high-resolution images through mapping the attenuation data as x-ray beam travels through the specimen. SMT has become available with the development of third-generation synchrotron facilities, which have provided a unique opportunity to obtain collimated and tunable high photon flux radiation. A high energy monochromatic x-ray beam generated from a synchrotron source passes through a specimen positioned on a rotation stage between the incoming x-ray beam and scintillator (Figure 4.1). Some of the photons are absorbed by the specimen, which primarily depends on the electron density distribution within the specimen and the energy of the x-rays.

The linear attenuation coefficient is strongly dependent on the atomic number of the elements within the sample. The transmitted x-rays are converted to visible light through a scintillator and recorded using a high-resolution detector. To obtain a 3D volumetric image, a series of projections must be acquired while rotating the sample typically from 0° to 180° with 0.1° to 1° increments. During this process, flat field images which map the incoming x-ray beam profile are also collected for the reconstruction process to normalize the measured transmission maps. Multiple scans at consecutive vertical specimen positions are performed if the height is longer than the beam height. Data processing can be summarized as dark field correction, normalization, determination of the rotation axis and reconstruction of the 3D volumetric data, which results in a stack of 2D slices (Rivers *et al.* 1999, Rivers *et al.* 2004). These slices contain the spatial distribution map of the x-ray attenuation of the specimen. In this study, the raw scan

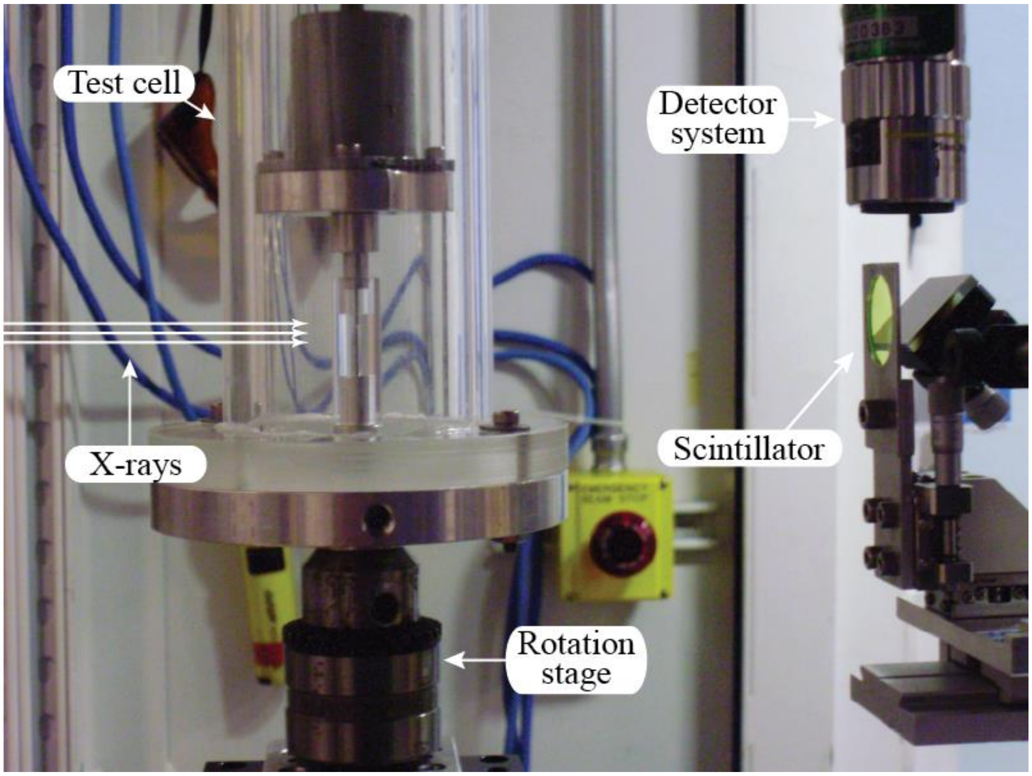

Figure 4.1. A close up of the SMT setup which shows incoming x-ray direction, test cell, and data acquisition system.

data is processed via user-written scripts in an Interactive Data Language (IDL) program, which uses the GridRec algorithm written in C to reconstruct 3D images.

3DXRD technique

3DXRD was developed by a research group from the Risø National Laboratory (Denmark) at the European Synchrotron Radiation Facility (ESRF, France), which commissioned the first dedicated instrument in 1999. The basic working mechanism of the 3DXRD method is tracking diffracted hard x-rays using a transmission-based data collection system (Figure 4.2). The x-ray radiation provided by the synchrotron storage ring passes through a series of specially fabricated optics, which produce a monochromatic high energy x-ray beam while maintaining the high brilliance. The main advantage of hard x-rays over low energy x-rays is the high penetration power, which makes it suitable for studying the bulk specimen behavior of various polycrystalline materials. The desired beam size in horizontal and vertical directions is determined based on the average grain size of the material and specimen thickness and is adjusted using a group of slits. Then, the high-energy x-ray beam impinges on the specimen, which is positioned on high precision rotational and translational stages between incoming beam and data acquisition system. Some crystallites of the illuminated specimen satisfy the Bragg condition and give rise to diffracted beams, which are transmitted through the specimen and recorded by a 2D area detector. Due to the high energy x-ray with short wavelength, the diffraction angles 2θ are smaller than at low energies, therefore several diffraction orders can be acquired on a single area detector. To probe the whole specimen, the specimen must be rotated perpendicular to the beam direction with angular rotation

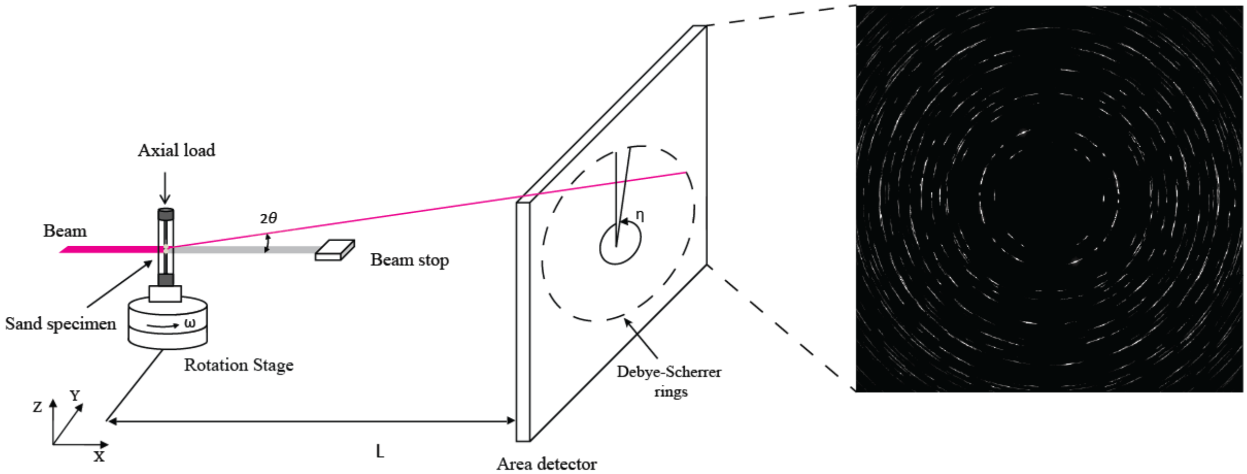

Figure 4.2. Schematic of the far-field 3DXRD setup and typical 3DXRD data including diffraction spots on the Debye-Scherrer rings.

increments ($\Delta\omega$). If the specimen dimensions are larger than the beam size, multiple scans are acquired at different positions.

The detector configuration is determined based on the objective of the experiment (e.g., 3D mapping of grains or investigating microstructural kinetics during typical processes). Since the objective of this study is to measure the grain deformation under compressive loading, a far-field detector configuration was adopted to probe the orientation and deformation in the grain lattice.

Experiments

Testing apparatus

The sand used in the experiments is a natural uniform silica sand known as ASTM 20-30 Ottawa sand with particle sizes between 0.595 mm (Sieve No. 30) and 0.841 mm (Sieve No. 20). The experiments were conducted using a specially designed test cell that consists of a loading system, a specimen mold, load cells, and a data acquisition system (Figure 4.3). The compressive load was applied using a high precision computerized stepper motor that can apply a displacement rate as small as 0.0125 mm/min. The specimen mold consists of an acrylic cylinder with a diameter of 15 mm and a 1 mm hole at the center. Two load cells were attached to the top and bottom of the specimen to measure load reduction due to friction between particles and the mold. This setup is supported by a hollow cylindrical acrylic chamber bolted to the top and bottom cell plates. Only three sand particles were placed inside the 1 mm hole as a column to eliminate plugging of particles during compression. The sand column was scanned before the axial load was applied; it was then loaded until the desired compressive load was reached, and the scan was performed while the

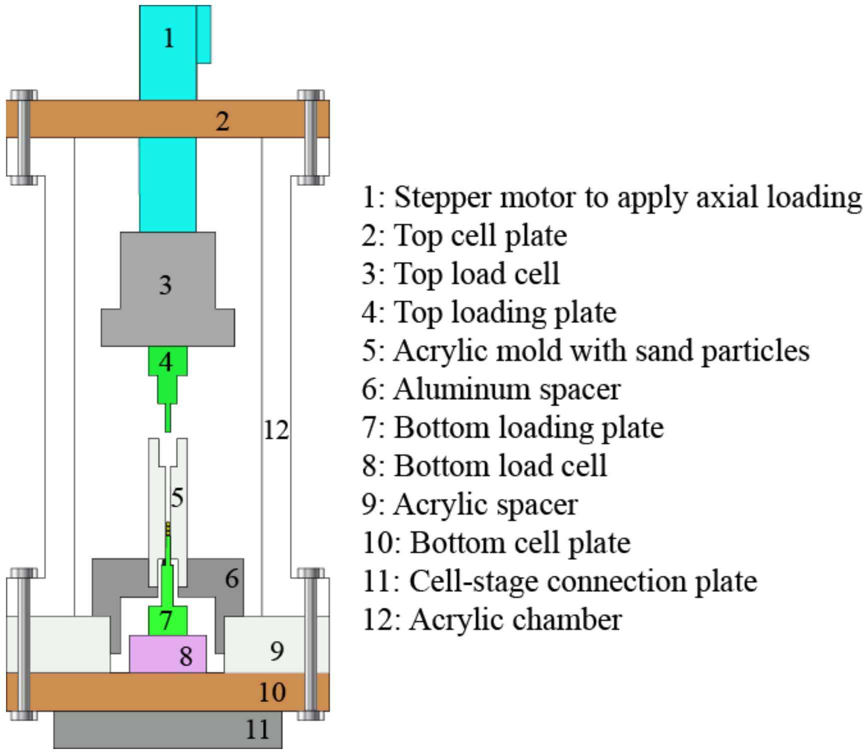

Figure 4.3. Schematic of 1D compression test cell.

stepper motor position was held in position. This procedure was repeated for consecutive load levels and scans.

SMT scans

The SMT scans were conducted at the Advanced Photon Source (APS), GeoSoilEnviroCARS (GSECARS) Sector 13 of the Argonne National Laboratory (ANL), Illinois, USA. The x-ray beam was monochromatized using a Si (111) double crystal monochromator that preserves the high flux of the x-rays. To obtain high-resolution images in a relatively small specimen size (~1 mm diameter × ~2.4 mm height), the attenuated x-rays were acquired by an imaging system consisting of a single crystal scintillator, a 5x microscope objective and a 1392 × 1040 pixel resolution CoolSnap HQ^2 CCD camera from Roper Scientific, which provided an image resolution of 4.95 μm/pixel. The scans were carried out at an x-ray energy of 23 keV. X-ray images were collected at 0.25° increments by rotating the specimen over 180° and applying 1 second exposure time, which produced 720 frames per scan. 3D SMT images were acquired at multiple load levels for three compression experiments.

3DXRD scans

The 3DXRD experiments were performed at the 1-ID beamline of the APS. The test cell was mounted on the high precision specimen stages, which provide translation in x, y, and z direction along with the rotation around the z-axis. The sand particles were illuminated by a high-energy x-ray beam with a size of 1.0 mm × 0.8 mm and an energy of 80.725 keV that corresponds to a wavelength of 0.15358 Å. 3DXRD data were acquired by rotating the specimen at a constant angular velocity about an axis perpendicular to the beam direction. The beam was centered to completely illuminate the 1 mm diameter that contains the particle column, and rotation scans were collected at three successive vertical levels. Diffraction data were acquired by an area detector that was positioned at a horizontal distance of 1593 mm (L in Figure 4.2) from the specimen. An intensity distribution image of the diffracted spots (called the ω-slice) was recorded at each rotation interval of $\Delta\omega$. The raw diffraction data consist of 180 stacked images recorded while the specimen was rotated in ω from -90° to 90° with $\Delta\omega = 1°$ integration intervals at each loading step for each particle. Three 1D compression experiments were conducted at displacement rates of 0.0125 mm/min, 0.05 mm/min, and 0.2 mm/min. Multiple 3DXRD scans were collected at various load levels.

Results

SMT imaging

An example load-displacement relationship of 1D compression experiments conducted during SMT scans is depicted in Figure 4.4a, which shows that the compressive load level increases gradually as compression progresses. Compressive forces, displacement, stress, and strain are taken as positive throughout this paper according to the sign convention in the field of geotechnical engineering. Some small load drops due to particle movement are observed before the major fracture of one of the particles which leads to a significant load drop. A scatter curve emerges after the initial fracture, which results from the continuing fracture of broken fragments of the fractured particle. The axial cross sectional images of the specimen acquired at consecutive

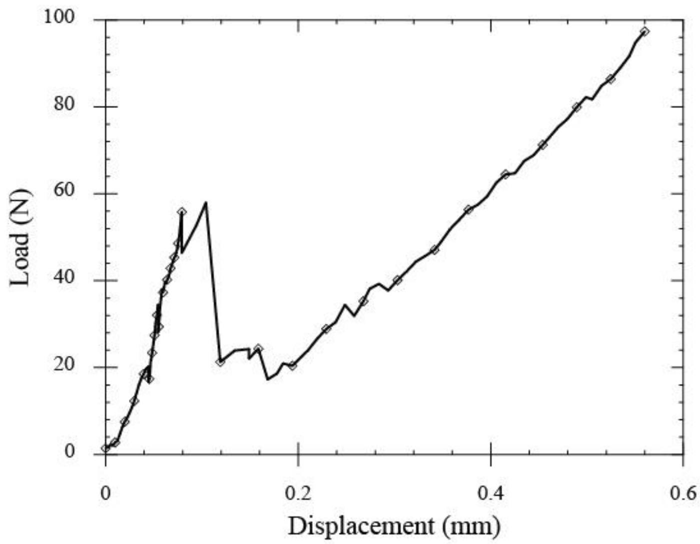

(a)

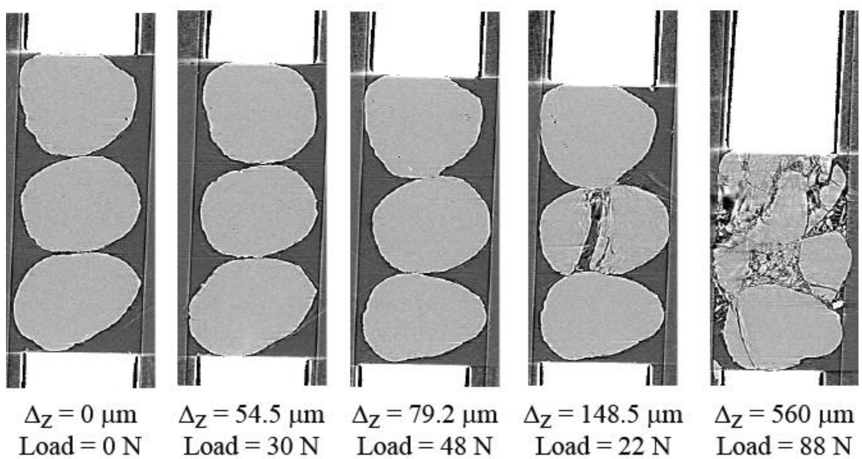

(b)

Figure 4.4. (a) Load versus displacement relationship for one of the 1D compression experiments that was conducted while acquiring the SMT scans, and (b) the axial cross-sectional images of the specimen acquired at multiple displacement levels.

load steps are shown in Figure 4.4b, which clearly demonstrates the compressive behavior of individual sand particles under 1D compression. Initially, particles slightly rearrange via rotation and/or translation, and reach a stable configuration in which lateral support is provided by the mold walls. Then, the column of particles resists the increasing compressive load until fracture occurs in the form of catastrophic splitting. Both fractured and intact particles continue to fracture as the compression progresses.

The advantages of combining SMT and 3DXRD data

SMT provides valuable 3D images of sand particles that cannot be obtained through the 3DXRD method. SMT images enable in situ monitoring of the fracture mechanism and particle kinematic behavior. Examining the 3D images of the specimen demonstrated that particles experience translation and/or rotation before fracture due to the interaction of discrete particles at the contact points. The positional change of sand particles resulted in the translation of diffraction spots in 3DXRD scans, which is not observed in the majority of the 3DXRD applications performed on metals. Therefore, the motion of sand particles due to axial loading has to be considered while evaluating the diffraction data. One of the drawbacks of the 3DXRD method is that it does not allow visualization of the initiation and propagation of fracture. This limitation was eliminated by using complementary SMT that has proven very helpful in the selection of the load steps for the 3DXRD measurements to investigate the evolution of lattice strain before fracture. In addition, compressive displacement can be measured with a high degree of precision by calculating the motion of loading platens or tracking particle positions in SMT images.

Measuring particle strain

Since only one or two sand particles were illuminated in all scans until the first particle fracture occurrence in the system, 2D diffraction images are composed of a limited number of separated diffraction spots on the Debye-Scherrer rings, which makes the data evaluation process easy to handle compared to 3DXRD data with overlapped spots. The analysis of the diffraction data was carried out by following a series of steps consisting of peak searching, indexing, and the computation of lattice stress-strain tensor components. First, the DIGIgrain program that was developed by Kenesei (2012) was used to perform several background corrections on the acquired raw diffraction images and to identify the diffraction spots by deploying a 3D peak search. The program provided a list of diffraction peaks along with their properties including position and intensity. Then, g-vectors (diffraction vectors) were computed based on the identified peaks with the Image11 transformation program (Wright 2005) which also enables to calibrate detector distance and beam center. These g-vectors were assigned to the corresponding grains with the help of the GrainSpotter indexing program (Schmidt 2010). The results are summarized in an output file that includes the indexed grains and their properties (orientation, 3D center of mass position, the list of associated diffraction peaks).

The next step is the determination of the elastic grain deformation that was executed using a Matlab script written by the authors. The lattice-strain was calculated by measuring the changes in the magnitude of g-vectors relative to the unloaded grain condition. The grain averaged strain tensor (ε_i) components were calculated based on the following equation:

$$\varepsilon_i = \frac{g_i - g_i^0}{g_i^0} \tag{4.1}$$

where g_i^0 and g_i are the length of the g-vectors in the unloaded and loaded cases, respectively. For each load level, the corresponding g-vectors were identified and compared with the initial strain-free condition. Details of the strain calculation process are presented in Alshibli *et al.* (2013).

Since all strain tensor components are obtained from the diffraction analysis, the grain stress (σ_i) could be derived using the general elastic constitutive relationship. The fourth-rank stiffness tensor, which relates strain to stress can be contracted to a six-by-six matrix in the Voigt contraction notation as follows:

$$\sigma_i = c_{ij}\varepsilon_j \qquad i,j = 1 \ldots 6 \tag{4.2}$$

where c_{ij} is the elastic stiffness tensor in contracted form. The anisotropic elastic structure of the quartz was taken into account while inferring stresses from the grain averaged strain tensors, and the elastic constants of quartz were obtained from Heyliger *et al.* (2003) The stress tensor components in the sample coordinate system were calculated from the measured strain tensor components using Equation (4.2) and appropriate coordinate system transformations.

The stress-strain relationships of the normal stress components of top particles in Tests 1, 2, and 3 are depicted in Figure 4.5 which demonstrates that σ_{xx} and σ_{yy} exhibit complex deformation behavior resulting from the combined effects of various micromechanical processes such as the translation and rotation of particles and the effect of boundary conditions. Moreover, σ_{xx} and σ_{yy} components are small relative to σ_{zz} component, reflecting the 1D loading mode. Also, the small Poisson's ratio in silica sand particles should be noted. Since shear strain components

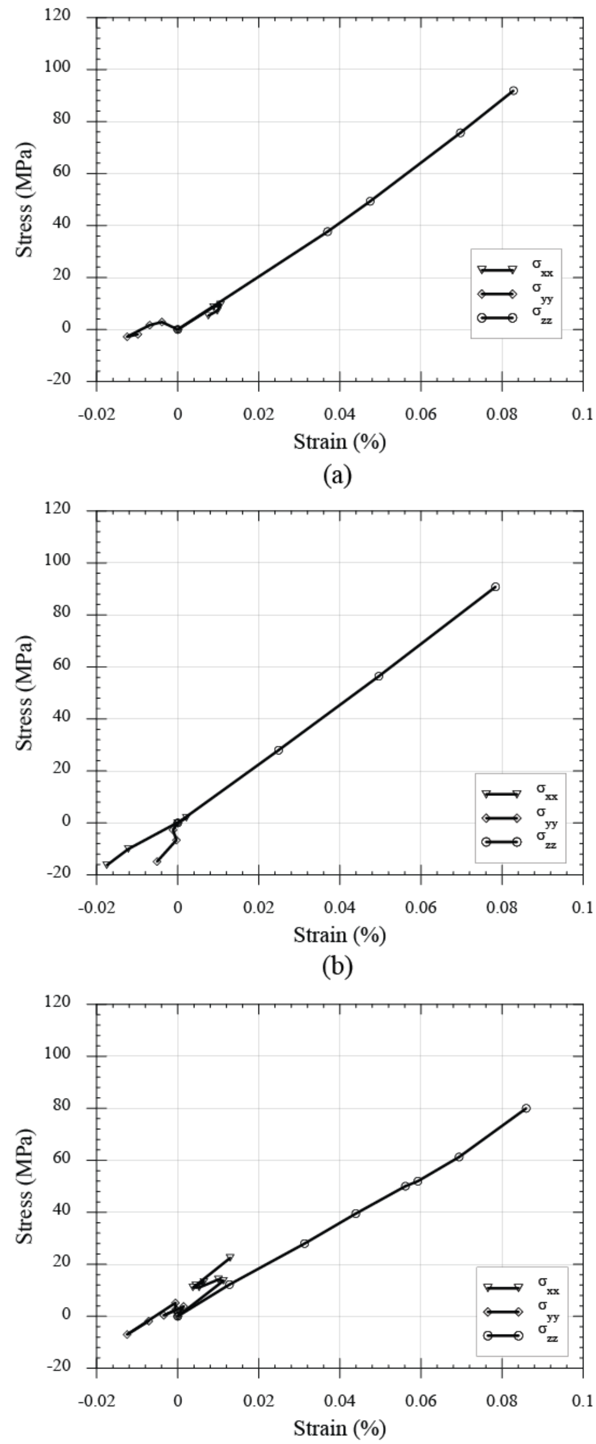

Figure 4.5. Stress-strain relationships for the normal stress components of the top sand particles in (a) Test 1; (b) Test 2; and (c) Test 3.

are very small compared to normal stress components in all cases, they were not plotted in Figure 4.5. The majority of the shear stress components are an order of magnitude smaller than the normal stresses and exhibited a nonlinear continuous variation throughout the loading, which is mainly governed by particle shape, contact point orientation, particle movement, and fabric. As depicted in SMT images shown in Figure 4.4b, particles rearrange during the deformation process and come in contact with the mold and neighbor particles in multiple directions, which produces a highly complex particulate system that is difficult to interpret.

Figure 4.6 shows the normal stress component in the loading direction (σ_{zz}) of all silica sand particles up to the fracture of one of the particles in the sand column. A nearly linear stress-strain relationship is evident in all sand particles under 1D loading as expected. The variation between components stems from several factors including particle motion, or interactions between particle and boundary conditions. Overall, the results show a very consistent elastic behavior in the direction of loading.

Conclusions

The SMT and 3DXRD techniques complement each other to provide insight into the constitutive behavior of silica sand particles that were subjected to 1D compression. The SMT imaging technique enabled in situ visualization of particle kinematic behavior and the evolution of fracture mechanism. The stress-strain relationship of silica sand particles under 1D loading was examined based on 3DXRD scans. The σ_{zz} stress component of all sand particles in the direction of loading varied linearly in agreement with the expectations. On the other hand, normal stress (σ_{xx}, σ_{yy}) and shear stress components are relatively small and exhibited inconsistent and nonlinear

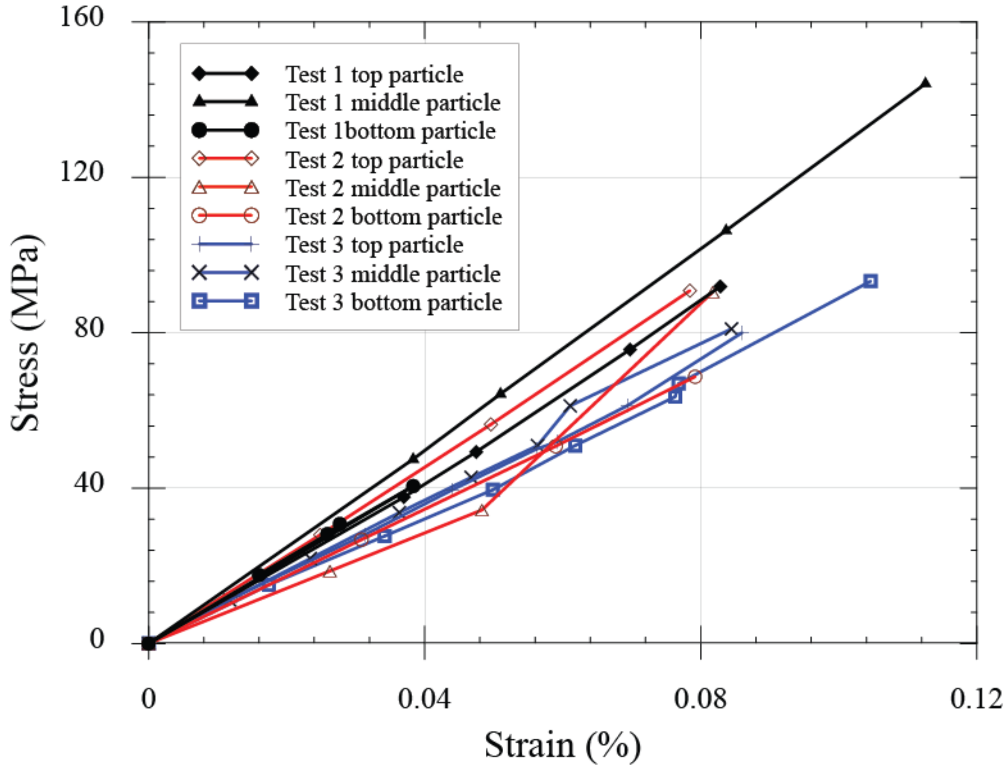

Figure 4.6. Strain versus normal stress (σ_{zz}) relationships of all sand particles of the three tests.

trends in the majority of the particles under the influence of various micro-scale processes. Combining SMT and 3DXRD offers excellent particle-level measurements that can be used to develop a micromechanics-based constitutive model of granular materials.

Acknowledgements

This material is based on work supported by the National Science Foundation (NSF) under Grant No. CMMI-1156436. The 3DXRD data were collected using the Beamline 1-ID and SMT scans were collected using Beamline 13 at the Advanced Photon Source (APS), Argonne National Laboratory (ANL), USA. We thank Dr. Mark Rivers of APS for help in performing the SMT scans. We also acknowledge the support of GeoSoilEnviroCARS (Sector 13), which is supported by the National Science Foundation-Earth Sciences (EAR-1128799), and the Department of Energy (DOE), Geosciences (DE-FG02-94ER14466). Use of the APS, an Office of Science User Facility operated for the DOE Office of Science by Argonne National Laboratory, was supported by DOE under Contract No. DE-AC02-06CH11357

References

Alshibli, K., Cil, M. B., Kenesei, P., and Lienert, U. (2013). "Strain tensor determination of compressed individual silica sand particles using high-energy synchrotron diffraction." *Granular Matter*, 15(5), 517-530.

Andò, E., Hall, S., Viggiani, G., Desrues, J., and Bésuelle, P. (2012). "Grain-scale experimental investigation of localised deformation in sand: a discrete particle tracking approach." *Acta Geotech*, 7(1), 1-13.

Borja, R. I., and Andrade, J. E. (2006). "Critical state plasticity. Part VI: Meso-scale finite element simulation of strain localization in discrete granular materials." *Computer Methods in Applied Mechanics and Engineering*, 195(37–40), 5115-5140.

Cundall, P., and Strack, O. (1979). "A Discrete Numerical model for Granular Assemblies." *Geotechnique*, 29(1), 47-65.

Hall, S., Wright, J., Pirling, T., Andò, E., Hughes, D., and Viggiani, G. (2011). "Can intergranular force transmission be identified in sand?" *Granular Matter*, 13(3), 251-254.

Hasan, A., and Alshibli, K. (2012). "Three dimensional fabric evolution of sheared sand." *Granular Matter*, 14(4), 469-482.

Heyliger, P., Ledbetter, H., and Kim, S. (2003). "Elastic constants of natural quartz." *J Acoust Soc Am*, 114(2), 644-650.

Jensen, D. J., Offerman, S. E., and Sietsma, J. (2008). "3DXRD characterization and modeling of solid-state transformation processes." *Mrs Bull*, 33(6), 621-629.

Kenesei, P. (2012). "DIGIgrain." < http://sourceforge.net/apps/trac/digigrain/wiki>.

Lauridsen, E. M., Poulsen, H. F., Nielsen, S. F., and Juul Jensen, D. (2003). "Recrystallization kinetics of individual bulk grains in 90% cold-rolled aluminium." *Acta Mater*, 51(15), 4423-4435.

Lienert, U., Han, T. S., Almer, J., Dawson, P. R., Leffers, T., Margulies, L., Nielsen, S. F., Poulsen, H. F., and Schmidt, S. (2004). "Investigating the effect of grain interaction during plastic deformation of copper." *Acta Mater*, 52(15), 4461-4467.

Manzari, M. T., and Dafalias, Y. F. (1997). "A critical state two-surface plasticity model for sands." *Geotechnique*, 47(2), 255-272.

Margulies, L., Lorentzen, T., Poulsen, H. F., and Leffers, T. (2002). "Strain tensor development in a single grain in the bulk of a polycrystal under loading." *Acta Mater*, 50(7), 1771-1779.

Martins, R. V., Margulies, L., Schmidt, S., Poulsen, H. F., and Leffers, T. (2004). "Simultaneous measurement of the strain tensor of 10 individual grains embedded in an Al tensile sample." *Mat Sci Eng a-Struct*, 387, 84-88.

Matsushima, T., Katagiri, J., Uesugi, K., Nakano, T., and Tsuchiyama, A. (2007). "Micro X-Ray Ct At Spring-8 For Granular Mechanics." *Soil Stress-Strain Behavior: Measurement, Modeling and Analysis*, H. Ling, L. Callisto, D. Leshchinsky, and J. Koseki, eds., Springer Netherlands, 225-234.

O'Sullivan, C., and Cui, L. (2009). "Micromechanics of granular material response during load reversals: Combined DEM and experimental study." *Powder Technol*, 193(3), 289-302.

Oddershede, J., Schmidt, S., Poulsen, H. F., Sorensen, H. O., Wright, J., and Reimers, W. (2010). "Determining grain resolved stresses in polycrystalline materials using three-dimensional X-ray diffraction." *Journal of Applied Crystallography*, 43(3), 539-549.

Offerman, S. E., van Dijk, N. H., Sietsma, J., Grigull, S., Lauridsen, E. M., Margulies, L., Poulsen, H. F., Rekveldt, M. T., and van der Zwaag, S. (2002). "Grain Nucleation and Growth During Phase Transformations." *Science*, 298(5595), 1003-1005.

Poulsen, H. F. (2004). *Three-dimensional X-ray diffraction microscopy: mapping polycrystals and their dynamics*, Springer.

Poulsen, H. F., Margulies, L., Schmidt, S., and Winther, G. (2003). "Lattice rotations of individual bulk grains: Part I: 3D X-ray characterization." *Acta Mater*, 51(13), 3821-3830.

Poulsen, S. O., Lauridsen, E. M., Lyckegaard, A., Oddershede, J., Gundlach, C., Curfs, C., and Juul Jensen, D. (2011). "In situ measurements of growth rates and grain-averaged activation energies of individual grains during recrystallization of 50% cold-rolled aluminium." *Scripta Materialia*, 64(11), 1003-1006.

Rivers, M. L., Sutton, S. R., and Eng, P. J. (1999). "Geoscience applications of x-ray computed microtomography." *Proceedings of SPIE: Developments in X-Ray Tomography II*, 3772, 78-86.

Rivers, M. L., Wang, Y., and Uchida, T. (2004). "Microtomography at GeoSoilEnviroCARS." *Proceedings of SPIE: Developments in X-Ray Tomography IV*, 5535, 783-791.

Russell, A. R., and Khalili, N. (2006). "A unified bounding surface plasticity model for unsaturated soils." *International Journal for Numerical and Analytical Methods in Geomechanics*, 30(3), 181-212.

Schmidt, S. (2010). "GrainSpotter v. 0.82. ." <http://fable.svn.sourceforge.net/svnroot/fable/GrainSpotter>.

Wright, J. (2005). "*ImageD11*." <http://sourceforge.net/apps/trac/fable/wiki/imaged11>.

CHAPTER 5

LATTICE STRAIN MEASUREMENT OF SILICA SAND USING 3D SYNCHROTRON X-RAY DIFFRACTION

This Chapter will be submitted for publication soon. Cil, M. B., Alshibli, K., and Kenesei, P., (2015). “Lattice strain measurement of silica sand using 3D synchrotron x-ray diffraction", *to be submitted*.

Abstract

3D synchrotron x-ray diffraction (3DXRD) and synchrotron micro computed tomography (SMT) techniques were utilized to monitor the lattice strain evolution and fracture behavior of natural Ottawa sand particles within a specimen composed of 35 particles. 3DXRD and SMT scans were acquired consecutively at multiple load levels during 1D compression experiment that was conducted on the sand specimen. 3DXRD technique was employed to measure the particle-averaged lattice strain within sand particles. In addition, the evolution and the mode of fracture of sand particles were investigated using high resolution 3D SMT images. The lattice strain measurements revealed that ε_{zz} component of the lattice strain tensor increases in most of the particles as the global compressive load increases, and the shear strain values are relatively smaller than the normal lattice strain components. Significant variation and fluctuations were observed in measured lattice strain values from one particle to another and from one load step to the next one as a result of major changes in the magnitude, direction and number of contact forces on each particle in the particulate system. SMT image analysis at the particle-scale showed that cracks in fractured sand particles generally initiate at contact points and propagate along the plane that connects the two contact points. The particles initially split into two or three major fragments followed by fracture into multiple small fragments. Micro-scale fracture analysis revealed that the position of contact forces and particle shape play a major role in the occurrence of particle fracture

in a sand assembly. The quantitative micro-scale results reported in this paper provides very valuable key measurements to advance our understanding of the non-homogenous force transmission mechanism in natural granular materials.

Introduction

Granular materials are commonly used in many disciplines such as engineering and science with wide applications in construction, manufacturing, processing, material handling, etc. The performance of applications and processes involving granular materials barely reach 60%, which indicates the lack of a comprehensive constitutive theory for such materials (Knowlton *et al.* 1994). Granular materials are composed of discrete particles with wide ranges of particle size and morphology, and their macroscopic behavior is governed by the complex micro-scale interactions of particles including interlocking, rotation, translation, and fracture. The majority of the current constitutive models are formulated based on the continuum theories and cannot accurately capture the fundamental behavior of granular materials since they do not take into account the discrete nature of granular media at the micro-scale level (e.g., Manzari and Dafalias 1997, Andrade and Borja 2006). However, it is well-known that failures in granular systems, which manifest as shear bands or diffuse bifurcation, initiate at the micro and meso-scales due to local instabilities. Therefore, developing a micromechanics-based constitutive model using particle-scale measurements is essential to fully characterize the deformation behavior of particulate systems. Such a model will help in providing optimized engineering solutions for maximum design performance. Although some constitutive models that considered microstructure have been developed by a few researchers (e.g., Wan and Guo 2001, Chang and Hicher 2005), they were not calibrated and validated using micro-scale properties from physical experimental measurements.

Particle kinematic properties and characteristics of force transmission mechanism are essential measurements to reveal the microscopic features of granular media and to develop micromechanics based constitutive models. However, acquiring such properties within a particulate system is a challenging task when one uses conventional experimental techniques. Recent advances in experimental and computational techniques opened a new era for researchers in the field of geomechanics. New powerful methods that allow examining the material response at the scale of individual particles has emerged in the last two decades. Significant progress has been made to characterize particle kinematics with the help of advanced imaging techniques such as x-ray Computed Tomography (CT) and synchrotron micro computed tomography (SMT). They can yield high-resolution 3D images (between 1 and 15 μm) of geomaterials which is sufficient for quantitative analysis in geomechanics studies (e.g., Hall *et al.* 2010, Hasan and Alshibli 2012). SMT and x-ray micro CT offer a unique opportunity to monitor deformation mechanisms in geomaterials under various loading conditions (e.g., Cil and Alshibli 2014) and capture the 3D kinematics (translation and rotation) of individual particles in granular soils with high accuracy (e.g., Andò *et al.* 2012, Druckrey and Alshibli 2014). Although they are powerful, the major shortcoming of these imaging techniques is their inability to measure interparticle forces.

Many studies investigated the force transmission mechanism in particulate systems and concluded that the majority of the applied stress is transmitted via column-like particle groups (force chains) that orient almost parallel to principal stress direction (Oda *et al.* 1982, Peters *et al.* 2005). Particles in force chains carry more than the average contact force, and the buckling of force chains is a key mechanism in the evolution of granular media deformation (e.g., Iwashita and Oda 2000, Rechenmacher *et al.* 2010). Distinct element method (DEM) simulations have been extensively used to compute interparticle forces and visualize force chains under compressive loading (e.g., Tordesillas 2007, O'Sullivan and Liang 2009, Cil and Alshibli 2014). However, the majority of the DEM models cannot mimic the actual 3D particle morphology and lack experimental validation. Although previous studies help to advance our understanding of the heterogeneous force network in granular materials, interparticle forces in natural granular assemblies such as sands is still the only missing key measurement to fully characterize the micromechanical behavior of particulate materials.

Recently, 3DXRD has emerged as a novel non-destructive technique to measure the volume-averaged lattice strain of individual particles within a granular assembly (Hall *et al.* 2011, Alshibli *et al.* 2013, Cil *et al.* 2014). Lattice strain tensors can be measured experimentally and used to compute the corresponding stress tensors using a general elastic stress-strain relationship. Then, the lattice stresses can be related to interparticle contact forces (Andrade *et al.* 2012), which provide a key information to characterize the force transmission mechanism in granular media. These lattice strain-stress measurements along with the 3D kinematics of particles have the potential to develop a micro-mechanics based constitutive model with real particle-scale data for the first time. Hall and Wright (2014) measured the average lattice elastic strain values of 30 synthetic single crystal silicone dioxide particles in a granular assembly. Alshibli *et al.* (2013) computed the strain tensor of individual particles in a column composed of three Ottawa silica sand particles subjected to 1D compression. This paper builds on the work of Alshibli *et al.* (2013), and focuses on measuring the particle-averaged lattice strain of a larger number of particles of a natural silica sand within a specimen subjected to 1D compression. In addition, the beamline incorporated SMT capabilities that can image the same specimen. The evolution of particle fracture and the deformation characteristics of the sand assembly were investigated using high-resolution 3D SMT images. The volume and kinematics of sand particles were calculated from SMT images that helped in tracking the position of particles to calculate the volume-averaged strain tensors from 3DXRD measurements.

Specimen and Apparatus Description

The experiment was conducted on natural uniform silica sand particles (a portion of sand known as F-75 Ottawa sand) with particles size portion between US sieve #40 (0.420 mm) and Sieve #50 (0.297 mm). F-75 Ottawa sand is a natural sand mined by the US Silica Company and its main constituent is α-quartz mineral (99%). 1D compression experiment was carried out using a specially designed test cell that includes a specimen mold, computerized stepper motor to apply axial loading, two load cells, and a data acquisition system (Figure 5.1). The specimen mold is an acrylic cylinder with an outer diameter of 15 mm and has a 1 mm diameter hole at the center to house sand particles. In order to quantify the friction force between sand particles and the mold, two load cells were attached to the top and the bottom of the specimen. 35 sand particles were carefully poured into the 1 mm hole and the specimen was subjected to vibration to densify it. The initial height of the specimen is ~1.97 mm. The test cell components were then assembled, and the test cell was mounted on the stage of the beamline in preparation for scanning.

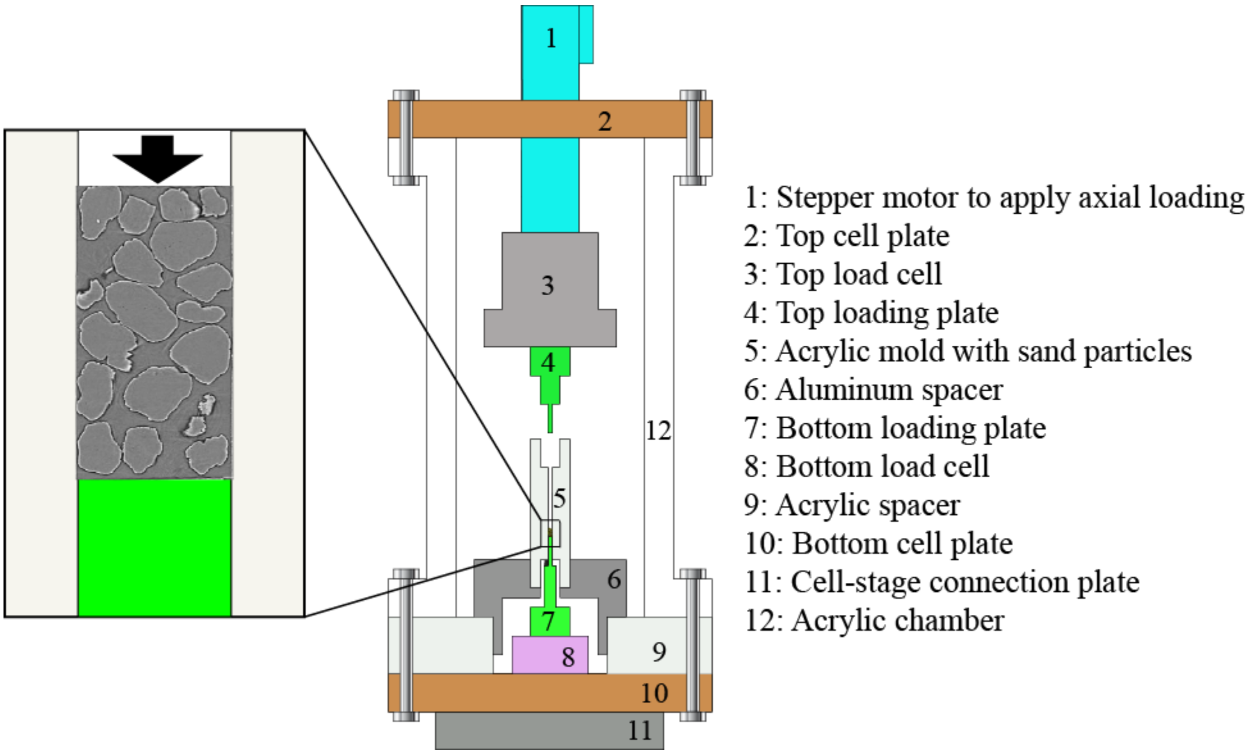

Figure 5.1. Schematic of the 1D compression test cell.

SMT and 3DXRD Scans

The SMT and 3DXRD scans were acquired at beamline 1-ID of the Advance Photon Source (APS), Argonne National Laboratory (ANL), Illinois, USA. The C hutch of 1-ID beamline was initially designed to conduct 3DXRD experiments. In a recent upgrade, SMT imaging capability was incorporated in the experiment setup (Figure 5.2). The test cell was mounted on a high precision positioning stage, which provides translation in x, y and z directions as well as rotation around the z-axis perpendicular to the incoming beam (ω rotation). SMT data acquisition system (scintillator and CCD camera) was mounted on a horizontal translation stage between the 2D panel detector and specimen (see Figure 5.2) and was moved along the beam direction while acquiring SMT scans. In order to prevent any damage to the 2D panel detector from possible diffractions of x-rays, a square metal plate with a hole at the center was positioned between the test cell and SMT data acquisition unit during SMT scans.

The SMT scans were acquired using 70.5 KeV x-ray energy which yielded a spatial resolution of 1 μm/pixel. In contrast to conventional absorption-based x-ray SMT, scans at high x-ray energies provide phase-contrast which highlights particle edges and boundaries. In each SMT scan, 900 frames were collected by rotating the specimen at 0.2° angular increments over 180° and acquiring images at 0.65 second exposure time.

3DXRD experiments were also performed at the same energy level that corresponds to a wavelength of 0.17586 Å. The scans were acquired at four different heights using a beam size of 0.5 mm x 1.0 mm (height x width), which provides a diffraction volume large enough to illuminate multiple sand particles per scan. At each scan layer, the images were acquired at every 1° angular position (rotation interval, $\Delta\omega = 1°$) while rotating the specimen from $\omega = 0°$ to $\omega = 180°$.

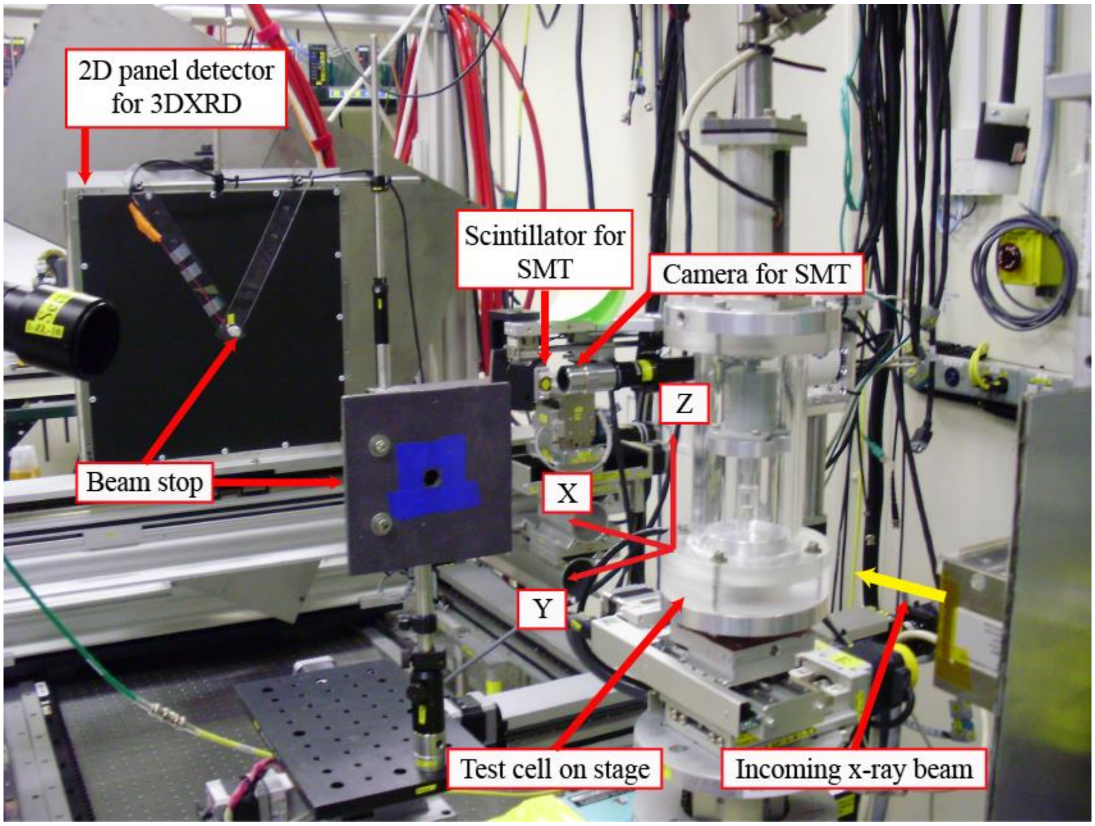

Figure 5.2. Experimental setups for 3DXRD and SMT measurements at 1-ID beamline of APS.

Diffraction data was recorded using an amorphous silicon flat-panel detector (model GE Revolution 41RT) positioned at a horizontal distance of 1391.905 mm from the specimen stage. The detector dimensions are 410 mm x 410 mm (2048 x 2048 pixels), and pixel size is about 200 μm x 200 μm (Lee *et al.* 2008).

Initially, the SMT and 3DXRD scans were acquired consecutively before applying any load to the specimen. Then, 1D compression was applied at a constant displacement rate of 0.2 mm/min. The loading was paused when the desired load level was reached, which leads to a small load relaxation in the system (Figure 5.3). Therefore, the scans were performed after waiting for a few minutes when the load relaxation reached to a very small rate. The stepper motor was held in position while acquiring the SMT and 3DXRD scans. This procedure was repeated for 8 different load levels. The SMT scan for load step #3 was skipped due to beamline time constraint.

Results

Specimen deformation under 1D compression

The load versus displacement relationship of the 1D compression experiment is depicted in Figure 5.3 which shows a small difference between the top and bottom cell readings. The load increases as the compression progresses, however it slightly decreases when the loading is paused for scanning due to load relaxation. At the beginning of the test, the rearrangement of particles resulted in a small drop in the axial load. Relatively high magnitude load drops and oscillation emerge at high load levels caused by fracture of silica sand particles within the assembly. The friction between the specimen and the acrylic mold increased as the compression proceeded due

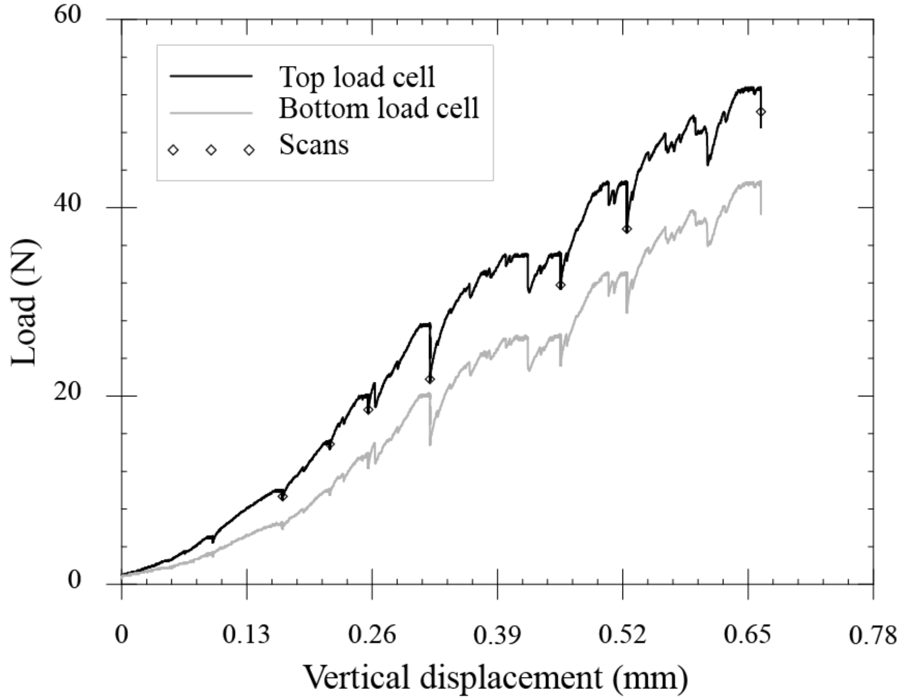

Figure 5.3. Load versus displacement relationship of 1D compression test on sand specimen.

to densification of specimen and tendency of particles to rearrange. Moreover, the fragments of fractured particles fill the void space between particles, which resulted in denser packing and jamming of particles inside the 1 mm hole. These two processes caused the difference between the top and bottom cell readings during loading.

Figure 5.4 shows axial cross sections of the 3D SMT images at different load levels, which allows monitoring the deformation behavior of the sand assembly and the evolution of particle fracture under 1D compression. The initial unloaded stage is labeled as Load 0 in Figure 5.4 which shows that the sand particles were densely packed and the orientation of particles was random. Few sand particles slightly rearranged via rotation and translation as the load increased during the first two load steps. In order to track the evolution of particle fracture in the specimen, the kinematic and fracture behavior of each sand particle was tracked throughout the experiment using SMT images. A sand particle is labeled as fractured in fracture analysis if it experiences major splitting into two or more fragments. The first particle fracture was observed at Load 4 (three particles fractured) and the number of fractured particles increased thereafter. 13 sand particles out of 35 did not exhibit any form of major particle fracture at the end of the 1D compression experiment. The majority of the sand particle fracture occurred in particles close to the loading platen which is in agreement with the observations reported in Cil and Alshibli (2014).

3DXRD results

An example detector image of the 3DXRD scan of silica sand is displayed in Figure 5.5 which contains the integrated intensities of the spots originated from several different grains. During the rotation of the specimen, some of the crystallographic planes in the illuminated volume

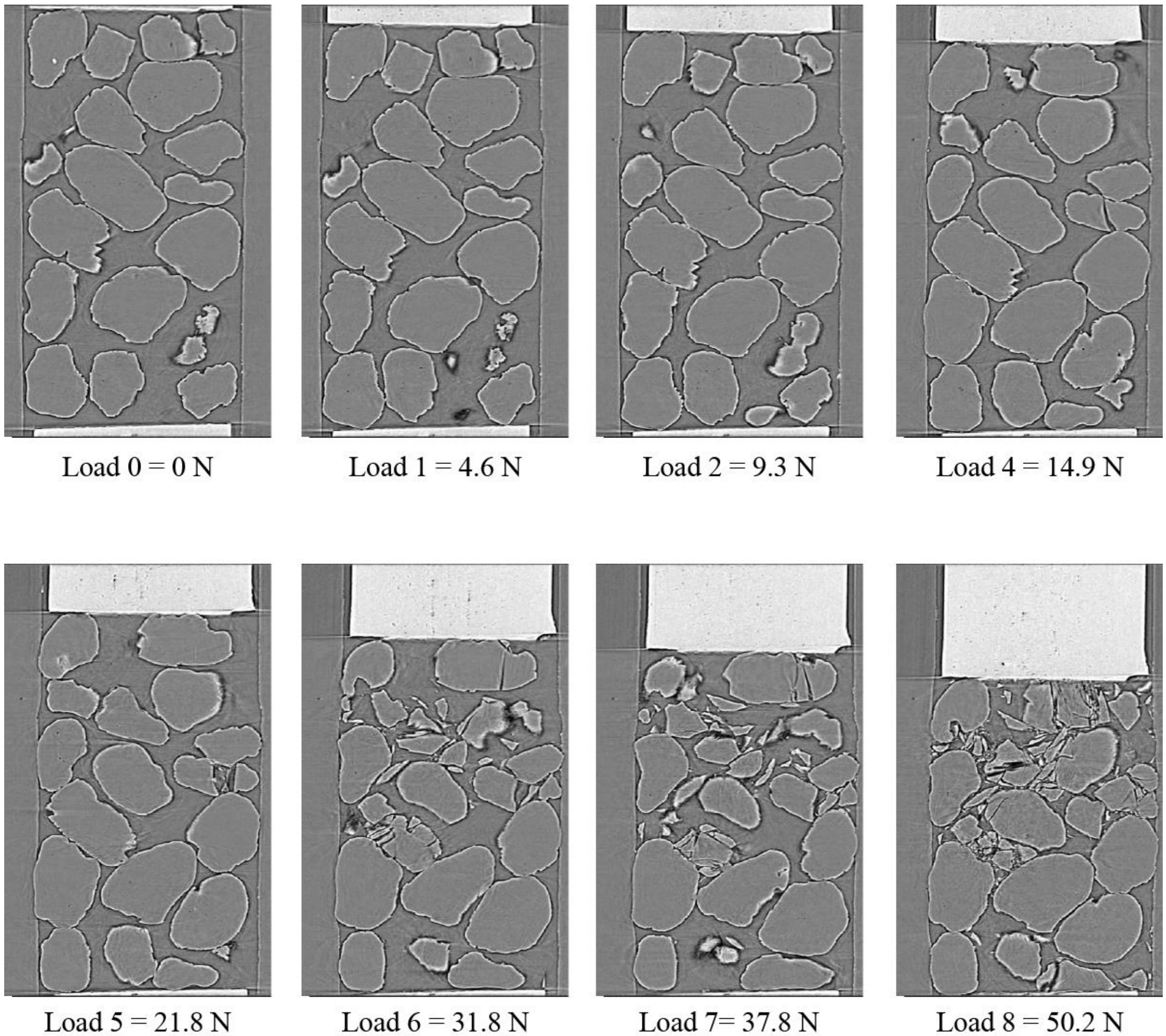

Figure 5.4. Axial cross-sectional SMT images of the specimen (at the center) at multiple load levels (specimen diameter = ~ 1mm).

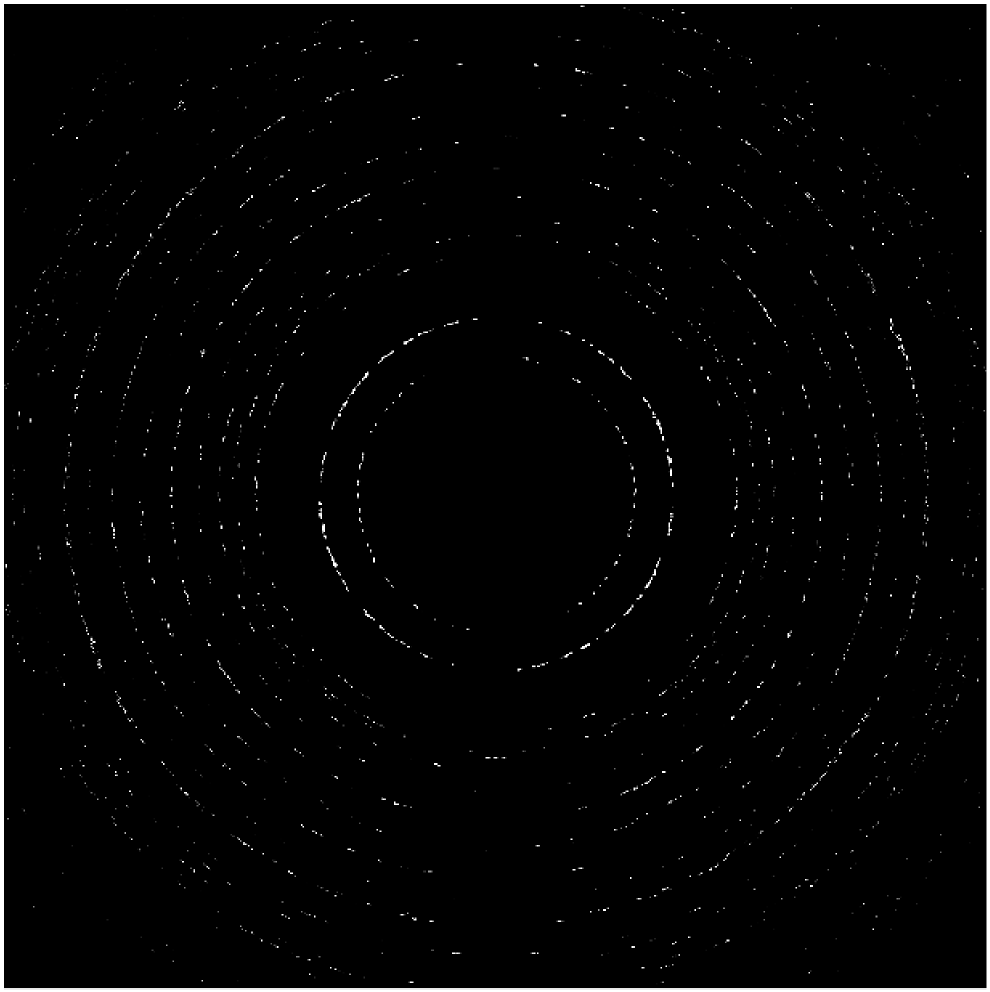

Figure 5.5. Example 3DXRD diffraction pattern of F-75 Ottawa sand.

satisfy the Bragg condition and give rise to diffraction beams which appear as spots on the detector image. The position of each diffraction spot is defined by three specific angular coordinates (2θ, ω and η) which is used to determine the orientation of the corresponding set of lattice planes. 2θ is the angle between transmitted beam and diffracted beam. ω is the angular position of the rotation stage. η is the azimuthal angle on the 2D panel detector and is measured relative to the vertical axis. In diffraction data processing, the Bragg reflection is described by the reciprocal lattice vector ($\mathbf{g}_{hkl}$) which is perpendicular to the crystallographic planes with lattice spacing (d^{hkl}) and its magnitude is equal to the reciprocal of d^{hkl}. Therefore, $\mathbf{g}_{hkl}$ ($1/d^{hkl}$) is in direct correspondence with lattice strain. More information about the geometric principles of 3DXRD technique can be found in Poulsen (2004).

3DXRD data analysis

The first step in far-field diffraction data analysis is the calibration of the experimental setup which was performed with the help of LaB_6 and CeO_2 powder diffraction patterns by taking advantage of their well-known crystal properties. HEXRD open-source software package (HEXRD 2014) was used to determine the calibration values. The calibration process provided the beam center, corrected specimen to detector distance, and the tilt of the detector. The raw diffraction images contain thousands of pixels, but only a small portion of the data includes useful diffraction peak data. Therefore, the properties of diffraction spots have to be identified and extracted from this large data set, which is also known as data reduction process. Peak searching was performed using DIGIgrain code which was developed by Kenesei (2012).

Since DIGIgrain software requires edf files as input, the raw GE files were initially converted to edf files. This conversion process split each GE file into 180 individual frames. Then, a correction algorithm was applied to each file which includes background correction, detector distortion, etc. For each full scan, all spots in the corrected files were consolidated into a single frame. DIGIgrain only identifies the spots in pre-defined 2θ regions which were determined by examining the spot positions in raw diffraction patterns. Finally, DIGIgrain peak searching was performed on the corrected images and an iterative scheme was adopted to obtain optimum DIGIgrain parameters for this data set. DIGIgrain outputs a simple text file which includes the list of identified peaks and their properties including center position, integrated intensity, statistical descriptors etc. The center of mass position of spots is computed in radial coordinates by DIGIgrain software. This approach eliminates the radial error in peak position computation, which is crucial in strain analysis since the applied stress also results in peak shifts in the radial direction.

Image D11 code of Wright (2005) was used to calculate g-vectors from indexed peak positions. Also, Image D11 has the option to calibrate detector parameters such as detector tilt and distance. Then, GrainSpotter code (Schmidt 2010) was used to index grains which is the assignment of the measured g-vectors to corresponding grains where they originate from. GrainSpotter provides a list of indexed grains that includes the center of mass position, orientation, and the list of the diffraction spots assigned to a particular grain. Finally, the lattice strain was calculated with the help of Matlab script written by the authors. The computation of the elastic strain tensor is based on the following simplified relationship: grain-averaged lattice strain is directly proportional to the 2θ shifts of reflections recorded in unloaded and loaded conditions. In this paper, lattice strain derivation is explained briefly and further details can be found in Margulies *et al.* (2002), and Alshibli *et al.* (2013). The lattice strain expression can be derived by differentiating Bragg's law and expressed as (Margulies *et al.* 2002):

$$\varepsilon_{hkl} = \frac{d_0^{hkl} - d^{hkl}}{d_0^{hkl}} = cos\theta_0 \Delta\theta \tag{5.1}$$

where ε_{hkl} is the strain measured perpendicular to a particular (*hkl*) plane. d^{hkl} and d_0^{hkl} are the lattice spacing of (*hkl*) plane in loaded and initial conditions, respectively. θ is the angle between the incoming beam and the scattering plane. The 2θ shifts of peak positions were evaluated by comparing the measured g-vectors in loaded and initial (unloaded) conditions. The change in g-vectors in each load step was determined by comparing the distorted lattice measurements with respect to initial unloaded condition. The same grain was tracked through different load steps by comparing the indexed spots obtained by GrainSpotter and those identified in η-*ω* maps. Since the experiment was conducted by rotating the specimen over an angular range from *ω* = 0° to 180°, particular set of planes that fulfill the Bragg condition give rise to diffraction spots on the detector twice during this rotation. These spots are known as Friedel pairs and they are scattered from the crystallographic planes (*hkl*) and ($\bar{h}\bar{k}\bar{l}$) of the same grain (Ludwig *et al.* 2009, Moscicki *et al.* 2009). The diffraction angles and the magnitudes of diffraction vectors of Friedel pairs are the same. Therefore, the lattice strain calculations were performed using Friedel pairs to minimize the error in the diffraction data analysis. Further information about the formulation and details of the lattice strain computation can be found in Poulsen (2004) and Alshibli *et al.* (2013).

Lattice strain results

The majority of the peaks were identified and several grains were indexed by GrainSpotter in each scan layer. The most challenging part of the diffraction data analysis was to match each indexed grain with the corresponding silica sand particle. Since the integrated intensity of each peak is directly proportional to the grain volume where it originates from, the integrated intensities of the peaks in the first ring ($2\theta = 2.37°$) were calculated for each indexed grain and compared with the sand particle volume data that were calculated from SMT images. Similar to 3DXRD scan layers, each SMT image was also divided into 4 layers, and an identification number was assigned to each particle (Figure 5.6). This matching process was repeated for each scan layer in all load steps. Most of the grains that were indexed and tracked in consecutive load steps were successfully matched with the corresponding sand particles in SMT images using this approach.

The axial load versus lattice strain relationships of 18 silica sand particles are presented in Figure 5.7 through Figure 5.12 (the order of sand particles is based on scan layer; bottom to top), which show the evolution of particle-averaged lattice strain components in global coordinate system as defined in Figure 5.2. Since the sand specimen is composed of discrete particles, they may translate and rotate independent of each other when loaded globally. It is challenging to track each grain in the same scan layer throughout the experiment due to the downward motion of particles. Therefore, some grains, especially the ones close to the top loading platen, can only be tracked up to a certain load level (e.g., Particle 22 in Figure 5.10, and Particle 18 in Figure 5.11). If a particle fractures, one of the major fragments of the particle was tracked if it was indexed. For each particle, normal strain components (ε_{xx}, ε_{yy}, ε_{zz}) and shear strain components (ε_{xy}, ε_{yz}, ε_{xz}) of lattice strain tensor are displayed in two separate plots. Since the load was applied in the axial

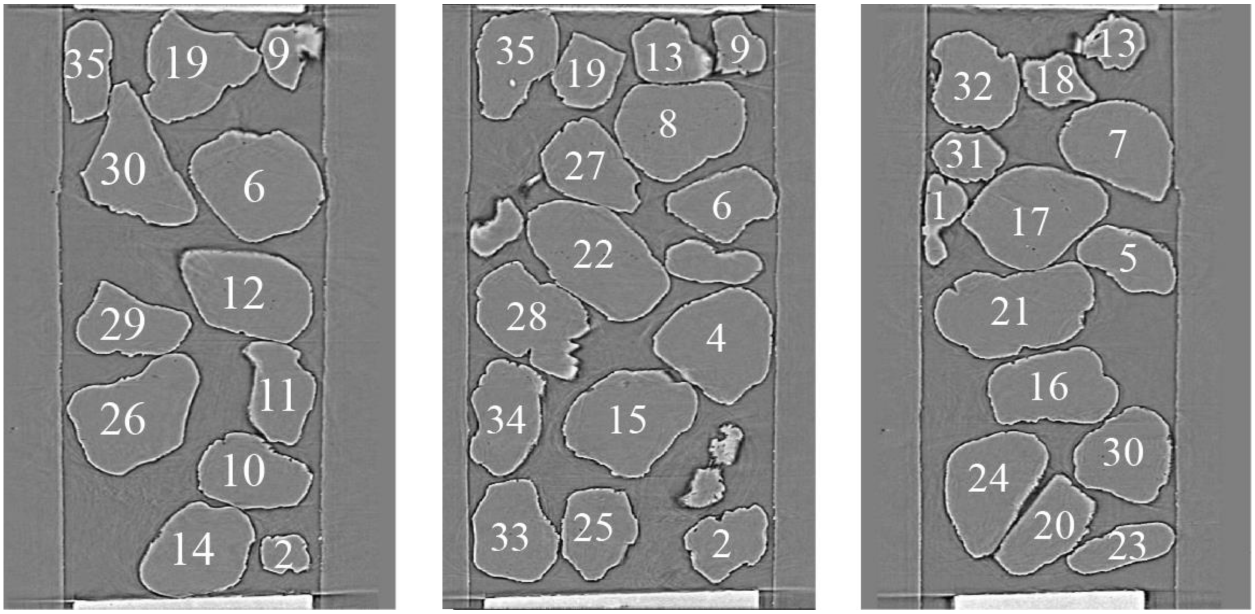

Figure 5.6. Assigned identification numbers of sand particles in SMT image analysis. Total number of particles in specimen: 35.

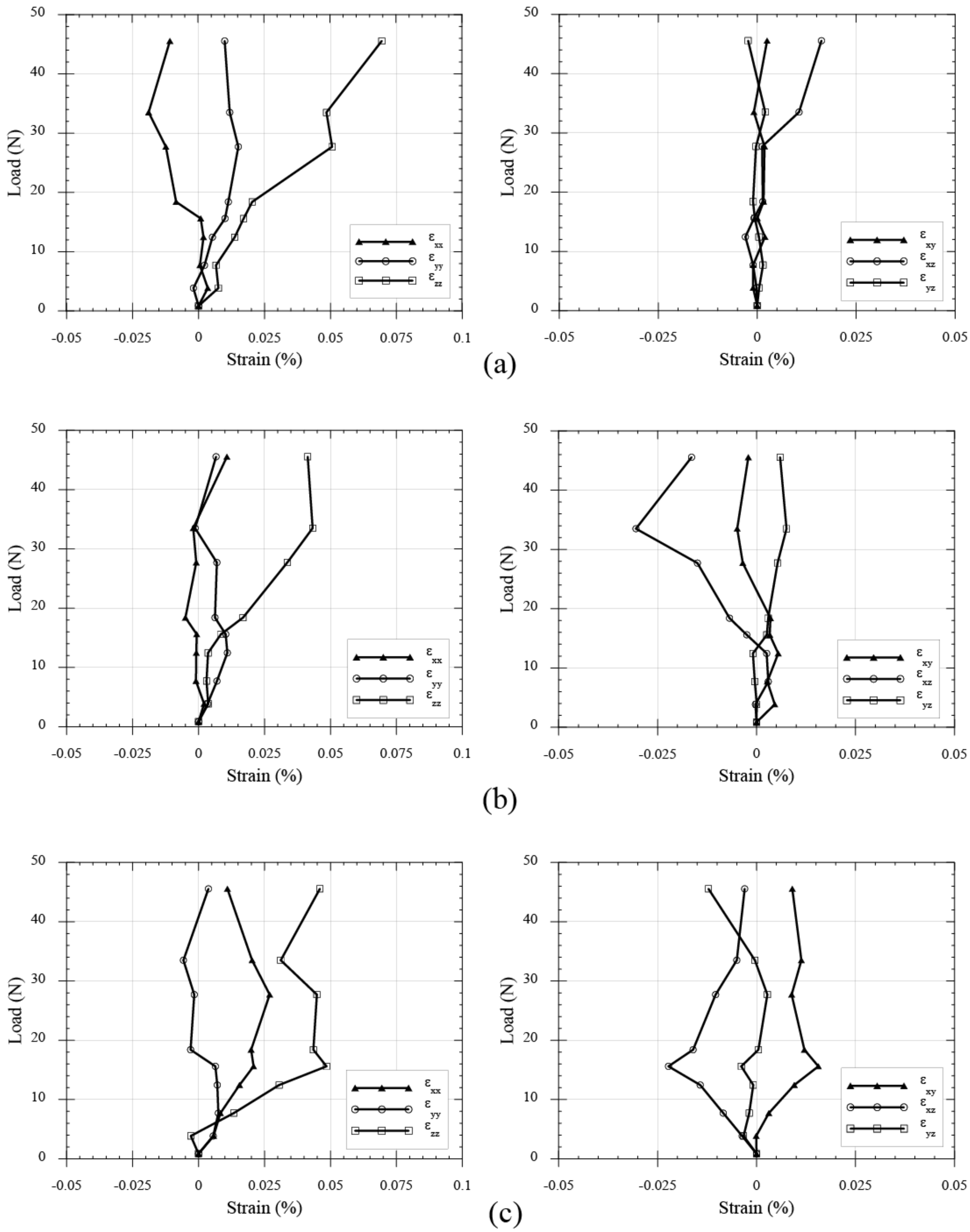

Figure 5.7. Evolution of particle-averaged lattice strain measurements as a function of axial load for (a) Particle 14; (b) Particle 33; and (c) Particle 34.

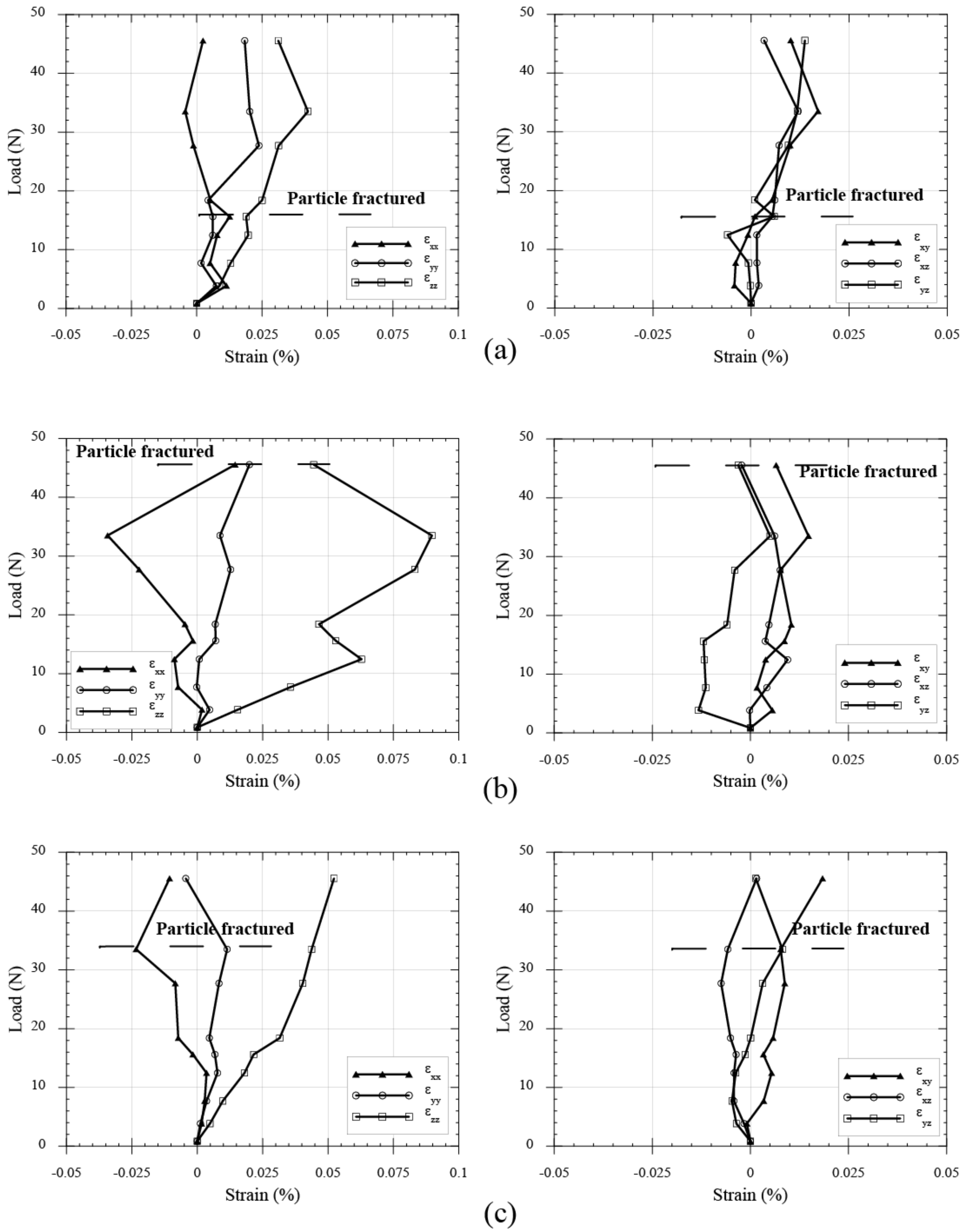

Figure 5.8. Evolution of particle-averaged lattice strain measurements as a function of axial load for (a) Particle 10; (b) Particle 2; and (c) Particle 21.

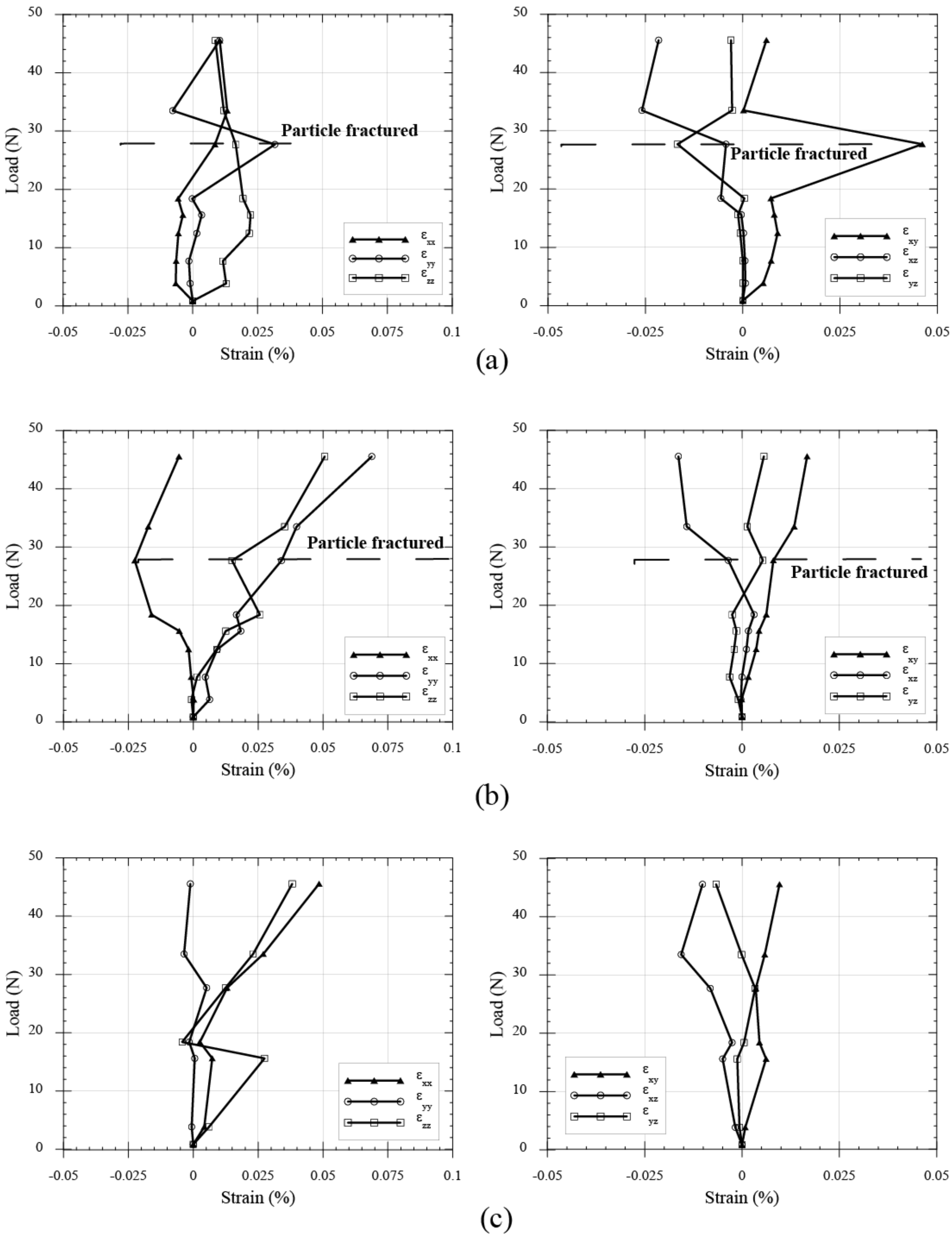

Figure 5.9. Evolution of particle-averaged lattice strain measurements as a function of axial load for (a) Particle 12; (b) Particle 16; and (c) Particle 4.

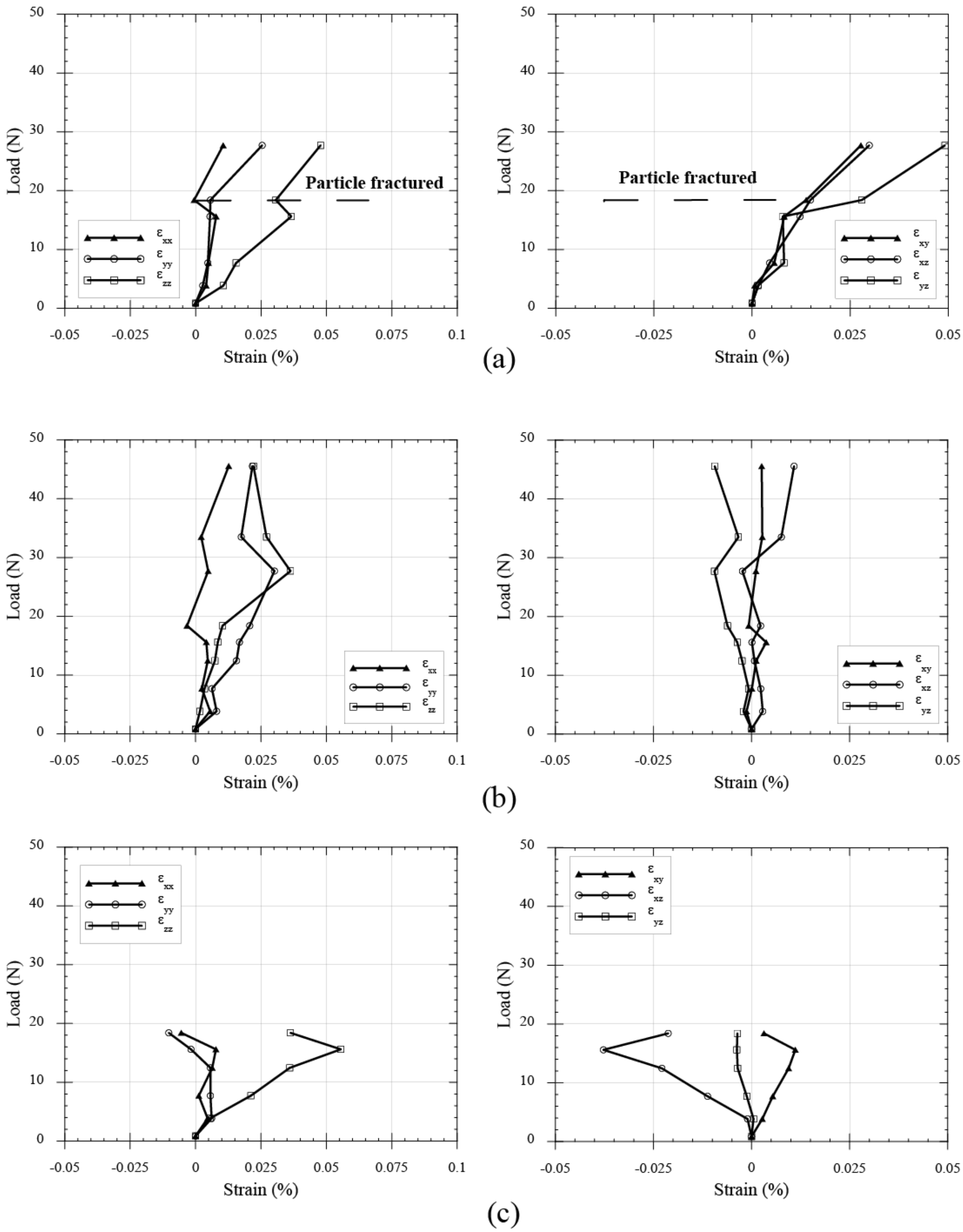

Figure 5.10. Evolution of particle-averaged lattice strain measurements as a function of axial load for (a) Particle 6; (b) Particle 7; and (c) Particle 22.

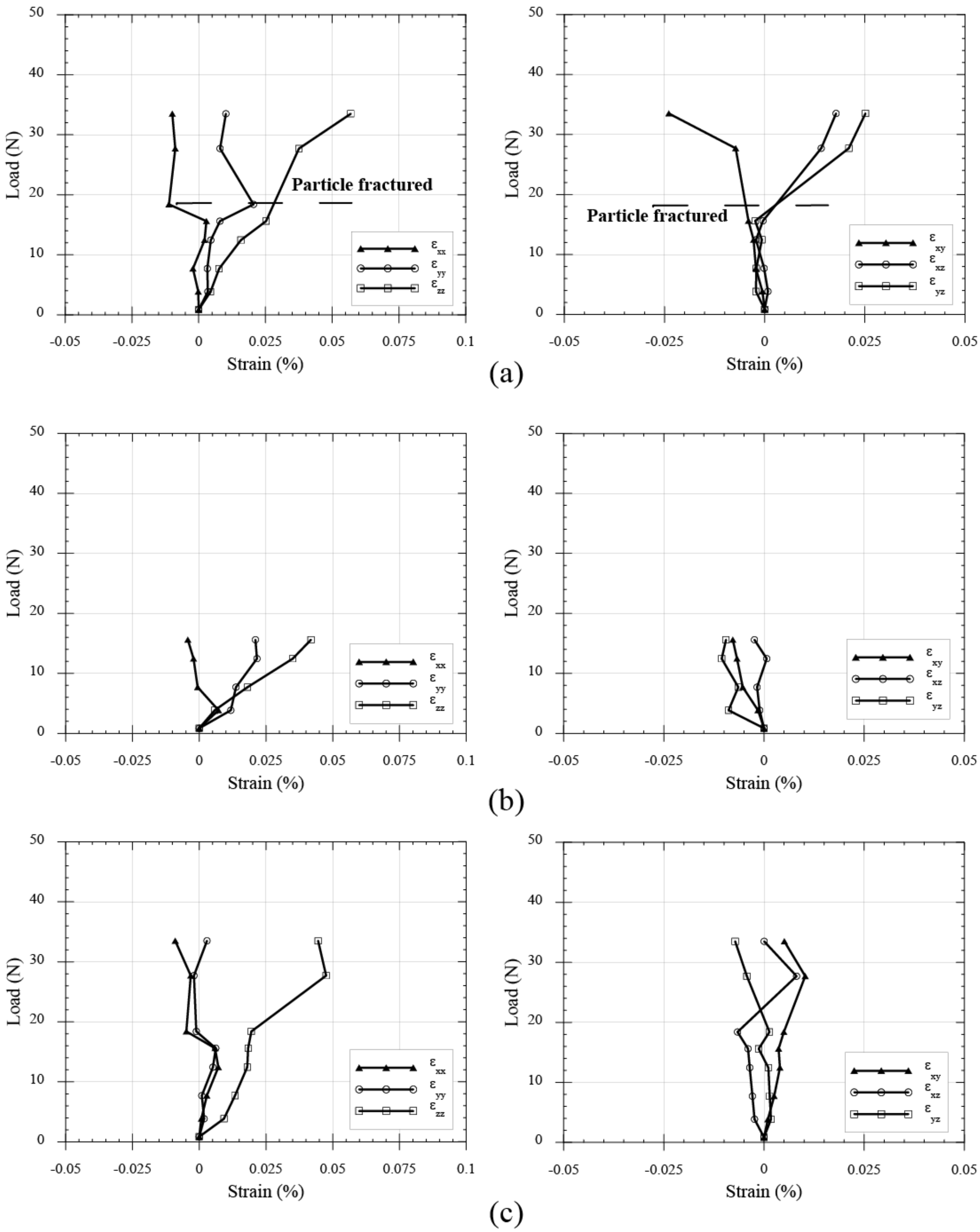

Figure 5.11. Evolution of particle-averaged lattice strain measurements as a function of axial load for (a) Particle 17; (b) Particle 18; and (c) Particle 35.

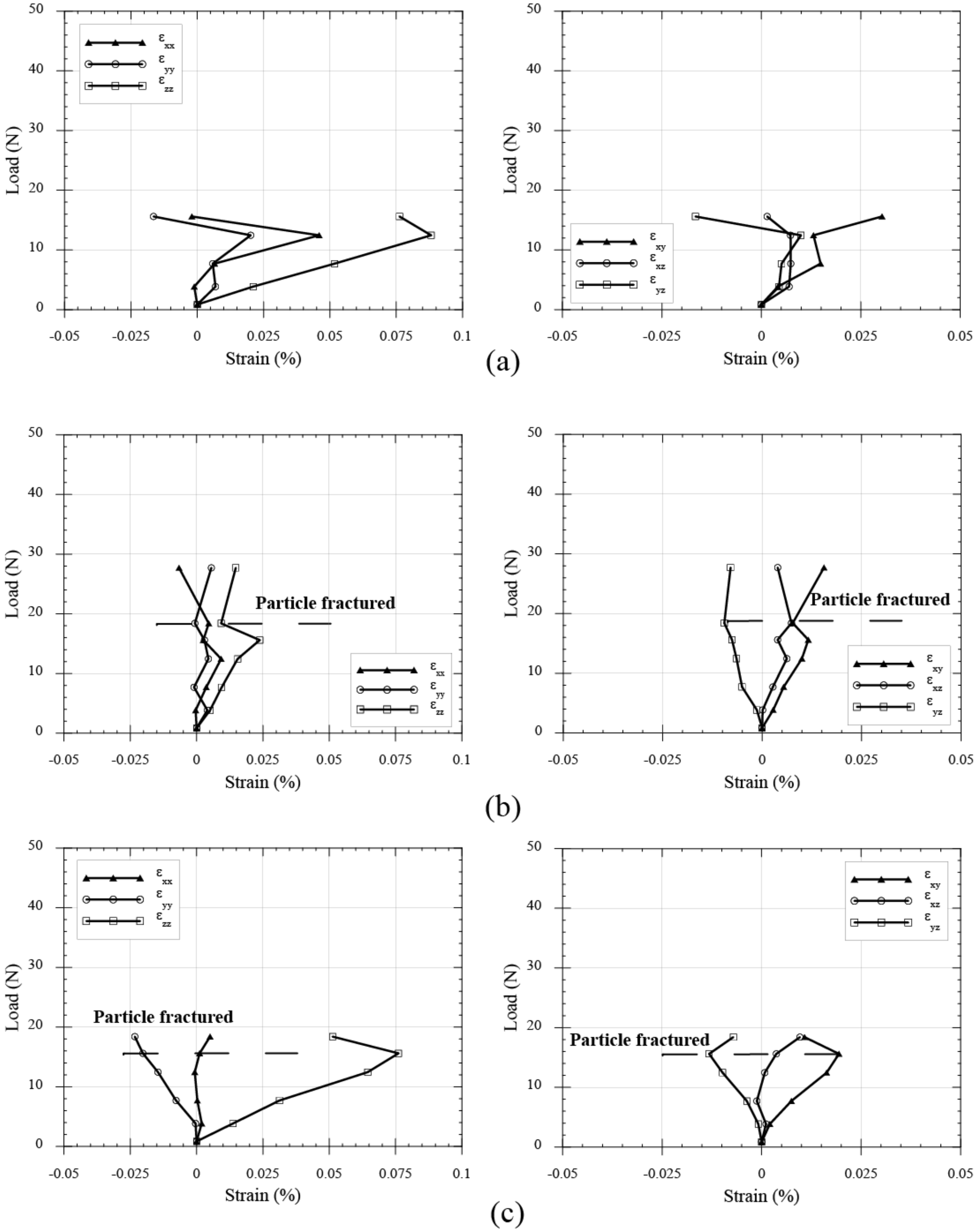

Figure 5.12. Evolution of particle-averaged lattice strain measurements as a function of axial load for (a) Particle 8; (b) Particle 19; and (c) Particle 9.

direction, ε_{zz} component of the lattice strain tensor increases within most of the particles as the compression load increases (e.g., Particle 14 and 33 in Figure 5.7, and Particle 10 and 21 in Figure 5.8). However, this trend was not observed in all the particles due to rather complex particle-scale interactions within the granular assembly.

Forces are transmitted through contact points between particles in granular materials. Each particle may have several contact points (Coordination Number, CN) and can be subjected to contact forces in various directions and magnitudes. Therefore, the ε_{xx} and ε_{yy} normal strain components of some particles increase in some cases positively or negatively (e.g., Particle 4 in Figure 5.9).The force transmission mechanism in particulate systems is very complex and difficult to analyze. Most of the particles in a granular assembly carry less than the average contact force, and the particles within force chains carry the majority of the axial load. As a result of this non-homogenous contact force network, the lattice strain of some sand particles increases as the axial load increases, however the measured strain values in some particles are relatively small (e.g., Particle 7 in Figure 5.10). Moreover, the rotation, translation, and fracture of individual sand particles during loading lead to rearrangement of neighboring particles and redistribution of the contact force network. Therefore, it is expected to measure a considerable variation and fluctuations in measured lattice strain values from particle to particle and from one load step to the next one as a result of major changes in the magnitude, direction and number of contact forces on each particle (e.g., Particle 34 in Figure 5.7, Particle 2 in Figure 5.8, and Particle 16 in Figure 5.9).

The shear strains were also computed for the indexed grains and displayed next to the normal strain plots. The shear strain values are relatively smaller than normal lattice strains. They generally exhibit a consistent trend up to the fracture of a particle or its contacting particle. The shear strain values do not vary significantly at the initial stages of loading; however the magnitude and direction of shear strains fluctuate significantly at greater applied loads, especially at the last two loading stages in many particles. The location and orientation of contact forces change considerably as a result of particle translation, rotation, and fracture, which leads to high variations in shear strains of some particles (e.g., Particle 10 in Figure 5.8, Particle 12 in Figure 5.9, and Particle 17 in Figure 5.11). Furthermore, changes in shear strains is relatively small in some particles. This may be due to the normal contact forces arising from the interlocking of particles in the densely packed specimen under 1D compression. In this study, all particle fracture occurred when $\varepsilon_{zz} < 0.12\%$, which is similar to the ranges of strain measurements reported by Alshibli *et al.* (2013). Hall and Wright (2014) reported lattice strain measurements between 0 - 0.15% for single crystal synthetic silicone dioxide particles with almost spherical shape, but the applied global axial load increased up to 70 N and they did not report any particle fracture.

Relationship between particle fracture and force transmission mechanism

One observation made during examination of the 3D SMT images show that some of the particles aligned almost vertically during 1D compression. Since the specimen is composed of 35 particles, there is a high chance that these sand particles are part of force chains in the sand assembly. The characteristics of particle fracture and evolution of these nearly vertically aligned sand columns were investigated by visually tracking individual sand particles in SMT images collaborated with lattice strain measurements. The orientation and arrangement of particles were examined using 3D renderings of sand particles generated from SMT images. Avizo Fire commercial image visualization software was used to identify particles. Initially, a smoothing filter was applied to the raw image. Since conventional threshold-based segmentation could not be implemented on these SMT images that were acquired at high x-ray energy, the particles were manually identified using the special tools available in the segmentation editor of Avizo Fire. Two of the nearly vertically aligned sand columns (columns 1 and 2) and their evolution between load steps 0 and 5 are displayed in Figure 5.13 and Figure 5.14, respectively. In addition, the CN of particles for load steps 0 through 5 and highest measured axial lattice strain are also added to Figure 5.13 and Figure 5.14. It was challenging to calculate the CN after Load 5 due to the multiple fragments that had emerged after the fracture of several particles. Sand columns 1 and 2 were selected for this analysis since initial particle breakages were observed in particles within these columns at Loads 4 and 5. The relative position of the selected particles within the specimen are highlighted in Figure 5.13a and Figure 5.14a. Three of the particles within column 1 fractured at Load 4, which demonstrates that some portion of the axially transmitted load was carried by these particles. Column 1 continued to carry some of the axial load in load step 5 despite the fracture of a few particles and Particle 5 continued to disintegrate further and Particle 6 fractured during Load 5 (see Figure 5.15). In sand column 2, Particle 19 and Particle 30 fractured in Load 5 as shown in Figure 5.16, and the measured ε_{zz} values increased for Particles 19, 22, 33 and 34 between Load 0 and Load 4 (see Figure 5.7, Figure 5.10, and Figure 5.12), which indicates that some of the axial force was transmitted through sand column 2. The analysis was performed until Load 5 since several fragments from fractured particles filled the void space within the specimen which made it difficult to identify particle fragments of vertically aligned particles and contact structure in SMT images.

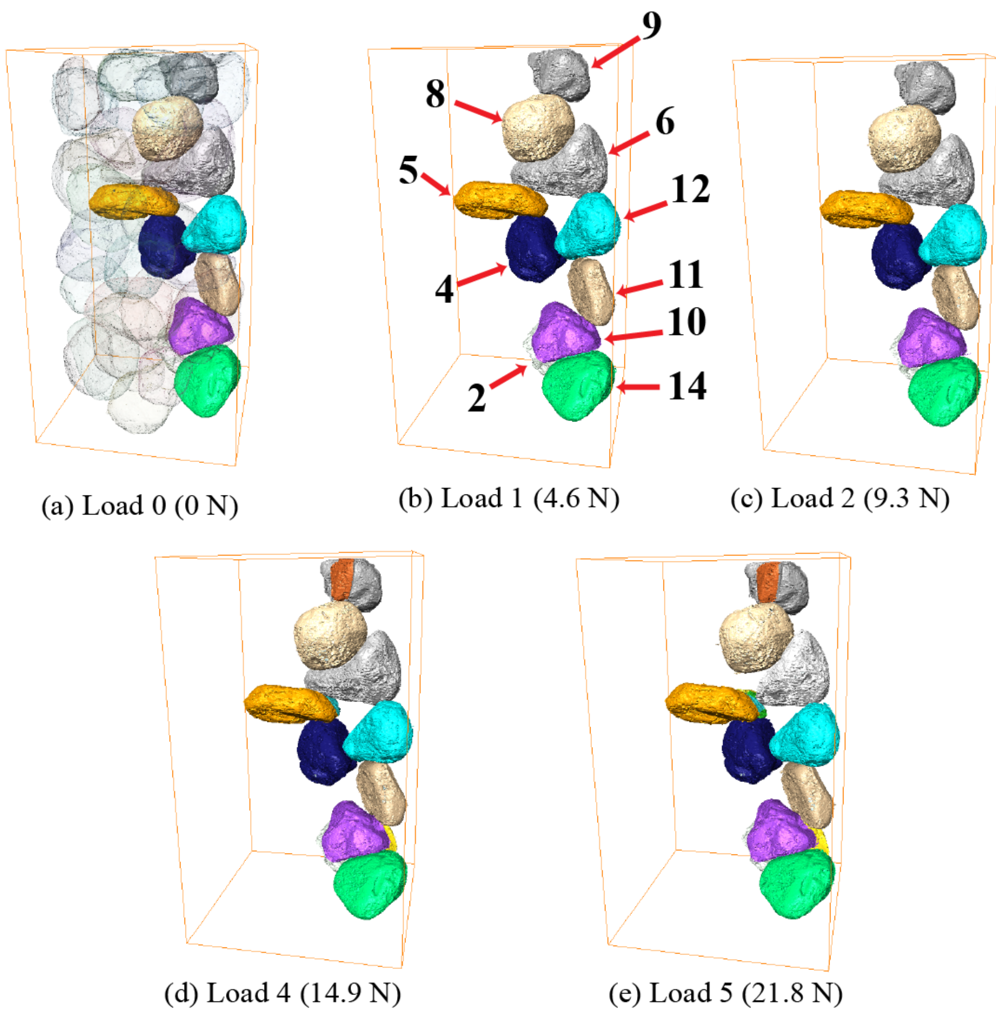

	Coordination number					Lattice strain
Sand Particle	**Load 0**	**Load 1**	**Load 2**	**Load 4**	**Load 5**	ε_{zz}* (%)
Particle 2	3	3	3	4	4	0.09
Particle 4	2	4	4	5	6	0.04
Particle 5	5	5	5	Fractured		
Particle 6	5	4	4	5	Fractured	0.04
Particle 8	6	6	6	7	8	0.09
Particle 9	3	3	3	Fractured		0.06
Particle 10	4	5	5	Fractured		0.02
Particle 11	3	3	3	4	4	
Particle 12	4	5	5	5	5	0.02
Particle 14	2	2	2	3	4	0.07
Specimen average	4.49	4.69	4.69	4.89	5.14	

* = Highest measured ε_{zz} before fracture

Figure 5.13. Evolution of sand column 1 between Load 0 and Load 5; CN, and highest measured axial strain of particles (Particle ID numbers are shown for selected particles).

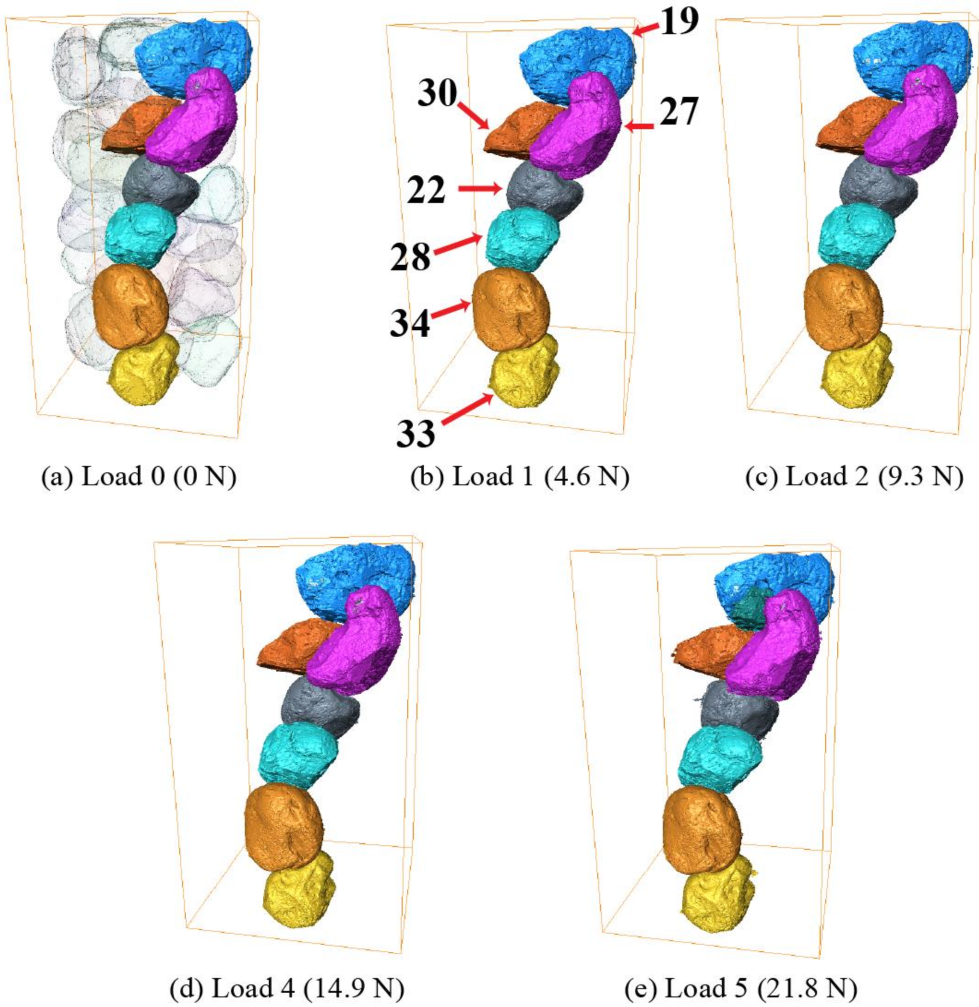

	Coordination number					Lattice strain
Sand Particle	**Load 0**	**Load 1**	**Load 2**	**Load 4**	**Load 5**	ε_{zz}*
Particle 19	6	6	6	6	Fractured	0.02
Particle 22	8	8	8	8	7	0.06
Particle 27	6	6	6	6	7	
Particle 28	7	7	7	7	7	
Particle 30	5	5	5	5	Fractured	
Particle 33	3	3	3	3	4	0.04
Particle 34	5	5	5	5	5	0.06
Specimen average	4.49	4.69	4.69	4.89	5.14	

* = Highest measured ε_{zz} before fracture

Figure 5.14. Evolution of sand column 2 between Load 0 and Load 5; CN, and highest measured axial strain of particles (Particle ID numbers are shown for selected particles).

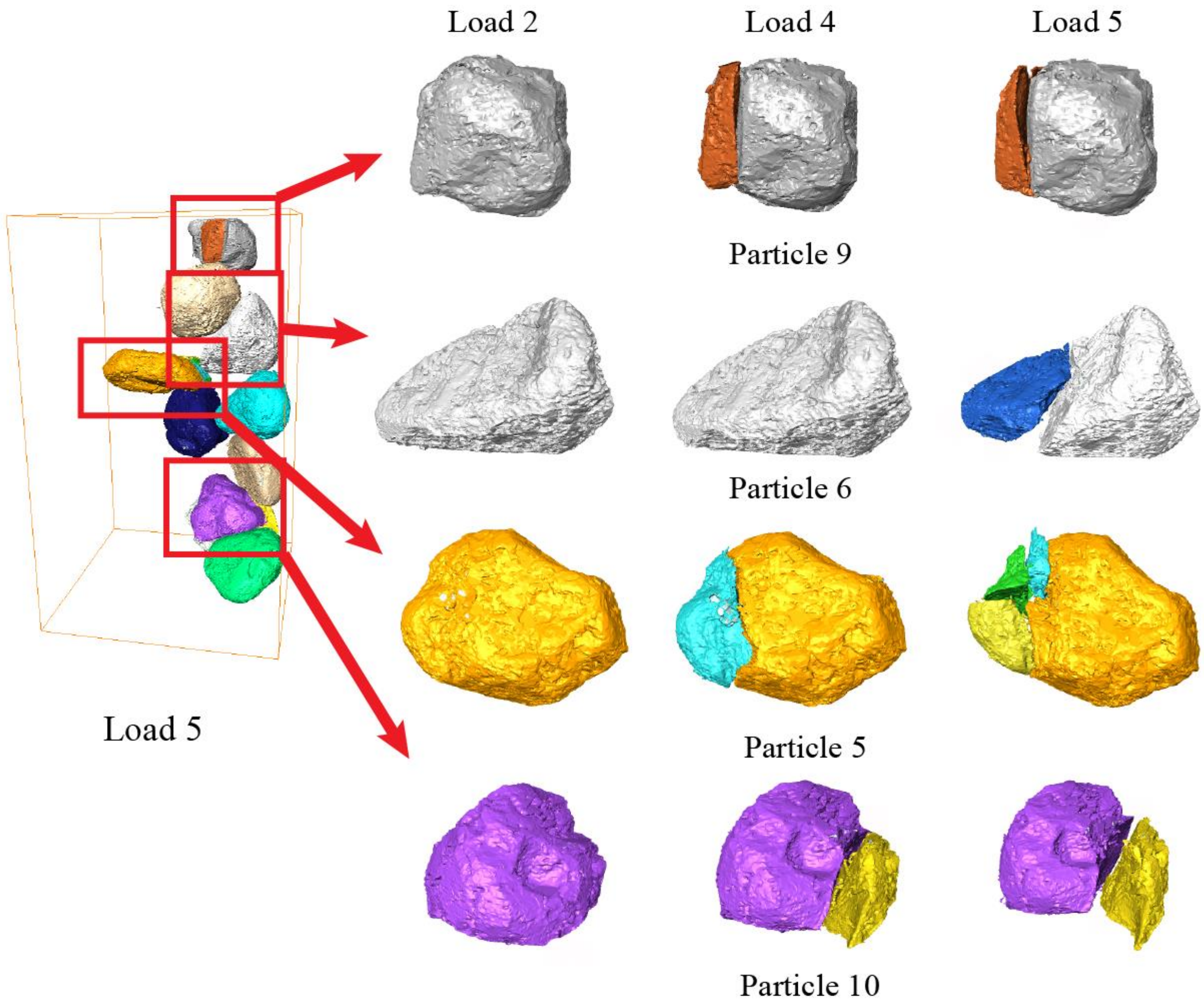

Figure 5.15. The position of fractured particles in the sand column 1 and their 3D view at load steps 2, 4 and 5 (orientations of the particles are altered to expose fragments after fracture).

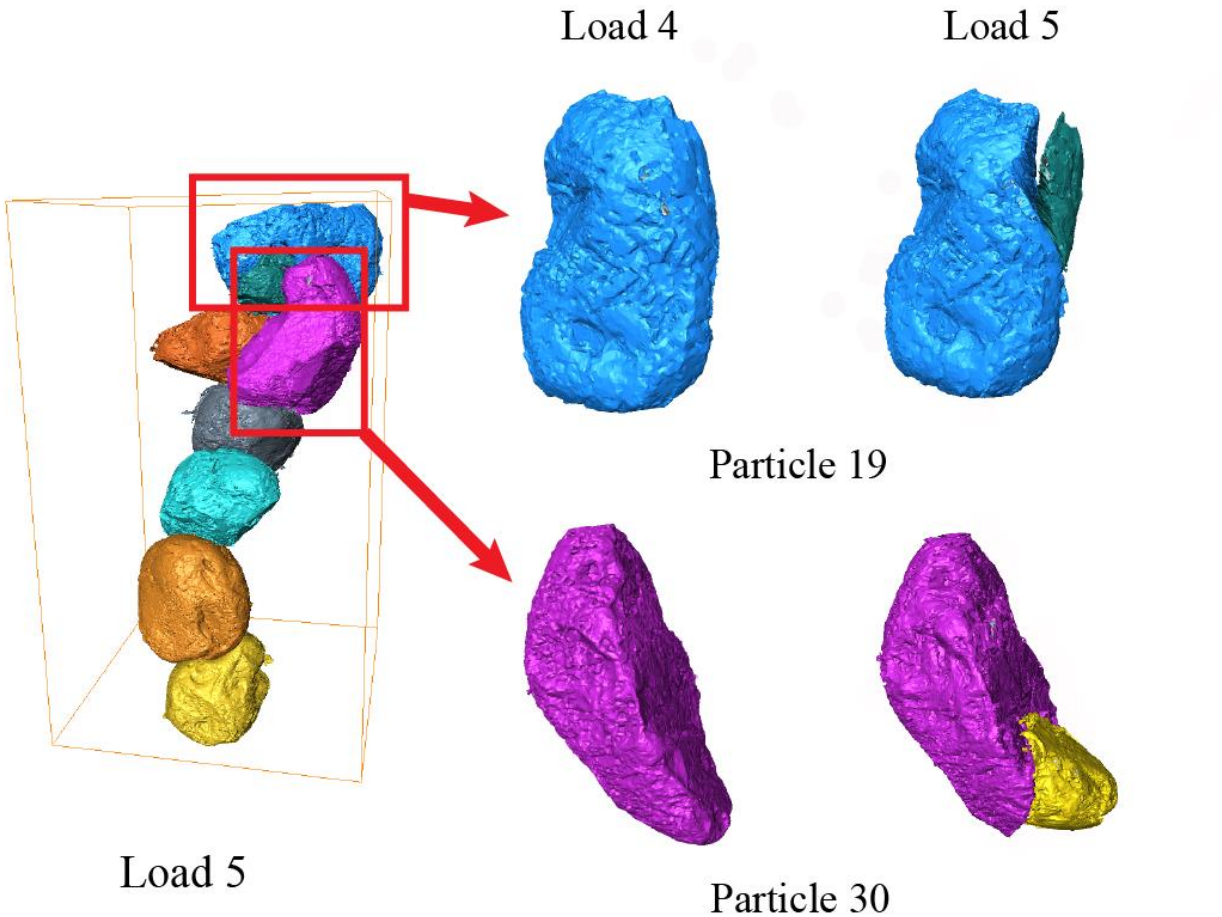

Figure 5.16. The position of fractured particles in the sand column 2 and their 3D view at load steps 4 and 5 (orientations of particles are altered to expose fragments after fracture).

The fracture strength of a sand particle is influenced by several factors including mineralogy, CN, the direction and position of contact forces, particle size, particle orientation, particle morphology, and the number and distribution of flaws. In this paper, each particle was carefully examined in order to understand the causes of fracture by considering the effect of CN, lattice strain, particle shape, and contact points of individual sand particles. The 3D renderings of fractured sand particles in columns 1 and 2 before and after fracture are displayed in Figure 5.15 and Figure 5.16, respectively. Particle 9 is located at the top corner of the specimen and has three contact points (CN =3). The CN did not change from Load 0 until fracture (the top plate, the mold wall in the lateral direction, and Particle 8 at its bottom). The shape of Particle 9 can be defined as sub-rounded. The fracture likely resulted from the contact forces applied by the top loading platen and Particle 8 below it. Particle 5 is an elongated particle with CN = 5. Although there are multiple contacts, the crack propagated along a slightly slanted vertical plane that connects particle contacts above and below it. Since the particle is elongated in the horizontal direction, it is vulnerable to axially applied forces. Therefore, the orientation and shape of Particle 5 might be important factors in the occurrence of fracture. Similar fracture modes were observed in Particles 6, 10, 19 and 30 (see Figure 5.15 and Figure 5.16). These 3D images demonstrate that all the particles fractured via splitting into two fragments, and the cracks formed along the plane that connected the contact points. Although other particles in columns 1 and 2 had similar CN (see Figure 5.13 and Figure 5.14), they did not experience fracture, which indicates that the coordination number is not the only determinant parameter of initial particle fractures in this sand assembly. The influence of a heterogeneous contact network needs be taken into account to characterize the onset of particle fracture.

The evolution and magnitude of lattice normal strains are also other useful measurements to understand the causes of fracture. The normal strain along the loading direction (ε_{zz}) increases in Particles 6, 8, 9, 10, and 14 in sand column 1 (see Figure 5.7, Figure 5.8, Figure 5.10, and Figure 5.12) and in Particles 19, 22, 33 and 34 within column 2, which also confirms that these sand columns carried a portion of the increasing global load from the beginning of the experiment. Some sand particles experienced higher normal strain values when compared to the fractured particles (e.g., Particles 2 and 14); however they did not fracture. Therefore, other factors such as the direction and position of contact points and particle shape have to be considered in fracture analysis. 3D renderings of sand particles before and after fracture (Figure 5.15 and Figure 5.16) demonstrated that a small fragment generally splits from the main sand particle in all cases. Due to the irregular shape of sand particles, a portion of the particle become vulnerable to fracture if contact forces act along these parts. The fracture of three particles at a relatively small load level (Load 4 = 14.9 N) also points to the considerable role of stress localization at these weak regions on the formation of fracture. As a result, only Particles 5, 9 and 10 in Sand Column 1 fractured at Load 4, and Particles 19 and 30 in Sand Column 2 fractured at Load 5, even though some other particles in these columns have smaller CN and experienced higher strains. It can be concluded that CN is not a main predictive parameter for the initial particle fractures in this data set. On the other hand, the position of contact forces and particle shape play a significant role in the occurrence of particle fracture in a sand assembly as well as the magnitude of contact forces. All particle edge breakages in Figure 5.15 and Figure 5.16; and particle fractures observed in relatively small strain values in some particles confirm this hypothesis. This analysis revealed that 3D high-resolution SMT images acquired during the deformation of sand assembly and lattice strain measurements provides a unique opportunity to gain insight into the fracture behavior of individual sand particles at the particle-level non-destructively. These micro-scale measurements demonstrate the great potential of these techniques to better understand and model the fundamental behavior of granular materials.

Conclusions

SMT and 3DXRD techniques were successfully utilized to monitor lattice strain evolution and fracture of natural Ottawa sand particles. The volume-averaged lattice strains of individual natural sand particles within a sand assembly were measured for the first time using 3DXRD. The evolution of lattice strain tensor as a function of the macroscopic axial load were calculated using the far-field diffraction data acquired at four different scan layers. The lattice strain measurements have shown that ε_{zz} value increases within most of the particles as the compression load increases. Since some particles carry very small loads due to the non-homogenous contact force network in granular materials, the lattice strain values of some sand particles were relatively small. When a particle fractures in a sand column, the measured lattice strain values vary considerably from one particle to another due to several factors including the number, position and magnitude of contacts, particle shape and size, and the orientation of the particle in the specimen.

The evolution of particle fracture was also investigated using 3D SMT images, which showed that some sand particles aligned in a column structure with a nearly vertical orientation in the specimen during loading. It was observed that particles which were part of these sand columns mostly experienced fracture. After particle fracture, these columns continued to carry a portion of the axial load. The cracks in fractured sand particles generally extend along the plane that connects the two contact points of the particle with the neighbor particles and this plane is more or less parallel to the axial load direction. In most cases, particles initially split into two or three fragments. Then, fragments experience further breakage as they continue to carry load. Micro-scale fracture analysis revealed that the position of contact forces and particle shape play a major role in the occurrence of particle fracture in a sand assembly, and CN is not the main predictive parameter for the initial particle fractures. 3DXRD and SMT techniques provide excellent particle scale measurements which can be used to derive micromechanics-based constitutive models.

Acknowledgments

This material is based on work supported by the National Science Foundation under Grant No. CMMI- 1362510. Any opinions, findings, and conclusions or recommendations expressed in this material are those of the authors and do not necessarily reflect the views of the National Science Foundation. The SMT and 3DXRD images were collected using the x-ray Operations and Research Beamline Station 1-ID at Argonne Photon Source (APS), Argonne National Laboratory. Use of the Advanced Photon Source, an Office of Science User Facility operated for the U.S. Department of Energy (DOE) Office of Science by Argonne National Laboratory, was supported by the U.S. DOE under Contract No. DE-AC02-06CH11357

References

Alshibli, K., Cil, M. B., Kenesei, P., and Lienert, U. (2013). "Strain tensor determination of compressed individual silica sand particles using high-energy synchrotron diffraction." *Granular Matter*, 15(5), 517-530.

Andò, E., Hall, S., Viggiani, G., Desrues, J., and Bésuelle, P. (2012). "Grain-scale experimental investigation of localised deformation in sand: a discrete particle tracking approach." *Acta Geotech*, 7(1), 1-13.

Andrade, J. E., and Borja, R. I. (2006). "Capturing strain localization in dense sands with random density." *Int J Numer Meth Eng*, 67(11), 1531-1564.

Andrade, J. E., Lim, K. W., Avila, C. F., and Vlahinic, I. (2012). "Granular element method for computational particle mechanics." *Computer Methods in Applied Mechanics and Engineering*, 241, 262-274.

Chang, C. S., and Hicher, P. Y. (2005). "An elasto-plastic model for granular materials with microstructural consideration." *International Journal of Solids and Structures*, 42(14), 4258-4277.

Cil, M. B., Alshibli, K., Kenesei, P., and Lienert, U. (2014). "Combined high-energy synchrotron X-ray diffraction and computed tomography to characterize constitutive behavior of silica sand." *Nuclear Instruments and Methods in Physics Research Section B: Beam Interactions with Materials and Atoms*, 324(0), 11-16.

Cil, M. B., and Alshibli, K. A. (2014). "3D analysis of kinematic behavior of granular materials in triaxial testing using DEM with flexible membrane boundary." *Acta Geotech*, 9(2), 287-298.

Cil, M. B., and Alshibli, K. A. (2014). "3D evolution of sand fracture under 1D compression." *Geotechnique*, 351-364.

Druckrey, A. M., and Alshibli, K. A. (2014). "3D Behavior of Sand Particles Using X-Ray Synchrotron Micro-Tomography." *Geo-Congress 2014 Technical Papers*, 2814-2821.

Hall, S., and Wright, J. (2014)."Characterisation of 3D force transmission in real granular media." *16th International Conference on Experimental MEchanics, Cambridge, United Kingdom*.

Hall, S., Wright, J., Pirling, T., Andò, E., Hughes, D., and Viggiani, G. (2011). "Can intergranular force transmission be identified in sand?" *Granular Matter*, 13(3), 251-254.

Hall, S. A., Bornert, M., Desrues, J., Pannier, Y., Lenoir, N., Viggiani, G., and Besuelle, P. (2010). "Discrete and continuum analysis of localised deformation in sand using X-ray mu CT and volumetric digital image correlation." *Geotechnique*, 60(5), 315-322.

Hasan, A., and Alshibli, K. (2012). "Three dimensional fabric evolution of sheared sand." *Granular Matter*, 14(4), 469-482.

HEXRD (2014). <https://github.com/praxes/hexrd>. (accessed October 10, 2014).

Iwashita, K., and Oda, M. (2000). "Micro-deformation mechanism of shear banding process based on modified distinct element method." *Powder Technol*, 109(1–3), 192-205.

Kenesei, P. (2012). "DIGIgrain." < http://sourceforge.net/apps/trac/digigrain/wiki>.

Knowlton, T. M., Klinzing, G. E., Yang, W. C., and Carson, J. W. (1994). "The importance of storage, transfer, and collection." *Journal Name: Chemical Engineering Progress; (United States); Journal Volume: 90:4*, Medium: X; Size: Pages: 44-54.

Lee, J. H., Aydiner, C. C., Almer, J., Bernier, J., Chapman, K. W., Chupas, P. J., Haeffner, D., Kump, K., Lee, P. L., Lienert, U., Miceli, A., and Vera, G. (2008). "Synchrotron applications of an amorphous silicon flat-panel detector." *J Synchrotron Radiat*, 15(5), 477-488.

Ludwig, W., Reischig, P., King, A., Herbig, M., Lauridsen, E. M., Johnson, G., Marrow, T. J., and Buffiere, J. Y. (2009). "Three-dimensional grain mapping by x-ray diffraction contrast tomography and the use of Friedel pairs in diffraction data analysis." *Review of Scientific Instruments*, 80(3), 033905-033909.

Manzari, M. T., and Dafalias, Y. F. (1997). "A critical state two-surface plasticity model for sands." *Geotechnique*, 47(2), 255-272.

Margulies, L., Lorentzen, T., Poulsen, H. F., and Leffers, T. (2002). "Strain tensor development in a single grain in the bulk of a polycrystal under loading." *Acta Mater*, 50(7), 1771-1779.

Moscicki, M., Kenesei, P., Wright, J., Pinto, H., Lippmann, T., Borbely, A., and Pyzalla, A. R. (2009). "Friedel-pair based indexing method for characterization of single grains with hard X-rays." *Mat Sci Eng a-Struct*, 524(1-2), 64-68.

O'Sullivan, C., and Liang, C. (2009). "Micromechanics of granular material response during load reversals: Combined DEM and experimental study." *Powder Technol*, 193(3), 289-302.

Oda, M., Konishi, J., and Nemat-Nasser, S. (1982). "Experimental Micromechanical Evaluation of Strength of Granular Materials: Effects of Particle Rolling." *Mech Mater*, 1, 269-283.

Peters, J. F., Muthuswamy, M., Wibowo, J., and Tordesillas, A. (2005). "Characterization of force chains in granular material." *Phys Rev E*, 72(4).

Poulsen, H. F. (2004). *Three-dimensional X-ray diffraction microscopy: mapping polycrystals and their dynamics,* Springer.

Rechenmacher, A., Abedi, S., and Chupin, O. (2010). "Evolution of force chains in shear bands in sands." *Geotechnique*, 60(5), 343-351.

Schmidt, S. (2010). "GrainSpotter v. 0.82. ." <http://fable.svn.sourceforge.net/svnroot/fable/GrainSpotter>.

Tordesillas, A. (2007). "Force chain buckling, unjamming transitions and shear banding in dense granular assemblies." *Philos Mag*, 87(32), 4987-5016.

Wan, R. G., and Guo, P. J. (2001). "Drained cyclic behavior of sand with fabric dependence." *J Eng Mech-Asce*, 127(11), 1106-1116.

Wright, J. (2005). "*ImageD11*." <http://sourceforge.net/apps/trac/fable/wiki/imaged11>.

CHAPTER 6

3D ASSESSMENT OF FRACTURE OF SAND PARTICLES USING DISCRETE ELEMENT METHOD

This Chapter is a modified version of the paper published in: Cil, M. B., and Alshibli, K. A. (2012). "3D assessment of fracture of sand particles using discrete element method." *Géotechnique Letters*, 2, 161-166.

Abstract

Shearing or compression of granular materials causes particles to translate and rotate relative to each other, interlock or fracture depending on their mineralogy, morphology, porosity, applied stresses and boundary conditions. Conventional soil plasticity theories consider mainly the stress level and density to predict soil failure and ignore the influence of particle fracture. However, recent research has shown that there is a strong relationship between granular particle fracture and plastic yielding and hardening. In this study, the fracture of individual silica sand particles was modelled by adopting the bonded particle model concept within the framework of the distinct element method (DEM). Individual three dimensional (3D) particles were generated as an agglomerate of a large number of small spherical sub-particles that were connected by parallel bonds that resist moment and tension at contact points. The tensile strength variation observed when testing natural silica sand was achieved by changing the shape of the particle, the size and distribution of the spherical sub-particles and their bond strength. The onset and propagation of cracks through the particle were investigated using DEM and verified experimentally using 3D synchrotron micro-computed tomography images of sand. The behavior across the scale from a single particle to a laboratory-size specimen is also presented and discussed.

Introduction

Fracture of particles plays an important role in determining the constitutive behavior and deformation characteristics of granular materials. Plastic deformation of granular materials has been modeled within the framework of frictional energy dissipation and hardening plasticity to describe the constitutive behavior of soils (e.g., Roscoe *et al.* 1958, Roscoe and Burland 1968). However, classical soil plasticity models do not capture the change in the constitutive behavior of granular materials since they ignore the clastic nature of particles. Particle breakage alters the dilatant behavior of sands at high stresses (Bolton 1986) and leads to the development of a linear normal compression line in one-dimensional (1D) compression experiments (Coop and Lee 1993, McDowell and Bolton 1998). It is also directly correlated to plastic yielding (McDowell and Bolton 1998, McDowell and Harireche 2002b) and a major contributor to the accumulation of strain in cyclic loading (Harireche and McDowell 2003). Furthermore, particle fracture influences the location of the critical state line (Cheng *et al.* 2005).

Most laboratory experiments focus on investigating particle fracture using relatively large specimens that are suitable for characterizing the bulk behavior of granular materials. There are still experimental limitations on measuring fracture of small individual sand particles. As a result, the distinct element method (DEM) can serve as an excellent tool to better understand the influences of particle fracture on soils engineering behavior. Most DEM models use incompressible rigid discs or spheres to represent soil particles which can not capture the plastic behavior, critical state, and stress-dilatancy relationships (Robertson and Bolton 2001). In the literature, individual particle fracture has been simulated using DEM by treating the particle as agglomerate of bonded spherical sub-particles (Robertson and Bolton 2001, McDowell and

Harireche 2002a, Cheng *et al.* 2003) or by substituting individual rigid particles with a group of particles based on a certain failure criterion (Tsoungui *et al.* 1999, Lobo-Guerrero and Vallejo 2005). McDowell and Harireche (2002a), McDowell and Harireche (2002b) and Cheng *et al.* (2003) demonstrated that single sand particles can be modeled in DEM using agglomerate of spherical sub-particles bonded by contact bonds to capture the stress variation of single particle fracture, the uniaxial compression of granular assembly, and the plastic hardening and yielding of sand. The agglomerate is generally composed of regularly packed spheres that are linked by contact bonds and the variation in tensile strength of crushable particle was achieved by a random removal of about 20% to 50% of the sub-spheres to mimic experimental variation of tensile strength. The tensile failure mode that causes particle fracture was not investigated in these studies and was not verified by experimental measurements.

Potyondy and Cundall (2004) proposed a numerical distinct element model called the bonded particle model (BPM) to model the fracture behavior of rocks. The rock was represented by a dense packing on non-uniform-sized circular or spherical particles bonded at their contact points. In the work of Potyondy and Cundall (2004), the BPM was applied to two-dimensional (2D) and three-dimensional 3D biaxial, triaxial, and Brazilian tests and for 2D tunnel simulation. In this paper, the fracture of individual silica sand particles was modeled in 3D DEM as an agglomerate of a large number of non-uniform-sized spherical sub-particles bonded together according to the BPM.

Experimental Work

Jaeger (1967) studied the crushing of rocks between two platens and proposed the following expression to calculate the tensile strength of particles:

$$\sigma = \frac{F}{d^2} \tag{6.1}$$

where σ is the characteristic tensile strength, F is the compressive force at failure, and d is the initial diameter of the particle. Voo (2000) and McDowell (2002) showed that Weibull statistical distribution captures the experimental variation of tensile strength of silica sand very well. The survival probability $P_s(d)$ of a particle is expressed as (Weibull 1951):

$$P_s(d) = exp\left[-\left(\frac{\sigma}{\sigma_o}\right)^m\right] \tag{6.2}$$

Where σ_0 is the characteristic tensile stress corresponding to a 37% survival probability, and m is Weibull modulus. σ_o is determined by plotting ln[ln(P_s)] versus random values of ln(σ).

In this paper, single particle fracture experiments were conducted on 87 particles of ASTM 20-30 Ottawa sand; a natural silica sand with well-rounded particles with a grain size between US sieves #20 (0.853 mm) and #30 (0.599 mm). In addition, three 1D compression experiments were conducted on a sand column composed of three sand particles using a special test cell. The sand particles were poured inside a 1 mm cylindrical hole at the center of a 15 mm acrylic cylindrical mold and were compressed at a constant displacement rate. A larger specimen (here called the "laboratory-size specimen") with a diameter of 4.32 mm and height of 6.41 mm of the same sand was also tested under 1D compression. Multiple synchrotron micro-computed tomography (SMT) scans were acquired on the specimens using beam-13D of GSECARS sector of the Advanced

Photon Source (APS), Argonne National Laboratory, Illinois, USA. Figure 6.1 shows axial cross sections of the SMT images of individual sand grains and the three columns of sand experiments as an example.

DEM Simulations

DEM simulations of granular particle fracture were performed using the commercial code PFC3D, which adopts the distinct element method (DEM) of Cundall and Strack (1979). Sand particles were represented by an agglomerate of non-uniform sized spherical sub-particles bonded together at their contact points by parallel bonds that act as a cementing material which can transfer force and moment between adjacent spheres. Strong force chains carry the majority of the load in the BPM. The densely packed assembly of spherical sub-particles was initially generated in a spherical shell element according to a size distribution defined by the maximum (R_{max}) and minimum (R_{min}) spherical sub-particles radii. Then, the assembly was subjected to a relatively low isotropic compression by increasing the spherical sub-particles' radii uniformly. Particles that have two or less contacts (except particles close to boundaries) were expanded and moved until a minimum of three contacts was achieved and parallel bonds were assigned to all contact points. All bonds between spherical sub-particles in each agglomerate have the same strength, which was chosen randomly from the normal distribution function defined by strength and the associated standard deviation values listed in Table 6.1.

Each agglomerate represents a single sand particle. It was stabilized by a cycling process under gravity to reach equilibrium and was then compressed between two parallel platens at a constant velocity up to fracture. The loading rate was determined by running simulations at

Figure 6.1. Axial sections of 3D SMT images of two single particles and three 1D compression experiments at progressive load levels (Δz represents the change in the height of sand column).

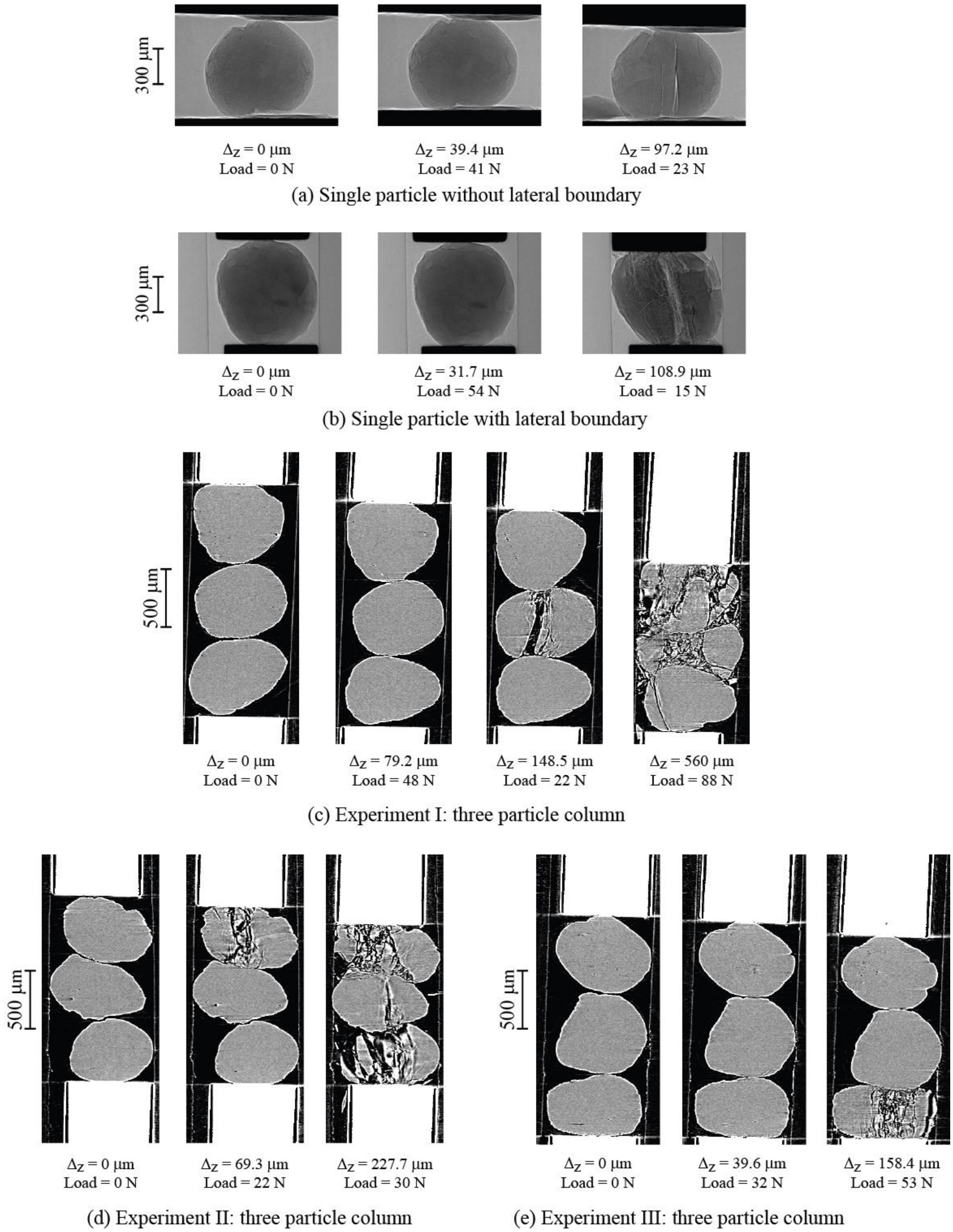

Figure 6.1. Continued.

different displacement rates to eliminate the effect of loading rate. The fastest displacement rate of 0.02 m/s that did not influence the material strength was selected as the optimum displacement rate. Figure 6.2 shows compressive load versus displacement of four DEM simulations and three example agglomerate configurations. The compressive load increases linearly up to a major fracture of the particle when it splits into small fragments. As a result, the load drops and increases in some cases, which is attributed to asperity damage and bond breakage at the end platen-particle contacts. Asperity fracture resulted in a significant load reduction and multiple peaks in some DEM simulations due to stress concentration in one or two spherical sub-particles which greatly influenced the fracture mode of the agglomerate. This issue was minimized by increasing the number of spherical sub-particles, which resulted in more contact points at the platen-agglomerate contact zone.

Compared with the published literature mentioned in the Introduction, a more realistic approach was adopted in this paper where the minimum diameter of spherical sub-particles, the bonding strength between spherical sub-particles, the shape and fabric of the agglomerate were altered in 40 different DEM simulations to mimic the mechanical and physical behavior of sand particles. Initially, the sensitivity of the model to each micro-parameter was examined by performing a series of simulations with varying parameter values. Particle size and packing density of spherical sub-particles have minor effects on the behavior of the agglomerate. Particle elastic modulus (E_c) and cement elastic modulus ($\bar{E}_c$) were chosen as 70 GPa based on laboratory experiments and literature (Azom 2012). The mean normal bond strength (σ) is directly proportional to σ_o and its standard deviation mainly governs the variation of tensile strength (m modulus in Weibull distribution). Shear bond strength (τ) has relatively negligible influence on

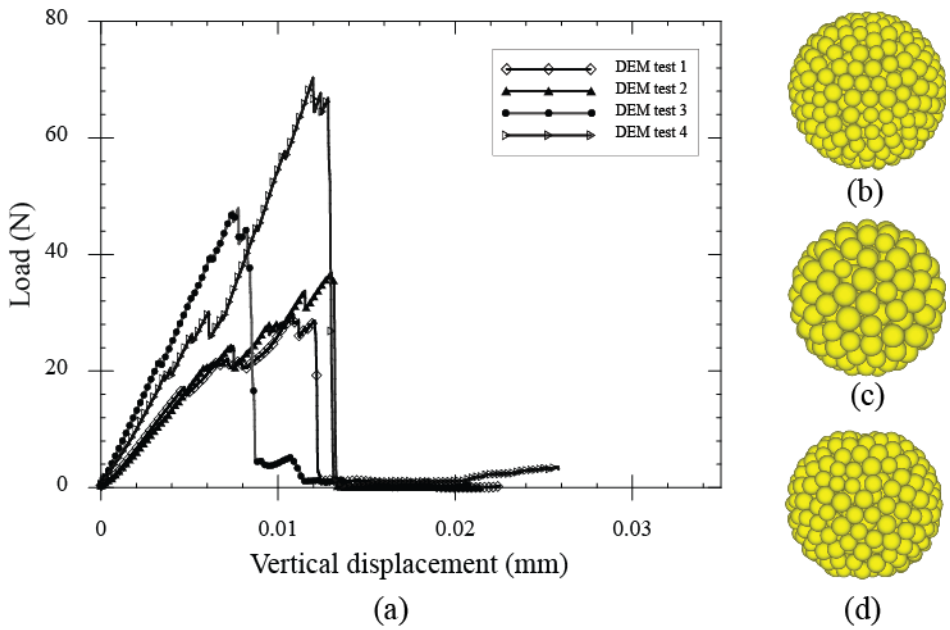

Figure 6.2. (a) Load-displacement relationship of four DEM single particle crushing simulations using 0.6 mm to 0.8 mm agglomerates of sub-spheres with (b) R_{min} = 0.035 mm; (c) R_{min} = 0.045 mm; (d) R_{min} = 0.035 mm and non-spherical shape.

material behavior; however both values were assumed equal to enable normal and shear bond failure. The standard deviation of material strength was set to zero and mean bond strength values of 625 MPa and 325 MPa reproduced the highest and lowest tensile strengths measured in the experiments. The bond strength was assigned through a random number generator using a mean bond strength of 475 MPa with a standard deviation of 150 MPa. The friction coefficient (μ) was set to 0.5. Table 6.1 presents a summary of DEM simulation parameters. Weibull probability distributions of laboratory experiments on individual sand particles and DEM simulations are depicted in Figure 6.3, which shows good agreement between the two results. The 37% characteristic tensile strength of sand particles is 131.5 MPa and 137.9 MPa in DEM and laboratory tests, respectively. Referring to Figure 6.3, the data did not fit the linear model well at low tensile stress. When a large number of particles are tested, few particles may have a low tensile stress and the exponential variation of the y-axis leads to low strength tail in the distribution.

Sand Fracture Behavior across the Scale

Additional 1D compression DEM simulations on a column composed of three particles and a relatively larger laboratory-size specimen were conducted in order to further verify the accuracy of the model, investigate the fracture behavior of sand across the scale, and examine the contact force interaction between agglomerates. Rigid spherical particles were generated according to the configuration of the particles in the SMT experiment (Figure 6.1c). The SMT images shown in Figure 6.1 represent cross sections of 3D images. Taking different sections of the 3D image of the sand columns reveals that some sand particles are not circular but rather close to ellipse geometry because the cross sections do not pass through the center of the particle. However, Ottawa sand

Table 6.1. Values of parameters used in DEM model (see Potyondy and Cundall (2004) for further explanation of parameters).

Parameter	Value
Diameter of agglomerate, D	0.6-0.8 mm
Wall stiffness	2 x 10^7 N/m
<u>Spherical sub-particles properties</u>:	
Mass density, ρ	2650 kg/m^3
Young Modulus, E_c	70 GPa
Minimum radius, R_{min}	0.035 mm & 0.045 mm
R_{max}/ R_{min}	1.2
Friction coefficient, μ	0.5
Normal stiffness/shear stiffness	2.5
<u>Parallel bond:</u>	
Bond radius multiplier, λ	1
Young Modulus, $\bar{E}_c$	70 GPa
Normal stiffness/shear stiffness	2.5
Mean normal strength, σ	475 MPa
Mean shear strength, τ	475 MPa
Normal and shear strength standard deviations	150 MPa

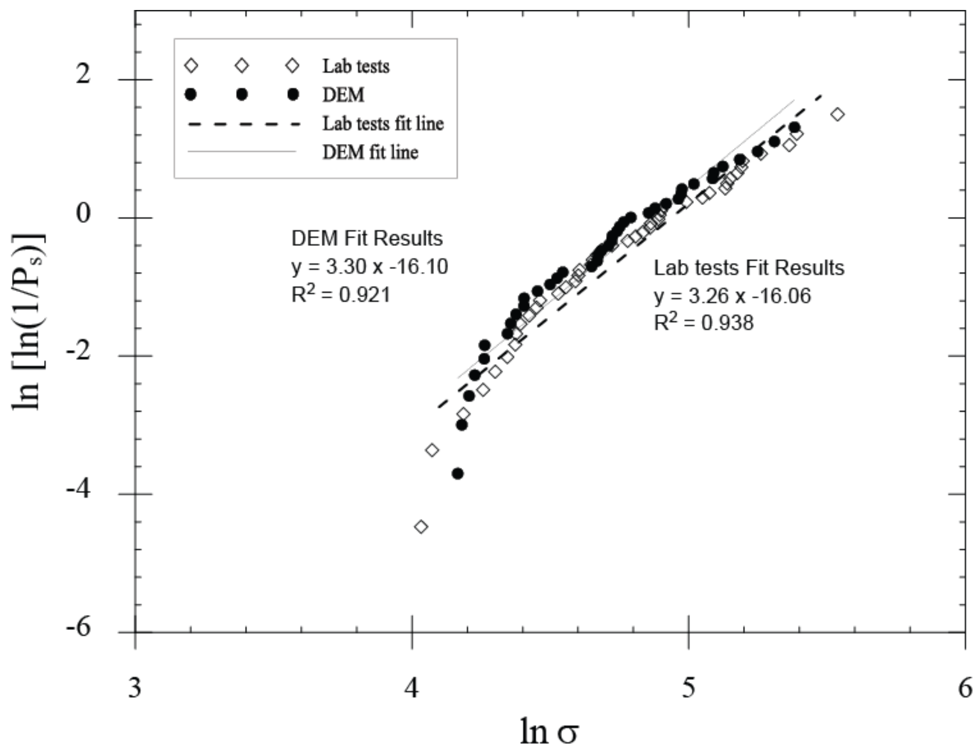

Figure 6.3. Weibull probability distribution for individual silica sand laboratory measurements and DEM simulations (40 simulations).

particles are still very close to a spherical shape. Changing the location of the cross section will influence the shape of 2D section of the 3D particle.

Each rigid DEM particle was substituted by arbitrarily rotated agglomerate that was generated according to the saved positions of spherical sub-particles. The specimen was compressed between rigid end platens at a constant velocity of 0.025 m/s. The load versus displacement relationships for the three sand column experiments and DEM simulations are shown in Figure 6.4, which clearly demonstrates that the proposed DEM model has successfully captured the constitutive behavior and brittle fracture of sand particles. In laboratory experiments, fragments of sand particles can contribute to the resistance to the applied load after a sharp load drop which is manifested in a more pronounced rise in the post-peak load. On the other hand, parallel bonds between spherical sub-particles break progressively and local fractures develop after the initial major fracture in the DEM agglomerate, which results in an oscillatory response after the peak load. Overall, there is a good agreement between DEM simulations and experimental results.

To further investigate the fracture behavior of sand across the scale, a larger laboratory-size specimen was also scanned and simulated using DEM (Figure 6.5). It is composed of 239 agglomerates and was subjected to 1D compression at a constant velocity of 0.1 m/s. Initially, the micro-properties that were determined in single crushing simulations were assigned to particles in the assembly. The yielding point of DEM was found to be less than half of that of a similar laboratory experiment (Figure 6.5d). Then, the DEM simulation of laboratory-size specimen was repeated after doubling the bond strength in each agglomerate which produced a good match with the laboratory test results. Such results demonstrated that DEM model micro-parameter calibration based on single particle fracture do not reproduce the stress-displacement behavior at larger scale

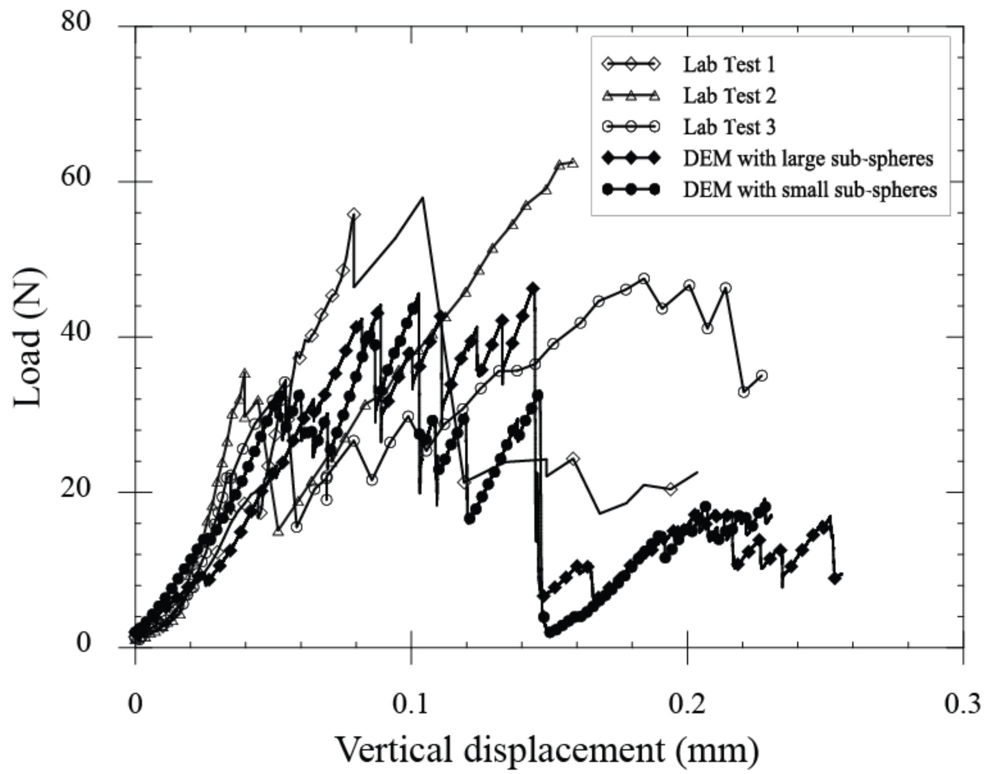

Figure 6.4. Laboratory and DEM results of 1D compression on column of three sand particles.

Figure 6.5. SMT and DEM images of single particle, column of three particles and laboratory size compression tests at different load levels. Numbers in parenthesis represent tensile (red) and shear (blue) bond breakages as (tensile, shear). (d) Comparison of responses of experiments and DEM simulations for single particle, column of particles and laboratory size specimen.

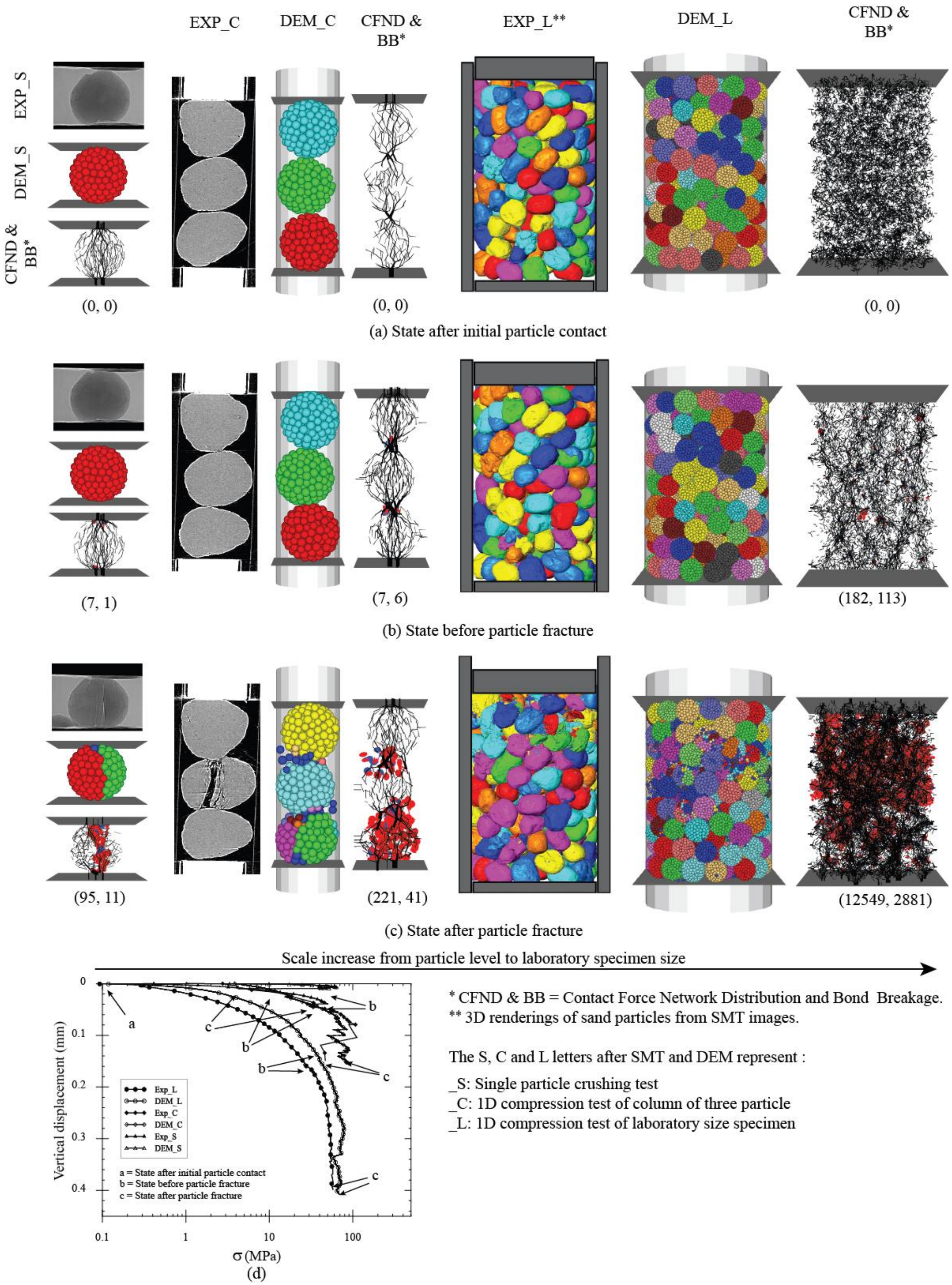

Figure 6.5. Continued.

because of the variation in real particle geometry, particle interactions, boundary conditions and strong force chains in the laboratory-size specimen.

Crack Onset and Propagation

When a particle is subjected to an increasing compressive load, a tensile stress is assumed to originate within a plane perpendicular to the loading direction. Diametric compression of the particle leads to stress concentration at contact points which is assumed as the flaw initiation zone. In order to investigate this crack formation hypothesis, SMT scans of single particle and 1D compression experiments were examined as the load was increased (Figure 6.1 & Figure 6.5). The results clearly show that particle breakage was initiated along the plane that connects the two contact points of the particle with adjacent particles. A few single particles and three similar 1D compression experiments were performed and scanned using SMT and the particles fractured via a brittle failure surface defined by the contact force direction as seen in Figure 6.1. This visualization demonstrates that the major crack mainly initiates from the compressive contact points, grows parallel to the plane that connects the contact points and eventually leads to particle breakage. The SMT images of single particle fracture (e.g., Figure 6.1a) show that silica sand fails via major split with no asperity damage.

SMT images provide valuable images of the crack formation mechanism experimentally. However, they do not provide any information about interior stress distribution within sand particles. Therefore, DEM was used as a tool to shed the light on tensile stress failure of compression-induced crack propagation. The initiation and propagation of the damage within individual sand particles was examined by tracking the bond breakage in the DEM agglomerates.

The number and locations of tension and shear cracks were monitored during the compression of agglomerates in different specimen sizes and the evolution of the bond breakage as the load increases is depicted in Figure 6.5. When the load increases, the bond between spherical sub-particles breaks mainly by tensile and shear stresses that are concentrated in a plane parallel to loading direction. The number of cracks in the agglomerate increases as the load increases. Tensile cracks (shown in red in Figure 6.5) are the dominant type of cracks when compared with shear cracks (shown in blue in Figure 6.5). Almost all cracks are parallel to each other and are concentrated along the plane of tensile strength in single particle crushing DEM simulations. A similar failure mode was observed in SMT image of the single particle fracture experiment (e.g., Figure 6.5a).

A similar crack mechanism was also observed in three-particle sand column compression, but the boundary walls slightly change the orientation of crack distribution. The 1D compression of 239 agglomerates reveals the interaction of clastic particles within the particulate assembly. The cracks mainly initiate at the contacts of agglomerates in the force chains that resist the majority of the axial load. When a particle fractures, the number of bond breakages increases rapidly, force chains collapse and new force chains develop. The onset and evolution of the cracks in Figure 6.5 validate the tensile failure theory that governs granular particle breakage under compressive loads and explains the complex loading mechanism and particle crushing characteristics in different scales.

Summary and Conclusions

A new DEM approach is proposed to simulate the fracture behavior of silica sand. Agglomerates of spherical sub-particles were generated according to BPM and successfully captured the elastic behavior, brittle particle breakage, and onset and progression of cracks. The proposed model offers significant improvements to capture the fracture of sand by incorporating material parameters that account for variations in experimental tensile strength. The fracture mechanics of sand particle under compression was characterized experimentally using 3D SMT images for the first time at the particle micro-scale. Silica sand particles fail in tension through a plane defined by the contact points of the particle with adjacent particles. The investigation of particle fracture at different specimen scales demonstrated that boundary conditions and particle interactions have significant effects on particle fracture. Moreover, the micro-properties of agglomerates based on single particle fracture do not reproduce the stress-displacement behavior at larger scale because of the variation in real particle geometry, particle interactions, boundary conditions and strong force chains in the laboratory assembly size.

Acknowledgments

This material is based upon work supported by the National Science Foundation under Grant No. (CMMI-1156436). Any opinions, findings, and conclusions or recommendations expressed in this material are those of the authors and do not necessarily reflect the views of the National Science Foundation. The SMT presented in this paper were collected using the X-ray Operations and Research Beamline Station 13-BMD at Argonne Photon Source (APS), Argonne National Laboratory. We thank Dr. Mark Rivers of (APS) for help in performing the SMT scans.

Use of the Advanced Photon Source was supported by the U.S. Department of Energy, Office of Science, Office of Basic Energy Sciences under Contract No. DE-AC02-06CH11357. Also, The authors thank Dr. David Potyondy of Itasca for his valuable comments and assistance.

References

Azom (2012). <http://www.azom.com/article.aspx?articleID=1114>. (accessed August 8, 2012).

Bolton, M. D. (1986). "The Strength and Dilatancy of Sands." Geotechnique, 36(1), 65-78.

Cheng, Y., Bolton, M., and Nakata, Y. (2005)."Grain crushing and critical states observed in DEM simulations." Powders and Grains 2005, Proc. 5th International Conference on Micromechanics of Granular Media, Stuttgart, 1393-1397.

Cheng, Y. P., Nakata, Y., and Bolton, M. D. (2003). "Discrete element simulation of crushable soil." Geotechnique, 53(7), 633-641.

Coop, M. R., and Lee, I. K. (1993)."The Behavior of Granular Soils at Elevated Stresses." Predictive soil mechanics : Proc. of the Wroth Memorial Symposium, London, 186-198.

Cundall, P. A., and Strack, O. D. (1979). "A discrete numerical model for granular assemblies." Geotechnique, 29(1), 47-65.

Harireche, O., and McDowell, G. R. (2003). "Discrete element modelling of cyclic loading of crushable aggreates." Granular Matter, 5(3), 147-151.

Jaeger, J. C. (1967). "Failure of rocks under tensile conditions." International Journal of Rock Mechanics and Mining Sciences & Geomechanics Abstracts, 4(2), 219-227.

Lobo-Guerrero, S., and Vallejo, L. E. (2005). "DEM analysis of crushing around driven piles in granular materials." Geotechnique, 55(8), 617-623.

McDowell, G. R. (2002). "On the yielding and plastic compression of sand." Soils Found, 42(1), 139-145.

McDowell, G. R., and Bolton, M. D. (1998). "On the micromechanics of crushable aggregates." Geotechnique, 48(5), 667-679.

McDowell, G. R., and Harireche, O. (2002a). "Discrete element modelling of soil particle fracture." Geotechnique, 52(2), 131-135.

McDowell, G. R., and Harireche, O. (2002b). "Discrete element modelling of yielding and normal compression of sand." Geotechnique, 52(4), 299-304.

Potyondy, D. O., and Cundall, P. A. (2004). "A bonded-particle model for rock." International Journal of Rock Mechanics and Mining Sciences, 41(8), 1329-1364.

Robertson, D., and Bolton, M. D. (2001)." DEM simulations of crushable grains and soils." Proc. Powders and Grains 2001, Sendai, 623-626.

Roscoe, K. H., and Burland, J. B. (1968)."On the generalized stress-strain behaviour of wet clay." In Engineering plasticity, Cambridge: Cambridge University Press, 535-609.

Roscoe, K. H., Schofield, A. N., and Wroth, C. P. (1958). "On The Yielding of Soils." Geotechnique, 22-53.

Tsoungui, O., Vallet, D., and Charmet, J. C. (1999). "Numerical model of crushing of grains inside two-dimensional granular materials." Powder Technol, 105(1-3), 190-198.

Voo, V. (2000). "Statistics of particle strength in a silica sand." MEng dissertation, University of Nottingham.

Weibull, W. (1951). "A Statistical Distribution Function of Wide Applicability." J Appl Mech-T Asme, 18(3), 293-297.

CHAPTER 7

3D EVOLUTION OF SAND FRACTURE UNDER 1D COMPRESSION

This Chapter is a modified version of the paper published in: Cil, M. B., and Alshibli, K. A. (2014). "3D evolution of sand fracture under 1D compression." *Geotechnique*, 64(5), 351-364.

Abstract

Three-dimensional (3D) synchrotron microtomography (SMT) and distinct element method (DEM) were used to investigate the evolution of particle fracture and deformation behavior of granular assembly subjected to k_o-loading condition. A series of 1D compression laboratory experiments were first conducted to better understand the effect of specimen aspect ratio (height-to-diameter ratio, H/D) on deformation behavior, which demonstrated that changing the specimen aspect ratio influences the stress-strain response of sand. 1D compression was simulated using 3D DEM model by mapping particle positions from SMT images. Crushable sand particles were modeled in DEM using agglomerates of spherical sub-particles that were bonded by parallel bonds. The DEM model successfully predicted the compressive behavior of specimens with different aspect ratios. The experimental and DEM results show that the onset of particle fracture and specimen yielding occur at the same strain level. The evolution and distribution of particle fracture was analyzed non-destructively at the particle and specimen scales using SMT images and the DEM model. The SMT images revealed that the majority of the particle fracture occurred in particles close to the loading platen. The onset of the fracture pattern of individual sand particles within the granular assembly was also examined at consecutive strain levels using SMT images and DEM simulation results. The development and collapse of force chains were investigated using DEM model and it was observed that the agglomerates that are part of a strong force chain mostly experience bond breakages. Combining SMT imaging technique and DEM simulations

provided valuable insight into complex micromechanical processes occurring during the compression of crushable granular materials.

Introduction

Many geotechnical engineering applications such as pile driving, blast loading, and high normal stress projects (e.g., heavy earth dams) may involve the fracture of sand particles. Particle breakage into small fragments alters not only the physical properties of granular materials including particle size distribution, but also their constitutive behavior. Therefore, a better understanding of the deformation characteristics of sand assembly in relation to particle fracture plays a critical role in developing robust models and better design guidelines. Many researchers have adopted experimental, analytical, and numerical approaches to investigate the response of granular materials under high stress conditions and to clarify the influence of particle fracture on this response. Many studies have employed experimental techniques such as high-stress triaxial experiments (e.g., Lade and Yamamuro 1996, Nakata *et al.* 1999), one dimensional (1D) compression experiments (e.g., Terzaghi and Peck 1948, Roberts and de Souza 1958, Yamamuro *et al.* 1996), and displacement-controlled single-particle compression experiments (e.g., Nakata *et al.* 1999, McDowell 2002, Cavarretta *et al.* 2010, Cil and Alshibli 2012).

Laboratory experiments generally draw conclusions based on the macro-scale measurements and are often useful in examining the effects of mineralogy, particle size, particle morphology, initial specimen density, and particle size distribution on the compression behavior of the particulate system (e.g., Hagerty *et al.* 1993, Nakata *et al.* 2001, Altuhafi and Coop 2011). However, such experimental results can not yield non-destructive fracture analysis since they only provide the stress-strain behavior of granular materials acquired at the external boundary of specimen during the test. Moreover, particle fracture information in laboratory experiments is obtained in post-test analyses by checking the change in grain-size distribution using sieve analysis or by visually inspecting the damage in individual particle morphology.

The particle fracture phenomenon was also investigated using theoretical and analytical models. For example, Kikumoto *et al.* (2010) enhanced the Severn-Trent sand constitutive model by incorporating the influence of particle size distribution changes on the deformation behavior of sands due to particle breakage. Cavarretta and O'Sullivan (2012) presented two simple analytical models to investigate the micromechanics of an irregular-shaped particle in terms of stability and deformation during individual particle compression tests. Bartake and Singh (2007) developed a mathematical model to predict the fracture strength based on particle size and specific gravity.

The experimental and theoretical approaches cited here significantly contributed to a better understanding of the complex processes involved in plastic deformation of soils; however, advanced computer models are an indispensable tool for gaining insight into underlying micromechanics that occur during the deformation of granular media. For example, Minh and Cheng (2013) simulated 1D compression experiments thanks to DEM with unbreakable rigid particles to investigate the role of particle size distribution on packing and compressive behavior. Some researchers modeled the compression of granular materials in DEM using crushable aggregates that were composed of spherical particles bonded at the contact points (e.g., Robertson and Bolton 2001, Harireche and McDowell 2003, Cil and Alshibli 2012). Lobo-Guerrero and Vallejo (2005b) implemented a different particle fracture approach involving the replacement of a rigid particle with a group of smaller particles with different diameters based on a tensile failure principle. Bolton *et al.* (2008) used DEM to investigate the micro-behavior of granular media for single particle compression and triaxial experiments. DEM approach was also used to show the relationship between yielding and onset of particle fracture in 1D compression simulations (McDowell and Harireche 2002) and to examine the effect of particle fracture on yielding, plastic deformation, and critical state soil mechanics (e.g., Cheng *et al.* 2004, Cheng *et al.* 2005, Wood and Maeda 2008). Vallejo *et al.* (2005) investigated the underlying micromechanical origins of the evolution of fractal size distribution in particulate media subjected to compressive stresses by conducting uniaxial compression experiments and 2D DEM simulations. They concluded that the intensity and distribution of force chains are found to be fractal, which is attributed as the cause for the development of fractal size distribution.

Despite extensive research on fracture phenomena in granular materials, a limited number of studies have considered monitoring particle fracture evolution under successive compressive loading. Lobo Guerrero and Vallejo (2005a) and Lobo-Guerrero *et al.* (2006) have used 2D DEM simulations to investigate the evolution of particle fracture under isotropic, biaxial and uniaxial loading conditions. They adopted particle replacement approach described earlier to model particle breakage. The amount and distribution of particle breakage were found to be different in a granular assembly subjected to isotropic and biaxial stress conditions (Lobo Guerrero and Vallejo 2005a). Furthermore, Lobo-Guerrero *et al.* (2006) found that particle breakage concentrates at the upper region in uniaxial compression tests and 2D simulations at the initial stages of loading, but then fracture spreads into other regions as compression proceeds. Also, Lobo-Guerrero and Vallejo (2010) employed the same approach for centrifuge testing and showed that fracture concentrates at the bottom of the container.

These DEM investigations provided promising results for future applications of computer modeling in soil mechanics and offered a better understanding of the influence of particle fracture on deformation behavior of particulate systems. However, due to computational limitations, most of the DEM simulations fail to reproduce the shape, dimensions and number of particles of laboratory specimens. In situ experimental characterization of the evolution of particle fracture within the particulate system is difficult using conventional techniques and has not been reported in the literature at the micro-level. The main objective of this paper is to examine the evolution of particle fracture and the deformation behavior of sand assemblies that were subjected to 1D compression loading using SMT technique and 3D DEM simulations. SMT is an excellent non-destructive 3D technique to quantify and visualize the deformation of granular assembly and permits monitoring particle kinematics and the dynamic evolution of particle fracture at the microscopic level. Since SMT experiments require a relatively small specimen size compared to typical laboratory specimens to acquire high resolution images at a relatively short scan time, a series of 1D laboratory compression experiments were first conducted to identify the effect of specimen size and aspect ratio on 1D compression behavior. The 1D compression of crushable silica sand particles was also modeled using 3D DEM by mapping the same specimen dimensions and particle positions from SMT images into the DEM model to investigate the micromechanical behavior of granular media.

1D Compression Experiments on Silica Sand

1D compression is a common laboratory procedure to study the plastic deformation of soils under k_o loading condition. Several 1D compression experiments were conducted on ASTM 20/30 silica sand at different specimen aspect ratios. ASTM 20/30 sand is a well-rounded natural uniform silica sand with particle sizes between US sieves #20 (0.841 mm) and #30 (0.595 mm) and has a specific gravity of 2.65. Four molds with diameters of 4.32 mm, 9.53 mm, 25.4 mm, and 50.8 mm were used in the experiments. To prepare a specimen, the required sand weight was first calculated based on the specimen dimensions and the target dry density. The sand was then poured in the mold and was subjected to vibration until the desired specimen dry density was achieved. The first set of experiments was conducted on specimens with diameters of 25.4 mm and 50.8 mm up to compressive stress of 90 MPa.

The second set of experiments was conducted using 4.32 mm and 9.53 mm diameter molds. The 4.32 mm diameter mold was also used in SMT scans. These molds were machined such that cylindrical tubes with various heights might be employed between the top and bottom loading platens, which permits changing the aspect ratio of the specimen. The desired specimen dry density was obtained by following the same procedure described earlier. Experiments with same specimen properties were generally repeated a few times and consistent results were obtained. Therefore, only some of the experiments are presented in this paper for brevity. Table 7.1 presents a summary of the laboratory experiments.

SMT Scanning

SMT is a non-destructive high-resolution imaging technique that can produce 3D images of the specimen using x-ray transmission. The specimen is placed between the x-ray source and the detector, and a high-energy monochromatic x-ray beam produced by synchrotron sources is attenuated as it travels through the specimen. The absorption level primarily depends on the

Table 7.1. Summary of the laboratory 1D compression experiments (e_{max} = 0.742, e_{min} = 0.502).

Exp.	Diameter, D (mm)	Height, H (mm)	Aspect Ratio (H/D)	Dry mass (g)	Initial void ratio, e_i
SMT_1	4.32	6.63	1.54	0.16	0.60
SMT_2	4.32	8.51	1.97	0.22	0.51
Exp_1	4.32	22.72	5.26	0.56	0.57
Exp_2	9.53	4.84	0.51	0.59	0.55
Exp_3	9.53	14.30	1.50	1.77	0.53
Exp_4	9.53	19.08	2.00	2.36	0.53
Exp_5	9.53	48.06	5.05	6.06	0.54
Exp_6	25.40	15.00	0.59	13.40	0.50
Exp_7	25.40	15.16	0.60	13.40	0.52
Exp_8	50.80	26.50	0.52	93.60	0.52
Exp_9	50.80	25.59	0.50	90.45	0.52

properties of the scanned object (chemical composition, and structure) and the energy level of the x-ray. A scintillator converts the transmitted beam to visible light, which is projected onto a detector and recorded by a high-resolution camera system. The captured projection represents the attenuation data of the specimen acquired at a certain projection angle. To generate a 3D map of the specimen, a set of 2D images needs to be recorded by detectors while the specimen is rotated on a high precision stage at small rotation increments from 0° to 180°. The acquired projections are processed with the help of computer code to reconstruct the complete 3D attenuation data of the specimen. SMT enables acquiring images with enhanced spatial resolution (characteristically between 1–10 μm), which makes it favorable among the 3D imaging techniques and is sufficient for quantitative analysis of images of granular media under various loading conditions.

In this paper, SMT scans for two specimens with a diameter of 4.32 mm were acquired under 1D compression (SMT_1 and SMT_2 in Table 7.1). The aspect ratios of the specimens were 1.54 and 1.97 for the first and second experiments, respectively. The SMT scans were conducted at GeoSoilEnviroCARS (GSECARS) Sector 13 of the Advanced Photon Source (APS), Argonne National Laboratory (ANL), Illinois, USA. The specimens were prepared in the same manner as the 1D compression experiments and were scanned using an energy of 30 keV, which provided a spatial resolution of 7.11 μm/pixel. Ten and five scans at small strain increments were acquired for the first and second experiments, respectively, to track particle interaction and fracture during 1D compression. The stress-strain results of experiments and the strain levels of SMT scans are depicted in Figure 7.1.

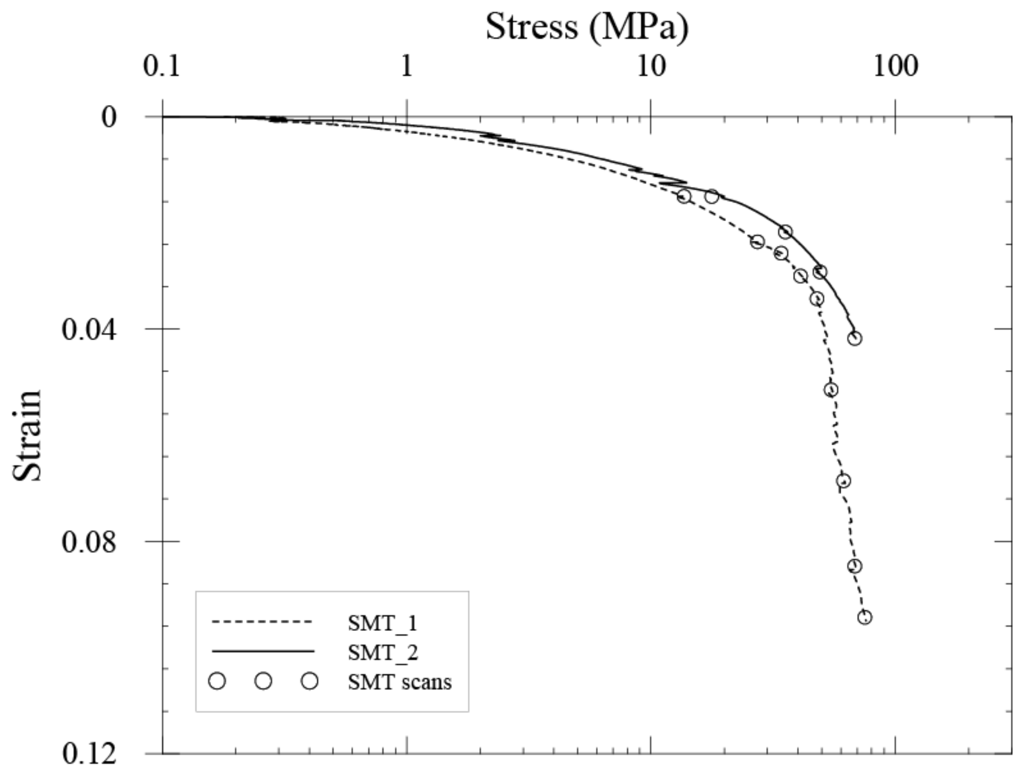

Figure 7.1. Stress versus strain relationships for SMT experiments and the associated scans points.

DEM Simulations

Silica sand particles were represented with crushable agglomerates of spherical sub-particles in PFC3D DEM software (Itasca 2008) to simulate particle fracture. Spherical sub-particles were bonded by parallel bonds that can transmit both force and moment. Parallel bond can be envisaged as cylindrical glue composed of uniformly distributed elastic springs lying between two bonded particles. Five contact parameters are used to define a parallel bond in PFC3D: parallel bond radius multiplier, parallel bond normal stiffness, parallel bond shear stiffness, parallel bond normal (tensile) strength and parallel bond shear strength. The radius of parallel bond is equal to the radius multiplier times the minimum radii of two bonded particles. Parallel bond stiffness and contact stiffness act in parallel. Forces acting on the two bonded particles result in tensile and shear stresses in the parallel bond. Parallel bond breaks when tensile or shear stress exceeds its specified strength limit. Then, the parallel bond is removed from the system and contact model becomes active if the two particles are still in contact (For more details see Itasca (2008)).

Numerical specimens are commonly generated using DEM with random packing of particles. In this study, 1D compression of silica sand particles was modeled by mapping the initial particle positions obtained from SMT scans into the DEM model. First, particles and the void space in reconstructed 3D SMT images were separated according to certain thresholding values, and each particle was labeled with a unique identification number (ID) using Avizo Fire commercial program which was also used to identify the coordinates of the center of the particle and the radius of the largest sphere inscribed inside the particle.

A cylindrical wall element bounded by rectangular loading plates at the top and bottom was generated in PFC3D to match the diameter and height of the experimental mold used in SMT scans. Spherical rigid particles were generated in the DEM model based on the particle positions and radii that were obtained from the SMT images. Then, the radii of particles were slightly modified in DEM model to closely match the void ratio of the experiments. The DEM specimen was then subjected to a cycling process to reach a state of equilibrium. The SMT image of the SMT_1 experiment has a coordination number of 5.79 with a standard deviation of 1.82. The DEM specimen has an initial average coordination (contact) number of 6.13 with a standard deviation of 1.70. The difference is due to a slight difference in particle morphology and packing configuration of the DEM assembly as compared to physical particles.

An agglomerate template that consists of densely packed spherical sub-particles was produced according to the Bonded Particle Model (BPM) material generation procedure introduced by Potyondy and Cundall (2004), as follows:

i. An assembly of spherical sub-particles was initially generated in a spherical shell element according to a uniform size distribution defined by the minimum (R_{min}) and maximum (R_{max}) spherical sub-particles' radii at a void ratio of 0.54 which was adopted by Potyondy and Cundall (2004) to obtain a densely packed assembly.

ii. The assembly was subjected to an isotropic compression by modifying the spherical sub-particles' radii uniformly.

iii. The number of particles that have two or less contacts was minimized by expanding and moving these particles while fixing other particles' positions until achieving a minimum of three contacts to obtain a densely packed agglomerate.

The generation process provided an agglomerate template to represent the crushable behavior of sand particles, and the positions and radii of spherical sub-particles of the agglomerate were stored in a text file for further analysis. Five different agglomerate templates were produced for each DEM simulation. Then, each rigid particle within the DEM specimen that was generated based on SMT imaging was substituted by arbitrarily rotated agglomerate, and parallel bonds were assigned at the contact points of the sub-particles within each agglomerate. The diameters of the agglomerates were modified to match the diameters of replaced rigid particles. The parallel bond value of each agglomerate was assigned according to a normal statistical distribution defined by a mean and standard deviation values. The sequence of the particle generation process from SMT images to a specimen with crushable aggregates is shown in Figure 7.2.

The DEM specimens were then subjected to a cycling process under zero friction to allow particles to rearrange and reach a state of equilibrium. After the relaxation period, the velocity of the top platen was slowly increased and the cylindrical specimen was compressed at a platen speed of 0.1 m/s. The loading rate was chosen slow enough to ensure a quasi-static loading condition which was verified by having negligible difference between the measured stresses on the top and bottom end platens. Furthermore, the bond breakages in agglomerates were tracked to examine the evolution of particle fracture in the DEM model and compared to experimental observations.

Effect of Specimen Size

As mentioned earlier, the SMT scans were performed on two relatively small specimen sizes (D=4.32 mm) with aspect ratios of 1.54 and 1.97 to acquire high-resolution images since using a typical aspect ratio (~0.5) for this small specimen diameter will result in only 2 to 3 sand

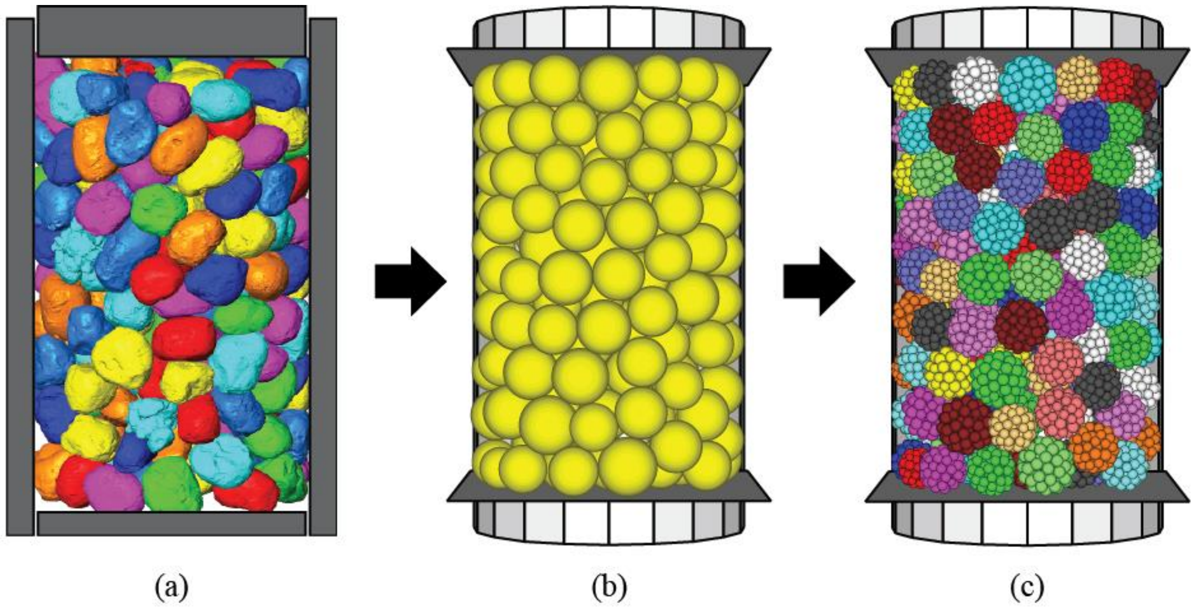

Figure 7.2. Sequence of the particle generation process: (a) 3D renderings of particles from SMT images, (b) DEM model with rigid particles, and (c) DEM model with crushable agglomerates of bonded spherical sub-particles.

particle layers in the axial direction, which does not provide conclusive results. Therefore, the authors performed the experiments at relatively high aspect ratios to allow the development of force chains and to minimize the boundary effects. Additional laboratory 1D compression experiments were also conducted to better understand the effects of specimen size and aspect ratio on the compressional behavior of sand. Specimens with similar dry densities and diameters of 50.8 mm, 25.4 mm, 9.53 mm and 4.32 mm were subject to 1D compression at a displacement rate of 0.02 mm/min (Table 7.1). Additional laboratory experiments were also conducted on 9.53 mm and 4.32 mm diameter specimens at various aspect ratios ranging from 0.50 to 5.26. The results of the experiments are shown in Figure 7.3, which demonstrates that the specimens exhibited similar stress-strain responses. The compressive stress increased sharply with compression at small strain level up to the yielding point, where significant changes of the slopes of compression curves are observed. The change in specimen diameter at the same aspect ratio led to slight changes in the stress-strain behavior. It is clear that the stress-strain curve shifts in the direction of the arrow shown in Figure 7.3 as the aspect ratio increases. The shift of the compression curve demonstrates that the aspect ratio of the specimen is an important factor in determining the yielding level of the sand. The results of 1D compression experiments at different aspect ratios and various specimen diameters show that increase in aspect ratio leads to a shift in the stress-strain curves if they are plotted on the same graph, but specimens with a high aspect ratio still exhibit an initial high stiffness and well-defined yielding followed by compression line similar to the specimens with low aspect ratio. The only effect of the aspect ratio is that specimen yields at smaller strain levels as the aspect ratio increases.

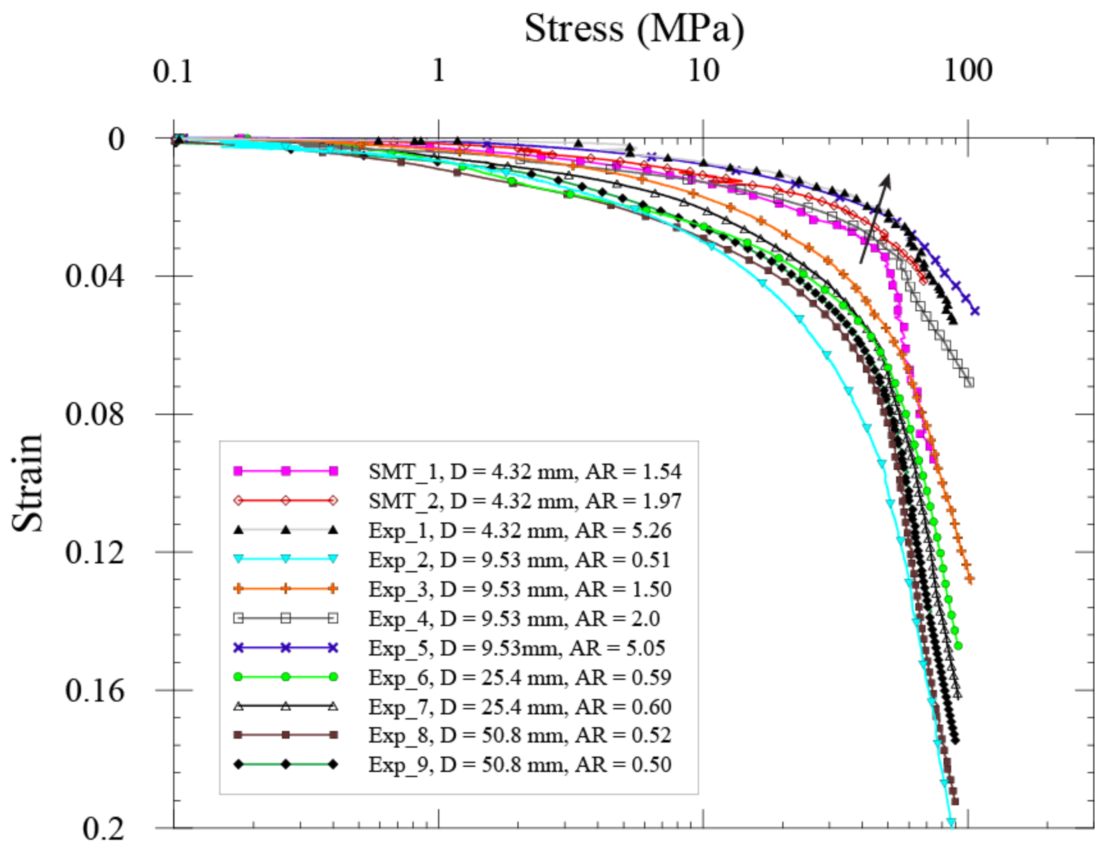

Figure 7.3. Stress versus strain relationships for 1D compression experiments conducted on ASTM 20/30 silica sand particles (AR = aspect ratio). Arrow indicates the effect of increase in specimen AR.

DEM Simulations Results

Effect of spherical sub-particle size

In 1D compression simulations, brittle silica sand particles were represented with agglomerates of spherical sub-particles. The number of spherical sub-particles determines the resolution of agglomerate model and results in a significant computational time for large specimen DEM simulations. One of the objectives of this paper is to replicate the laboratory specimen dimensions and the number of particles in DEM for various specimen sizes. Therefore, the number of particles that constitutes agglomerate must be small to run simulations in a reasonable time. To quantify the effect of spherical sub-particle size on the stress-strain response of the assembly, SMT_1 test (239 agglomerates) was simulated with four different agglomerate configurations by only varying the R_{min} value of the spherical sub-particle size distribution in agglomerate templates. The agglomerate diameter in templates was 0.7 mm. Table 7.2 presents a summary of the properties of spherical sub-particles used in these simulations.

The stress-strain curves for the four agglomerates are depicted in Figure 7.4, which shows that the DEM simulation results exhibited almost the same response up to the yielding point when the compression curve began to slightly fluctuate due to particle fracture within the assembly. Progressive bond breakage in the agglomerates caused a slight scatter in the stress-strain trend especially at high strain levels. All DEM simulations exhibited similar compression curves up to the 6% strain level when multiple particle breakage emerged. This sensitivity analysis demonstrated that the variation of the spherical sub-particle size in four agglomerates has no significant influence on the deformation behavior of the assembly. As a result, the following DEM

Table 7.2. Summary of the DEM simulations to determine the effect of spherical sub-particle size

Simulation ID	R_{min} (mm)	R_{max}/R_{min}	Number of spherical sub-particles in one agglomerate
SSP_1	0.075	1.2	69
SSP_2	0.06	1.2	129
SSP_3	0.052	1.2	198
SSP_4	0.045	1.2	281

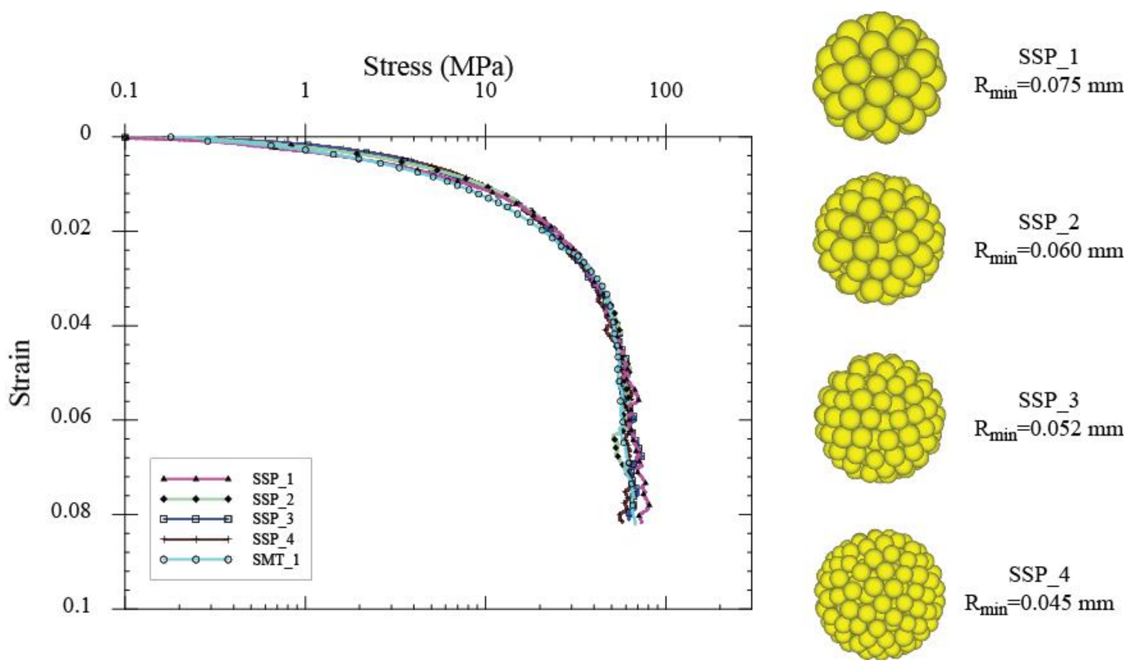

Figure 7.4. Stress-strain relationships for agglomerates composed of different size of spherical sub-particles and four typical example agglomerates.

simulations were conducted using the agglomerate templates with the lowest number of spherical sub-particles (SSP_1) to decrease computational time.

1D DEM model validation

The yielding of silica sand is directly related to the fracture strength of individual particles. Recently, Cil and Alshibli (2012) calibrated the model parameters of bonded agglomerates based on the single particle compression tests of ASTM 20/30 sand; however, these parameters underestimated the stress-strain behavior of laboratory size specimen in 1D compression test. Therefore, the micromechanical model parameters of agglomerates in this paper were inferred from Cil and Alshibli (2012) and final parameter values were determined by adopting an iterative calibration scheme. The SMT_1 experiment was taken as a reference in the calibration process. The influence of both particle stiffnesses and parallel bond stiffnesses were considered while matching the initial stiffness response of the experiment. Parallel bond normal stiffness (k_p^n) was initially estimated using the following expression (Itasca 2008):

$$k_p^n = \frac{\bar{E}_c}{R_a + R_b} \tag{7.1}$$

where $\bar{E}_c$ is the parallel bond modulus, and R_a and R_b are the radii of bonded particles. $\bar{E}_c$ was taken as 70 GPa (Cil and Alshibli 2012) and, $R_a + R_b$ was assumed as 0.15 mm because of the variations in agglomerate size and spherical sub-particle size. These values yielded k_p^n = 4.7 x 10^{14} N/m. During the model calibration using trial and error procedure, k_p^n was determined as 7.0 x 10^{14} N/m and parallel bond shear stiffness (k_p^s) was chosen as 3.0 x 10^{14} N/m with k_p^n/k_p^s ratio of 2.3. These bond stiffness values are proven to be good in capturing the brittle fracture behavior of sand particles. The mean and standard deviation values of bond strength distribution were varied to capture the yielding stress and post-yield response of the experimental result. It was observed that the mean bond strength value is proportional to the yielding point during compression. Moreover, the standard deviation of the bond strength distribution influences the post-yield compression behavior of the system and changes the yielding point. Since these two parameters have a combined effect, the calibration of the model required a series of fine-tuning simulations to obtain a response similar to the one observed in the experiment. The mean bond strength value of agglomerates was found to be higher than the one used in single particle compression simulations (for more information see Cil and Alshibli (2012)). Table 7.3 lists all the simulation parameters that were determined based on the calibration process.

Two additional 1D compression simulations were also performed to validate the DEM model without changing the calibration parameters. The SMT_2 experiment was simulated according to the procedure described earlier. In addition, Experiment_1 was also modeled in DEM by generating particles randomly inside the cylindrical container due to the lack of SMT images, which provided an additional case to increase the confidence in the proposed DEM model. The number of agglomerates used in SMT_1, SMT_2 and Experiment_1 simulations was 239, 323, and 848, respectively. A comparison of the experimental and DEM results is presented in Figure 7.5, which demonstrated that the DEM model successfully captured the 1D compressional behaviors of specimens with different aspect ratios. The initial stiffness and yielding points were captured very well by the model in all simulations. Both experimental and DEM simulation results began to fluctuate after the yielding point due to particle fracture. The shift of the yielding point to smaller strain values as the aspect ratio increases was also successfully captured by the DEM

Table 7.3. Values of parameters used in the DEM model

Parameter	Value
Agglomerate:	
Density	2650 kg/m^3
Spherical Sub-Particles' properties:	
R_{max}/ R_{min}	1.2
Friction coefficient	0.5
Normal and shear stiffness	8.0×10^6 N/m
Parallel Bond:	
Bond radius multiplier	1
Normal stiffness	7.0×10^{14} N/m
Shear stiffness	3.0×10^{14} N/m
Mean normal and shear strength values	750 MPa
Normal and shear strength standard deviations	175 MPa

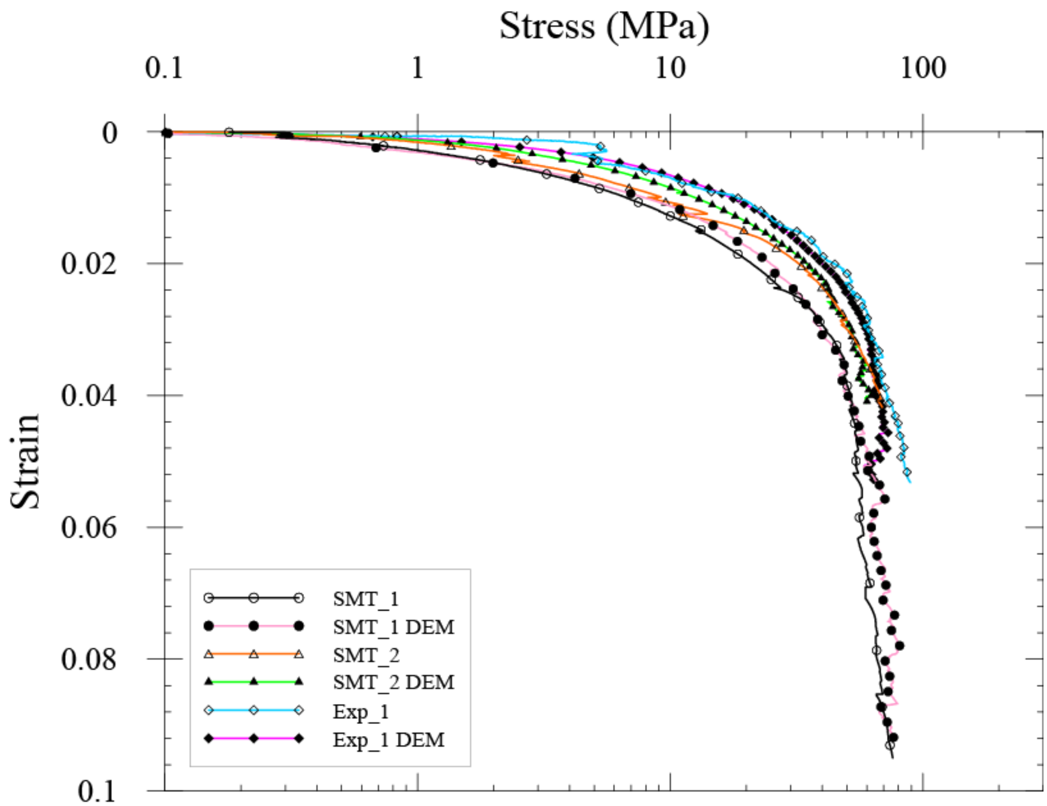

Figure 7.5. Comparison of laboratory experiments and DEM results.

model. The compression curve of DEM simulations does not increase continuously at the final stages of the simulations but rather exhibits more fluctuations when compared to the experimental results. Such behavior is more noticeable for the Experiment_1 simulation, which experienced more compressive displacement at the same strain level and particle fracture compared to the other two experiments. Overall, it can be concluded that the developed 1D DEM compression model with crushable agglomerates can reproduce the stress-strain behavior of silica sand particles with different specimen aspect ratios.

Particle Fracture Behavior

Qualitative analysis of 1D compression experiments

The deformation behavior of silica sand assembly and the evolution of particle fracture under 1D compression were examined using 3D SMT images and DEM simulations. SMT data provide valuable in situ measurements of particle fracture at the particle level, but additional micro-contact measurements such as force chains can be obtained only with the DEM model. Axial cross sections of the 3D SMT images and the DEM model taken at multiple strain levels for the SMT_1 and SMT_2 experiments are displayed in Figure 7.6 through Figure 7.9. In order to show the evolution of particle fracture, numerical agglomerates at the central axial cross section of the DEM specimen were also included in Figure 7.7 and Figure 7.9. The DEM images display the contact force network scaled by 50 N and the distribution and type of bond breakages (micro-cracks) denoted by light (green) and dark (brown) hexagons to represent the parallel-bond tension (normal) and parallel-bond shear failures, respectively.

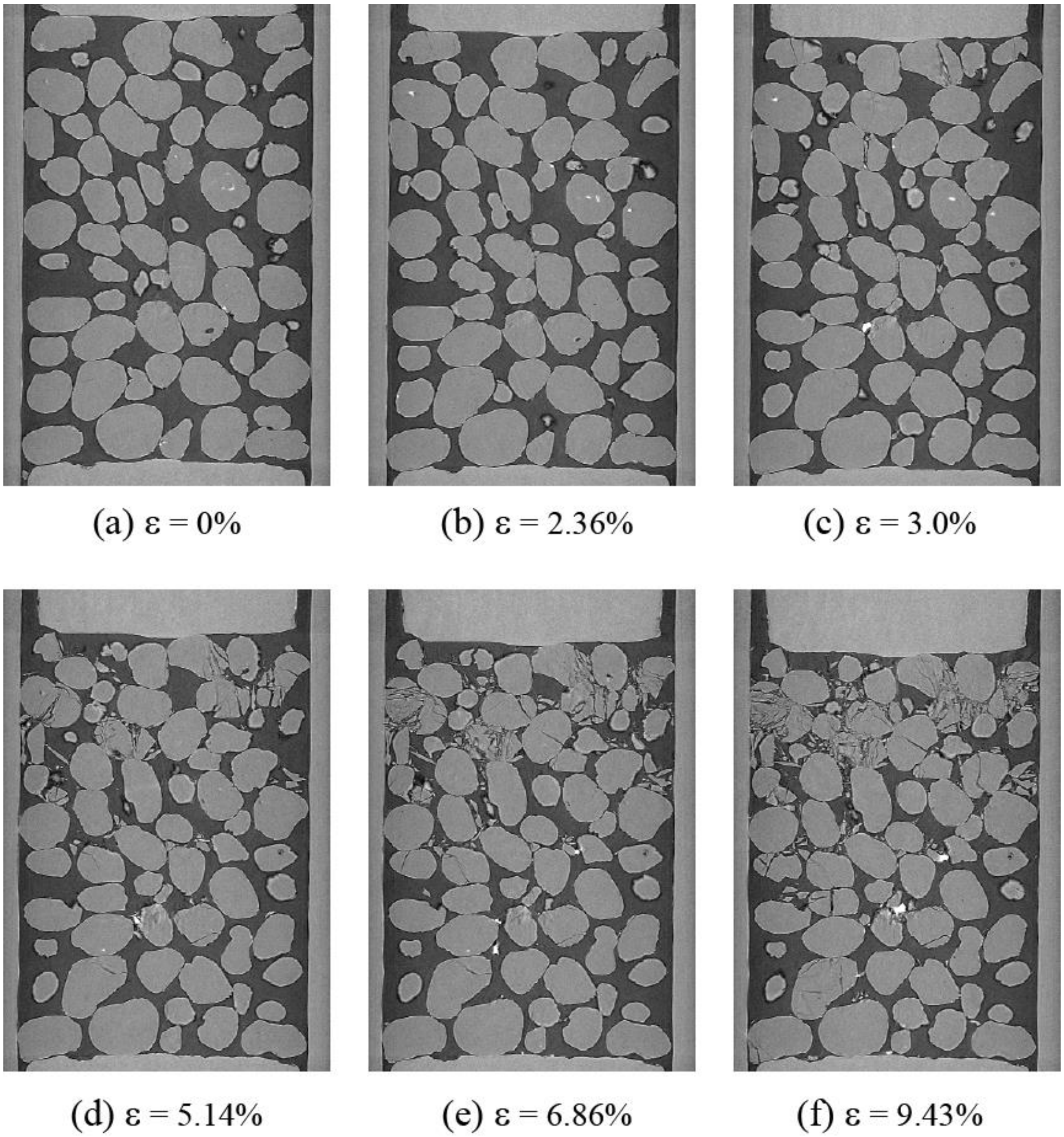

(a) ε = 0% (b) ε = 2.36% (c) ε = 3.0%

(d) ε = 5.14% (e) ε = 6.86% (f) ε = 9.43%

Figure 7.6. Axial cross sectional images of SMT_1 experiment specimen at multiple strain levels.

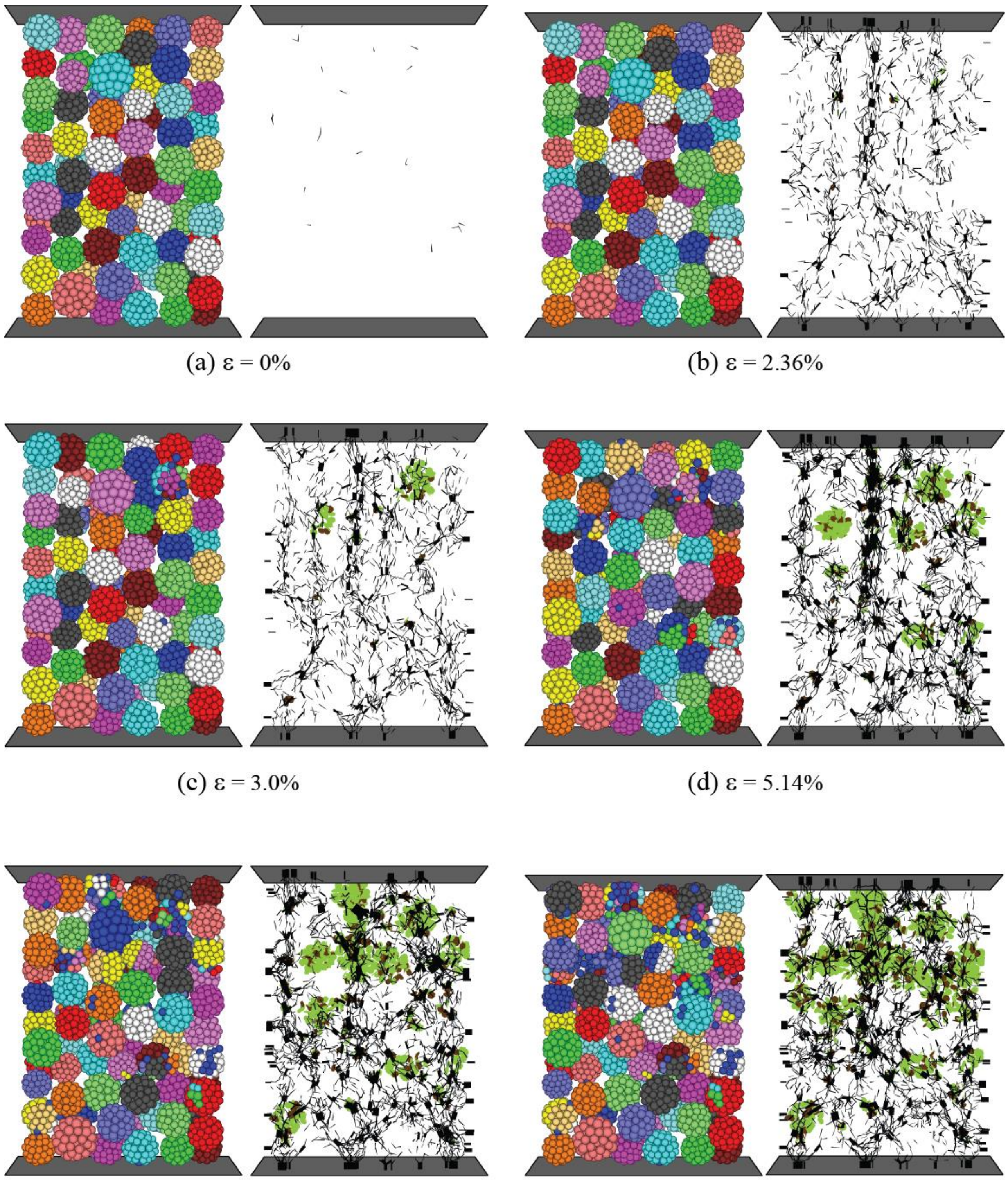

Figure 7.7. Axial cross sectional images of SMT_1 DEM specimen at multiple strain levels.

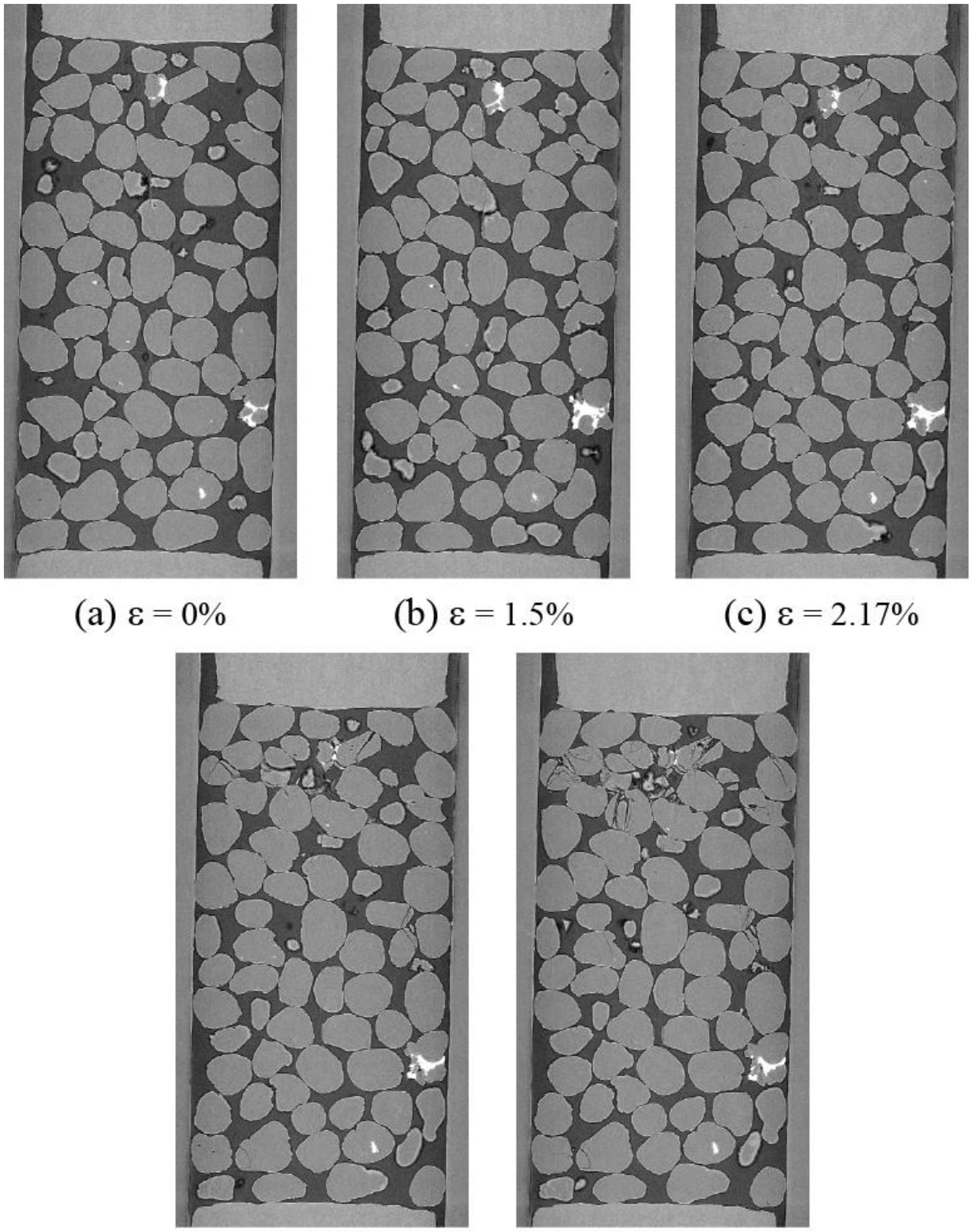

(a) ε = 0% (b) ε = 1.5% (c) ε = 2.17%

(d) ε = 2.92% (e) ε = 4.18%

Figure 7.8. Axial cross sectional images of SMT_2 experiment specimen at multiple strain levels.

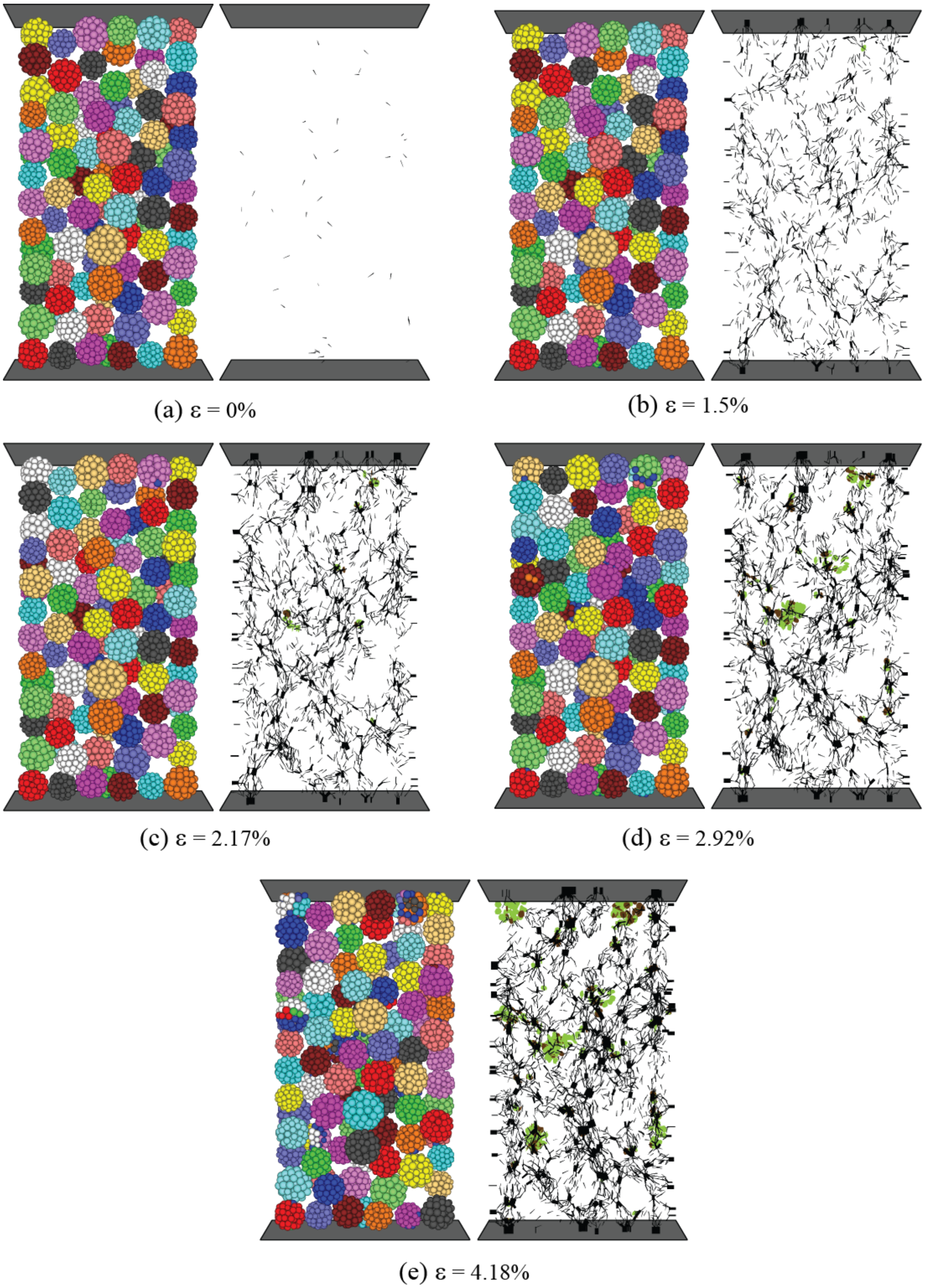

Figure 7.9. Axial cross sectional images of SMT_2 DEM specimen at multiple strain levels.

The initial unloaded states of the packed assemblies in SMT images shows the initial positions of the particles where no particle breakage was observed as expected (Figure 7.6a and Figure 7.8a). The few bright pixels observed in some SMT images are ferrous oxides (FeO) within the sand matrix and are ignored in the analysis. Since the specimen is composed of uniform particles and has a small size, it is not easy to prepare a very dense specimen. Sand particles undergo a small initial densification as they rearrange via rotation and translation as the axial compressive stress increases. The DEM model images for the initial stages of compression revealed that a strong force chain network began to develop and carried the majority of the axial load as the axial compression increased (Figure 7.7b and Figure 7.9c). Particle asperities began to break off from parent particles at ~2% compressive strain level, especially within the top half of the specimen, but no damage was noticed at the bottom half of the specimen in SMT images.

The first sign of particle fracture in the form of catastrophic splitting was observed at ~2.2% strain level in SMT images (Figure 7.6 and Figure 7.8). Few particles fracture within the upper half of the specimen. Similarly, the DEM model also predicted major agglomerate fractures in the specimen at ~2.2% strain level. It is also interesting to notice that the initiation of particle fracture and specimen yielding occurred at about the same strain level, which is in agreement with the findings of Coop and Lee (1993) and McDowell and Bolton (1998), who attributed yielding to onset of particle fracture; however, they did not present in situ experimental evidence to substantiate their suggestion. The analyses of SMT images revealed that the number of particles experiencing fracture increased as compression proceeds, and most of the breakage events occur near the top end platen of the specimen. Particle edge breakages were also much more frequently observed in SMT images throughout the specimen at higher strain levels. After the yielding point, many fractured particles continue to carry some load, which leads to the evolution of smaller fragments made from fractured particles (Figure 7.6 and Figure 7.8). As compression continues, more particle fracture in the upper half of the specimen is observed in the SMT images (Figure 7.6e-f and Figure 7.8e) as well as a small number of particles fractured in the bottom half. Since the fragmentation of the broken particles continued during the compression, some of the fractured particles have been reduced to many miniscule particles. At this stage, the small pieces created by means of particle fracture in the upper half of the mold have been compacted, filling the void space around them (Figure 7.6f). The number of micro-cracks in the DEM specimen also increased and concentrated at certain locations at the last stage of the simulation (Figure 7.7e-f and Figure 7.9e), which indicated that fractured agglomerates continue to experience further bond breakages. Similar to our observations based on the analyses of SMT images and DEM simulations, Lobo-Guerrero *et al.* (2006) reported that particle fracture concentrates at the upper part of the specimen at early loading stages of uniaxial compression experiments and 2D DEM simulations. Then, fracture spreads to other regions of the specimen as compression continues.

Lobo Guerrero and Vallejo (2005a), Lobo-Guerrero *et al.* (2006) and Lobo-Guerrero and Vallejo (2010) used 2D DEM simulations to visualize the evolution of particle fracture using 2D DEM which takes less computational time compared to 3D DEM using the same number of particles. Furthermore, it is easier to characterize and track the contact force network, the evolution of particle fracture and particle kinematic behavior in 2D simulations. However, 2D models do not reproduce the experimental void ratio of the granular materials, which significantly influences the macroscopic behavior of particulate system. On the other hand, 3D DEM approach allows modeling of out of plane particle interactions which is more representative of the actual material response. In this paper, 3D DEM modeling is employed using the concept of agglomerate with bond breakages, that better models the dynamic interactions resulting from the fracture of particles in the granular assembly and allows monitoring the propagation of fracture within the agglomerate via bond breakage tracking compared to 2D simulations that adopt particle-replacement technique.

The contact force network of the DEM model is also presented in Figure 7.7 and Figure 7.9 along with the bond breakages to show the relationship between the load transmission mechanism and the evolution of particle fracture. The contact force distribution of the specimen helps in identifying the onset and the collapse of strong force chains throughout the specimen. Figure 7.7 and Figure 7.9 also demonstrate that strong force chains form at random locations axially. Moreover, almost all bond breakages occur in agglomerates that lie within strong force chains. SMT images enable determining the contact network including the location of contact points, normal to the contacts and centroid of sand particles with a high accuracy in 3D. Normal to contact network data help to determine possible load transfer orientations based on the arrangement of particles in SMT images; however SMT does not provide measurements of inter-particle contact forces. A comprehensive analysis is required to understand the link between changes in normal to contact plots and the load transmission mechanism in granular assembly. Since many normal to contact vectors emerge due to the fragments of fractured particles, it is difficult to track changes in the system at high strain levels. This subject will be presented in detail in a future paper.

To show the onset and propagation of particle fracture phenomenon at the particle level, the fracture evolutions of two single sand particles within the specimen were monitored throughout the SMT scans as an illustrative example (Figure 7.10a-b). Initially, the specimen transformed into

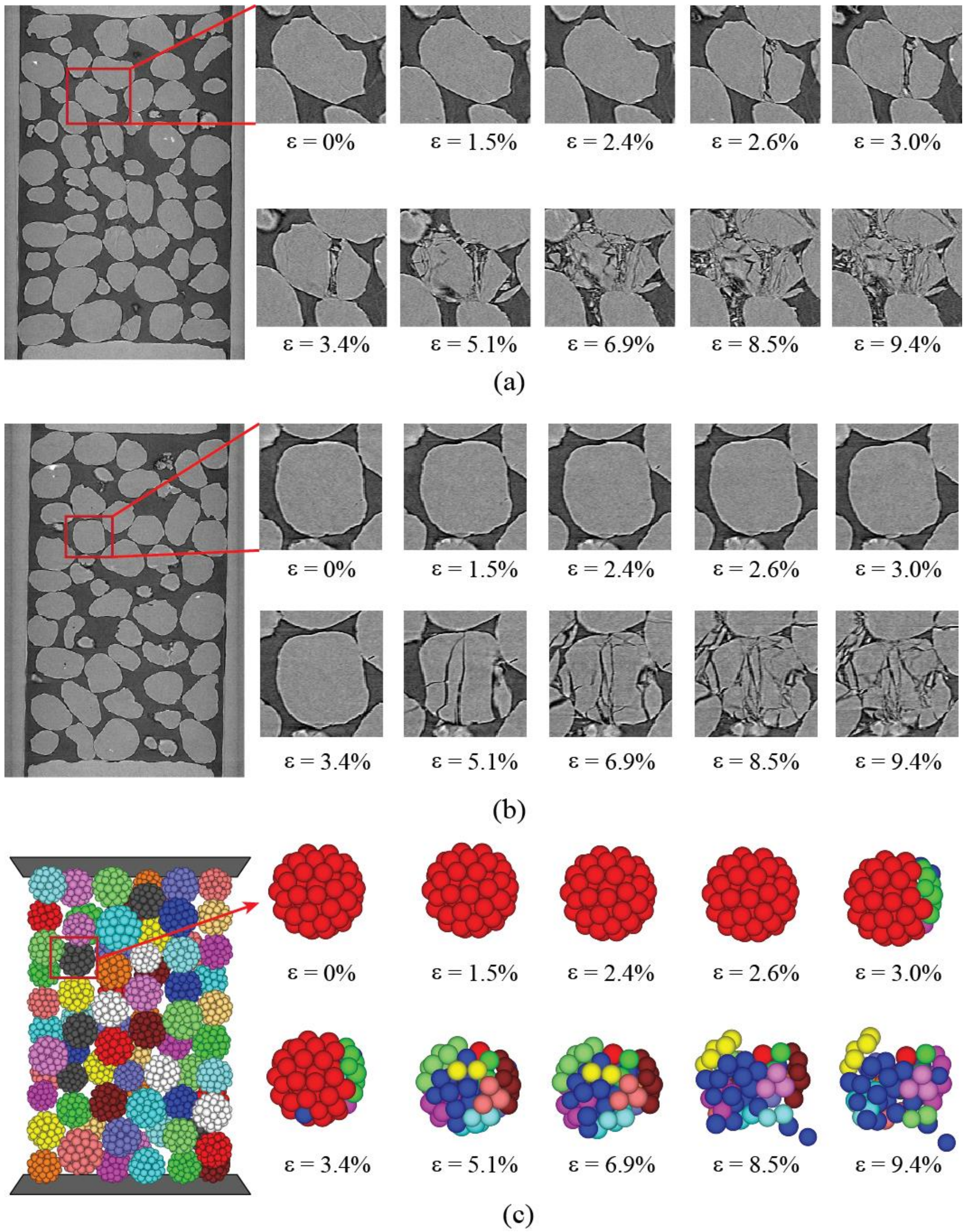

Figure 7.10. Example fracture mechanisms of single particles during 1D compression; (a) and (b) in SMT images; and (c) in DEM model.

a more dense state under 1D compression, which led to the rearrangement of both sand particles. Then, particles split into multiple fragments at ~2.6% and ~5.1% strain levels. The crack propagated through the highly loaded contact points of particles, which is in agreement with the cracking mechanism observed in SMT images of particle compression tests reported by Cil and Alshibli (2012). Then, the fragmentation of particles continued intensively at higher strain levels. It is also important to note that not only particle fragments but also some contacting particles exhibit fracture at higher strain values. Furthermore, the evolution of fracture mechanism of an agglomerate within the DEM specimen is shown in Figure 7.10c. The broken fragments that separated from the agglomerate were colored with different colors to show fragmentation. The agglomerate experienced the first fracture at 3% strain level and then, many broken pieces emerged and separated from the original agglomerate structure as the compression proceeded.

In spite of many attempts to characterize the fracture behavior of sand particles under compressive stresses, the dynamic evolution of the particle fracture within the assembly had not yet been reported in the literature due to the limitations of conventional experimental techniques. SMT images of two experiments were carefully examined to monitor in situ evolution of particle fracture. Each sand particle in the specimen was labeled with an identification number, and its response during 1D compression was tracked using 3D SMT images. The particle is recognized as fractured if it exhibits a major failure in the form of splitting and only original sand particles were considered in this analysis not the broken fragments emerge after fracture. The distribution and evolution of particle fracture as a function of axial strain for the SMT_1 and SMT_2 experiments is depicted in Figure 7.11, which confirms the previous observation that most of the particle fracture took place close to the top end platen. In the horizontal x-y plane, the fractured particles

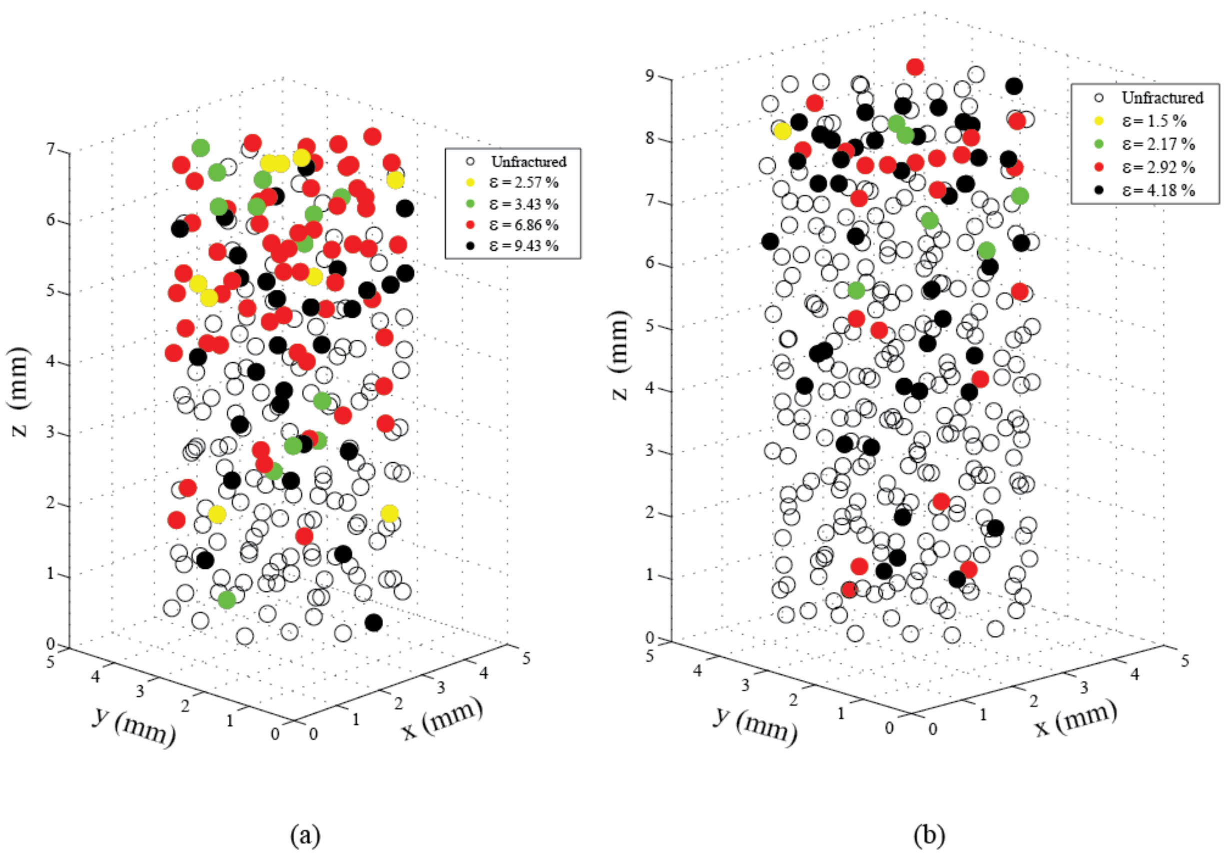

Figure 7.11. Distribution and evolution of particle fracture in the silica sand specimen as a function of compressive strain in (a) SMT_1; and (b) SMT_2 experiments. Color codes represent the strain level particle fracture.

were not concentrated at certain locations but rather were distributed randomly. It is also interesting to note that many contacting particles experienced fracture, which indicated that force chains do not always redevelop at new locations, but that broken fragments continued to carry load and lead to the fracture of neighboring particles. In other words, the distribution of particle fracture evolution demonstrated that a particle is vulnerable to fracture if its neighbors fracture.

The evolution of bond breakages of agglomerates in SMT_1 and SMT_2 simulations are shown in Figure 7.12. The agglomerates were color-coded at three consecutive strain levels based on five different percent bond breakage ranges which represent the magnitude of damage and fragmentation in particles. SMT_1 simulation results demonstrated that agglomerates with high percent bond breakages mostly concentrated at the middle and top region of the specimen, which is in agreement with the experimental observations. It is difficult to determine the distribution of percent bond breakages in SMT_2 simulation due to the small number of damaged agglomerates, but more bond breakages are present at the top half of the specimen compared to the bottom half. Overall, Figure 7.12 allows monitoring the development of agglomerate fracture at the specimen level. In 2D biaxial simulations, Lobo-Guerrero *et al.* (2006) visualize the evolution of particle fracture with similar conclusions, but the present 3D model provides 3D analysis which is more representative than 2D analysis.

Quantitative analysis of 1D compression experiments

The visual inspection of SMT data and DEM model results permits monitoring the dynamic deformation characteristics of granular assembly under 1D compression. However, quantitative analysis is necessary to assess the extent of particle breakage in the assembly. The number of

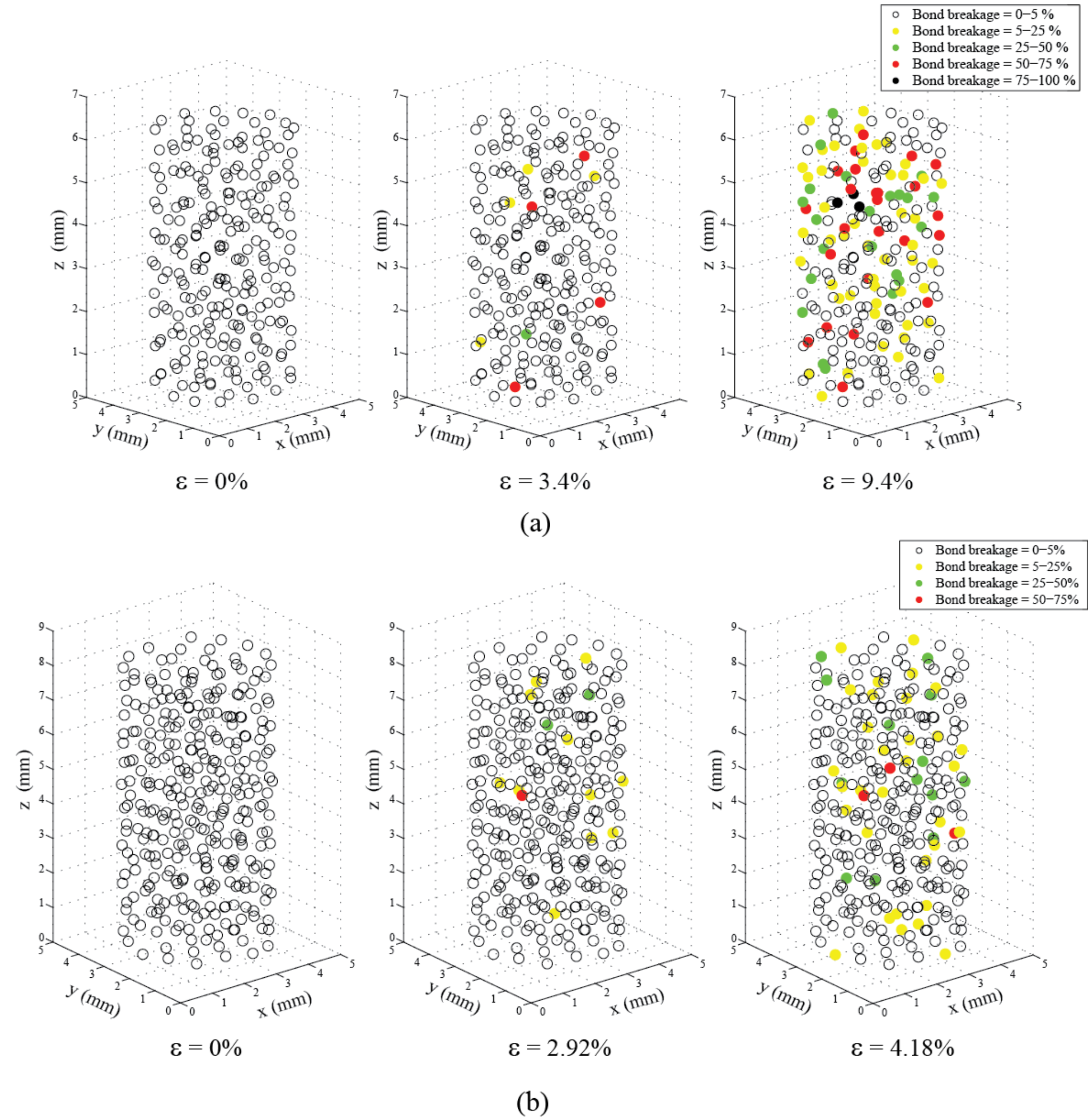

Figure 7.12. Distribution and evolution of bond breakages in agglomerates as a function of compressive strain in (a) SMT_1 DEM simulation; and (b) SMT_2 DEM simulation.

fractured particles was counted in both experimental and DEM specimens to provide a quantitative measure of the damage. Silica sand particles that experienced major damage were counted in SMT images, whereas fracture of particle edges, broken fragments or asperity damage were ignored. A particle was assumed as fractured if it split catastrophically into two or more fragments. Similarly, the micro-cracks in each DEM agglomerate were monitored and the agglomerate was considered fractured when the number of bond breakages is either equal or greater than 5% of the initial total bonds. The 5% limit was determined based on the bond breakages observed in agglomerates, which represents the transition from asperity damage stage to a major splitting mode.

The evolution of the percentage of fractured particles as a function of axial strain is shown in Figure 7.13a, which demonstrates that there is a good agreement between DEM and experimental results. DEM simulations slightly underestimate the percentage of fractured particles especially in SMT_1 simulation, which can be attributed to variation in 5% limit value in the fractured agglomerates. Both DEM and SMT specimens exhibited a small percentage of particle fractures up to ~2.2% strain level, which is the same as the yielding point of the specimen. Particles began to fracture after this stage, and the percentage of fractured particles initially increased in a nearly linear fashion, but the slope of the curve slightly decreased after 5% strain in the SMT_1 experiment results. The variation of the percentage of bond breakages (the ratio of the number of bond breakages to the initial total number of bonds) as a function of axial strain was also displayed in Figure 7.13b. Bond breakage in DEM simulations initiate at ~1.9% strain level due to the asperity damages in the agglomerates, which occurs as failure of a few bonds at highly loaded contact points. The percentage of bond breakages increased gradually, and bonds mostly break in the form of normal bond failure. Fractured particles in the experiments and bond

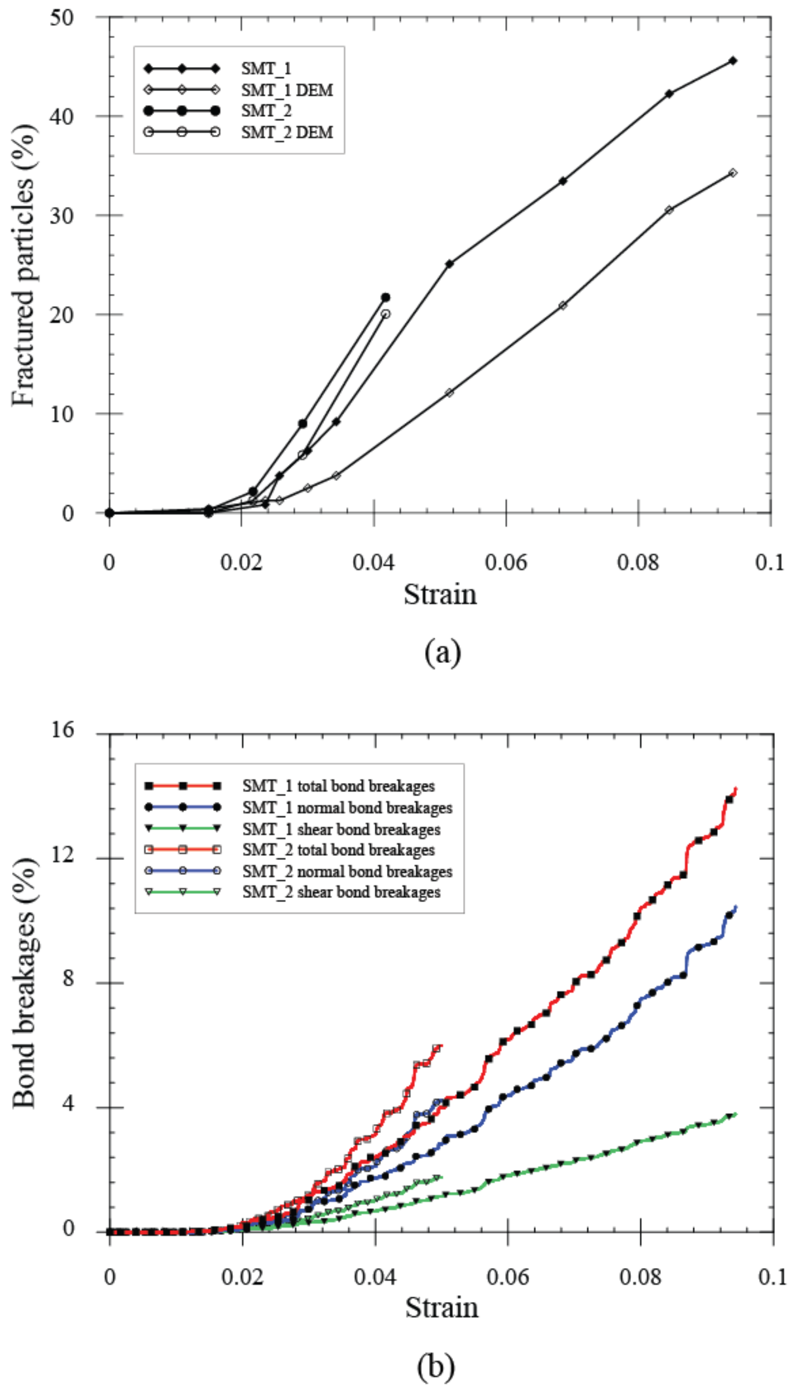

Figure 7.13. Evolutions of (a) particle fracture, and (b) bond breakages in agglomerates as a function of strain under 1D compression.

breakages in agglomerates exhibited similar variation under 1D compression. These results demonstrate that the yielding point coincides with the onset of particle fracture, and the rate of major splitting of the sand particles declines slightly after ~5% strain in a uniformly graded particulate system subjected to 1D compression.

Conclusion

The fracture behavior of uniformly graded sand assembly subjected to 1D compression was examined using SMT imaging and DEM simulations. A set of 1D compression experiments with various specimen sizes showed that an increase in the specimen diameter results in slight changes in the stress-strain curve and an increase in the aspect ratio causes the yielding point to shift to smaller strain levels. In situ observation of the 1D compression of silica sand particles using 3D SMT images revealed that particle fracture does not evolve homogenously throughout the specimen, but rather concentrates at certain locations close to the end loading platen. The evolution of particle fracture was monitored at particle level using 3D SMT images and it was observed that particles are found to be susceptible to fracture if their neighbors have already experienced fracture. Moreover, experimental and simulation results indicated that the onset of major particle failure in the form of splitting coincides with the specimen yielding level.

The contact force network generated by means of the DEM model allowed monitoring the formation of strong force chains and demonstrated that parallel bonds mostly break in agglomerates that were subjected to high contact forces in strong force chains. Quantitative analysis of SMT images showed that sand fracture initiated with yielding and increased progressively as the compression continued. The SMT and DEM techniques are powerful tools for gaining insight into the 1D compression of brittle silica sand particles.

Acknowledgments

This material is based on work supported by the National Science Foundation under Grant No. CMMI-1156436. Any opinions, findings, and conclusions or recommendations expressed in this material are those of the authors and do not necessarily reflect the views of the National Science Foundation. The SMT images presented in this paper were collected using the x-ray Operations and Research Beamline Station 13-BMD at Argonne Photon Source (APS), Argonne National Laboratory. We thank Dr. Mark Rivers of APS for help in performing the SMT scans. We also acknowledge the support of GeoSoilEnviroCARS (Sector 13), which is supported by the National Science Foundation, Earth Sciences (EAR-1128799), and the US Department of Energy (DOE), Geosciences (DE-FG02-94ER14466). Use of the Advanced Photon Source, an Office of Science User Facility operated for the DOE Office of Science by Argonne National Laboratory, was supported by DOE under Contract No. DE-AC02-06CH11357. Also, we thank Dr. David Potyondy of Itasca for his valuable comments and assistance.

References

Altuhafi, F. N., and Coop, M. R. (2011). "Changes to particle characteristics associated with the compression of sands." *Geotechnique*, 61(6), 459-471.

Bartake, P. P., and Singh, D. N. (2007). "A generalized methodology for determination of crushing strength of granular materials." *Geotech Geol Eng*, 25(2), 203-213.

Bolton, M. D., Nakata, Y., and Cheng, Y. P. (2008). "Micro- and macro-mechanical behaviour of DEM crushable materials." *Geotechnique*, 58(6), 471-480.

Cavarretta, I., Coop, M., and O'Sullivan, C. (2010). "The influence of particle characteristics on the behaviour of coarse grained soils." *Geotechnique*, 60(6), 413-423.

Cavarretta, I., and O'Sullivan, C. (2012). "The mechanics of rigid irregular particles subject to uniaxial compression." *Geotechnique*, 62(8), 681-692.

Cheng, Y., Bolton, M., and Nakata, Y. (2005)."Grain crushing and critical states observed in DEM simulations." *Powders and Grains 2005, Proc. 5th International Conference on Micro-mechanics of Granular Media, , Stuttgart*, 1393-1397.

Cheng, Y. P., Bolton, M. D., and Nakata, Y. (2004). "Crushing and plastic deformation of soils simulated using DEM." *Geotechnique*, 54(2), 131-141.

Cil, M. B., and Alshibli, K. A. (2012). "3D assessment of fracture of sand particles using discrete element method." *Géotechnique Letters*, 2(July-September), 161-166.

Coop, M. R., and Lee, I. K. (1993)."The behaviour of granular soils at elevated stresses." *In Predictive soil mechanics: Proceedings of the Wroth Memorial Symposium*, (G. T. Houlsby, and A. N. Schofield eds), *London, UK*, Thomas Telford, 186-198.

Hagerty, M., Hite, D., Ullrich, C., and Hagerty, D. (1993). "One-Dimensional High-Pressure Compression of Granular Media." *Journal of Geotechnical Engineering*, 119(1), 1-18.

Harireche, O., and McDowell, G. R. (2003). "Discrete element modelling of cyclic loading of crushable aggreates." *Granular Matter*, 5(3), 147-151.

Itasca (2008). *Particle Flow Code in Three Dimension (PFC3D) Version 4.0*, Itasca, Consulting Group Inc., Minneapolis, MN.

Kikumoto, M., Wood, D. M., and Russell, A. (2010). "Particle Crushing and Deformation Behaviour." *Soils Found*, 50(4), 547-563.

Lade, P., and Yamamuro, J. (1996). "Undrained Sand Behavior in Axisymmetric Tests at High Pressures." *Journal of Geotechnical Engineering*, 122(2), 120-129.

Lobo-Guerrero, S., and Vallejo, L. (2010)."Crushing of Particles under Simulated Static and Centrifuge Forces." *Proc. GeoFlorida 2010: advances in analysis, modeling, and design*, (D. O. Fratta, A. J. Puppala, and B. Muhanthan eds), *Palm Beach, Florida*, American Society of Civil Engineers, 550-559.

Lobo-Guerrero, S., Vallejo, L., and Vesga, L. (2006). "Visualization of Crushing Evolution in Granular Materials under Compression Using DEM." *International Journal of Geomechanics*, 6(3), 195-200.

Lobo-Guerrero, S., and Vallejo, L. E. (2005b). "DEM analysis of crushing around driven piles in granular materials." *Geotechnique*, 55(8), 617-623.

Lobo Guerrero, S., and Vallejo, L. E. (2005a). "Analysis of Crushing Of Granular Material under Isotropic and Biaxial Stress Conditions." *Journal of the Japanese Geotechnical Society : soils and foundation*, 45(4), 79-87.

McDowell, G. R. (2002). "On the yielding and plastic compression of sand." *Soils Found*, 42(1), 139-145.

McDowell, G. R., and Bolton, M. D. (1998). "On the micromechanics of crushable aggregates." *Geotechnique*, 48(5), 667-679.

McDowell, G. R., and Harireche, O. (2002). "Discrete element modelling of yielding and normal compression of sand." *Geotechnique*, 52(4), 299-304.

Minh, N. H., and Cheng, Y. P. (2013). "A DEM investigation of the effect of particle-size distribution on one-dimensional compression." *Geotechnique*, 63(1), 44-53.

Nakata, Y., Hyde, A. F. L., Hyodo, M., and Murata, H. (1999). "A probabilistic approach to sand particle crushing in the triaxial test." *Geotechnique*, 49(5), 567-583.

Nakata, Y., Hyodo, M., Hyde, A. F. L., Kato, Y., and Murata, H. (2001). "Microscopic Particle Crushing of Sand Subjected to High Pressure One-Dimensional Compression." *Journal of the Japanese Geotechnical Society : soils and foundation*, 41(1), 69-82.

Potyondy, D. O., and Cundall, P. A. (2004). "A bonded-particle model for rock." *International Journal of Rock Mechanics and Mining Sciences*, 41(8), 1329-1364.

Roberts, J. E., and de Souza, J. M. (1958)."The compressibility of sand." *Proc. A. Soc. for Testing Mat., Philadelphia, PA*, ASTM, 1269-1277.

Robertson, D., and Bolton, M. D. (2001). "DEM simulations of crushable grains and soils." *Powders and Grains 2001*, 623-626.

Terzaghi, K., and Peck, R. B. (1948). "Soil mechanics in engineering practice." Jon Wiley and Sons, Inc., New York, NY, 65-67.

Vallejo, L., Lobo-Guerrero, S., and Chik, Z. (2005). "A Network of Fractal Force Chains and Their Effect in Granular Materials under Compression." *Fractals in Engineering*, J. Lévy-Véhel, and E. Lutton, eds., London, UK, Springer, 67-80.

Wood, D. M., and Maeda, K. (2008). "Changing grading of soil: effect on critical states." *Acta Geotech*, 3(1), 3-14.

Yamamuro, J., Bopp, P., and Lade, P. (1996). "One-Dimensional Compression of Sands at High Pressures." *Journal of Geotechnical Engineering*, 122(2), 147-154.

CHAPTER 8

3D MODELING OF SAND PARTICLE FRACTURE USING DISCRETE ELEMENT METHOD AND SYNCHROTRON MICRO-TOMOGRAPHY IMAGES

This Chapter is a modified version of the paper published in: Cil, M. B., and Alshibli, K. A. (2014). "3D Modeling of Sand Particle Fracture Using Discrete Element Method and Synchrotron Micro-Tomography Images." *Geo-Congress 2014 Technical Papers*, 2822-2829.

Abstract

The fracture behavior of individual silica sand particles subjected to uniaxial compression was investigated using synchrotron micro-tomography (SMT) and distinct element method (DEM). SMT was used to acquire in situ three-dimensional (3D) images of individual sand particles up to the fracture stage. Single particle compression experiments were modeled in DEM by adopting the bonded particle model to generate crushable agglomerates composed of a large number of small sub-particles. By mapping the particle shape from the SMT images into the DEM model, the agglomerate shape was matched with the physical 3D shape of the tested sand particles. After considering hexagonal close packing and cubical packing approaches in the agglomerate generation stage, hexagonal close packing was chosen as it more closely captured the overall deformation behavior and fracture mode of sand particles.

Introduction

Granular materials exhibit fracture of individual particles in many engineering and science applications when they are subjected to high compressive/shearing loading conditions (e.g., pile driving and heavy earth dams). Since particle fracture significantly influences the constitutive behavior of granular media, understanding the fundamental properties of particle fracture helps to better understand and predict the response of crushable particles and aggregates.

Many researchers conducted laboratory experiments including uniaxial single particle compression (McDowell 2002, Cavarretta *et al.* 2010), one-dimensional (1D) compression (Hagerty *et al.* 1993, Altuhafi and Coop 2011), and high-pressure triaxial experiments (Nakata *et al.* 1999) to investigate the behavior of granular materials at high loading conditions, and the effects and characteristics of particle fracture. The limitations of experimental techniques encouraged many researchers to utilize from numerical models to examine the underlying mechanisms of particle fracture in a virtual environment. As a result, distinct element method (DEM) has been widely used to simulate fracture phenomenon and to further gain insight into micro-mechanical processes occurring during the deformation of crushable particles (e.g., McDowell and Harireche 2002, Bolton *et al.* 2008, Cil and Alshibli 2012) .

Generally, the crushable nature of particles is represented either by bonding spherical particles as agglomerate (Cheng *et al.* 2003, Wang and Yan 2013) or replacing the particle with a group of small particles based on a specific failure criterion (Lobo-Guerrero and Vallejo 2007, Ben-Nun *et al.* 2010). These studies provide valuable information about the deformation characteristics of granular materials; however, the primary limitation of the published literature is the lack of representing 3D physical shape of particles. The objective of this paper is to reproduce the physical shape of the individual sand particles in DEM simulations using 3D SMT images.

Experiment

SMT scans

Single particle compression experiments were conducted on a natural silica sand known as ASTM 20-30 Ottawa sand with a particle size between US sieves #20 (0.599 mm) and #30 (0.853 mm). Individual sand particles were compressed between two flat loading platens at a displacement rate of 0.05 mm/min using a high-precision computerized stepper motor.

The SMT scans were conducted at the Advanced Photon Source (APS), GeoSoilEnviroCARS (GSECARS) Sector 13 of the Argonne National Laboratory (ANL), Illinois, USA at an x-ray energy of 28 keV which provided an image resolution of 1.96 μm/pixel. Initially, the specimen was scanned, and then the axial load was applied until the desired compressive load was reached. The stepper motor was stopped, and a relaxation period was provided for axial load to reach a constant level, after which the SMT scan was performed. This procedure was repeated for consecutive load levels. The deformation behavior of the sand particle under 1D compression is depicted in Figure 8.1.

DEM simulations

The crushable silica sand particles were represented in DEM model with agglomerates that consist of a large number of spherical sub-particles bonded by parallel bonds at the contacts. By mapping the particle shape from the SMT images into the DEM model, the agglomerate shape was matched with the physical 3D shape of the tested sand particles.

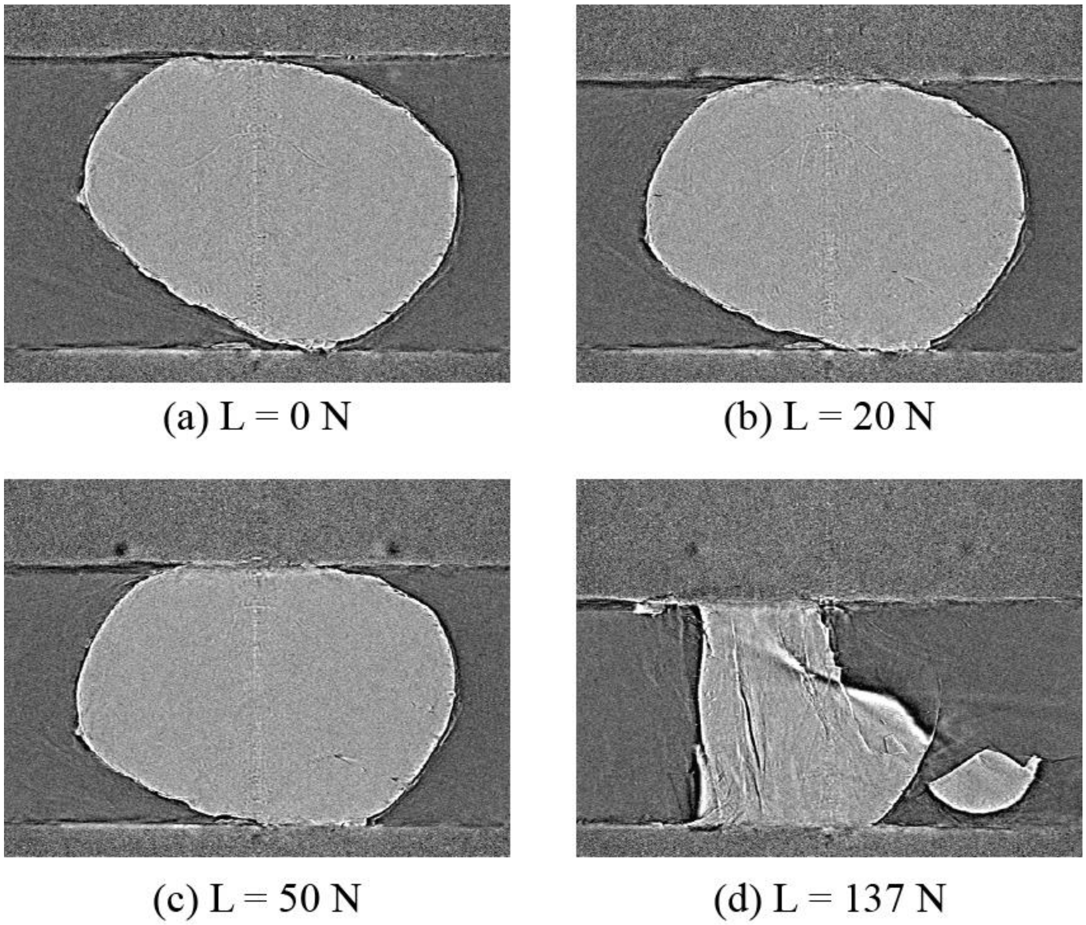

Figure 8.1. Axial cross-sectional SMT images of the sand particle acquired at different load levels.

SMT images are 3D array structures that contain the spatial distribution map of the x-ray attenuation of the specimen. Raw scan data needs to be analyzed to extract the 3D sand particle structure. The first step in image analysis is to identify and separate each constituent material in the image, which was performed with the help of segmentation process in Avizo Fire commercial image visualization software. This method uses thresholding approach and assigns 1 and 0 values for particles and voids, respectively. Then, the 3D volume data was saved as a text file to transfer particle shape information to the DEM model. The 3D view of the sand particle after segmentation is shown in Figure 8.2a.

Two regular sub-particle packing approaches were considered in this study to represent sand particle morphology. Dense random packing of sub-particles was not implemented due to difficulties in generating complex shape from SMT images. The cubical packing approach generated a sphere for each voxel with a value of 1 in the 3D segmented volume data. The diameter of the sphere is equal to one side of the voxel (pixel), and the sphere was generated based on the location of the voxel. However, this approach led to a high number of spheres for the DEM model, which caused excessive computational time. To increase the efficiency of the model, contacting spheres inside the agglomerate were replaced with spheres that had diameters three times larger than the diameter of the small spheres. To preserve the overall external shape of the sand particles, boundary particles were not included in the replacement process. The agglomerate with cubical packing is denoted as Agglomerate_1 (Figure 8.2b).

Hexagonal close packing (hcp) was also investigated as an alternative sub-particle packing to generate 3D agglomerate structures. Hcp provides a higher density than the cubical packing in a unit cell with monosized particles and enables transferring the applied load to

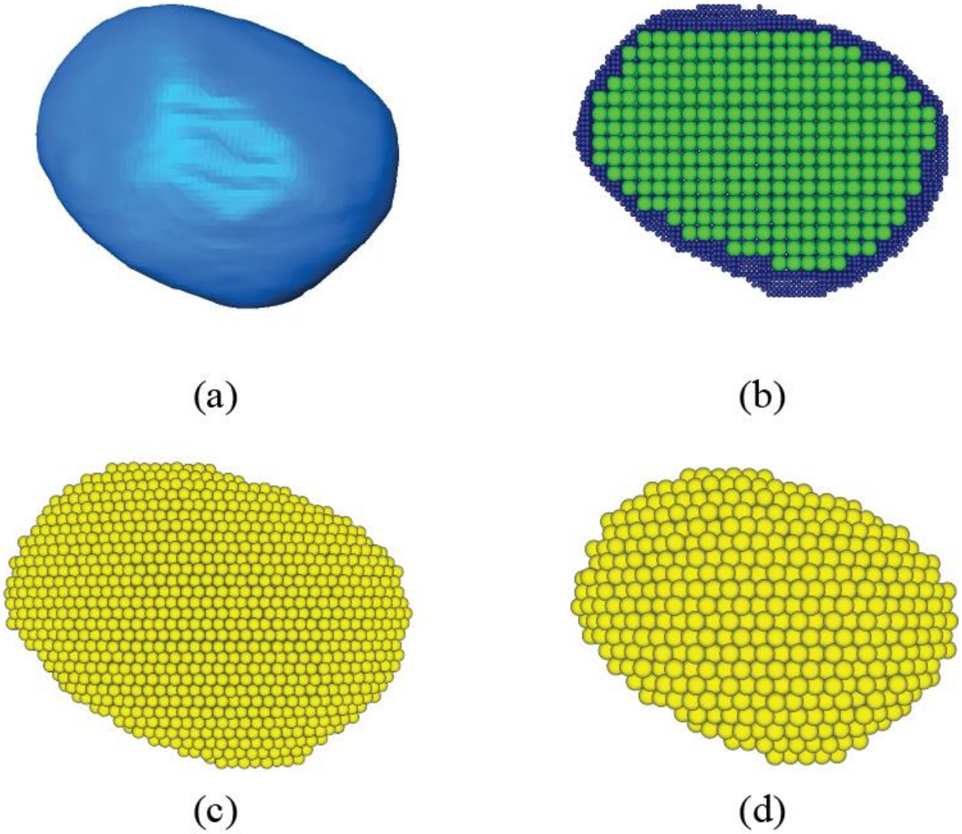

Figure 8.2. (a) 3D view of the sand particle after segmentation; (b) axial cross sectional image of the Agglomerate_1; 3D view of the (c) Agglomerate_2, and (d) Agglomerate_3.

contacting neighbors in various directions. However, with hcp, it is difficult to replace small spheres with larger ones. Therefore, two agglomerates with different sub-sphere sizes (small sub-spheres in Agglomerate_2 and larger sub-spheres in Agglomerate_3) were simulated in DEM model to identify the sub-sphere size effect on the deformation behavior (Figure 8.2c-d).

After the particle generation process, the agglomerate was stabilized under gravitational force. Finally, the top loading platen was generated and the agglomerate was subjected to uniaxial compression by moving the top and bottom loading platens simultaneously towards the particle. The loading rate was selected slow enough to ensure quasi-static specimen response. Furthermore, the bond breakages in agglomerates were monitored to examine the evolution of particle fracture in the DEM model.

The values of the DEM model parameters were determined via a calibration process which was performed by running a series of uniaxial compression simulations with Agglomerate_3 to match the simulation results with the experimental response of silica sand particle. The calibration procedure demonstrated that the failure load of the agglomerate is directly related to the parallel bond strength, which was observed more clearly in Agglomerate_2 and Agglomerate_3 simulations. Initially, the agglomerate may exhibit rotation, sliding or asperity damage based on the interaction at the particle-loading platen interface until reaching a stable configuration. The elastic modulus of the system after the initial response is mainly governed by the stiffness of particles. Since model parameters have a combined effect on the overall deformation response of the agglomerate, a trial and error iterative approach was adopted to select final parameter values. A summary of the DEM model parameters is listed in Table 8.1.

Table 8.1. Values of parameters used in the DEM model.

Parameter	Cubic packing	Hexagonal close packing
Spherical Sub-Particles:		
Density	5061 kg/m^3	3581 kg/m^3
Radius	0.007 mm	Agglomerate_2 = 0.016 mm
	0.021 mm	Agglomerate_3 = 0.024 mm
Friction coefficient	0.5	0.5
Normal and shear stiffness	1.0×10^6 N/m	1.0×10^6 N/m
Parallel Bond:		
Bond radius multiplier	1	1
Normal stiffness	7.0×10^{14} N/m	7.0×10^{14} N/m
Shear stiffness	3.0×10^{14} N/m	3.0×10^{14} N/m
Normal and shear strength	185 MPa	185 MPa

Results

SMT image interpretation

The SMT images shown in Figure 8.1 revealed that the sand particle exhibited an initial small rotation at the beginning of the experiment until reaching a more stable configuration. Then, the particle began to resist the applied compressive force and the load increased gradually in a nearly linear fashion. There might be very minor asperity damage at the particle-platen interface, which is very difficult to distinguish even in these high-resolution images. Finally, the particle fractured in the form of catastrophic splitting and many fragments emerged after the failure.

DEM simulation results

The load-versus-displacement relationships of three single particle compression simulations along with the experimental result are presented in Figure 8.3, which shows that Agglomerate_2 and Agglomerate_3 successfully captured the deformation behavior of the sand particle. In both cases, the load increases with displacement and particle fracture results in a sharp load drop. In the laboratory experiment, the sand particle fractured at a higher displacement level than the agglomerates. The difference is mainly attributed to complex initial interactions at the particle boundary-loading platen zone, which are difficult to quantify and may result in asperity damage, rigid rotation and translation of particle based on particle morphology and orientation.

Figure 8.4 displays the agglomerates after fracture. Hexagonally packed agglomerates fractured in the form of a major splitting parallel to the axial load in a similar mode as the silica sand particle fracture shown in Figure 8.1. It is interesting to note that these agglomerates split into

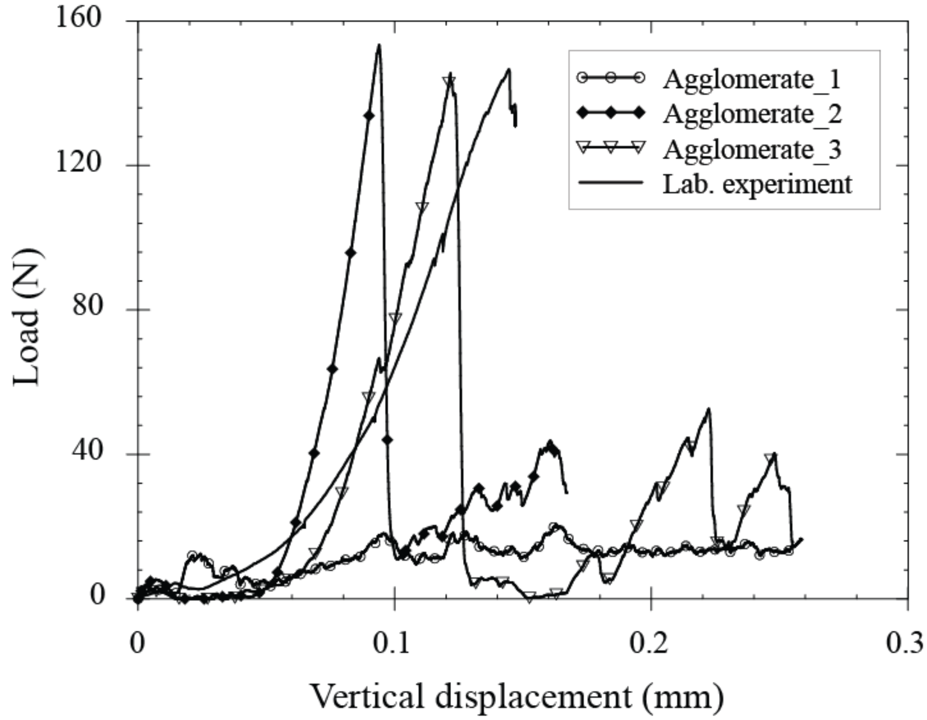

Figure 8.3. Load-displacement relationships of the single particle compression in laboratory experiment and DEM simulations.

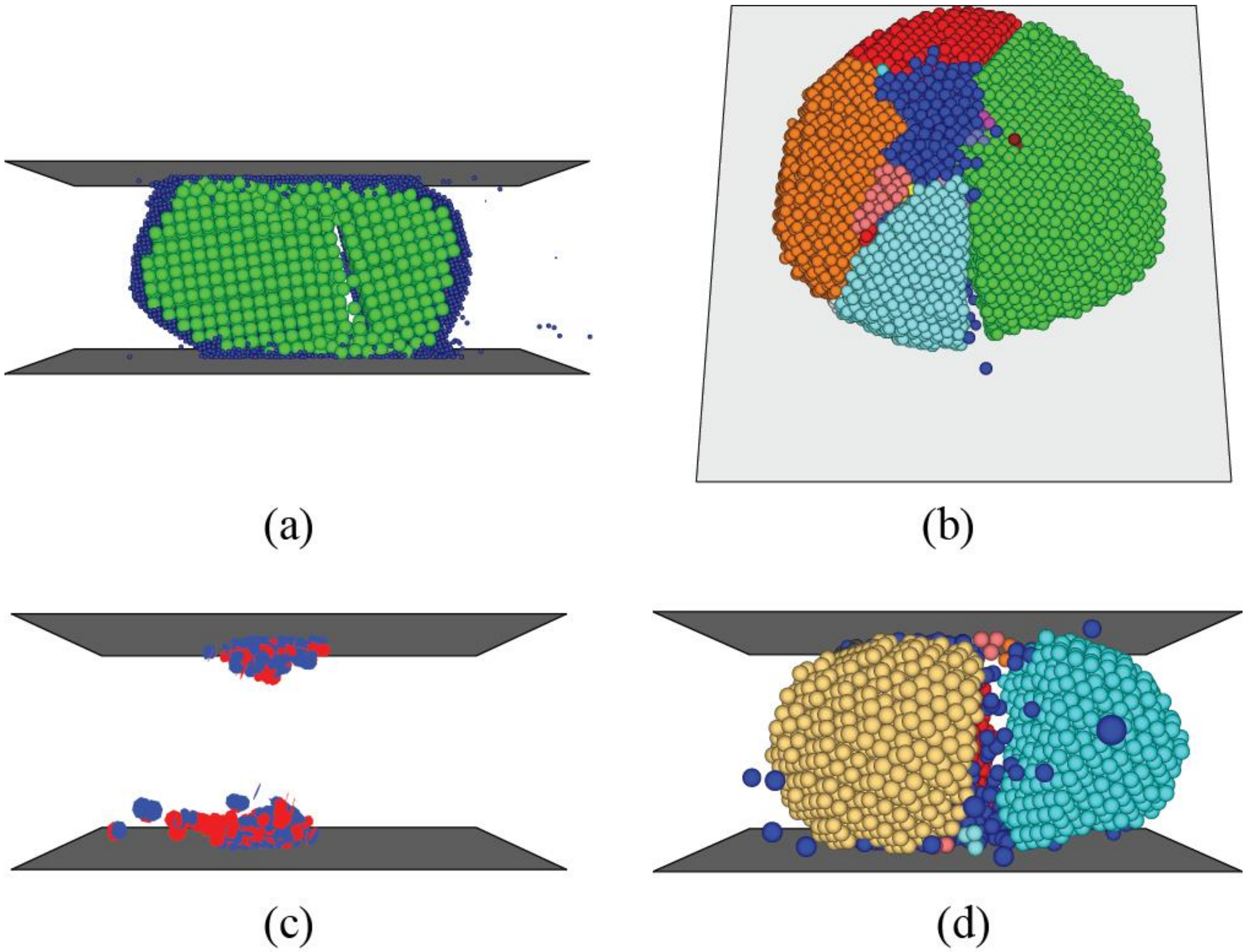

Figure 8.4. (a) Axial cross-sectional view of Agglomerate_1 after fracture; (b) plan view of the Agglomerate_2 after fracture; (c) bond breakages in Agglomerate_3 before fracture; (d) front view of the Agglomerate_3 after fracture.

a few major fragments in multiple directions as a result of hexagonal packing. The initiation of fracture in Agglomerate_3 (Figure 8.4c) displays the distribution and type of bond breakages (micro-cracks). Bond breakages are denoted by red and blue hexagons that represent parallel-bond normal failure and parallel-bond shear failure, respectively. Fracture initiates at the agglomerate-loading platen contact interface and propagates axially. 266 normal and 543 shear bond failures out of 25707 initial parallel bonds had formed in the agglomerate just before the major splitting. On the other hand, Agglomerate_1 exhibits a completely different response compared to experimental data. The axial cross-sectional view of Agglomerate_1 after the fracture is displayed in Figure 8.4a. Since small boundary particles do not have a well-connected load transfer system with the large particles inside the agglomerate, boundary particles break and split from the agglomerate structure during compression. This configuration resulted in a scatter load-displacement response which is well below the failure point of the experimental result. After the breakage of boundary particles, the larger spheres transmit the axial load until they fracture by splitting.

Conclusions

The deformation behavior and fracture mechanism of individual sand particle under 1D compressional loading was monitored using SMT and modeled in DEM with agglomerate of bonded spherical sub-particles. The high-resolution SMT images reveal that particle morphology and particle-platen contact configuration highly influence the deformation response of the sand particle. The 3D physical shape of sand was reproduced in DEM model by mapping the 3D volume data from SMT images. The agglomerate with hexagonal sub-sphere packing better captures the fracture behavior of sand particles than the agglomerate with cubical sub-sphere packing.

Acknowledgments

This material is based on work supported by the National Science Foundation under Grant No. (CMMI-1156436). Any opinions, findings, and conclusions or recommendations expressed in this material are those of the authors and do not necessarily reflect the views of the National Science Foundation. We also thank Dr. Mark Rivers of APS for help in performing the SMT scans. We acknowledge the support of GeoSoilEnviroCARS (Sector 13), which is supported by the National Science Foundation, Earth Sciences (EAR-1128799), and the U.S. Department of Energy (DOE), Geosciences (DE-FG02-94ER14466). Use of the Advanced Photon Source, an Office of Science User Facility operated for the DOE Office of Science by Argonne National Laboratory, was supported by DOE under Contract No. DE-AC02-06CH11357.

References

Altuhafi, F. N., and Coop, M. R. (2011). "Changes to particle characteristics associated with the compression of sands." *Geotechnique*, 61(6), 459-471.

Ben-Nun, O., Einav, I., and Tordesillas, A. (2010). "Force Attractor in Confined Comminution of Granular Materials." *Phys Rev Lett*, 104(10), 108001.

Bolton, M. D., Nakata, Y., and Cheng, Y. P. (2008). "Micro- and macro-mechanical behaviour of DEM crushable materials." *Geotechnique*, 58(6), 471-480.

Cavarretta, I., Coop, M., and O'Sullivan, C. (2010). "The influence of particle characteristics on the behaviour of coarse grained soils." *Geotechnique*, 60(6), 413-423.

Cheng, Y. P., Nakata, Y., and Bolton, M. D. (2003). "Discrete element simulation of crushable soil." *Geotechnique*, 53(7), 633-641.

Cil, M. B., and Alshibli, K. A. (2012). "3D assessment of fracture of sand particles using discrete element method." *Géotechnique Letters*, 2, 161-166.

Hagerty, M., Hite, D., Ullrich, C., and Hagerty, D. (1993). "One-Dimensional High-Pressure Compression of Granular Media." *Journal of Geotechnical Engineering*, 119(1), 1-18.

Lobo-Guerrero, S., and Vallejo, L. (2007). "Influence of pile shape and pile interaction on the crushable behavior of granular materials around driven piles: DEM analyses." *Granular Matter*, 9(3-4), 241-250.

McDowell, G. R. (2002). "On the yielding and plastic compression of sand." *Soils Found*, 42(1), 139-145.

McDowell, G. R., and Harireche, O. (2002). "Discrete element modelling of yielding and normal compression of sand." *Geotechnique*, 52(4), 299-304.

Nakata, Y., Hyde, A. F. L., Hyodo, M., and Murata, H. (1999). "A probabilistic approach to sand particle crushing in the triaxial test." *Geotechnique*, 49(5), 567-583.

Wang, J., and Yan, H. (2013). "On the role of particle breakage in the shear failure behavior of granular soils by DEM." *International Journal for Numerical and Analytical Methods in Geomechanics*, 37(8), 832-854.

CHAPTER 9

3D ANALYSIS OF KINEMATIC BEHAVIOR OF GRANULAR MATERIALS IN TRIAXIAL TESTING USING DEM WITH FLEXIBLE MEMBRANE BOUNDARY

This Chapter is a modified version of the paper published in: Cil, M. B., and Alshibli, K. A. (2014). "3D analysis of kinematic behavior of granular materials in triaxial testing using DEM with flexible membrane boundary." *Acta Geotech*, 9(2), 287-298.

Abstract

This paper describes the constitutive behavior and particle-scale kinematics of granular materials in three-dimensional (3D) axisymmetric triaxial testing using the distinct element method (DEM). PFC3D code was used to run the DEM simulations using a flexible membrane boundary model consisting of spherical particles linked through flexible contact bonds. The overall deformation behavior of the specimen was then compared with the specimen with rigid boundary and experimental measurements. Computed tomography (CT) was used to track the evolution of particle translation and rotation within a laboratory triaxial specimen in 3D. The DEM model of the flexible membrane specimen successfully predicted the stress-strain behavior when compared with laboratory experiment results at different confining pressures. The DEM results showed that the rigid specimen applies a uniform deformation and leads to non-uniformities in the confining stress along the particle-boundary interface in the lateral direction. In contrast, the flexible specimen better replicates the uniformly applied confining stress of a laboratory triaxial experiment. The 3D DEM simulations of the specimen with flexible membrane over-predicted particle translation and rotation in all directions when compared to a laboratory triaxial specimen. The difference between the particle translation and rotation distributions of DEM specimens with rigid and flexible membrane is almost negligible. The DEM specimen with flexible membrane produces a better prediction of the macroscopic stress-strain behavior and deformation

characteristics of granular materials in 3D DEM simulations when compared to a specimen with rigid membrane. Comparing macro-scale response and particle-scale kinematics between triaxial simulation results of rigid versus flexible membrane demonstrated the significant influence of boundary effects on the constitutive behavior of granular materials.

Introduction

Researchers widely use the axisymmetric triaxial test in soil mechanics to determine the constitutive behavior of soils. It involves enclosing a cylindrical soil specimen inside an elastic latex membrane to isolate it from the surrounding confining medium. Understanding the fundamentals of specimen behavior in triaxial testing has been a challenge for the geotechnical research community as many experimental and numerical studies were limited to identifying the factors that affect the macro-scale response in triaxial testing. Some researchers have used surface digital imaging techniques (e.g., Alshibli and Sture 2000, Rechenmacher and Finno 2004) to measure strain localization or shear band properties. Such methods are limited to external surface measurements, which are not necessarily representative of the internal properties of the specimen. The internal structure (or fabric) of the specimen is better examined using x-ray computed tomography (CT) to monitor the evolution of deformation and the change in soil fabric (e.g., Desrues *et al.* 1996, Shi *et al.* 1999, Hasan and Alshibli 2010a). Although extensive research has been published to describe the constitutive behavior and deformation characteristics of granular materials, none of these techniques provided a comprehensive 3D evaluation of the relationship between particle-scale kinematics and the specimen macro-scale response.

Distinct element method (DEM), introduced to the geotechnical engineering community by Cundall and Strack (1979), is an explicit numerical approach to model the movement and interaction of individual particles. Since continuum-based constitutive models ignore the independent motion of discrete elements in a granular assembly, the complex disintegration and flow of the particulate system is better modeled with DEM rather than continuum theory. DEM is a powerful technique for providing insight into particle translation and rotation, contact forces and contact points, which are impossible to measure using conventional laboratory techniques. Particle-level kinematics acquired from DEM simulations will enhance our understanding of the mechanics of particulate materials.

The properties and the implementation scheme of the boundary conditions in DEM simulations greatly influence the response of the granular system. A rigid boundary is the most commonly used boundary condition in triaxial simulations of cylindrical specimens (e.g., Lu and Frost 2010, Hasan and Alshibli 2010b) and parallelepiped specimens (e.g., Belheine *et al.* 2009). The rigid boundary is suitable for end-platen representation in triaxial and direct shear tests; however, it does not apply a uniform lateral stress and hinders the onset and growth of strain localization (shear band) in triaxial simulations (Cheung and O'Sullivan 2008). A hydrostatic boundary, proposed by Ng (2004) as an alternative boundary condition for triaxial tests to simulate the chamber confining fluid, does not require additional boundary elements and decreases computational time. Some DEM simulations adopted a periodic boundary that assumes the specimen is surrounded by identical elements in all directions (Ng 1999, Thornton 2000). This technique generally allows a uniform strain field and eliminates the boundary effects; however, its application for triaxial testing is difficult due to the specimen's cylindrical shape. To properly reproduce the flexible latex membrane, researchers have variously used a flexible membrane that is generally modeled using stress-controlled flexible boundary (Cui *et al.* 2007, Wang and Tonon 2009), flexible membrane with multiple rigid cuboid elements (Lee *et al.* 2012), or a flexible bonding approach (Iwashita and Oda 1998, Wang and Leung 2008). Boundary particles are detected and the membrane forces are distributed to these particles in the stress-controlled flexible membrane (Cheung and O'Sullivan 2008). Since no boundary elements are used in this approach, the membrane–specimen interaction could not be examined. In the flexible bonding approach, the membrane is represented by particles linked by flexible contact bonds. Flexible membrane with bonded particles was commonly implemented in 2D biaxial simulations. de Bono *et al.* (2012) recently applied this technique on 3D triaxial simulations of bonded particulate assembly at high pressures. Cheung and O'Sullivan (2008) presented a detailed review of the lateral boundary conditions within the framework of DEM.

A limited number of DEM models used the flexible membrane in triaxial testing simulations to represent experimental boundary conditions. Some of these studies are limited to 2D, which cannot reproduce the physical 3D test conditions accurately (Iwashita and Oda 1998, Evans and Frost 2008, Wang and Leung 2008). 3D implementation of flexible membrane generally requires a complex formulation or expensive computational power (Kuhn 1995, Uthus *et al.* 2008, O'Sullivan and Cui 2009). The main objective of this paper was to develop the flexible membrane with bonded particles in 3D triaxial testing using DEM and compare the particle-scale kinematics with experimental measurements and DEM simulation for a specimen with rigid boundary. As opposed to continuous latex membrane, discrete flexible membrane is made from linked discrete spherical particles that can stretch and contract similar to flexible membrane; however the confining stress which is uniformly exerted onto the latex membrane surface using air or water is reproduced in discrete flexible membrane by applying a certain force to each membrane particle at discrete location. This approach enables mimicking the flexible nature of latex membrane in DEM with a limited number of particles.

Adopting a flexible membrane with bonded particles in 3D offers a significant improvement in triaxial simulations. The properties of the membrane particles can be modified easily, and detecting the boundary particles is unnecessary. Moreover, it allows the investigation of membrane–specimen interaction and provides a computationally efficient numerical solution if the radii of membrane particles are not very small compared to the particle size and dimensions of the specimen since using a large number of membrane particles will result in a significant increase in simulation time. Researchers generally verify the accuracy of the DEM models either by visual comparison of the motion of particles in laboratory and numerical tests (Cleary 2000) or by comparing the macro-scale load response of particulate system with laboratory experiments (O'Sullivan and Cui 2009). In this paper, the DEM triaxial simulation is validated by comparing the stress–strain response of the DEM model with the laboratory triaxial experiments. In addition, the kinematics of particles in 3D laboratory experiments were characterized using CT and compared with DEM simulations using flexible and rigid membrane boundaries to examine the capabilities of the DEM model in simulating particle level interactions. This study did not attempt to make the DEM predictions of particle kinematic behavior match the experimental measurements, but rather to predict these measurements in DEM model and compare them with experimental values.

Experimental Data

The CT scans reported in this paper were performed at NASA/Marshall Space Flight Center (MSFC) CT facility in Huntsville, Alabama, USA. The MSFC CT scanner is a third generation system called FlashCT manufactured by HYTEC Inc., Los Alamos, New Mexico, USA. It is located in a large shielded room that provided ample space to situate our testing equipment next to the CT scanner to conduct in situ scans. To be able to track the movement of particles, one must have a reference for individual particles. Since it was impossible to track rotation of solid spherical particles, white plastic "pearls," 6.5 mm in diameter, with holes through the center, were used in the experiment. A cylindrical specimen with an initial diameter of 46.3 mm and a height of 114.8 mm was prepared to a bulk dry density of 0.57 g/cm^3 and was held under constant vacuum confinement of 25 kPa. Only the middle portion of the specimen was scanned to avoid the influence of end platens. It was labeled with two thin aluminum plates attached to the membrane surface (Figure 9.1) for spatial reference for the CT images. The test cell was placed on the stage of the CT scanner and kept in place until all scanning completed.

The scanning window was kept constant for all scans performed on the specimen. Three CT scans were acquired for the specimen at compression axial strains of ε_z = 0, 7.8, and 13.7%.

The specimen was initially scanned before compression (i.e., when ε_z = 0%) using 100 keV energy and a current of 1.8 mA. The specimen was then compressed to 7.8% global axial strain using the GeoJac loading system while stationed on the stage of the CT system (Figure 9.1a). The loading was then paused and the CT scanning was performed. The process was repeated for the following scan. It took approximately 10 minutes to scan the volume between the two aluminum plates for each case. Post-scan data processing took approximately 5 hours per scan producing about 568

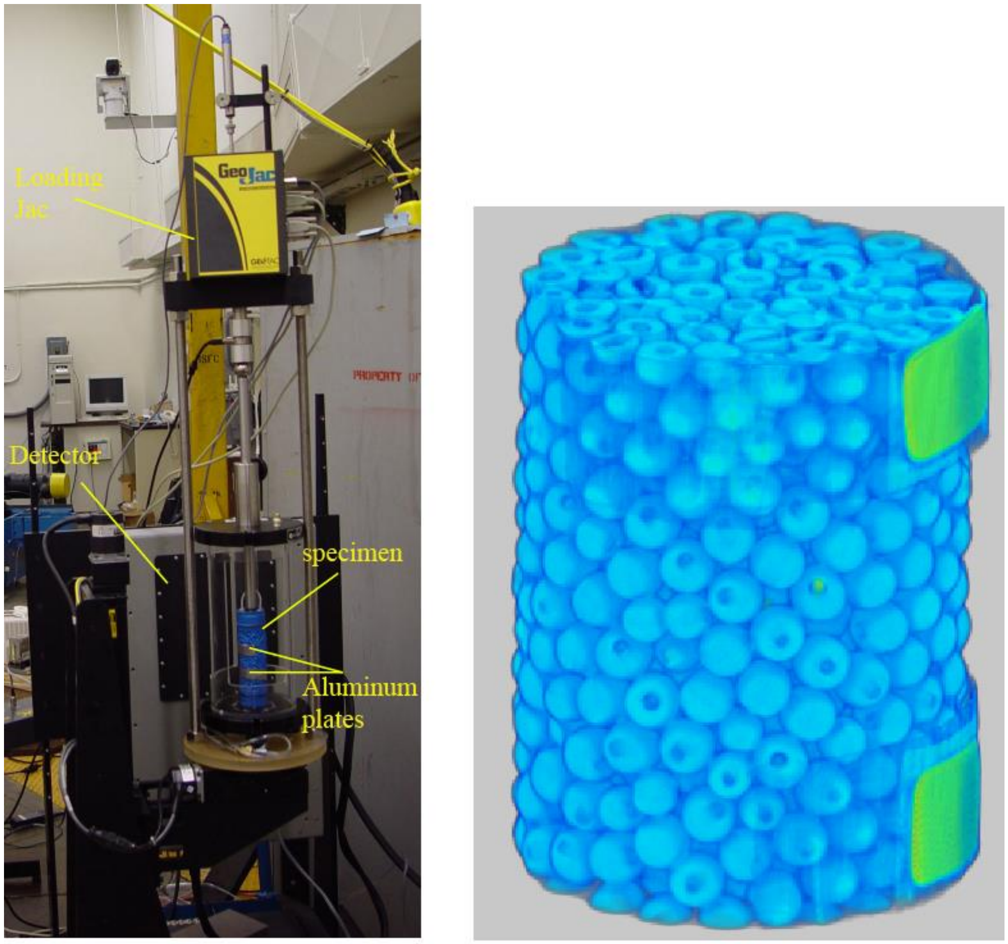

(a) (b)

Figure 9.1. (a) CT scanning setup and (b) CT image before compression.

slices per scan. The CT images have a spatial resolution of 0.11 mm/voxel. All 400 particles between the aluminum plates were tracked in subsequent scans and their translation and rotation angles were quantified as described by Alshibli and Alramahi (2006).

To calibrate and validate the DEM model, two additional triaxial experiments were conducted at 50 kPa and 100 kPa confining pressures. Table 9.1 summarizes the specimen properties; the CT specimen labeled as Test 1. All experiments were compressed at a constant displacement rate of 1 mm/min.

Implementation of the Flexible Membrane Boundary into 3D DEM Triaxial Model

The authors implemented the flexible membrane boundary into triaxial test model using PFC3D software Version 4.0 (Itasca 2008). The DEM model was carried out in four main stages: (i) generation of the specimen at the desired void ratio, (ii) isotropic compression of the specimen, (iii) replacement of lateral rigid walls with flexible membrane, and (iv) compression of the specimen via moving rigid loading platens in the axial direction. Initially, the top and bottom end platens and the lateral cylindrical wall were generated to house the specimen. The lateral cylindrical wall represents the confining stress applied to the specimen. To generate a specimen with the desired void ratio inside the developed DEM cylindrical shell, radii expansion theory (Itasca 2008) was employed. Table 9.2 summarizes the properties of the model elements. The assembly of particles was then subjected to cycling to eliminate large overlaps between particles and to reach the state of equilibrium in the system. This initial configuration represents a packed specimen at the desired void ratio, which is the same as the void ratio of the real specimen. 819, 2303 and 2303 particles were used in Test 1, Test 2 and Test 3 DEM simulations, respectively.

Table 9.1. Summary of the experiments

Experiment	σ_3 (kPa)	Diameter (mm)	Height (mm)	Density (g/cm^3)	Void ratio (e)
Test 1	25	46.3	114.8	0.57	0.637
Test 2	50	70.8	138.1	0.57	0.640
Test 3	100	70.7	138.2	0.57	0.636

Table 9.2. Values of parameters used in DEM model

Parameter	Value
Specimen particles:	
Particle specific density	920 kg/m^3
Particle radius	3.25 mm
Inter-particle friction coefficient	0.26
Normal stiffness	2×10^6 N/m
Shear stiffness	1×10^6 N/m
Membrane particles:	
Particle specific density	800 kg/m^3
Particle radius	0.85 mm
Normal stiffness	0.5×10^4 N/m
Shear stiffness	0.5×10^4 N/m
Normal bond strength	1×10^{10} Pa
Shear bond strength	1×10^{10} Pa

The DEM specimen was subjected to an isotropic consolidation in triaxial testing first followed by deviatoric loading. The confining stress in triaxial DEM simulation was kept constant using a servo-control mechanism, which controls the velocities of the cylinder wall and end platen walls automatically until the rigid walls are replaced with a flexible membrane. Then, a flexible cylindrical wall composed of spherical particles linked with contact bonds is substituted for the lateral rigid wall. After square and hexagonal particle arrangements were explored for the flexible membrane, the hexagonal layout was found to be more appropriate due to contribution of six neighboring particles around each membrane particle for continuity. 90, 135 and 135 membrane particles with a radius of 0.85 mm were used in each row to encase the specimen for Tests 1, 2, and 3, respectively. Membrane particles were small enough to eliminate the flow of particles out of the specimen. Then, the spheres that represent soil particles were fixed in their positions, and the membrane force was distributed onto membrane particles to apply the confining pressure (Figure 9.2a). The confining force applied to each membrane particle was computed based on the quadrilateral area defined using the centers of neighboring membrane particles as illustrated in Figure 9.3. The confining force was applied to each membrane particle and was made equal to the product of quadrilateral area (described in Figure 9.3) and the desired confining pressure. It acted towards the center of the specimen. Since the center of specimen was located at the origin, the magnitude of the membrane particle force was decomposed into x and y components proportional to the position of the sphere (membrane particle) relative to the center of the specimen.

The interaction between the membrane particles and the two end platens was eliminated by specifying a small gap between them to minimize end effects. Particles located at the top and bottom rows of the membrane can move parallel to the loading platens in the axial direction (z-

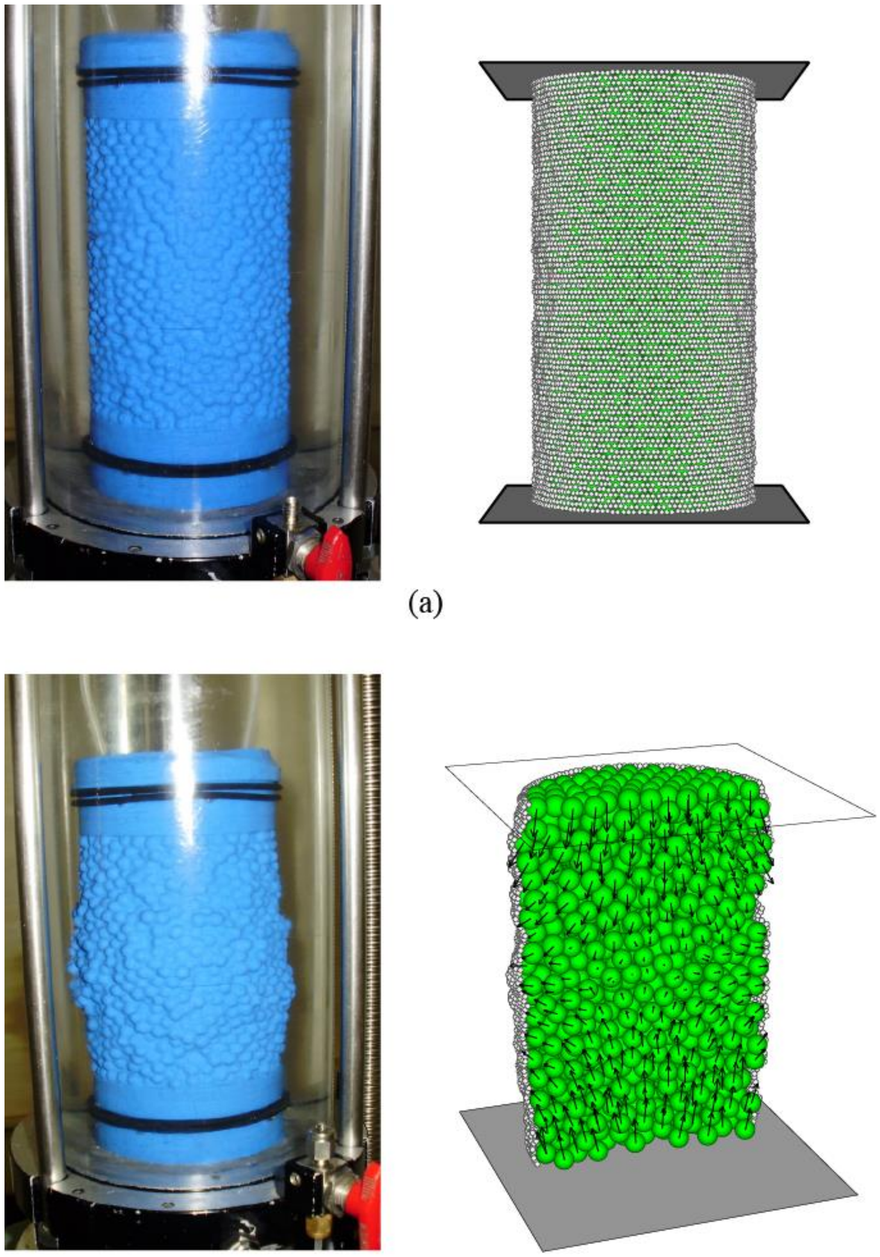

(a)

(b)

Figure 9.2. Experiment and DEM triaxial specimens (a) after isotropic compression and (b) after the shearing stage.

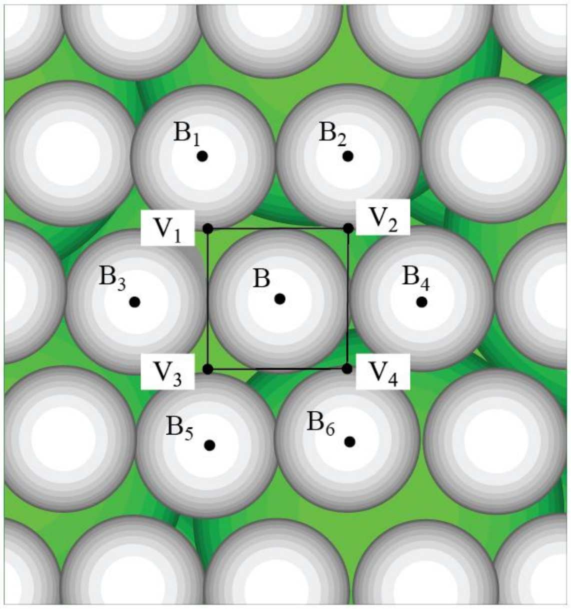

$$V_1 = \frac{\frac{(B + B_3)}{2} + B_1}{2}$$

$$V_2 = \frac{\frac{(B + B_4)}{2} + B_2}{2}$$

$$V_3 = \frac{\frac{(B + B_3)}{2} + B_5}{2}$$

$$V_4 = \frac{\frac{(B + B_4)}{2} + B_6}{2}$$

Figure 9.3. Illustration of the effective area calculation of a membrane particle. V_1, V_2, V_3, and V_4 are the vertices of the quadrilateral. B_1, B_2, B_3, B_4, B_5, and B_6 represent the coordinates of neighboring particles of membrane particle B.

direction) to maintain the gap. Moreover, these edge particles are restricted from movement in the lateral direction (i.e., x- and y-directions) to represent the end platen-specimen transition zone. The vertical spacing between the centers of membrane particles was initially equal to particle diameter in hexagonal layout, which provides a gap between them to prevent excessive overlap between membrane particles during axial compression of the specimen. Since the geometry of the flexible membrane changes during the DEM simulation, the forces applied on the membrane particles were updated to keep the same confining stress according to the procedure described earlier. Finally, the shearing phase was implemented by moving the top and bottom end platens simultaneously at a constant velocity of 0.05 m/s. The loading rate was chosen slow enough to ensure a quasi-static loading condition. Axial stress was calculated by measuring the forces acting on the rigid top and bottom end platens.

Example images of the experimental and DEM specimens at the end of the shearing stage are depicted in Figure 9.2b. Because the laboratory specimen was photographed while the triaxial cell was filled with water, the specimen size appears larger due to refraction through water and the Lexan chamber. Only half of the DEM specimen is shown in Figure 9.2b, and the displacements of particles on the axial plane through the center of specimen are represented with arrows. A similar deformation pattern was observed in experimental and DEM specimens. Particles move towards the middle of the specimen when the compressive load is applied simultaneously from top and bottom end platens. Sheared particles move outwards, and the specimen expands laterally at the middle section (bulging) in both specimens.

The deformation of the flexible membrane and its interaction with specimen are the most important aspects of the calibration of the DEM model. The flexibility of the membrane was governed by the contact bond behavior between membrane particles. The default contact bond model in PFC3D assumes constant normal and shear stiffnesses at the contact. The force-displacement relationships in normal and shear directions are determined based on the contact stiffnesses and are calculated as (Itasca 2008):

$$F^n = -K^n U^n \tag{9.1}$$

$$F^s = k^s U^s \tag{9.2}$$

where F^n is the normal contact force, K^n is the normal stiffness at the contact, U^n is the relative normal displacement (overlap or separation under tensile forces), F^s is the total shear contact force, k^s is the shear stiffness at the contact, and U^s is the total shear displacement measured relative to initial contact position. The relationships described by Equations (9.1) and (9.2) imply that the elastic modulus of the DEM membrane under tensile forces is related to contact stiffnesses between membrane particles and primary interaction occurs in normal direction. Since contact bond acts only in a vanishingly small area, direct modulus comparison between latex membrane and numerical membrane is difficult. Therefore, the membrane particles' stiffnesses were calibrated based on the deformation of a real membrane per unit length assuming the same thickness of both membranes. This approach gave relatively low particle normal stiffness (1.2 kN/m), and the DEM membrane particles accumulated at certain locations during the application of confining pressure due to high flexibility. Therefore, stiffnesses of the membrane particles were determined by considering the effect of other model parameters. Model parameters were calibrated through trial and error to match the stress-strain behavior of a laboratory experiment and to provide an elastic membrane behavior in the DEM simulation. Membrane particles' normal and shear stiffness values were found to be 5 kN/m.

The low stiffnesses of membrane particles might lead to slightly higher contact overlap in specimen-membrane particle interactions compared to the overlap occurring between particles with high stiffnesses. Since all triaxial DEM simulations were conducted at relatively low confining pressures (25 kPa to 100 kPa), and confining forces were distributed onto 90 and 135 membrane particles in each row, the overlap caused by the confining force applied on each membrane particle was relatively small compared to the radii of specimen particles and is appropriate for specimen-soft membrane interaction representation. Therefore, the standard contact model was adopted for membrane particles in lieu of generating a more complex alternative contact model with different tensile and compressive stiffness behavior. Based on our parametric evaluation, we found that the bonding strength between membrane particles has no effect on the stress-strain behavior. However, it was found that the flexible bond between membrane particles breaks at low tensile strength values and the membrane loses its continuity. Therefore, the magnitude of membrane bonding needs to be higher than the tensile force generated between the membrane particles. Furthermore, a series of DEM simulations performed by varying only interparticle friction coefficient showed that an increase in the inter-particle friction coefficient of specimen particles results in a higher deviator stress, which is in agreement with Thornton (2000)'s findings.

Validation of the DEM Simulations

The DEM model parameters were calibrated using Test 2 experimental results. The calibrated DEM model was then used to run simulations for Tests 1 and 3 to validate the model. Figure 9.4a depicts the results of the DEM simulations with flexible membrane and laboratory experiments. The laboratory experiments exhibited an oscillatory response due to slip-stick between the particles since the specimen is composed of mono-sized spherical particles with identical surface properties and morphology (Alshibli and Roussel 2006). There was good agreement between the DEM simulations and laboratory experiments. The deviator stress gradually increased and reached a nearly constant value, which continued until the end of the tests. The initial slope and the post-peak response of the laboratory experiments are closely captured by the DEM model using the flexible membrane. Additional triaxial simulations were conducted using a rigid cylindrical boundary at three confining pressures (25 kPa, 50 kPa and 100 kPa) to investigate the influence of membrane properties on the behavior of granular materials. The same model parameters were used for rigid and flexible boundary simulations. The stress-strain relationship comparison of two membrane approaches showed in Figure 9.4b which demonstrated that DEM simulations using the rigid membrane exhibited similar stiffness trend initially, but they slightly underestimated the deviator stress in the post-peak regime compared to the DEM model with flexible membrane boundary.

Contact Forces

DEM triaxial simulations provide an insight into the micro-mechanical kinematics and force chains within the fabric of granular materials. Examining the evolution of contact force

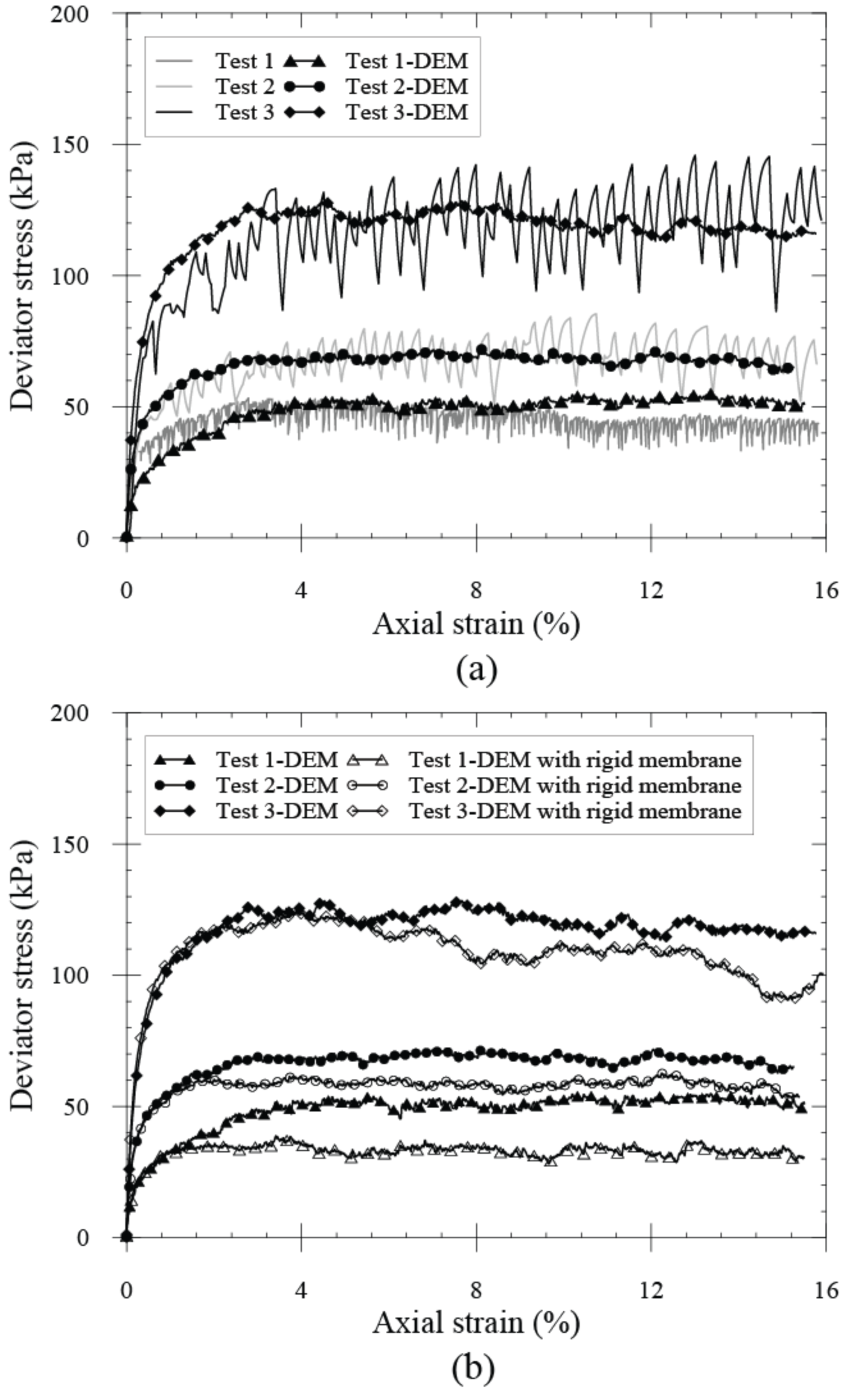

Figure 9.4. Axial strain versus deviator stress comparison of (a) laboratory experiments and DEM simulations with flexible membrane and; (b) DEM simulations with flexible and rigid membranes.

distribution during the simulation process provides unique information about the force transmission mechanism that occurs during triaxial testing. The contact force distributions of the triaxial simulation with rigid and flexible membranes at nominal compressive axial strain (ε_z) values of 0, 1.0, 2.0, 4.0, 7.8, 12% are shown in Figure 9.5. The 3D contact force networks are scaled by 20 N which provides the same thickness scale for the magnitude of contact forces at all strain levels. In contrast to 2D representation, plotting the contact force variation in 3D enables examining out-of-plane forces and force transmission geometry in all directions. The contact force between two touching particles is represented by a straight line that connects the centers of the two particles or particle-to-rigid boundary. The thickness of the line is directly proportional to the magnitude of the contact force. A randomly oriented homogenous contact force network is observed in both horizontal and vertical directions due to isotropic consolidation in triaxial tests with a flexible membrane before loading (ε_z = 0%). In contrast, the rigid membrane cannot apply a uniform confining pressure along the boundary, which resulted in the development of major chains of contact forces and stress concentrations in the lateral direction (Figure 9.5b). When the specimen was loaded in the axial direction, the values of contact forces began to increase, especially at certain locations for the specimen with flexible membrane. This network demonstrates the development of stronger force chains with nearly vertical orientation in the central region to resist the applied axial stress up to the peak stress state. Continuous shearing leads to anisotropy in the contact force chain network. The force chains continued to collapse with new chains developing at different parts of the specimen during the loading (see variation in Figure 9.5). Secondary contact force chains that carried smaller loads also supported the major force chains that carried the majority of the applied deviator stress.

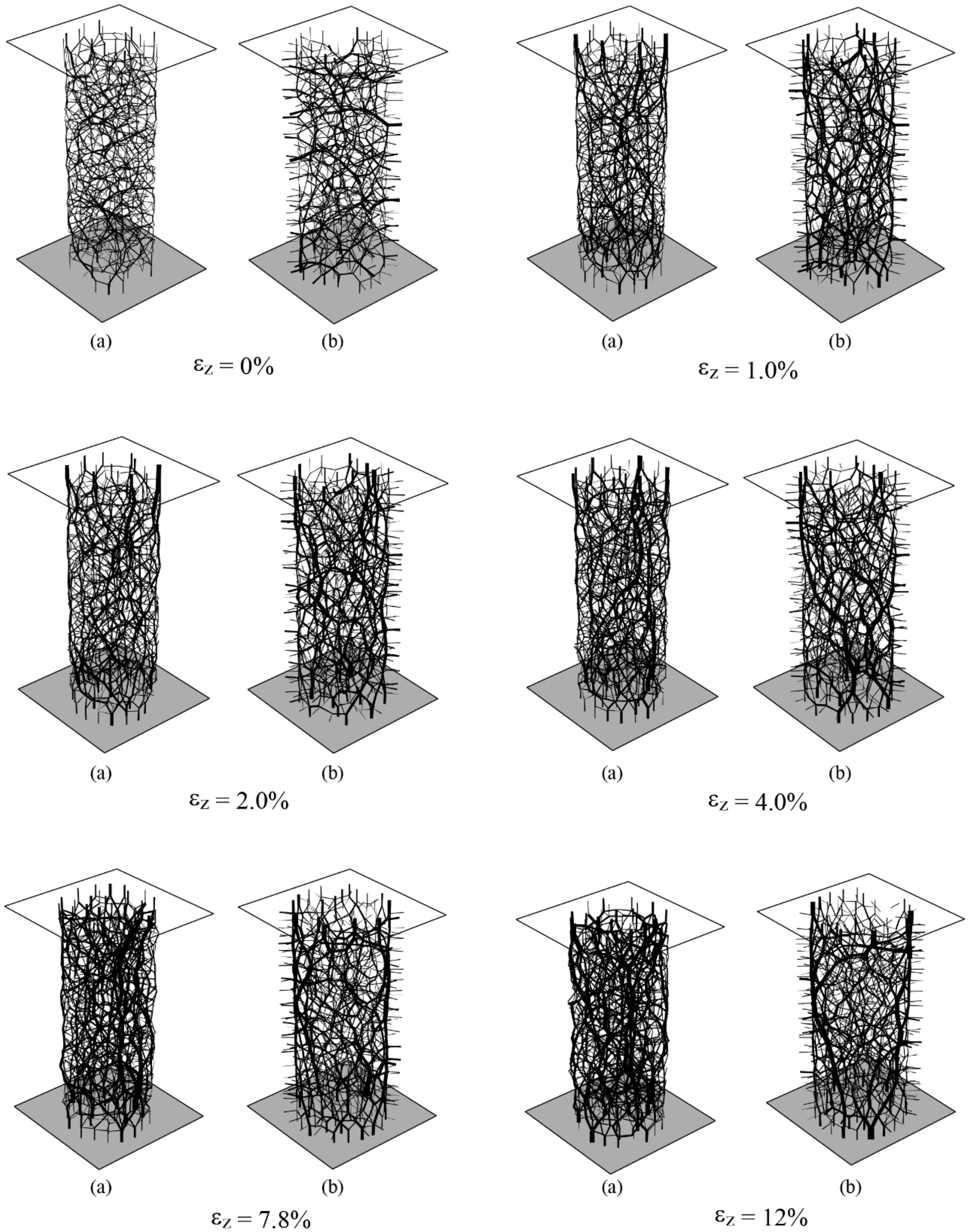

Figure 9.5. Contact force distribution of triaxial simulation using (a) flexible membrane and (b) rigid membrane.

The force chains undergo a different evolution process in the triaxial simulation with rigid membrane. High contact forces form throughout the simulation at the rigid membrane-specimen interface. Moreover, a strong force network generally develops at random locations and extends towards the rigid wall. The magnitudes of force chains at high strain levels are smaller than the ones of the flexible membrane case, which might be attributed to the stress localizations along the rigid membrane boundary. This pattern demonstrates the significant effect of rigid wall on contact force distribution.

Particle Kinematic Behavior

The CT scans discussed earlier provide a unique data set for examining the DEM simulation reproduction capabilities in terms of kinematics at the particle level since they represent 3D experimental measurements. The experiment was conducted on ideal spherical particles that can be easily modeled using DEM. Therefore, a possible DEM model error due to particle shape is eliminated in this analysis.

DEM is primarily used to model the interaction and kinematics of granular materials. Therefore, confirming the capability of DEM in simulating the particle displacement increases confidence in using it as a tool to predict the behavior of granular materials. The displacements of particles (Δx, Δy, Δz) in x, y, and z directions (where x and y axes lie in the horizontal plane or the axisymmetric plane and z is in the axial direction) and cumulative particle rotations (θ_x, θ_y, θ_z) about the x, y, and z axes are presented using normalized frequency distribution histograms, which are shown Figure 9.6 through Figure 9.8. As mentioned earlier, axial loading was modeled by moving both rigid end platens against each other at a constant velocity to maintain monotonic

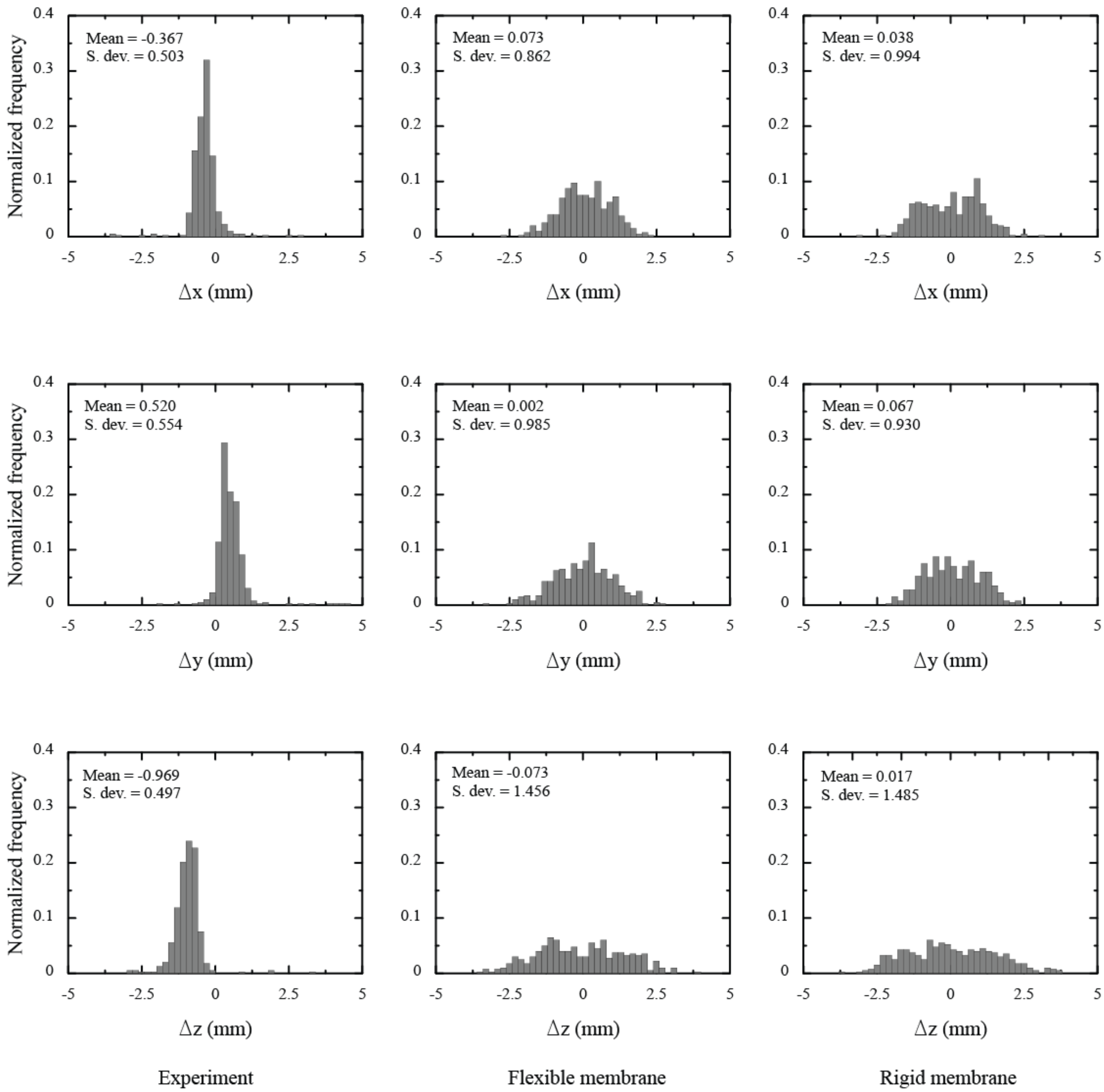

Figure 9.6. Frequency distribution histograms of particle translation at 7.8% strain in laboratory experiment, DEM triaxial simulations with flexible membrane and rigid membrane.

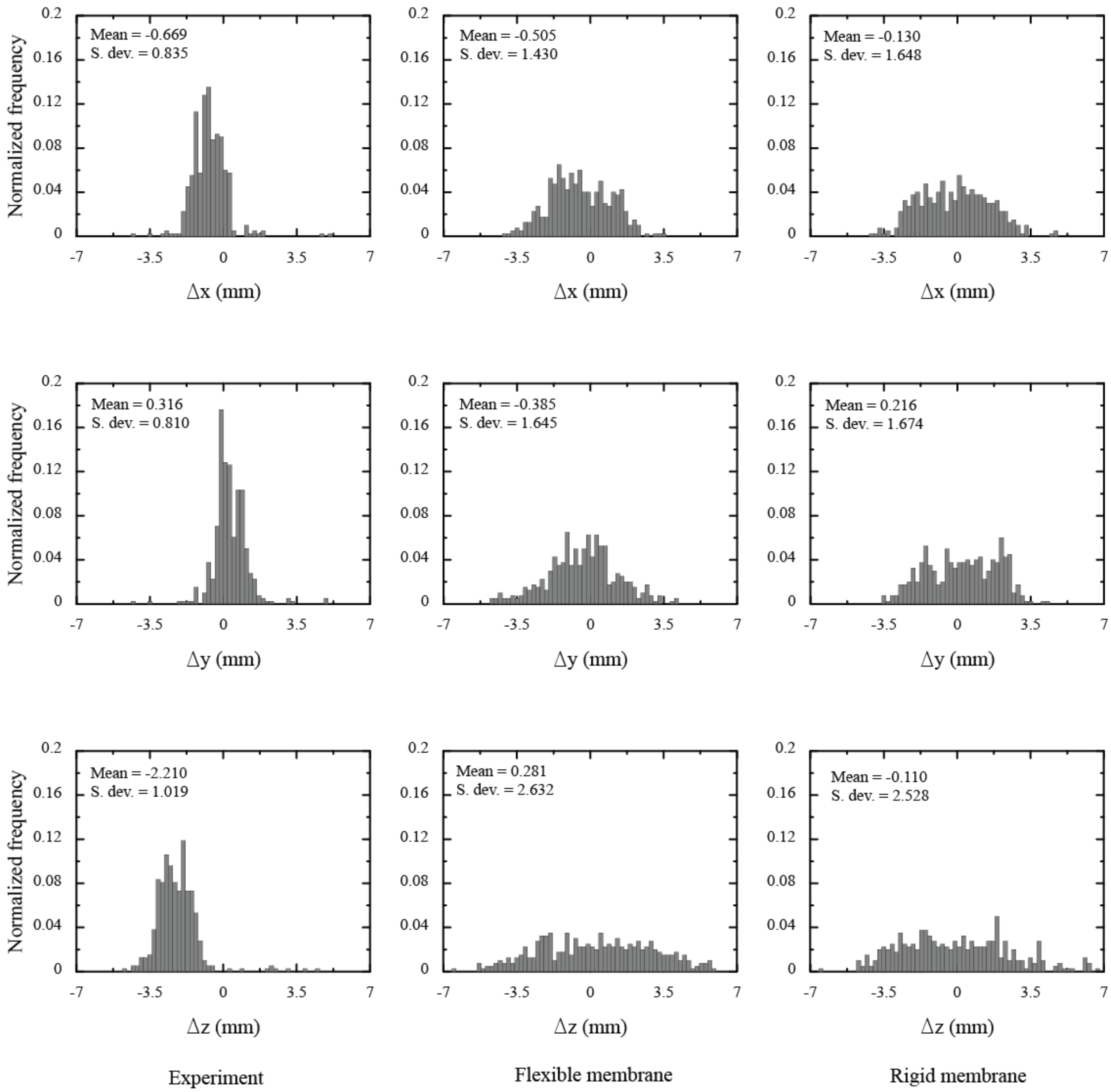

Figure 9.7. Frequency distribution histograms of particle translation at 13.7% strain in laboratory experiment, DEM triaxial simulations with flexible membrane and rigid membrane.

loading and symmetrical deformations. Due to this loading condition, particles located close to the end platens have higher displacement values compared to those close to the middle of the specimen in the axial direction. As mentioned earlier, the CT scans were limited to the middle portion of the specimen, which included enough particles (400) for a reliable statistical analysis. The measurements shown in Figure 9.6 through Figure 9.8 are for 400 particles located in the middle half of DEM specimens for better comparison with the measurements of the CT specimen.

The translation of particles at 7.8% and 13.7% strain of the CT specimen and DEM simulations with flexible and rigid membranes are shown in Figure 9.6 and Figure 9.7. Referring to Figure 9.6, experimental measurements exhibit smaller translations values (Δx, Δy, and Δz) when compared with the rigid and flexible membrane simulations. The mean values of Δx and Δy distributions for the experiment are slightly skewed towards negative and positive values, respectively. On the other hand, the means of translation distributions in x and y directions in both DEM simulation results are close to zero; and the standard deviations of distributions are almost same in the DEM rigid and flexible membrane models. Most particles exhibit negative Δz in the experiment because loading was applied from the top of the specimen. The translations in the z-direction (Δz) in both DEM cases have a wide displacement distribution with a mean value close to zero due to loading via both end platens at the same time. Similar trends are observed in Figure 9.7. More translation is recorded as the compression increased, which is expected. The translations in the x and y directions (Δx and Δy) of flexible membrane case are slightly skewed towards the negative values, which indicates the flow of particles towards the membrane. In summary, the DEM model overestimates the translation of particles compared to the laboratory measurements, and the difference between the variations of the distributions is negligible for the rigid and flexible membrane specimens.

Δx and Δy distributions in Figure 9.6 and Figure 9.7 demonstrate the influence of lateral boundary on particle kinematic behavior. The statistical analysis of results showed that flexible membrane distributions better fit the normal distribution compared to the rigid membrane ones. It appears that the flexible membrane offers less restraint for particles to move and rotate in the lateral direction, which resulted in irregular deformed shape. On the other hand, the rigid membrane applies a uniform lateral deformation by moving the planar lateral wall rigidly towards/away from the specimen, which leads to similar inward/outward displacement of particles along the height of the specimen. Since the stress on the rigid wall was determined according to the particles in contact with it, the wall position was controlled based on the movement of contacting particles. As shown in the contact force network, some particles have high contact forces at the specimen-boundary interface. An irregular boundary due to large particle size and a limited number of particles in a relatively small specimen also contributed to the development of stress concentrations near the rigid wall. Therefore, when the particles with high contact forces move outwards laterally due to axial compression, the rigid wall will expand to keep the confining pressure constant even though many particles near the boundary have smaller contact forces compared to these particles. This behavior leads to similar translation of particles located at same radial distance relative to the specimen center in the horizontal plane due to rigid radial movement of the lateral boundary. Particles close to the rigid boundary will have higher translation than those at the center of specimen. This configuration results in a wider non-normal distribution of displacements in specimen with rigid boundary for x–y plane translations compared to the flexible membrane case.

Monitoring particle rotation helps to clarify the details of the particle-scale deformation mechanism. Iwashita and Oda (2000) found that high particle rotation occurs within the shear band for circular particles in 2D DEM biaxial compression simulations with flexible boundaries. However, Cheung and O'Sullivan (2008) stated that rigid lateral boundary leads to the development of multiple high rotation gradients in different locations in 2D biaxial simulations. To further investigate the capability of DEM in capturing particle rotation in 3D, cumulative particle rotations were monitored and compared with the results obtained using CT images (Alshibli and Alramahi 2006). The cumulative particle rotations at 13.7% strain value are presented using frequency distribution histograms as shown in Figure 9.8, which demonstrates that particles in the CT experiment exhibit less rotation than DEM particles. The mean values of the rotations are close to zero (between -2.55° and 1.00°), which indicates that particles do not have preferable clockwise or counter-clockwise rotations. Moreover, particles in both DEM simulations exhibited similar rotational behavior in the three directions. The standard deviation of rotations in DEM simulation with rigid membrane is almost same as the flexible membrane case. It appears that translation and rotation of particles have similar trends. It is interesting to observe that DEM simulation results with both rigid and flexible membranes produced higher particle translation and rotation when compared to experimental measurements in 3D. The findings of this paper clearly present the first DEM triaxial simulations in 3D that document particle kinematics and compare them with 3D experimental measurements quantitatively. One may conclude that the 3D DEM analysis yields similar rotation and translation distributions with rigid and the flexible membrane models.

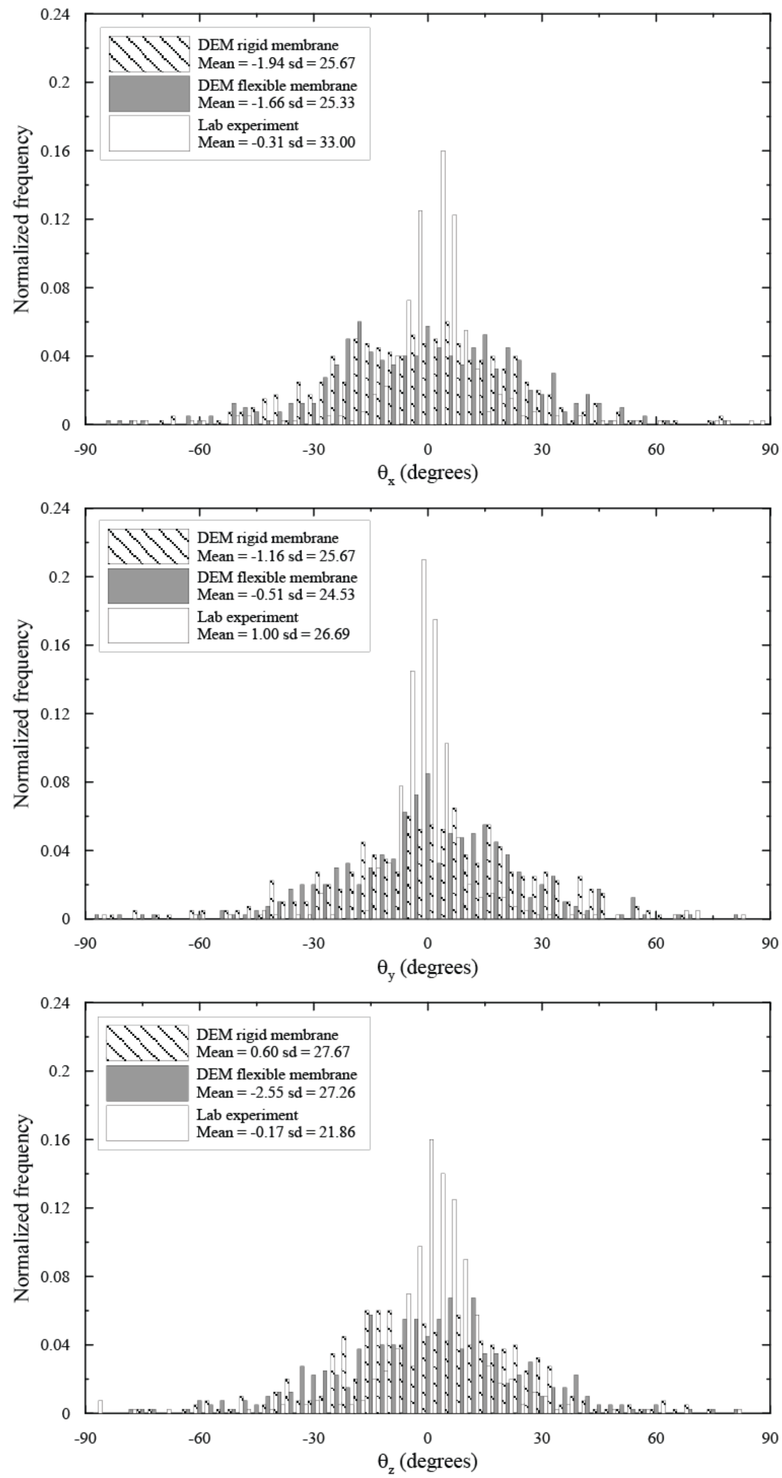

Figure 9.8. Frequency distribution histograms for rotations at 13.7% axial strain.

Conclusions

Triaxial test is simulated in 3D within the framework of DEM using a flexible membrane and a rigid membrane boundary. The flexible membrane was composed of spherical particles that were linked by flexible contact bonds. The DEM model was successfully validated using experimental triaxial measurements that were conducted on spherical plastic beads at different confining pressures. The results showed that the flexible membrane can replicate the experimental boundary conditions better than a rigid membrane.

The column-like force chains that resist the majority of the applied axial load are quantified and displayed using contact force distribution network. A randomly oriented contact force network was initially observed for the DEM specimen with flexible membrane, which evolved to orient themselves mostly in the direction of the major principal stress. The force chains undergo a different evolution process in the triaxial simulation with a rigid membrane. High contact forces form throughout the simulation at the rigid membrane-specimen interface, which clearly demonstrates the profound influence of rigid membrane boundary.

The CT scans provided unique experimental measurements of particle kinematics to compare with DEM simulations in 3D. The DEM simulations over-predict the translation of particles in all directions when compared to experimental measurements with similar distributions of particle translation in specimens with rigid membrane and flexible membrane model. Also, 3D DEM over-predicts particle rotation compared with experimental measurements. The difference between the particle rotation distributions of DEM specimens with rigid and flexible membrane is found to be negligible. In contrast with rigid membrane, the use of flexible membrane in 3D DEM simulation produces closer prediction for the constitutive behavior and deformation characteristics of granular materials. The lack of agreement at particle kinematics between CT measurements and the DEM model calibrated based on macro-scale response of physical test reveals that DEM models may need to be calibrated according to both macro- and particle-scale behavior of granular assembly in near future by using advanced experimental techniques to have more confidence in the DEM results.

Acknowledgments

This material is based on work supported by the National Science Foundation under Grant No. CMMI-1156436. Any opinions, findings, conclusions or recommendations expressed in this material are those of the authors and do not necessarily reflect the views of the National Science Foundation. Also, the authors thank Dr. Ron Beshears, Mr. David Myers, and Mr. Buddy Guynes of NASA/Marshall Space Flight center for helping us to perform the CT scans.

References

Alshibli, K., and Roussel, L. E. (2006). "Experimental investigation of slip-stick behaviour in granular materials." *International Journal for Numerical and Analytical Methods in Geomechanics*, 30(14), 1391-1407.

Alshibli, K. A., and Alramahi, B. A. (2006). "Microscopic Evaluation of Strain Distribution in Granular Materials during Shear." *Journal of Geotechnical and Geoenvironmental Engineering*, 132(1), 80-91.

Alshibli, K. A., and Sture, S. (2000). "Shear Band Formation in Plane Strain Experiments of Sand." *Journal of Geotechnical and Geoenvironmental Engineering*, 126(6), 495-503.

Belheine, N., Plassiard, J. P., Donzé, F. V., Darve, F., and Seridi, A. (2009). "Numerical simulation of drained triaxial test using 3D discrete element modeling." *Computers and Geotechnics*, 36(1–2), 320-331.

Cheung, G., and O'Sullivan, C. (2008). "Effective simulation of flexible lateral boundaries in two- and three-dimensional DEM simulations." *Particuology*, 6(6), 483-500.

Cleary, P. W. (2000). "DEM simulation of industrial particle flows: case studies of dragline excavators, mixing in tumblers and centrifugal mills." *Powder Technol*, 109(1–3), 83-104.

Cui, L., O'Sullivan, C., and O'Neill, S. (2007). "An analysis of the triaxial apparatus using a mixed boundary three-dimensional discrete element model." *Geotechnique*, 57(10), 831-844.

Cundall, P., and Strack, O. (1979). "A Discrete Numerical model for Granular Assemblies." *Geotechnique*, 29(1), 47-65.

de Bono, J., McDowell, G., and Wanatowski, D. (2012). "Discrete element modelling of a flexible membrane for triaxial testing of granular material at high pressures." *Géotechnique Letters*, 2(October-December), 199-203.

Desrues, J., Chambon, R., Mokni, M., and Mazerolle, F. (1996). "Void ratio evolution inside shear bands in triaxial sand specimens studied by computed tomography." *Geotechnique*, 46(3), 529-546.

Evans, T. M., and Frost, J. D. (2008)."Membrane Effects on Microstructure Evolution in 2D DEM Experiments." *ASCE GeoCongress 2008*, (A. N. Alshawabkeh, K. R. Reddy, and M. V. Khire eds), *New Orleans, Louisiana*, 958-965.

Hasan, A., and Alshibli, K. A. (2010a). "Experimental assessment of 3D particle-to-particle interaction within sheared sand using synchrotron microtomography." *Geotechnique*, 60(5), 369-379.

Hasan, A., and Alshibli, K. A. (2010b). "Discrete Element Modeling of Strength Properties of Johnson Space Center (JSC-1A) Lunar Regolith Simulant." *Journal of Aerospace Engineering*, 23(3), 157-165.

Itasca (2008). *Particle Flow Code in Three Dimension (PFC3D) Version 4.0*, Itasca, Consulting Group Inc., Minneapolis, MN.

Iwashita, K., and Oda, M. (1998). "Rolling Resistance at Contacts in Simulation of Shear Band Development by DEM." *Journal of Engineering Mechanics*, 124(3), 285-292.

Iwashita, K., and Oda, M. (2000). "Micro-deformation mechanism of shear banding process based on modified distinct element method." *Powder Technol*, 109(1–3), 192-205.

Kuhn, M. R. (1995). "A flexible boundary for three-dimensional dem particle assemblies." *Engineering Computations*, 12(2), 175-183.

Lee, S. J., Hashash, Y. M. A., and Nezami, E. G. (2012). "Simulation of triaxial compression tests with polyhedral discrete elements." *Computers and Geotechnics*, 43, 92-100.

Lu, Y., and Frost, D. (2010)."Three-Dimensional DEM Modeling of Triaxial Compression of Sands." *GeoShanghai 2010 International Conference*, (R. Meier, A. Abbo, and L. Wang eds), *Shanghai, China*, 220-226.

Ng, T.-T. (1999). "Fabric Study of Granular Materials after Compaction." *Journal of Engineering Mechanics*, 125(12), 1390-1394.

Ng, T.-T. (2004). "Triaxial Test Simulations with Discrete Element Method and Hydrostatic Boundaries." *Journal of Engineering Mechanics*, 130(10), 1188-1194.

O'Sullivan, C., and Cui, L. (2009). "Micromechanics of granular material response during load reversals: Combined DEM and experimental study." *Powder Technol*, 193(3), 289-302.

Rechenmacher, A. L., and Finno, R. J. (2004). "Digital image correlation to evaluate shear banding in dilative sands." *Geotech Test J*, 27(1), 13-22.

Shi, B., Murakami, Y., Wu, Z., Chen, J., and Inyang, H. (1999). "Monitoring of internal failure evolution in soils using computerization X-ray tomography." *Engineering Geology*, 54(3–4), 321-328.

Thornton, C. (2000). "Numerical simulations of deviatoric shear deformation of granular media." *Geotechnique*, 50(1), 43-53.

Uthus, L., Hopkins, M. A., and Horvli, I. (2008). "Discrete element modelling of the resilient behaviour of unbound granular aggregates." *International Journal of Pavement Engineering*, 9(6), 387-395.

Wang, Y., and Tonon, F. (2009). "Modeling Triaxial Test on Intact Rock Using Discrete Element Method with Membrane Boundary." *Journal of Engineering Mechanics*, 135(9), 1029-1037.

Wang, Y. H., and Leung, S. C. (2008). "A particulate-scale investigation of cemented sand behavior." *Can Geotech J*, 45(1), 29-44.

CHAPTER 10

CONCLUSIONS AND RECOMMENDATIONS

Summary and Conclusions

In this dissertation, two powerful experimental techniques, 3DXRD and SMT, were combined with DEM method to characterize the underlying micromechanics of granular materials. The volume-averaged lattice strain measurements of individual silica sand particles within a sand assembly subjected to 1D compressional loading were measured for the first time using 3DXRD. The evolution and distribution of particle fracture and deformation characteristics of a mass of sand particles were monitored in situ non-destructively across the scales via 3D SMT imaging technique. In addition, DEM simulations were first calibrated and validated using laboratory experiments. Simulations were then used to model and quantify micro-scale processes including contact force network and the fracture mechanics of crushable agglomerates. Such micromechanical information not only provides insight into the micromechanics occurring during the deformation of particulate systems, but also helps to better understand the role of particle-scale interactions in macroscopic response. The summary of the dissertation findings is as follows:

1. 3DXRD provides exciting opportunities for researchers in the geomechanics community since it allows direct measurement of the constitutive behavior of individual particles in granular crystalline materials such as silica sands. Initially, the lattice strain measurements were obtained from a column composed of three sand particles as proof of concept. The results were consistent in three experiments and demonstrated that the axial normal strain ε_{zz} exhibited a linear response in the range of $0\text{-}10^{-3}$ to the applied axial load between 0-30 N up to particle fracture, and the volumetric strain decreased almost linearly as the axial load increased.

2. The measured lattice strain tensors were analyzed and used to compute corresponding stress tensors using general elastic constitutive relationship. The σ_{zz} stress component of all nine sand particles in the direction of loading varied linearly in agreement with the expectations. These quantitative stress-strain measurements at the particle level are very valuable for developing, validating or calibrating micromechanics-based finite element and discrete element models to predict the constitutive behavior of granular materials.

3. 3DXRD technique was applied to a specimen composed of larger number of sand particles. ε_{zz} value increased in many particles as the compression proceeded. Moreover, significant variation and fluctuations were observed in the measured lattice strain tensor components, which is attributed to the complex deformation behavior and non-homogenous contact force network of the sand assembly. When a particle fractures, the measured lattice strain values vary significantly from particle to particle due to several factors including the number, position and magnitude of contacts, particle shape and size, and the orientation of particle in the specimen.

4. The fracture mechanics of sand particles under 1D compression was characterized noninvasively using 3D high resolution SMT images for the first time at the particle and laboratory-size specimen scales. The in situ visualization of individual sand particles demonstrated that a major crack initiates from the highly loaded contact points, and propagates parallel to the plane that connects the contact points, and eventually particle fracture occurs in the form of catastrophic splitting with no evidence of local asperity damage.

5. The SMT images revealed that particle fracture does not evolve homogenously throughout the specimen, but rather concentrates at certain locations close to the loading platen. Quantitative analysis of SMT images showed that sand fracture initiates with yielding and increases progressively as the compression continues.

6. DEM simulations indicated that the model parameters of agglomerates calibrated based on the single particle compression experiments were unable to reproduce the stress-strain behavior at laboratory specimen size due to variation in boundary conditions, particle interactions and heterogeneous force transmission in larger specimen sizes. Contact force networks in 1D compression experiment simulations showed that bond breakages occur in agglomerates that are subjected to high contact forces in strong force chains.

7. In DEM simulations, most of the bond breakages in agglomerates are concentrated along the plane that extends between highly loaded contact points until catastrophic splitting, which is similar to the failure mode of sand particles observed in SMT images. Moreover, the majority of bond breakages were in the form of tensile (normal) failure in crushable agglomerates. The SMT images and DEM results also revealed that the onset of particle fracture and specimen yielding occur at the same strain level in the 1D compression test.

8. Crushable agglomerates can closely capture the 3D physical shape of sand in DEM model by mapping the 3D volume data from SMT images. However, this approach requires a high number of spherical sub-particles in agglomerates to better mimic the overall shape of particles. Single particle compression simulations that adopted this approach and SMT images demonstrated that particle morphology and particle-platen contact configuration highly influence the fracture behavior of the particle.

9. Triaxial test simulations showed that DEM simulation with flexible membrane better replicates the uniformly applied confining stress of a laboratory triaxial experiment compared to the triaxial simulation with rigid lateral boundary. The DEM model that was calibrated based on the macro-scale response of laboratory test failed to capture the particle kinematics of laboratory specimen characterized using CT. These results show that DEM models may need to be calibrated according to both macro- and particle-scale behaviors of granular assemblies in the near future by using advanced experimental techniques.

Recommendations

The following recommendations are proposed for future work:

1. The 3DXRD technique can be used to measure the lattice strain of individual particles in larger specimen sizes under different loading conditions such as axisymmetric triaxial testing. Such micro-scale measurements will help to better understand and characterize the failure mechanisms such as shear bands in granular materials.

2. The calculated volume-averaged lattice stresses can be related to interparticle contact forces, which provide key information to characterize the force transmission mechanism in granular media. Knowing lattice strains, stresses, and particle kinematic behavior provides a unique opportunity to formulate and develop a micromechanics-based constitutive model to fully characterize strength properties and deformation characteristics of granular materials based on real particle-scale data for the first time.

3. The crushable agglomerates that closely match the 3D physical sand particle morphology extracted from the SMT images can be used to model particle fracture in larger specimen sizes if higher computational power becomes available. Moreover, different packing configurations of spherical sub-particles such as random packing can be used to increase the efficiency of the model.

4. Particle fracture phenomenon in saturated and partially saturated granular materials can be investigated in 3D using SMT imaging technique as demonstrated in this dissertation. Moreover, the influence of the size and distribution of flaws within sand particles on fracture strength may be identified using very high resolution SMT images (pixel resolution = 0.7 – 1 μm).

VITA

Mehmet Burak Cil was born and raised in Turkey. He graduated from Bogazici University in Istanbul, Turkey with a Bachelor of Science degree in civil engineering in July 2009. After finishing his undergraduate study, he came to Louisiana State University to pursue his graduate study and received a Master of Science degree in civil engineering in August 2011. He started his Ph.D. study in the geotechnical engineering program in the Civil and Environmental Engineering Department at University of Tennessee under the supervision of Dr. Khalid Alshibli in August 2011. His research interests include numerical modeling, non-destructive imaging using x-rays and neutrons, energy geotechnology, experimental soil mechanics and geotechnical engineering.